Linking micellar phases to peptide supramolecular hydrogels

Thesis submitted in accordance with the University of Liverpool requirements for the degree of

Doctor of Philosophy

by

Andre Joao Zamith Cardoso

Department of Chemistry

December 2017

UNIVERSITY OF LIVERPOOL

Supervised by:

Professor Dave J. Adams

Chemistry Department, University of Liverpool

Examined by:

Dr Cécile Ayako Dreiss

Institute of Pharmaceutical Science, King's College London

Dr Tom McDonald

Chemistry Department, University of Liverpool

DECLARATION

I hereby certify that this dissertation constitutes my own product, that where the language of others is set forth, quotation marks so indicate, and that appropriate credit is given where I have used the language, ideas, expressions or writings of another.

I declare that the dissertation describes original work that has not previously been presented for the award of any other degree of any institution.

Signed,

____

Index

Acknowledgements

I am very thankful to Prof. Dave Adams and the University of Liverpool for the vote of confidence, guidance, financial support, critical scientific observations, and the exciting opportunity to be part of a growing world-class leading research laboratory.

I am thankful to the British Society of Rheology, Institut Laue-Langevin, STFC Rutherford Appleton Lab and the Macromolecular Chemistry Group UK, part of a joint interest from the Royal Chemistry Society and the Society of Chemical Industry, for the travel grants, awarding me oral communications of our research, experiments and broadening my analytical and polymer chemistry knowledge. I am very thankful to Dr Cécile Ayako Dreiss and Dr Tom McDonald for the very good feedback, discussions and corrections to this thesis.

Many thanks to Lin Chen, Jaclyn Raeburn, Matthew Wallace, Ana Castilla, Laura Mears, and Hugh Peters for the discussions and feedback on some of my Thesis chapters. I am thankful to Dr. Marco Marcello and the Centre for Cell Imaging, Liverpool, for the training, continuous support and advice with regards the LSCM imaging; Dr. Luning Liu and Matthew Faulkner for the training, support and guidance with the AFM experiments; Prof. Peter C. Griffiths and Dr. Beatrice N. Cattoz for the discussions and support with the SANS experiments; Dr. Bill Frith and Steve Goodyer for helpful rheology discussions.

I am very grateful to my parents, Manuel Cardoso and Judite Zamith Cruz for the constant support, financial support, conscious scepticism and experience making their own PhD thesis. I am thankful to them for being brave to deal with seeing their son leave home at 18 to study abroad for 10 years, help me adapt and be resilient during several unexpected situations along the way.

To my grandparents, who supported me while they were alive and made me appreciate life with their guidance. Despite not being able to fully support you over your last years, I will never forget all the moments of brilliance we had during my childhood and the constant trust in me during my Thesis research.

To my aunt Maria Emilia and uncle Zé Augusto, my cousins Miguel and Pedro, all a fantastic source of happiness, fun times and support, without whom I would have never been able to collect grapes and make wine during some weekends away. To my beloved family Luis, Ana, Zé Silveira and Cesaltina Duarte for their spark of joy.

To my partner Ella Houston who believed in me throughout, cared with the love only

she can give and made me so many unforgettable surprises, creative inspirational nanotechnological works of art and funny stories. To her family, John and Julie Houston for refreshing support, teaching me some survival and technical skills, many laughs, relaxed and good moments.

To my close friends, Francisco Fechas, Eduardo Bicacro, Anca Rapcencu, Miguel Coelho, Konstantin Luzyanin, Vasilis Tzoganis, Joe Steele, Steve Goodyer, Jim Barker, Jonathan Wooler, Mark Goodwin and Andrew Aspinal for all the good moments, inspiration to self-improve, make me feel home and genuine friendship.

List of Publications

Cardoso, A. Z., Mears, L. L. E., Cattoz, B. N., Griffiths, P. C., Schweins, R., & Adams, D. J. (2016). Linking micellar structures to hydrogelation for salt-triggered dipeptide gelators. *Soft Matter*, *12*(15), 3612–3621.

Raeburn, J., Mendoza-Cuenca, C., Cattoz, B. N., Little, M. a., Terry, A. E., Zamith Cardoso, A., Adams, D. J. (2015). The effect of solvent choice on the gelation and final hydrogel properties of Fmoc–diphenylalanine. *Soft Matter, 11*(5), 927–935.

Wallace, M., Cardoso, A. Z., Frith, W. J., Iggo, J. A., & Adams, D. J. (2014). Magnetically Aligned Supramolecular Hydrogels. *Chemistry - A European Journal, 20* (50), 16484–16487.

Li, T., Kalloudis, M., Cardoso, A. Z., Adams, D. J., & Clegg, P. S. (2014). Drop-casting hydrogels at a liquid interface: the case of hydrophobic dipeptides. *Langmuir : The ACS Journal of Surfaces and Colloids*, *30*(46), 13854–60.

Cardoso, A. Z., Alvarez Alvarez, A. E., Cattoz, B. N., Griffiths, P. C., King, S. M., Frith, W. J., & Adams, D. J. (2013). The influence of the kinetics of self-assembly on the properties of dipeptide hydrogels. *Faraday Discussions*, *166*, 101.

Raeburn, J., Zamith Cardoso, A., & Adams, D. J. (2013). The importance of the self-assembly process to control mechanical properties of low molecular weight hydrogels. *Chemical Society Reviews*, *42*(12), 5143–56.

Selection of Oral Presentations

During this Thesis I have contributed with oral presentations: at the *Non-Newtonian Club* of the *British Society of Rheology*; at the Arrested Gels conference (Cambridge); at a science and industry meeting in P&G, organised by the Directed Assembly Network, UK; and a talk at the *Macro group UK*, supported by the joint interest of the *Royal Chemistry Society, UK* and the *Society of Chemical Industry, UK*.

Summary

Supramolecular peptide solutions and hydrogels are pathway-dependent multi-scale structured materials. This Thesis investigates three major aspects that impact on the self-assembly pathway. Firstly, the importance of the kinetics is investigated in the dipeptide gelators self-assembly pathway. Second, a proposed gelator-solvent phase diagram suggested a worm-like phase and an entangled worm-like micellar phase for N-protected dipeptide gelators. Thirdly, some links between hydrogel network structure and gelator solution phase properties were identified over multiple length scales for a particular class of peptide-based low molecular weight gelators (LMWG). These links allows some predictions to be made on the mechanical properties of peptide hydrogels triggered by salts based on the solution phase properties.

A new method based on carbon dioxide acidification of specific gelator solutions formed unusual membrane hydrogels. This unusual heterogeneous hydrogel formation occured when the gelator's apparent pK_a was a pH unit close to the final pH and the starting gelator solution did not have a high viscous solution at the high pH (typically above pH 10.5). This membrane hydrogel phase had similar viscoelastic properties to the intermediary transition state previously found with pH-switch methods in bulk hydrogel formation (from high to low pH). The carbon dioxide method was also capable of forming bulk hydrogels for gelators with apparent pK_a significantly above the final pH. This method was thoroughly investigated with 6-bromo-2-naphthalene-alanine-valine (BrNapAV).

This research also focused on the first detailed phase diagram of an individual gelator solution phase, in this case of 2-naphthalene-diphenylalanine (2NapFF), an N-protected dipeptides over three orders of magnitude in concentration and between temperatures of 15 °C and 45 °C. The solution phase of 2NapFF was found to go through a range of micellar transformations with an increase in concentration from free-surfactant, spherical aggregate phase, worm-like micellar phase and packed worm-like micellar phase. The critical micellar concentrations (cmc's), at which phase transitions occur, and the minimum gelator concentrations (mgc) with calcium nitrate salt solutions were found for 2NapFF. The common trends in the 2NapFF solution phase were extended to a library of 17 gelators.

It was found that the 2NapFF peptide hydrogel phase is structurally connected to the corresponding solution phase. This allows prediction of the final properties of the Calcium-hydrogels (Ca-hydrogels) from the starting conditions of the corresponding peptide surfactant solutions, based on consideration of the solution phase diagram and self-assembly process. These results showed that the 2NapFF solutions could form Ca-hydrogels in a concentration from 0.02 wt% to 1.0 wt%, corresponding to three orders of magnitude in complex modulus. It was also found that the presence of worm-like micelles in the solution phase was linked to mechanically stronger Ca-hydrogels. The gelation by addition of the calcium salt shifted the worm-like micellar concentration region and changed the microstructure to increase packing. The concentration was found to correlate with the mechanical properties with an exponential function with a 1.99 coefficient, typical for cross-linked networks and biopolymer gels.

Finally, four types of microscopy techniques were used to conduct a structural analysis on multiple length scales with: optical microscopy, scanning electron microscopy, confocal microscopy and atomic force microscopy. A new open-source fibre tracking software was used on microscopy images and the structural parameters obtained were characterised by: fibre and worm diameter, bundle diameter, persistence length, contour length, nematic order, and type of fibre. These results suggest that microscopy interpretation of hierarchical structured materials has to be done for a specific length scale image, only relate to the features of length scale covered from the size that image to the resolution of the image. The Ca-hydrogel nanofibres in between a concentration of 0.01 and 1.0 wt% had the main nanofibre width of 20.5 ± 4.3 nm measured by SEM. There were also detectable fibres with an extended width from tenths of nanometres to few micrometres. Laser Scanning Confocal Microscopy (LSCM) measurements allowed a microstructural snapshot of the Ca-hydrogels. Additionally, LSCM identified that in solution phase no correlation is observable between the microstructure (persistence length of the fibre bundles) and the complex modulus G*, while for the Ca-hydrogel phase, the persistence length of the nanofibre bundles increases with the increase G*. The worm-like structures were found to be highly oriented in the solution phase across concentrations from 0.1 wt% to 1.0 wt%. In the Ca-hydrogel phase, the degree or oriented structures increased from 0.05 wt% to 1.0 wt%.

Abbreviations

1Nap - 1-Naphthalene
1NapFF - 1-Naphthalene-diphenylalanine
^{1}H-NMR - ^{1}H-Nuclear Magnetic Resonance (or NMR)
2Nap - 2-Naphthalene
2NapFF - 2-Naphthalene-diphenylalanine
2NapAA - 2-Naphthalene-dialanine
A - Alanine
a_0 - head group area, see equation 3.1
A_S - cross-sectional area
AFM - atomic force microscope
APC1 - peptide gelator described in Chapter 1, reference [182]
BCF - bond correlation function
BrNap - Br-Naphthalene
BrNapFF - Br-Naphthalene-diphenylalanine
BrNapAV - Br-Naphthalene-Alanine-Valine
BrNapFG - Br-Naphthalene-phenylalanine-glycine
BrNapAG - Br-Naphthalene-alanine-glycine
c - related to a concentration
cac - critical aggregation concentration
Ca^{2+} - divalent cation
$CaCl_2$ - calcium chloride
CaF_2 - calcium fluoride
$Ca(NO_3)_2$ - calcium nitrate
cmc - critical micellar concentration
CD - circular dichroism
CO_2 - carbon dioxide
CO_3^{2-} - carbonate
cryo-SEM - cryogenic modified scanning electron microscope
cryo-TEM - cryogenic modified transmission electron microscope
CTAB - cetyl trimethylammonium bromide
DCl - deuterium chloride
DLS - dynamic light scattering

DMSO - dimethyl sulfoxide

DN1 - de novo 11 amino acid hydrogelator mentioned in Chapter 1, reference [318]

DNA - deoxyribonucleic acid

D_2O - deuterium oxide

ddH_2O - double distilled water

EDX - energy-dispersive X-ray

F - phenylalanine

FF - diphenylalanine

FM - free molecule in solution

Fmoc - 9-fluorenylmethoxycarbonyl group

FmocFF - 9-fluorenylmethoxycarbonyl-diphenylalanine

FTIR - fourier-transform infrared spectroscopy

G - glycine

G_0 - plateau modulus

G' - storage modulus

G'' - loss modulus

G* - complex modulus

GdL - glucono-δ-lactone

HFIP - 1,1,1,3,3,3-hexafluoroisopropanol

H_2S - hydrogen sulfide

HCl - hydrocloric acid

H_2CO_3 - carbonic acid

HCO_3^- - bicarbonate

I - isoleucine

ILL - Institut Laue-Langevin, Grenoble

LMWG - low molecular weight gelators

LSCM - laser scanning electron microscopy

K - lysine

K_{aw} - air to water partition coefficient

KCl - potassium chloride

l_C - critical hydrocarbon length, see equation 3.1

L_c - contour length, Chapter 5

l_C - average length between the bundle crosslinks

$<L_c>$ - average contour length
L_w - lowest maximum fibre width of the histograms
$l_{p,B}$ - persistence length of fibre bundles
L_{EE} - average end-to-end distance
LogP - partition coefficient
LSCM - laser scanning confocal microscope
L-STM - liquid phase scanning tunnelling microscopy
M_{75} - median up to the 3rd quartile (lower 75 % of the data)
MAX1 - protein fibril made of two segments of interchanging lysine and valine residues, linked by a four-residue turn-forming segment
MAX8 - protein fibril made of 20-residues similar to MAX1
mgc - minimum gelation concentration
N - overall number of nanofibres present in the bulk of the hydrogel
NA - numerical aperture
n.a. - not available
NaCl - Sodium chloride
NaOH - Sodium hydroxide
NaOD - Sodium deuteroxide
Nap- - used with dipeptides, to describe the LMWG type of naphthalene-dipeptides
n.d. - not determined
NH_2 - amino group
OH - hydroxyl group
OH^- - hydroxyl ion
Oxd - 4-methyl-5-carboxy-oxazolidin-2-one group
PA - peptide amphiphiles
pCO_2 - carbon dioxide pressure
pD - similar to pH for deuterium ion concentration
PFE - peak force error
pH - represents the acidity or alkalinity of a solution on a Log scale, equal to $-\log_{10} c$, where c is hydrogen ion concentration in moles per litre.
pH_i - initial pH of a solution or gel
pH_f - final pH of a solution or gel

pK_a - acid dissociation constant
PP - packing parameter, see equation 3.1
PTFE - polytetrafluoroethylene
pXRD - powder x-ray diffraction
Q_1 - 1st quartile (medium of lower half of the data)
R^2 - coefficient of determination in statistics
RT - room temperature
S_{2D} - 2D order parameter
SANS - small angle neutron scattering
SD - standard deviation
SDS - sodium dodecyl sulphate
SEM - scanning electron microscopy
TEM - transmission electron microscopy
SM - spherical micelle
T - absolute temperature
TetrahydroNap - tetrahydronaphthalene
$t_{exp\ (CO_2)}$ - time of exposure to CO_2
TFA - 2,2,2-trifluoroethanol
T_g - glass transition temperature
TGA - Thermogravimetric analysis
UV - ultra-violet light
V - valine
VER - viscoelastic region
Vl - volume
V_T - hydrocarbon tail volume, see equation 3.1
Vis - visible
Wet-AFM - aqueous environment atomic force microscope
WLC - worm-like chain
WLM - worm-like micelles
Y - tyrosine
γ - shear rate
$\dot{\gamma}$ - strain
γ_{break} - strain at which $G' = G''$

δ - frequency

η - viscosity

λ - persistence length (or L_p)

ξ - mesh size

τ - shear stress

τ_R - relaxation time

χ - molecular constraints

ϕ - fibre thickness or diameter

Amino acids and single letter acronyms

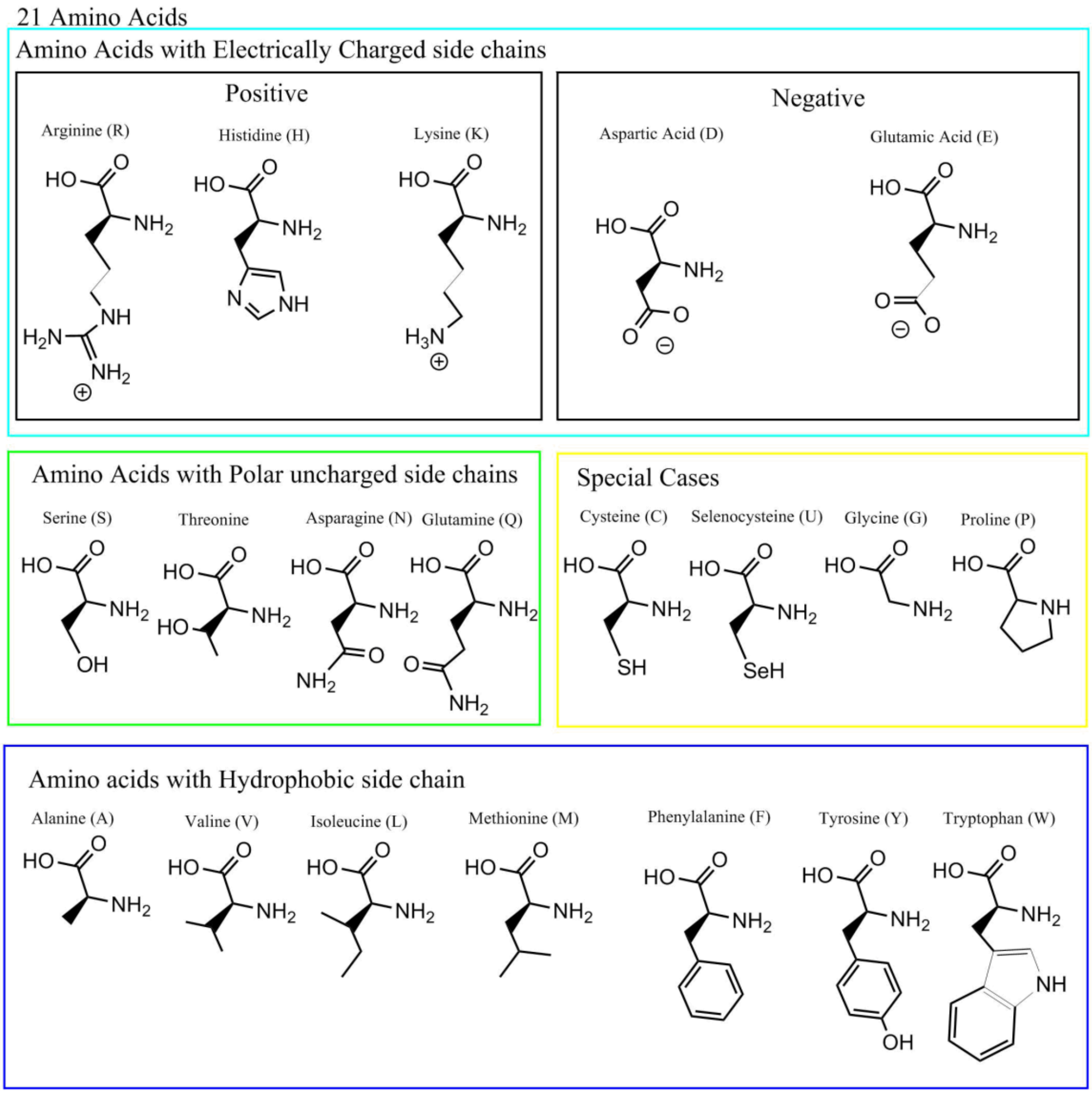

Chapter 1

1. Introduction

1.1. Supramolecular peptide-based low molecular weight gelators

Supramolecular self-assembled materials allow fabrication at multiple length scales.[1–10] This property was can be observed in nature's molecular systems, such as the cytoskeleton of cells or the molecular motors that give mobility to single cell organisms.[11,12] Some molecules can be self-assembled by non-covalent interactions to form hydrogels.[10,13] Hydrogels can be defined as structures formed from colloidal suspensions of a solid dispersed in water.[14–16] These are typically viscoelastic materials.[17,18] Viscoelasticity is observed when the relation between stress and strain changes based on time, or with frequency, if discussed in terms of a frequency domain. In the context of supramolecular hydrogels, low molecular weight peptides are an advantageous choice of building block.[10,19,20] They have significantly well-understood peptide chemistry, potential biocompatibility and the ability to mimic nature complex machines and functions, amongst other properties.[21–25] The minimalistic use of single N-protected amino acids, dipeptide or tripeptides already offers a wide range of molecular sequences and the possibility to investigate the design rules of these materials.[10,26] This Thesis aims to extend the understanding of the peptide self-assembly design procedures and discover methods to form low molecular weight hydrogels using a range of N-protected dipeptides.

1.2. Structure and length scales of supramolecular hydrogels

Supramolecular self-assembled materials are composed of repeating self-assembled low molecular weight units, also called supramolecular polymers.[14,27–29] The building blocks are typically composed of amorphous or semi-crystalline structures into nanoscale anisotropic structures, as opposed to crystals.[30] Supramolecular self-assembled peptide hydrogels are composed of nanoscale anisotropic structures.[31–34] This anisotropy is usually identified by cross-polarized optical microscopy. Non-covalent bonds such as π-π stacking, hydrogen bonding, dipole-dipole interactions, non-specific van der Waals interactions, electrostatic interactions, hydrophobic interactions and repulsive steric forces form these nanoscale structures in the supramolecular gels.[35,36] The relative importance of different non-covalent interactions in self-assembly peptide systems is still under debate.[37–40] Peptide-based supramolecular hydrogels form as a result of combinations of these forces. These forces counterbalance the high entropic energy cost of molecular aggregation in favour of self-assembly. Some groups have designed gelator molecules that could transform non-covalent self-assembled structures into polymer systems (i.e. covalently linked). For example, this can be achieved by cross-linking disulfide bonds or diacetylene bonds within the self-assembled gelator.[41–44]

The structures formed by self-assembly can extend over hundreds of micrometres in length, whilst being just a few nanometres in diameter.[10] The microstructure is formed by the entanglement and cross-linking of the fibre-like anisotropic structures and results in a self-sustained network.[10,18,20,45] These fibres appear flexible at the nanoscale because of their bending. The lateral association of the primary self-assembled filaments forms the entanglements and junction points of the microstructure (Fig. 1.1).[13,46,47] These are physical cross-links, not chemical bonds. Surprisingly, at the microscale, the fibre networks of peptide hydrogels can retain water with a minimum concentration of approximately 0.1 wt% of the structuring peptide.[48] This effect is a result of the molecular transition from a soluble phase to an insoluble phase.[18,49] At the macroscale, these hydrogels can be transparent and in some cases have tuneable mechanical[47,50–52] and optical-electronic properties.[53–55] The hierarchical structures of peptide hydrogels have an impact in the response to mechanical stress and aging effects.[56–68] These hierarchical and aging effects have also been identified through molecular dynamic simulations.[69,70] Since the peptide hydrogels are inherently structuring, the structure and mechanical properties have been a central aspect of research by various groups in the past years.[66,71–75]

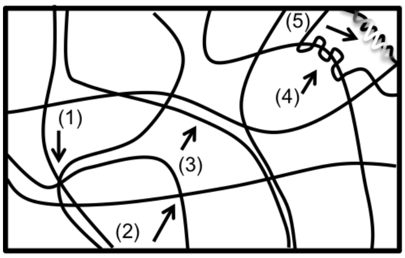

Figure 1.1 – Peptide hydrogel microstructure representation with different nanofibre elements (arrows): dense nucleation regions (1), cross-links (2), lateral association (3), entanglements (4), and intertwined junctions (5).

The varied self-assembly of structures at multiple length scales is linked with the hierarchical structure and selected monomer sequence. Uljin recently suggested that the research revolution observed in peptide nanotechnology materials (e.g. hydrogels, organogels and bare surface assembled structures) is comparable to the DNA nanotechnology observed in the past decades.[76] However, the possible variations in peptide self-assembly bring challenges in understanding the design rules but also more opportunities to build more complex materials and functions with simple building blocks. The monomers of the supramolecular systems are called gelators and the self-assembly process to form a hydrogel is termed hydrogelation. The nanostructures that are involved with gelators and hydrogelation can be as varied as nanofibres, nanosheets, nanoribbons, flower-like structures, nanotubes, core-shell particles, micellar systems, vesicles and rod-like structures.[72,77,78] These can be identified using a range of microscopy (e.g. wet-AFM, SEM, confocal microscopy) and scattering techniques (e.g. small angle neutron scattering).

It is not presently known how specific peptide structures correlate with how they assemble. However, Gupta et al. used a descriptor-based approach with limited design rules to find gelators.[79] The link between packing and nanostructures is also not fully understood. However, there has been a reported attempt based on cryo-TEM data.[24]

The ability to understand peptide self-assembly and gel formation is fundamental to the progress of peptide nanotechnology as well as comprehension of nature’s self-assembly phenomenon. This has been reviewed in the case of amyloid-based systems.[6] The discovery and development of applications of these novel materials in consumer beneficial products requires the control of the bulk structuring, surface activity and delivery/release of an active ingredient/drug.[71] These features usually define the functionality of the material.

1.3. Motivations for the use of supramolecular peptide hydrogels as materials

Low molecular weight peptide hydrogel materials have been used in a vast variety of proof of concept applications in past years. Some of the key characteristics that attract the current foreseen applications are: the biocompatibility for biomedical engineering;[80–83] the optical[84–87] and conductive[3,88–91] properties for energy applications; the ability to easily modify peptides with different functional groups to make a library of peptide-based compounds (e.g. using protein engineering);[26,92–95] the environmentally friendly and sustainability of processes using biodegradable peptide-based molecules;[21,96,97] the ability to encapsulate drugs, active ingredients or functional foods;[71,98,99] and anti-microbial hydrogels.[100–102] Peptide supramolecular hydrogels can be designed to make specific interactions. A range of molecular mechanisms can function as on-off or dynamic/responsive switch: pH or ionic strength,[48,50,103–107] solvent change,[49,50,108–110] temperature,[103,111–113] concentration of gelator,[36] magnetic fields,[114–116] light,[117] and mechanical stress.[50,84,104,118] The self-assembly methods developed up to this year are discussed in Section 1.11.

In peptide-based gels, one of the main challenges is to find functional peptides. Ideally, it would be beneficial to use a sequence of amino acids without modifications, as they could be easily biocompatible for a range of applications in the human body or in the environment.[71] The protein/peptide enzymatic degradation systems already exist in the ecosystem, some examples of these have been used to further control self-assembly.[119,120] Additionally, biotechnological synthesis routes could be used rather than partially or fully synthetic synthesis.[121]

A variety of peptide systems alone are known to form crystals instead of hydrogels. In some cases, crystals can provide significant understanding of intermolecular interactions in some molecular systems. However, in the context of peptide hydrogels, these are avoided because the product of self-assembly is usually a kinetically trapped state.[122–127] A material is in a kinetically trapped state when its structure was controlled by time or the speed of reaction, as opposed to controlled by temperature or energetically minimised. It was shown by a combination of diffraction and fibre x–ray techniques that the gelators may well pack in a different form in the crystals than the packing arrangements in the self-assembled hydrogel structure.[30,122] For example, the research group of Gorbitz investigated extensively the structures of a range of dipeptides and found that these form a fascinating diversity of porous crystal-like structures.[128–131] These results suggested a link between the specific amino acid sequences and preferred packing arrangements.[131] In parallel, Gazit and collaborators found that some selected dipeptides could form a range of nanostructures and behave with unexpected physical and chemical properties for biological materials when prepared by different processes.[132–135] Some of these nanostructures formed materials with potential applications in the optical, electronic and biosensor fields.[115,135–137] However, the resulting self-assembled materials did not expand from molecular packing to the macroscale and instead formed thin films. These did not result in hierarchical structures or macroscopic materials. The dipeptide IF (all amino acids will be referred to throughout as their one letter acronyms) is an exception to these peptide-only nanomaterials, because this dipeptide is able to form hydrogels.[33] The range of opportunities to find a new peptide system increases with the number of amino acids used. This increased number of permutations allows several potential candidates to possibly result in peptide hydrogels, with similar functionalities. This could also impact on the difficulties of patenting the invention, as it is the case with the myriad country-dependent rules for patents with DNA sequences.

Computer simulations could help define the design rules for finding new peptide based hydrogels. Computational work by Prybytak *et al*. show that asymmetric interactions could form chiral fibrillar structures when the molecular unit has an oblate ellipsoid structure.[69] This results in the amphiphilic nature of the self-assembled structures. In a separate study, molecular dynamic simulations indicate that some modified-dipeptides and tripeptides have higher aggregation propensity when compared with large libraries of dipeptides and tripeptides combinations.[79,138] Computational approaches could allow a scan over the sequence space. However, our current computational tools still require long processing times and extreme boundary conditions to limit the complexity. At present, these models cannot be fully validated by exceptional experimental cases, some which require long run times, outside the convergent simulation boundary conditions.[71]

1.4. Applications of peptide supramolecular hydrogels

Some modified single amino acid and dipeptide systems can indeed form peptide hydrogels. One of the first findings with regards to minimal peptide-based self-assembly systems came from work conducted by the research group of Bing Xu.[139–141] Other groups have expanded the research into identifying a variety of structure-property relations, described the self-assembly mechanisms and discovered materials with tuneable functionalities for a range of applications.[142–147] Fig. 1.2 shows some examples of the most sophisticated peptide gel systems and successes in translating peptide gels research into proof-of-concept applications.

Recently, Smith *et al*. reported significant achievement in biomedical engineering and peptide hydrogel material chemistry. They demonstrated the advantages of using a multiphase transitioning peptide hydrogel system for suturing ultra-small vessels (Fig. 1.2a).[148] In this delicate surgical procedure, the mechanical properties of a peptide hydrogel were precisely designed at the amino acid level to form a responsive

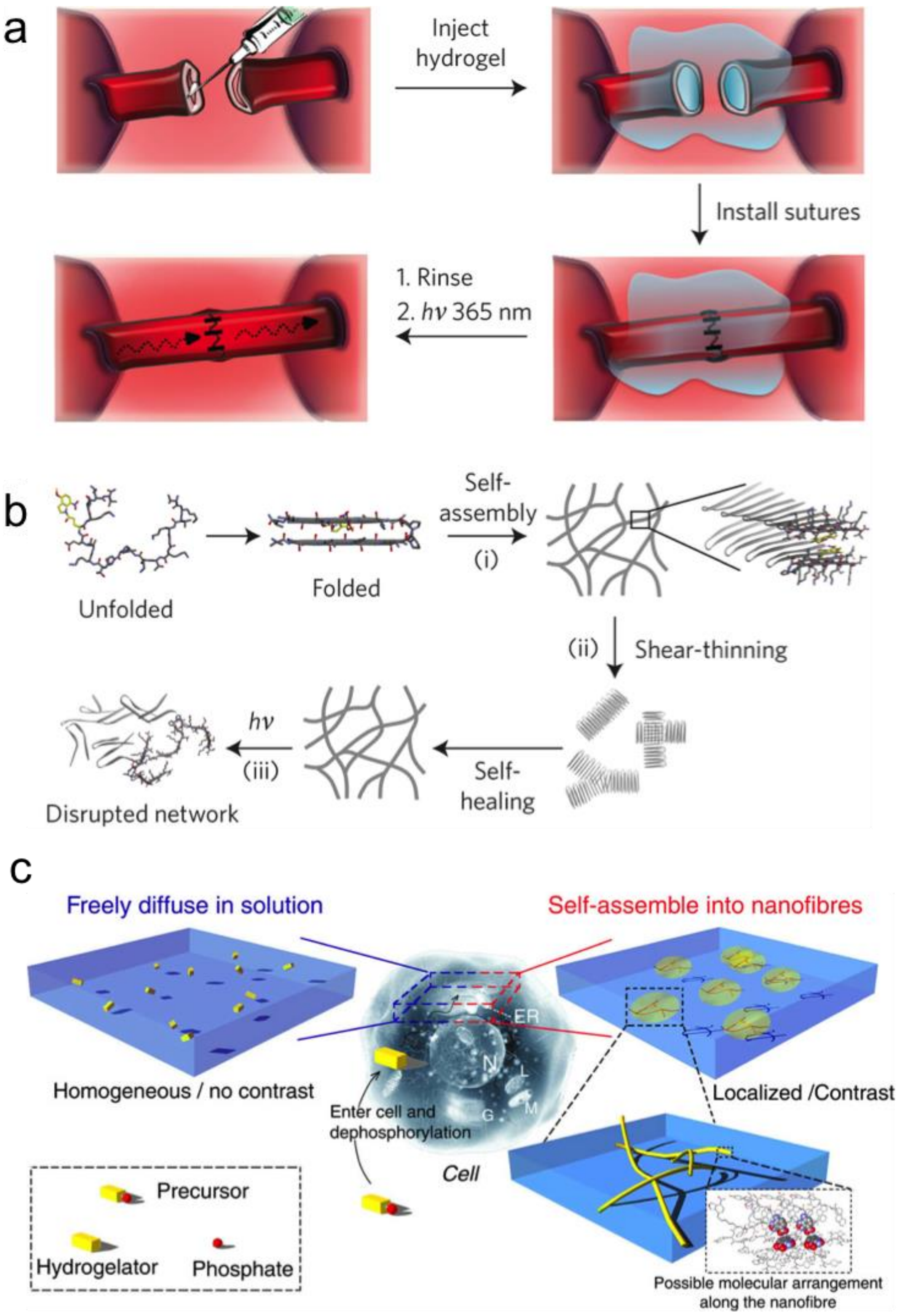

Figure 1.2 – Three examples of peptide hydrogels used in biomedical applications. Scheme of the peptide hydrogel system and its use in light-mediated suturing of ultra-small vessels (a, b).[148] At the macroscopic level (a), the hydrogel is injected into the region of the collapsed vessel (step 1), which aids suturing (step 2). Finally, the region is rinsed and irradiated to clear the hydrogel with a gel-to-sol transition (Step 3). At the molecular and microstructure level (b), the multiple transitions of the peptide APC1 are shown: triggered folding and self-assembly, shear thinning, recovery and irradiation-triggered gel-sol transition. Imaging cells is possible with enzyme-triggered supramolecular self-assembly inside cells (c).[149] The enzymatic conversion of a precursor gelator forms a more hydrophobic molecule that self-assembles into nanofibres. These nanofibres have more fluorophores within each pixel than the rest of the solution. As the fluorophores within nanofibres are localized, the nanofibres fluoresce more brightly than the solution and generate the contrast. Reprinted with permission from Nature Publishing group.[148]

multiphase transition system. After a first self-assembly step, a shear thinning transition is used to break the entanglements and the gel is allowed to re-heal, promoting a sol to gel phase transition (Fig. 1.2b). Secondly, a light trigger disassembles the gel to a sol phase transition after completion of the suturing process. Different groups have reported on the formation of responsive hydrogels.[21,150–155] The responsiveness could be designed to find protein-protein interactions,[156] detect toxic H_2S,[152] or respond to environmental changes in mechanical or chemical properties (e.g. pH).[21]

At an even lower, sub-micro level of structure, Xu's research group highlighted that it is possible to use enzyme-instructed self-assembly in a cellular environment to trigger intracellular formation of supramolecular nanofibres and functions (Fig. 1.2c).[157,158] In this case, the nanofibres can control the cell fate of cancer cells.[149] This process takes advantage of cellular enzymes to regulate the viscosity of the intracellular environment and therefore it can selectively regulate cell death. Imaging of these cells is possible due to the localized self-assembly inside cells (Fig. 1.2c).

Some types of non-covalent bonds (e.g. delocalized π-π electrons) appear to form a semi-conducting layer of electron-hole pairs by their lateral packing arrangements.[159–162] Several peptide-based nanomaterials were found advantageous for energy-harvesting, however most of these do not form hydrogels.[162] Park's research group showed advantageous modified dipeptide hydrogels in optically conductive devices, which mimic photosynthesis (Fig. 1.3a, page 8).[163] The conductive properties of biomaterials may be used in environmentally friendly electronic paper in the future.[164] However, these preliminary studies have shown that slight modification in the sequence may allow materials to be designed with different structural, mechanical, optical or conductive properties.[77,165–168] Interestingly, some systems have magnetic susceptibility[114,116,169] and thus, the self-assembled peptides can be piezo-electric.[170]

Recently, a number of research groups have been successful in controlling chemical reactions by the adjustment of the catalytic properties of modified self-assembled peptide-based materials.[150,171] For example Stupp's research group devised a peptide self-assembly system which is capable of hydrogen production by peptide self-assembled systems (Fig. 1.3b, page 8).[172] In this peptide amphiphile model (Fig. 1.3 – b1 and b2), gelation is triggered by a salt change, which increases the storage modulus for some of the tested salt-switched peptide systems (Fig. 1.3 – b3). This results in a ribbon microstructure and a self-sustaining hydrogel (Fig. 1.3 – b4).

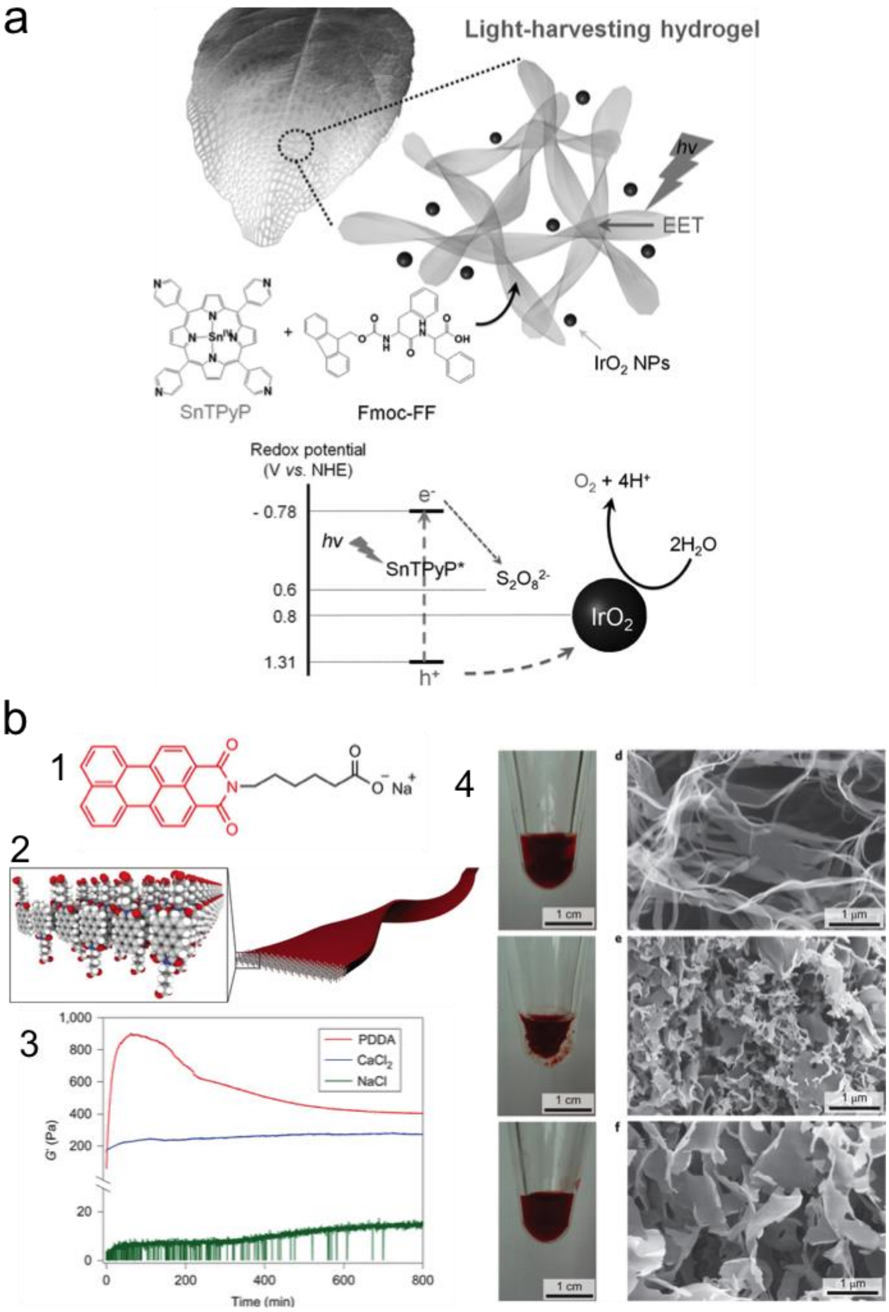

Figure 1.3 – Two examples of optical and conductive properties in peptide-based self-assembly systems that are applied in energy harvesting. (a) Scheme of visible light-driven water oxidation by self-assembled light harvesting multicomponent peptide-based hydrogel, using FmocFF and metalloporphyrins. (b) Self-assembled catalytic system for hydrogen production: (1) molecular structure; (2) schematic representation of the antiparallel packing; (3) rheological properties showing the storage modulus as function of time with different salts; (4) gelation of peptide amphiphile ribbons with and without salt solutions: solution no added salt (top), $CaCl_2$ (middle), NaCl (bottom). Modified with permission from John Wiley and Sons (a) and Nature Publishing group (b).[163,172]

These varied examples show that peptide nanotechnology offers high variability in specificity of binding and functionality. A number of minimalistic self-assembly model molecules have been used to study the peptide based hydrogels. Some groups have attempted to screen virtual peptide libraries to identify key aspects of potential gelators.[79,173] Peptide amphiphiles and fluorenylmethyloxycarbonyl-dipeptides (Fmoc-dipeptides) were some of the first to be investigated either by serendipity or the ease of access of common peptide synthesis chemistries.[174]

1.5. Types of peptide supramolecular hydrogels

Xu *et al*. compiled one of the most comprehensive reviews to date on peptide-based self-assembled materials, including peptide-based hydrogels in 2015.[10] In Figure 1.4, some of the most investigated gelators are shown: Fmoc-tyrosine[139,141,147,175–177] (FmocY, Fig. 1.4a), Fmoc-diphenylalanine[24,105,109,178,145,179,180] (FmocFF, Fig. 1.4b), MAX1[21,125,181–184] (Fig. 1.4c), and one of the peptide amphiphiles investigated and modified by Stupp and collaborators (Fig. 1.4d).[36,42,43,72,185–194]

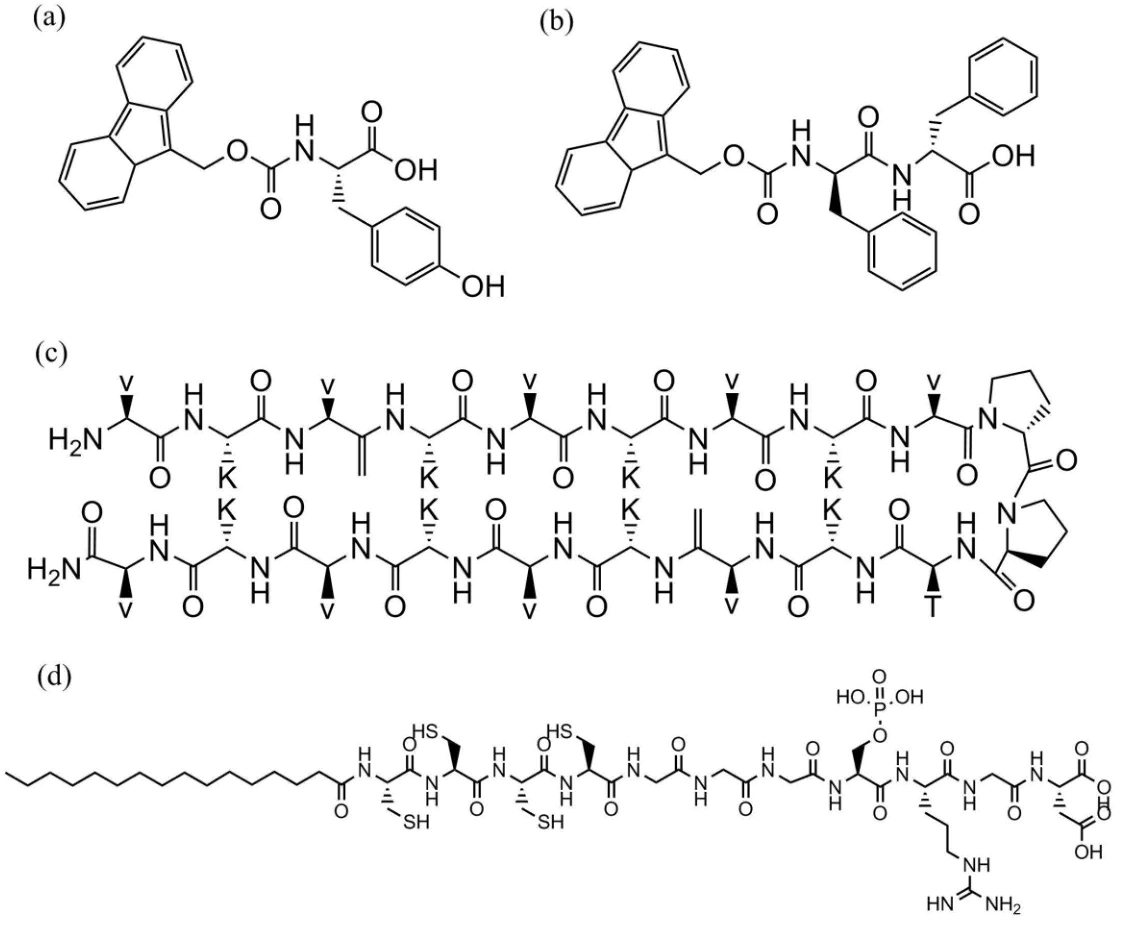

Figure 1.4 – A range of studied peptide-based gelators: (a) Fmoc-tyrosine (FmocY), [139,141,147,175–177] (b) Fmoc-diphenylalanine (FmocFF),[24,105,109,178,145,179,180] (c) MAX1 peptide,[21,125,181–184] (d) mineralization-inducing peptide amphiphile.[36,42,43,72,185–194]

A number of research groups rapidly reported the discovery of a variety of methodologies to form self-assembled hydrogels in the past 20 years.[10] These different self-assembly processes were further optimized by different research groups. Following this greater control in self-assembly process, the diversity of low molecular weight gelators (LMWG) expanded to different N-protected amino acids, dipeptides, tripeptides and larger five amino acid sequences, in most cases biologically inspired.[10] A library of peptides diversified the opportunities in targeting specific functionalities in peptide hydrogels because of a range of protective groups such as substituted naphthalenes, pyrene, carbazole, phenanthracene, anthracene. Some of these were shown to form hydrogels.[10,95]

1.5.1. FmocY type of peptide supramolecular hydrogels

FmocY (Fig. 1.4a) and Fmoc-phenylalanine (FmocF) are similar gelators, however they have different behaviours. It was found that the microstructure of hydrogels formed with FmocF is more flexible than the microstructure of FmocY.[147] This difference in microstructure flexibility impacts on the different gel permeability of the hydrogels to molecules of different molecular weights. FmocY has a maximum molecular weight of 1 kDa for molecules to remain permeable in the hydrogel, while FmocF is permeable to molecules of a wide range of molecular weights. Therefore, the slight difference in structure between FmocY and FmocF has a significant impact on the structural and mechanical properties when the same self-assembly process is used. Interestingly, if different self-assembly processes are used to self-assemble FmocY into a hydrogel, these lead to gels with different properties.[175] Two approaches were reported to form hydrogels with FmocY. The first process uses the desphosphorylation of a precursor gelator (i.e. FmocY-phosphate) into FmocY by addition of an enzyme. The second process uses the dissolved version of FmocY (i.e. deprotonated FmocY) changed by a decrease in solution pH below the apparent pK_a of FmocY to form self-assembled hydrogels. Yang *et al*. outlined that the FmocY hydrogel enzymatically gelled at pH 9.7 at 37 °C resulting in a storage modulus (G') and loss modulus (G″) of 1000 Pa and 300 Pa, respectively.[141] In a later investigation, gelation of the same FmocY with a pH-switched method at a pH_{final} of 6 at the same temperature and similar concentration resulted in hydrogels with G' and G″ of 4000 Pa and 1000 Pa, respectively.[139] Their circular dichroism (CD) results suggested differences in packing at the molecular level could be related to different mechanical properties in addition to the differences in pH. Other groups also reported different mechanical properties with this gelator.[175–177] These are likely to be related to different self-assembling kinetics.[18] Recent studies of these gelators using particle tracking and dynamic light scattering indicate specific size-dependent interactions exist at different length-scales of the peptide network.[51,52,123,195] In terms of further modification and expansion in functionality, it was found that an analogue of FmocY, the FmocFFY, could be further modified with irradiation to crosslink the nanofibres.[196] The crosslinking is initiated by a ruthenium catalysed photochemical process. If two tyrosine residues are in close proximity, these can be linked to form a dityrosine adduct.

1.5.2. FmocFF type of peptide supramolecular hydrogels

A further interesting case study is the heavily investigated FmocFF (Fig. 1.4b), a N-protected dipeptide. FmocFF gel has one of the highest reported G', of between 10 kPa to 21 kPa,[17,24,197] and unconventional mechanical properties. Other supramolecular systems have also reported reversible or self-healing properties.[111,184,198] The FmocFF gel reported mechanical properties were at first controversial because different communications reported significantly different storage and loss modulus values.[17,24,94,178,179,197] This was later interpreted and identified by different research groups as slight nuances in the self-assembly process.[59,105,104] For example, the process temperature, presence of salts, changes in solvent and solvent ratios, time of assembly (aging), mode of agitation, presence of additives or type of mechanical measurements were found to be critical parameters to obtain highly reproducible measurements.[59,105,104,199] Importantly, the FmocFF case study appeared in the literature as a platform to identify the typical self-assembly mechanism, which presented a complex number of steps and hierarchical structure formation, gradually understood over a range of publications by different research groups. Another scientific question, which rose with this family of Fmoc-dipeptides, was the relevance of the identified crystal structures and packing parameters. The varied experimental and computational methods obtained contributed to the actual understanding of the peptide-hydrogel properties. At the molecular scale, spectroscopy measurements suggested a β-sheet structure should be present in the dipeptide hydrogels and π-π stacking interactions and hydrophobic interactions had an important role in the formation of nanofibres.[24,179] However, these interactions are not always required to form self-assembling hydrogels.[40,70,200,201] At the same scale, diffraction measurements suggested that particular sequences of gelators have defined lattice parameters, however, this is in disagreement with the observations that peptide hydrogels are not crystalline materials.[30] Crystals of FmocFF can grow by solvent exchange method. Xerogels (i.e. dried hydrogels) and diffraction prepared hydrogel samples may well form crystalline or semi-crystalline regions depending on the modified-dipeptide investigated. After 7 years from the first publication, sufficiently large crystals of FmocFF were grown by a solvent switch method to reveal a crystal structure.[49] This however does not present the ribbon nature of the FmocFF hydrogel system, therefore suggesting that the crystal structure is a different packing arrangement to the hydrogel state. As in other gelator systems, organic solvent or drying effects may well lead to a structure modification.[202]

1.5.3. MAX1 type of peptide supramolecular hydrogels

The MAX1 gelator is a versatile LMWG.[21,182] This gelator has similar properties to the Fmoc-based peptide systems (Section 1.5.1 and 1.5.2). The MAX1 is composed of 20 amino acids and only initiates the self-assembly process after a self-folding event (Fig. 1.4c). This conformational change results from the designed molecular folding promoted by two strands of alternating valine (V) and lysine (K) residues, connected by a type II' turn sequence (-V^{D}PPT-). The folding into a β-hairpin molecule, resembling a molecular zipper, can be modulated with its solution properties – temperature, pH, salt concentration, gelator concentration, self-assembling kinetics[21,111,182] – in a similar way as the Fmoc-peptide based gelators. The final hydrogel properties can be modulated by the folding events of MAX1, because only the folded form of MAX1 self-assembles into nanofibres and forms hydrogels. For example, here, self-assembly occurs when the pH of the solution is above its apparent pK_a, because with a pH below this value the presence of positively charged K residues causes repulsion and unfolding of the peptide. When the pH is increased above the apparent pK_a of the lysine's, repulsion is reduced and intramolecular folding occurs.[21,111,182] The hierarchical self-assembly process is mainly dominated by hydrogen bonding and hydrophobic interactions between the β-hairpins. These forces promote the facial and lateral association of the nanofibres and the formation of a microstructure, which leads to hydrogelation.[21,111,182]

1.5.4. Peptide amphiphile (PA) type of peptide supramolecular hydrogels

In the peptide nanomaterials field, a vastly developed family of LMWG is the peptide amphiphile (PA).[36,42,185–194] Peptide amphiphiles have a hydrophobic region, a hydrophilic region and, in most cases, a more complex region with an active ingredient and functional region (Fig. 1.4d).[36] Also, they are typically composed of modified peptides by an aliphatic chain, which largely enhances the hydrophobic region and the characteristic packing of these gelators. In most cases, they form cylindrical packed nanofibres with re-healing, extremely versatile synthesis and biocompatible properties.[36] The gelators typically pack in a radial manner in relation to the fibre axis. This system also offers a range of self-assembly processing methods such as by control of pH, salt, and concentration (Section 1.11).[82,189–191,193,203]

1.6. The importance of the self-assembly process in peptide supramolecular hydrogels

Findings obtained with a variety of peptide-based self-assembly models suggest that a common feature between every different gelator system is the influence on the self-assembly process to the final hydrogel properties and functions. This phenomenon has been well documented in the case of a variety of formulation methods used with the same emulsion systems for several decades.[204,205] Independently of the sequence or complexity of the peptide system, different self-assembly methods or processes can lead to different properties, as shown by the examples of Fmoc-peptides, oligopeptides, and peptide amphiphiles.[73,192] In another example, Liao *et al*. studied the self-assembly pathways in solution and in a range of substrates for the peptide amphiphile NapFFKYp (p-small case denotes phosphorylated, in this case in Y).[206] In solution, the peptide undergoes a nucleation-driven process into nanofibres and aging effects twists the fibres. On surfaces, the monomer forms nanofibres and sheet-like structures. The sheet-like structure is composed of rod-like structures and the thickness is substrate dependent. Water can transform the nanosheets into the nanofibres. Molecular dynamic simulations show that the dominant drivers for self-assembly are hydrophobic and ion-ion interactions. In another example, a peptide conjugated to 4-methyl-5-carboxy-oxazolidin-2-one (Oxd) moiety forms ß-sheets and supramolecular helices composed of π-π stacking interactions and intermolecular N-H•••O=C bonds.[207] These materials can form both for organogels and hydrogels. In this minimalistic peptide-conjugated model, Tomasini *et al*. shown that the Oxd-moiety was fundamental in their sequence to form low molecular weight gelators (LMWG).[207] With their peptide-Oxd-focused research, they found that various modifications in the building blocks resulted in different gels. For example, their bolamphiphilic and Fmoc-containing derivatives formed materials with a range of structural and functional properties.[207] In a separate study, Berger *et al*. recently reported on a combination of DNA nanotechnology with peptide nanotechnology.[54] In their investigation, they present a hybrid peptides-nucleic acids system that has both the Watson-Crick base pairing interactions with non-covalent peptide stacking interactions. Similarly to DNA nanotechnology, the ability to direct self-assembly to pre-defined functions of the materials is likely to become commonplace in peptide nanotechnology. Therefore, the varied functionalities, potential applications discovered and the ability to understand and control self-assembly at multiple length scales strongly motivated us to extend the research into peptide supramolecular systems to discover new functional materials.

1.6.1. Self-assembly process in peptide supramolecular hydrogels

Dipeptide-based gelators are the main supramolecular hydrogel model systems used in this Thesis. These are a class of LMWG, which can form full bulk hydrogels. They consist of a modified dipeptide, typically N-protected (as in the case of this Thesis) with an aromatic group by a linker group (Fig. 1.5).

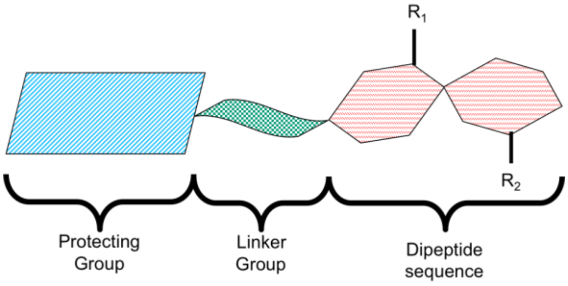

Figure 1.5 – Three main regions of a modified dipeptide system studied in this thesis: protecting group, linker group and dipeptide sequence.

Gelators self-assemble into nanofibres, these in turn self-assemble by facial and lateral nanofibre packing to form an entangled microstructured network (Fig. 1.6). The first step to prepare a typical peptide-based hydrogel is to dissolve the gelator in an appropriate solution. In this solution, the gelator can transition to another homogeneous or heterogeneous solution because of the switch to a lower solubility of the gelator's new form or molecular environment. This is initiated by a triggered mechanism (e.g. pH, salt, temperature changes, induced mechanical stress, light activation, biocatalytic – enzymatic conversion, among others). Another important aspect, investigated further in this Thesis is that, prior to the self-assembly process, the so-called solution phase could already be in a self-assembled state (Fig. 1.6). In this case, the multiple weak hydrophobicity and electrostatic forces may well dominate a weakly bound gelator into micellar phases. Our and other groups have reported on experimental observations and molecular dynamic simulations of micellar phases in the starting solution phase (Fig. 1.6).[208–210] With N-protected dipeptides, our group has observed micellar structures at high pH,[209] while with similar peptide amphiphile systems, other groups have also reported micellar phases prior to hydrogel formation.[190,211,212]

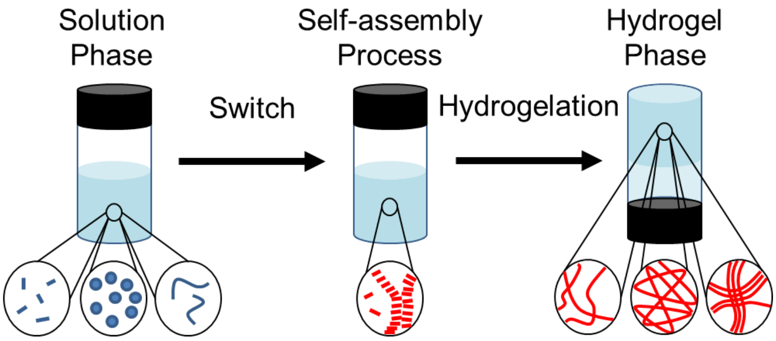

Figure 1.6 - Scheme showing the self-assembly process from a solution phase to a hydrogel phase. In both the solution and the hydrogel phase, three different structure possibilities are suggested. The different colours between the initial and final structures formed marks a change in the self-assembly.

1.6.2. How does the self-assembly process works?

Self-assembly works as a gel formation method because the LMWG can be initially fully dissolved in water or an initial organic solvent miscible in water and, by the action of a switch, this LMWG is kinetically trapped without phase separation, therefore forming a hydrogel. This phenomenon happens because the gelator molecules can change from a weakly bound, sterically hindered or electrostatic repulsion state into an anisotropic state, with a preferential unidirectional coordinated packing arrangement. This phenomenon is further investigated in this Thesis with a range of LMWGs and self-assembly processes which allow the molecular transition to be followed by various techniques. This transition period is investigated in Chapter 2 and the initial solution phase behaviour is investigated in Chapter 3. The correlation between these two phases is discussed in Chapter 4.

1.6.3. Hierarchical Self-assembly in peptide supramolecular hydrogels

In order for the self-assembly to occur, inter- and intra-molecular forces have been found to dominate the self-assembly process at different length scales.[45,213–216] These forces act at different length scales.[214] In this Thesis, the molecular and nanoscale forces are studied in parallel to the phenomenon observed at the different length scales.

These are categorised as (1) molecular structure conformation, (2) nanoscale molecular packing, (3) microscale, and (4) macroscale (Fig. 1.7).

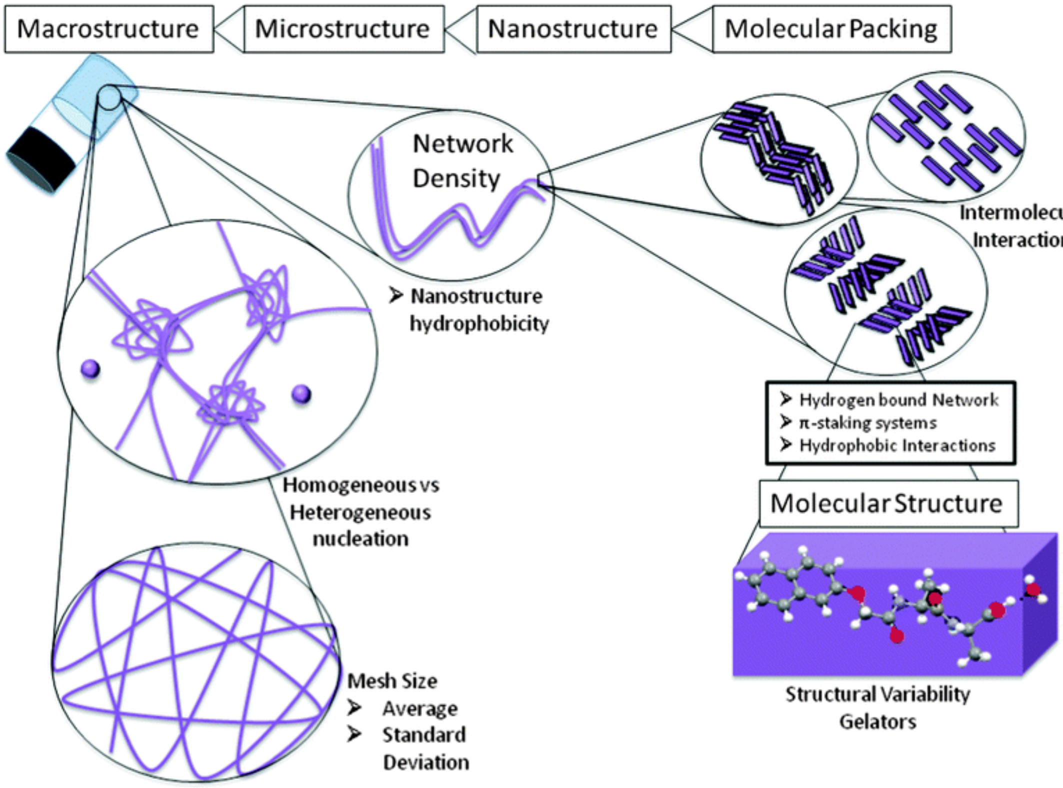

Figure 1.7 - Schematic showing the different levels of assembly leading to gelation. The process can affect all levels of the assembly. The molecular structure can be changed but the emergent phenomena resulting from those changes have been so far difficult to predict and control (Section 1.6.3.4). The three different molecular packing models illustrate possible variability in packing of the molecules. Microstructure can be dramatically different even though the molecular packing may be very similar. The final dynamic equilibrium of the nanostructure and macrostructure properties can also be varied. This figure is reprinted with permission of the Royal Chemistry Society.[18]

It is important to note that throughout this thesis the term peptide micelles and peptide fibres are used to describe very similar peptide structures. The term micelles is commonly used in surfactant literature and is here denoted to characterise the structures formed in the solution phase of the peptide self-assembly. For example worm-like micelles are an elongated micellar structure. The term peptide (nano)fibre is used here to describe the elongated structures that form the hydrogels. In peptide supramolecular material science the term nanofibre is commonly used, in most circumstances used to refer to structures, which are possibly micellar structures.

1.6.3.2. Molecular structure conformation

Above the atomic level, the covalently bonded atoms form molecules with specific molecular constrains of charge, density, shape and preferential electron cloud maps at their surface. This scale is here denoted as the molecular scale. It comprises the molecular conformation, which a molecule adopts depending on the intra-molecular and solvent-molecular interactions. These intra-molecular interactions and preferential conformational states are probabilistic states, which may bend the energy landscape depending on the neighbouring solvent/gelator molecules. For example, solvent density, polarity, and temperature all have an effect on the adopted conformation and solvent bounding interactions. In the case of the MAX1 peptide (page 12), the first step in the self-assembly process is the self-folding into a zipper conformation, possible energy minimised states or a kinetically trapped state,[106,168,217] which are still under discussion for a number of other gelator systems.[218] Other minimal gelators (LMWG with modified oligopeptides), for example the range of Fmoc-dipeptides and naphthalene-dipeptides were shown to form hydrogels only under a certain range of concentrations, pH, temperature, mechanical stress and solvent.[49,50,105,197,209,219–221] The necessary conditions are likely to interfere with this first, and critical, step in the self-assembly at molecular length scale, where the self-assembly process is triggered.

If the solution concentration is above a critical micellar concentration (cmc) or aged for a set amount of time, the molecules are likely to interact and form inter-molecular interactions.[48,92,124,219,222,223] The cmc relates to a transition state, which in some further added molecules form micelles, an aggregated molecular arrangement. An apparent gel melting temperature, T_{gel}, is usually referred to as the maximum temperature at which a gel has the characteristic viscoelastic properties or passes the inversion vial test.[103,224–226] The first developed methods used a temperature triggered sol-to-gel transition to trigger the gel formation.[174] Most gelator systems are strongly pH dependent as the solubility and hydrophobicity of the gelator can be modified. This occurs when the solution pH is adjusted because of the unevenly balanced free electron cloud in the gelator molecules (e.g. available –OH and –NH groups) or amphiphilic character of some gelators. Therefore, this can be used to trigger the self-assembly because changes in solubility trigger the kinetically driven self-assembly.[47,124,227] Some gelators are just weakly bonded enough so that applied mechanical stress (e.g. suction of a gel into a syringe) breaks the entanglements and reinitiates a self-healing phenomenon under low shear forces or a static incubation at a set temperature.[16,50,228] The mode of agitation or applied sample shear stress can impact on the final microstructure of the gel.[105,104] Shear alignment of gelator molecules has also been shown to promote gelation, when used in combination with a change in the overall ionic content, presence of salts.[34] The solvent change can also be used by itself. Several groups have shown that a transition of a dissolved gelator solution in an organic solvent (miscible in water) into water can be used to form hydrogels.[49,66,109,193] These examples indicate that most self-assembly triggers act at the molecular scale. Therefore, the second step in the self-assembly process occurs from the single molecule conformation and possibly a pre-arranged or randomly oriented micellar state into the formation of dimers, trimers and ultimately over millimetre long extended nanostructures.

1.6.3.3. Nanoscale molecular packing by non-covalent bonds

A range of predominantly directional, non-covalent inter-molecular interactions promotes the anisotropy of the nanostructures formed at the molecular packing scale (Fig. 1.7). The inter-molecular forces, which dominate the supramolecular hydrogel formation, are π-π stacking, hydrophobic interactions, electrostatic interactions, chiral dipole-dipole interactions, and repulsive steric forces.[36,208] Time-lapsed measurements of different gelator systems suggest that the configuration present at the packing of gelator molecules dictates the nanostructures formed.[50,217] The variety of nanostructure packing that have been identified as present in supramolecular hydrogels ranges from nanofibres, nanosheets, nanospheres, nanorods, nanodiscs, and nanochannels.[10,78] These are likely linked with the molecular packing of the gelators at particular conformations (See Fig. 1.7, e.g. helical packing, columnar packing, staggered packing). X-ray fibre diffraction, cryo-transmission electron microscopy (cryo-TEM), selected area electron diffraction and liquid phase scanning tunnelling microscopy (L-STM) measurements of semi-crystalline features of single nanofibres have given strong indications that the hydrogen bonding and π-π stacking are preferential in the fibre axis.[229,180,198,230]

1.6.3.4. Microscale hydrogel network

Above the nanoscale, the hydrogel microscale characterises dynamics of the interactions between the nanostructures (Fig. 1.7). At this self-assembly scale the hydrophobic forces between the nanostructures, nanostructure surface groups, and single nanostructure mechanical properties have an important role in the facial and lateral association of the nanostructures.[168] At this length scale, the type of junction points and cross-links defines the microstructure (defined in Fig. 1.1, page 2).[13] Note that these are significantly different from the covalently bonded macromolecular polymer chemistry interactions. At this scale, the gelator concentration and therefore the nanostructure concentration impacts on the nanostructure density and dimensions (Fig. 1.7), discussed further in Chapter 3. Another important aspect in the microstructure formation is the kind of nanostructure kinetics. The kinetics of self-assembly can be cooperative or non-cooperative dynamics.[219,231,232] If the self-assembly occurs by an initial seed dimer or trimer which trigger faster kinetics, the self-assembly is cooperative. Alternatively, the self-assembly is called non-cooperative if every newly self-assembled molecule adds to the aggregate at the same rate of conversion. The spatial initiation of self-assembly at the nanoscale also plays an important role in the microstructure. We have shown that the different self-assembly initiation, using different solvent switch self-assembly processes, may in turn result in different microstructure and mechanical properties.[49] A relative dominance of multiple fibre nucleation-initiated self-assembly – heterogeneous microstructure – against more single-nucleation per fibre self-assembly – homogeneous microstructure – impacts on the homogeneity of the hydrogel microstructure. The dimensions of the nanostructure and microstructure typically impacts on the turbidity and optical properties of the hydrogel.[233]

1.6.3.5. Macroscale hydrogel properties

The final length scale of interest is the macroscale (Fig. 1.7). This is the scale of observing and interacting with materials for macroscopic applications, such as mechanical structuring or tissue engineering.[234] At this scale, the mechanical properties emerge from the series of scale-dependent interactions or hierarchical structures. Typically, shear-dependent viscosity tests, storage and loss modulus dependence with shear and frequency, and finally self-healing or recovery properties (e.g. recovery after shear and time of recovery) are used to characterise the mechanical properties of the hydrogels. Certain biomedical applications depend not only on the biocompatibility, but also on the macroscale mechanical performance, turbidity or degree of transparency.[234] The mechanical functionality is crucial for the hydrogel ability to be injected, to be recovered [125,228] and to be used in cardiac patches.[235]

1.7. Functionalised dipeptide gelators

Most literature in LMWGs focus on finding the impact of a specific molecular structure (e.g. FmocF) or small sequence changes (e.g. FmocY, FmocFF) in the outcome of gelation.[209,236,237] This Thesis focuses on (1) understanding the impact of the self-assembly process, such as the pH-switch methodologies, with a particular set of gelator molecules (in Chapter 2, mostly with BrNapAV – Fig. 1.8a – and in Chapter 3, 4 and 5 with 2NapFF – Fig. 1.8b), and (2) narrowing down the full understanding of the process in one gelator is important to comprehend what features of the hydrogel are process dependent. Additionally, there is an expansion of the findings for these two particular gelators to a range or gelators of a similar structure with different amino acids and protective group functionalisations. The selection of the BrNapAV in Chapter 2 stemmed from the serendipitous findings on that same chapter regarding a different macrostructre of the hydrogel. In Chapter 3, 4 and 5, the focus on 2NapFF results from findings from our group dipeptide library that indicated this gelator is versatile at forming gels from a pool of naphthalene-protected gelators.[30,48,95,237]

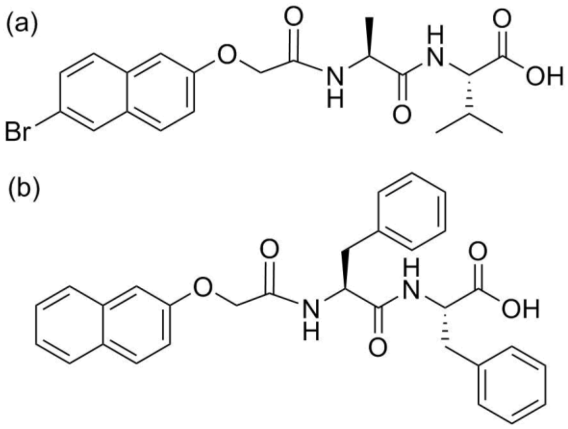

Fig. 1.8 – Chemical structure of BrNapAV (a) and 2NapFF (b): the mostly used peptide supramolecular gelators used in this Thesis.

1.8. Selection of the LMWG molecular structure

The selection of the modified-dipeptide systems was chosen based on: (1) most promising gelators for further applications; (2) prior literature knowledge regarding the variety of methods that can be used; and (3) highest mechanical properties of those particular gelators which were shown to successfully form hydrogels.[95,197,209] Most of these gelators were solely found to form hydrogels under a particular set of conditions. However, the variety of nanostructures, properties and functionality is still lacking in understanding for a range of self-assembly processes. The effect of a range of peptide sequences and protective groups in the gelator structure was already investigated elsewhere for a range of larger peptide amphiphiles and LMWG based on modified dipeptides.[94,166,168,214,229,236] Most of these systems are chiral.[238] In the case of some Fmoc- and naphthalene-protected gelators, some reports in the literature suggested biocompatibility and therefore biomedical applications.[10,21] Furthermore, reports suggest that the link between Fmoc and amine groups are acid resistant, however they can be easily cleaved with a base.[239,240] Therefore, the use of Fmoc group linked by a carbonyl group to the peptide sequences forms a base sensitive linkage. The cleavage of the Fmoc-group from a gelator was shown during the self-assembly process of an optically tuneable peptide self-assembly system.[55] On the other hand, the naphthalene and linker group are preferred to an Fmoc and linker group in peptide-based self-assembly molecular structure, because using the common pH-switch process, the dissolved solution is at high pH in the first step of sample preparation. Therefore, most dipeptide gelators used throughout this Thesis are naphthalene-based (Nap-dipeptides). A study of the apparent pK_a and predicted logP of most of the gelators used here was conducted previously.[236] The ability to select gelator molecules based on the expected pH dependence allowed us to distinguish a self-assembly process effect from sequence-dependent effect.

1.9. Chemical and physical properties of peptide supramolecular hydrogels

The search for links between physical and chemical properties of a hydrogel material and its molecular structure were at first investigated by several groups working with peptide-based hydrogel materials.[18,35,50,94,105,109] Using this approach, Chen *et al*. found that the selection of increasing hydrophobic amino acids for the dipeptide sequence resulted in hydrogels with increasingly high mechanical properties.[236] This link could be explained by different non-covalent bonds, different initiation of the packing and transition into the self-assembly process at a higher pH. Our group was also able to show that the mechanical properties could be tuned by the molecular environment (i.e. solvent mixtures).[50] The self-assembly process using pH switch methods results from a transition in the protonation of the carboxylic group of the gelators reducing charge repulsion and allowing the attractive hydrophobic interactions between gelators.[47] A good example of this effect is the cases shown by Chen *et al.*, where gelators with high log P were found to have a high apparent pK_a high log P and a lower cmc.[48] Gelators with these characteristics have more propensity to be effective gelators at higher final pH. The partition coefficient, P, is a measure of how hydrophilic – low log P – or hydrophobic – high log P. The apparent pK_a of the modified dipeptide gelators was also shown to vary with concentration and temperature, similar to alkyl soap fatty-acid based systems.[48] A general trend was observed between the more hydrophobic modified-dipeptides and their lower minimum gelation concentration (mgc).[48] In that same publication, the use of different gelator systems allows guidance of molecular design rules to make an informed selection of the gelator molecular structure, interactions and function. In separate work, research groups identified that the diphenylalanine was a core motif required for the formation of self-assembled nanostructures from the β-amyloid sequence into peptide-based sequences.[130,241] Other research have found that the solid-liquid surface interactions dictate different self-assembly phenomena using the same peptide sequence.[242–246] Furthermore, interactions and dynamic features of the dipeptide hydrogelation, prior to self-assembly (solution phase), during self-assembly and after completion of self-assembly process can be analysed by ^{1}H-NMR spectroscopy.[247] This technique is extremely valuable to understand the dynamics of percentage of gelator assembled against the percentage of gelator mobile in solution.[202,248]

1.10. Energy landscape and kinetics of peptide self-assembly

All of the interactions described above in a peptide-based self-assembly system can be depicted as the average sum of their kinetic or energy minimisation events by a conceptual energy landscape map. During the self-assembly process, a cascade of jumps in the energy state of the gelator molecules is a reflection of its conformation/shape, charges and interactions with its molecular environment. Some publications focussed on clarifying the behaviour of the peptide-based systems show that the self-assembly process significantly impacts the final hydrogel properties.[18,25,46,47,73,122,124,166,202,227,247] These publications also identify gelation as a kinetically trapped state (Fig. 1.8). A kinetically trapped state is designated to a self-assembled system by which the molecular packing and hierarchical features of a system are strictly time-dependent and are controlled by the kinetics of the self-assembly, as opposed to energetically minimized, or being in the thermodynamic minimum.

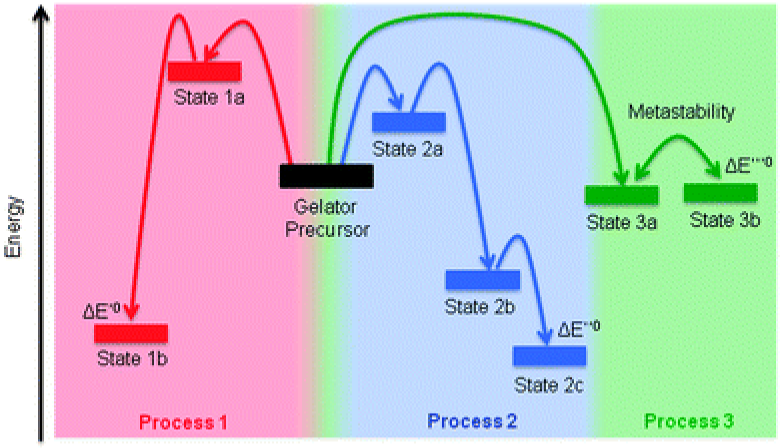

Figure 1.8 - Gelation can be thought of as a kinetically trapped state, rather than the thermodynamic minimum. The process of assembly may result in different pathways being followed. This figure is reprinted with permission of the Royal Chemistry Society.[18]

Other recent publications suggest that selected self-assembly processes of peptide-based gelators could lead to an energetically favourable state and be at an energy minimum.[127,249] However, reports from different groups suggest that their gelators show energy landscapes indicative of metastable and kinetically trapped states.[122,221] Fig. 1.8 illustrates the representation of a hypothetical energy landscape of a gelator when it is in different molecular environment conditions. This shows that different methods could lead to low energetically minimised states in that energy landscape region, so called kinetically trapped states.[122,250–252] This is significantly different to the funnel energy minimisation theories used to describe the single or multiple protein folding systems[253,254] or single crystal energy minimisation.[255] In related Fmoc-dipeptide system, a biocatalytic self-assembly process suggested that the formed structures preferentially form thermodynamically stable nanostructures.[249] In this case, no translucent hydrogels were formed. Instead, a weak and opaque suspension of nanostructures was formed. Recently, the use of different pathways was shown to form two separate self-assembly systems. In this work, Tantakitti *et al.* used an annealing step followed by a dilution step and the same methods in an opposite order with further addition of salt on both cases. These different paths resulted in a metastable state, a kinetically trapped state, if the dilution step was used first or in a thermodynamic stable product, if the annealing step was used first.[127]

Based on these reports regarding the competition between thermodynamic minimum and kinetically trapped states, it could well be that a particular state in LMWG self-assembly should be associated to the particular length-scale. Each of those intrinsically connected with an energy minimum or a kinetically trapped case. In the observations of kinetically trapped or energy minimising systems described, the self-assembly system appears to depend on the self-assembly processes. With most cases indicating a kinetically dominated self-assembly. In some cases, the structures formed could be in an energy minimum at a particular length scale, while the same system at another length scale could be in a kinetically trapped state. Therefore, the length scale should be associated to a particular energy landscape. Note that this is a separate case to the identification of crystal polymorphs because in the crystal polymorphs case, the molecular packing extends from the molecular scale (e.g. molecular conformation) to the millimetre scale (i.e. a macroscopic scale). Hence, in peptide-based supramolecular hydrogels, multiple energy landscapes could well be connected to different length scales. Within this perspective, it is possible that at lower length scales the energy well is deeper, while as the length scale increases (i.e. nanometre and microscale) there are several energy wells and they are less deep to allow kinetically trapped states. In the latter case, the relaxation times of the structures is temporally much larger in comparison to the self-assembly timescale at molecular length scales.

1.11. Switches of the self-assembly process

The self-assembly process is the hydrogelation method that triggers a series of multi-scale controlled aggregation events, from the folding of individual gelator molecules, molecular packing arrangements (e.g. parallel or anti-parallel β-sheet, α-helix, columnar stacking), nanostructure formation and microstructure. Self-assembly can be triggered and modulated by different conditions and steps of self-assembly. However understanding the link between self-assembly trigger/process and self-assembly stages is not always a trivial aspect to comprehend.[256]

1.11.1. Temperature-switch method

One of the first self-assembly to be described consists on a heat and cool ramp to solubilise and assemble the gelators during the cooling stage.[174] This method was shown to be applicable to several gelator systems.[50,103,111–113] Although one of the simplest methods to form a gel, this method does not always allow a fine control over the structure at multiple length scales, most importantly the microstructure of the peptide assemblies, visibly by a change in turbidity between samples. This lack of self-assembly robustness is likely because of temperature differences across the hydrogel during the cooling step and convective flows in the solution phase. All of these temperature-changing effects are prone to interfere with the self-assembly kinetics. As a result, more controllable methods were attempted by exploiting the possibility of increased gelator solubility by deprotonation of the carboxylic group.

1.11.2. pH-switch method

A N-protected dipeptide hydrogel was first shown to be processed by a pH-change to form transparent hydrogels by the Bing Xu research group (Fig. 1.9).[257] First, a high pH solution is dissolved with sodium hydroxide (NaOH). Secondly, this transparent solution was triggered by the addition of an acid (i.e. hydrochloric acid) to form hydrogels. Later approaches for more hydrophobic gelators first required a combination of the heating/cooling, sonication and high pH conditions were reported to successfully dissolve the gelator into a transparent solution.[24,179] However, despite being the first successful method to form a transparent peptide hydrogel under certain biometrically compatible processing conditions: temperature, concentration, pH – this method

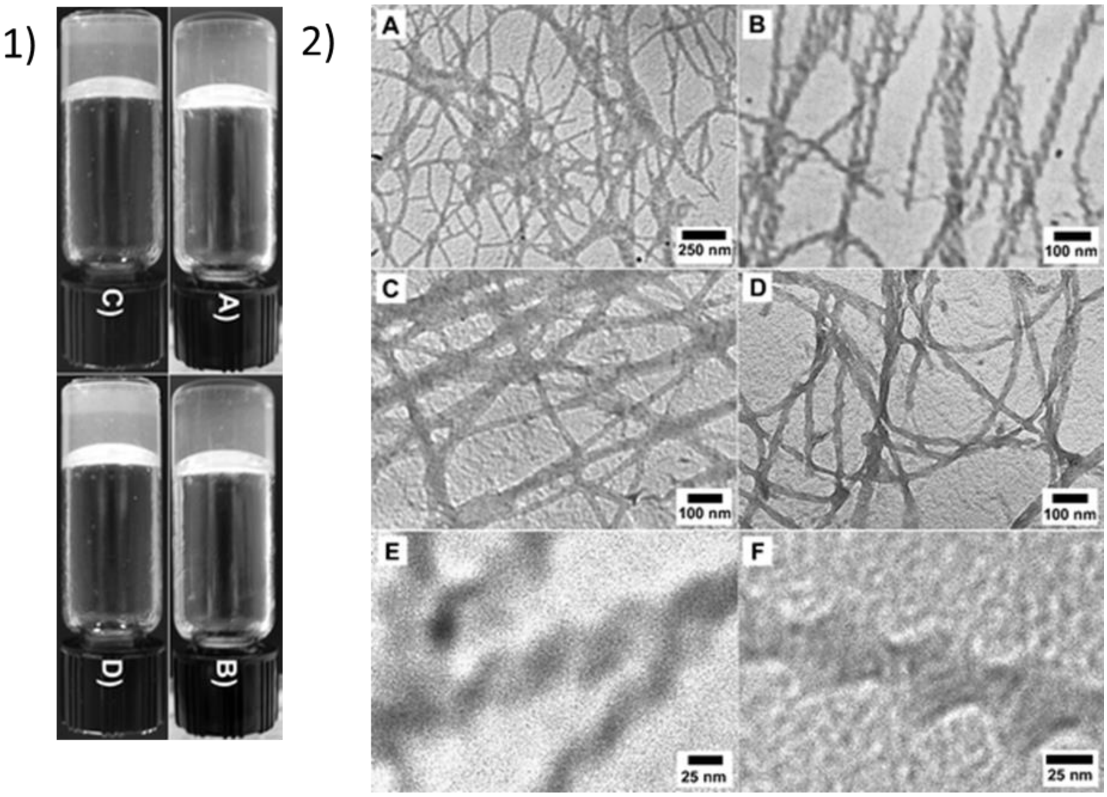

Figure 1.9 – Optical images of gels used by Bing Xu's research group A) 2NapGG, B) 2NapG(d)A, C) 2NapGA, D) 2NapGS (1). TEM images of the same hydrogels in (1), with 1.A, 1.B, 1.C and 1D correspond to 2.A, 2.B, 2.D, and 2.C in (2), additionally 2.E and 2.F are magnifications of 1.B and 1.C, respectively. This figure is reprinted with permission of the Royal Chemistry Society.[257]

resulted in lack of reproducibility in the hydrogel mechanical properties between similar processing conditions used in different reports.[105,104] In the peptide self-assembly case, the impact on the final mechanical properties depends not only on the initial conditions but also on the processing conditions (e.g. mixing).[24,105,104,179,221]

Several other peptide hydrogel systems have been shown to form gels by a pH-switch self-assembly processes.[47,106,107,141,202,227,257,258] Despite the versatility of the method, the drop-wise addition of an acid to a basic solution of a gelator was a diffusion limited method and dependent on the mode of agitation/mixing conditions because the drops of acid would have to diffuse across the solution to initiate the self-assembly process homogeneously, first in the regions in contact with diffusion from the acid drop deposited/mixed. In order to avoid this kinetic dependence on the mixing method, our group developed a pH-switch method to maintain homogeneity of the self-assembled structures.[47,52,124,227] This pH-switch method used the hydrolysis of glucono-δ-Lactone (GdL) into gluconic acid – slow process – in order to gradually lower the pH after GdL has been fully dissolved in solution – faster process (Fig. 1.10).[47] This method has been used now by several groups to investigate the importance of the self-assembly kinetics due to the slow pH-change.[25,30,46,47,52,124,122,227,259,260]

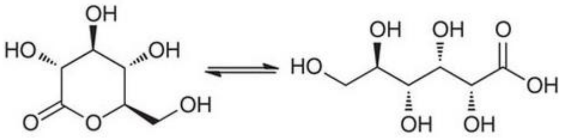

Figure 1.10 – Hydrolysis of glucono-δ-Lactone (GdL) into gluconic acid is used as a pH-switch self-assembly method.

Berillo *et al*. modified the microstructure of the gel using a combined cryogenic method with the GdL pH-switch method.[260] Recently, our group has investigated a range of anhydride molecules which can all hydrolyse to form acids which lower the pH, allowing further control of the kinetics of gelation and final mechanical properties.[261]

The link between the pH-trigger can be usually interpreted as a two-stage process in hydrogelation.[24,179,227,262] First, after the gelation is initiated, gelator molecules form elongated anisotropic structures, fibrils. This is typically followed by the lateral association of the fibrils in nanofibres at the apparent pK_a of the gelator, which can laterally associate and entangle to form the nanofibre network (i.e. microstructure) of the hydrogel. The Ulijn research group, with a range of analytical measurements used to monitor the gelation of FmocFF, explained this two stage self-assembly process typical of pH-switched systems.[24,179]

Self-assembly can also be triggered with a light-switch process.[117] This could also be described as an indirect pH-switch method, because it uses an auxiliary photo-acid generator to lower the pH at the irradiated areas. Equivalently, an alternative electrochemistry method uses the oxidation of hydroquinone in sodium chloride, which in turn lowers the pH of the solution, to trigger the hydrogelation below the apparent pK_a of the gelator.[263] The light-triggered self-assembly process and the electrochemically-triggered self-assembly process both allow temporally- and spatially-patterning of the supramolecular hydrogels with a UV mask[117] or electrodes,[263] respectively. Other groups have shown that a light-triggered cleavage of a pro-gelator[264] and the light-triggered change in gelator phase (i.e. because of a conformational change)[265] are means to directly use light on the gelator to control hydrogelation.

1.11.3. Salt-switch method

The early observations of solvent ionic dependency in the gelation process[258] and the significance of the use of buffers in natural protein folding,[266] protein stability[267,268] and biomimetic case studies[36,269–272] indicated that addition of salts and electrostatic interactions could in turn serve as a self-assembly trigger. The properties of surfactant systems can be modulated by their ionic interactions with the presence of salts.[273] In particular, the formation of worm-like micelles can be typically triggered and adjusted by: the addition of salts with counter ions to the gelator, lowering temperature below a melting temperature, pH to change the solvability of a gelator, charge of ions used, increase in shear rate and increase in concentration above a critical point.[273] For example, in a related block copolymer micellar system, it was shown that the addition of salts induces micellar growth in an anionic surfactant.[274] Furthermore, it was shown that aggregation occurred because of more efficient charge screening and more efficient packing of the head groups.[274] Similarly, with modified peptide gelators, the salt-switch method consists of adding and dissolving a salt in a homogeneous peptide solution, which consequently changes the gelator electrostatic repulsion or conformation to trigger the molecular packing. Further studies focused on the impact of different salts.[15,107,209,220] For example, our group has investigated the effects of salts with different anion valency, the impact of gelators with different hydrophobicity and the recovery behaviour of salt-triggered hydrogels (Fig. 1.11).[209] It was found that the ability to form hydrogels correlates with the hydrophobicity of the gelators, which determines the worm-like micellar formation at high pH.[209] Additionally, the ability to use this method with a range of gelators and a variety of functional groups was also shown.[209] The Ulijn research group found that the strength and melting point of the hydrogels correlated with the Hofmeister series (classification of ions in order of their ability to salt out or salt in proteins).[220] In their research, they have found for Fmoc-dipeptides with anion solutions ranging from chaotropes (structure breakers) to kosmotropes (structure makers) that kosmotropes increase the hydrogel chirality, mechanical strength and melting temperature. They have also observed that kosmotropes formed nanostructures with long bundles while chaotropes showed shorter entangled fibres. In separate research, it was found that the presence of sodium salts was shown to affect the cmc of Fmoc-amino acids solutions.[275] It was also found for a particular gelator, FmocYL what depending on the anions used, the nanostructure could be either nanofibre networks or spherical aggregates.[220]

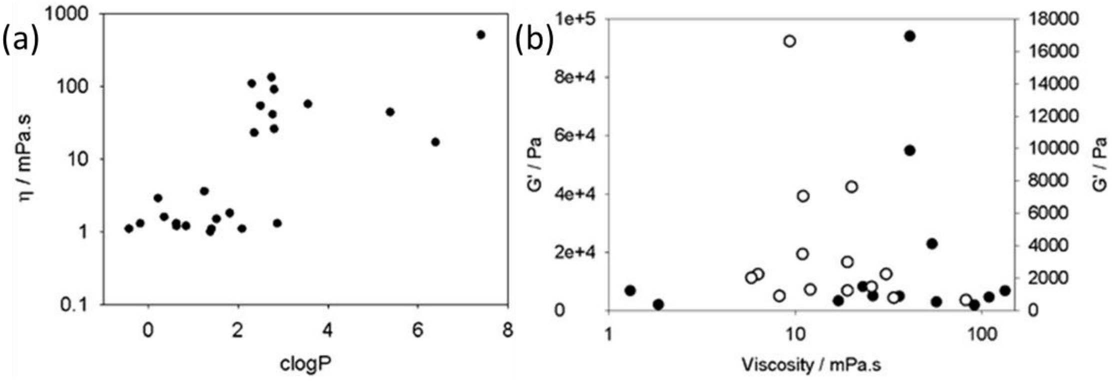

Figure 1.11 – Relation between viscosity and calculated logP for a range of modified dipeptide LMWG (a). The initial solutions viscosity was found unrelated with the mechanical properties of hydrogels of different gelators (b). This Figure is reprinted with permission of the Royal Chemistry Society.[209]

1.11.4. Solvent-switch method

In parallel to the work on pH-switch and salt switch, it was discovered that the gels could be made by a solvent change method. First, the gelators are fully dissolved in concentrated selected good organic solvent, such as 1,1,1,3,3,3-hexafluoroisopropanol (HFIP) or dimethyl sulfoxide (DMSO), and subsequently mixed with water to form a peptide hydrogel with approx. 0.5 w/w% of gelator.[94,146,145] This self-assembly process is here referred as solvent-switch method. It has also been used to successfully form hydrogels with a range of gelators, including peptide-based LMWG.[49,50,59,108–110,276] The research group of Qi used a two-step process to make hydrogel mixtures by using first a solvent-switch method to dissolve Fmoc-FF and this was followed by a dilution in water and polysaccharide stock solution mixtures.[98] Pont *et al*. shown that modified dipeptide systems self-assembled by a DMSO solvent-switch method were tolerant of the presence of polymer additives from 10 to 20 wt%, by maintaining their mechanical properties.[199] Li *et al*. showed that peptides hydrogels had solvent induced handness.[108] Reddy *et al*. demonstrated that the bare YF dipeptide resulted in completely different nanostructures when assembled using 2,2,2-trifluoroethanol (TFE) or by HFIP, forming microspheres or microribbons, respectively.[277] Recently, we have also identified that differences in the self-assembly kinetics and microstructure, were linked with the use of different solvent switch methods.[49] A comprehensive review by Lan *et al*. focuses on the solubility parameters of solvents in the ability to form supramolecular gels.[110]

1.11.5. Other self-assembly methods

Peptide hydrogels are formed above a minimum gelation concentration (mgc). Not surprisingly, some gelators that can be dissolved in a solvent system can form different peptide hydrogels by adjusting the concentration and aging of a gelator.[36] Aging of a gelator is defined as incubating the hydrogel at a set temperature over a period of time.

Aromatic groups with delocalized π-electrons have anisotropic diamagnetic susceptibility,[278] for example shown with low molecular weight organogelators.[279] Firstly, it was found that diphenylalanine dipeptides with a ferrofluid were able to align in magnetic fields.[115] Subsequently, Hill *et al*. reported that the same dipeptide alone could be aligned with strong magnetic fields to form aligned nanotubes.[114] Recently, our group has reported on the planar alignment of modified dipeptide hydrogel fibres with magnetic fields.[116] This result suggests that the self-assembly process can be further modified by strong magnetic fields.

Mechanical stress can modify and trigger the self-assembly of several gelators.[84,104,280] In the case study with peptide amphiphiles used by Shimada *et al*., the potential gelators were shown to irreversibly form a hierarchical structure after a 100 s^{-1} shear is applied in a solution of the PA spherical micelles with low viscosity.[281] After a specific shear rate is applied, the secondary structure changes from α-helix to β-sheet (molecular scale), the spherical micelles transform irreversibly into worm-like micelles (nanoscale), and the solution shows a gel-like behaviour (macroscale).[281]

In the past 8 years, a significant interest in controlling hydrogelation with catalytic- or biocatalytic-driven chemical reactions which introduce an additional form of controlling the self-assembly process.[149,282–284] These strategies use enzymes to trigger self-assembly inside cells, biocatalytic approach (Fig. 1.3b).[149]

It is important to refer that the initial and final pH of a gelation process is important to maintain reproducible results even if the main trigger for gelation does not involve pH (Fig. 1.12).

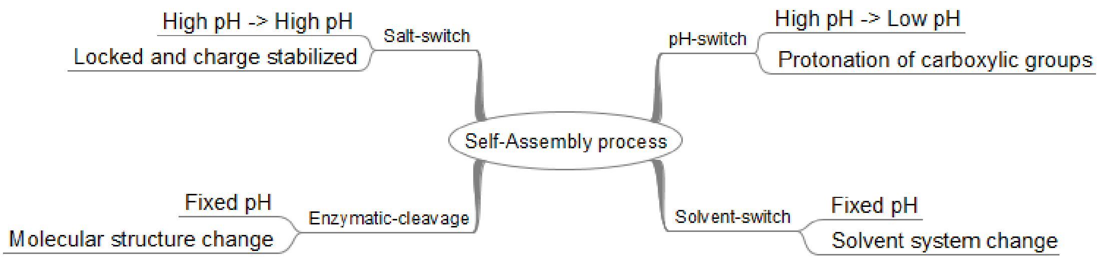

Figure 1.12 – Some of self-assembly processes, their respective pH transition and driving force for the gelation. Note that this is the most developed processes used in combination of N-protected dipeptide gelators with unprotected carboxylic groups, the focus of this Thesis.

Several research groups have dedicated their research to evaluate the impact of the process in the peptide self-assembly.[49,50,182,221,251,283–286] Across these investigations, it is clear that the control process of the self-assembly kinetics and formation of kinetic traps are important to investigate the system’s correlations between structure, molecular environment and functionality.

1.12. Thesis aims and research hypotheses

Firstly, this Thesis describes self-assembly processes for a range of N-protected dipeptide hydrogels (Chapter 2). A new method of gelation using a carbon dioxide gas atmosphere to kinetically trap the self-assembly is studied first with a range of gelators. The new method study is narrowed down to the unconventional gel macroscopic membrane structure formed with the BrNapAV gelator. The self-assembly of this gelator with this new CO_2 method is described and compared with other self-assembly methods using the same gelator. Finally, a range of ways for optimizing and adjusting the new self-assembly method are outlined.

In Chapter 3, a 2NapFF gelator solution phase is fully characterised. For the first time, the solution phase of a protected-dipeptide gelator is mapped in an extended phase diagram with concentration from 0.001 wt% to 1.0 wt% and temperature from 15 °C to 45 °C. The phase transitions over three orders of magnitude in concentration are investigated in the state prior to hydrogelation of a particular gelator (2NapFF). In this Chapter, the different characterisation methods used to probe the solution phase are examined and their results cross-interpreted. The interpretations of the solution phase of this particular gelator are validated and extended to a modified-dipeptide library of 17 gelators by single point measurements.

Following the solution phase characterisation, the characterisation of the corresponding hydrogel phase is also conducted (Chapter 4). This is used to assess the links between the solution phase and the hydrogel phase mechanical and intermolecular packing properties. The links found suggest that solution phases above the first cmc of the gelator are able to form salt-triggered hydrogels because of the likelihood for formation, or already existing, worm-like micellar structures in the solution phase and with the sol–to–gel transition.

In Chapter 5, the hydrogel network structure at multiple length scales is examined. The structural features from macroscale to nanoscale in the solution and hydrogel phase were analysed with four types of microscopy: optical microscopy, scanning electron microscopy, confocal microscopy and atomic force microscopy. Here, the structural features are evaluated at different length scales and related to the mechanical properties measured at those length scales. With a new (2015) fibre-tracking and imaging analysis open-source software developed by Usov and Mezzenga, FibreApp,[287] further mechanical parameters such as orientational distribution, persistence length are evaluated. To the best of our knowledge, this was the first attempt to use this fibre tracking software for mechanical characterisation of synthesised low molecular weight peptide-based solutions and hydrogels.

1.13. References

1. P. Terech and R. G. Weiss, *Chem. Rev.*, 1997, 97, 3133–3160.
2. R. G. Weiss and P. Terech, *Molecular Gels*, Springer Netherlands, Dordrecht, 2006.
3. M. Reches and E. Gazit, *Curr. Nanosci.*, 2006, 2, 105–111.
4. S. I. Stupp, V. LeBonheur, K. Walker, L. S. Li, K. E. Huggins, M. Keser, and A. Amstutz, *Science*, 1997, 276, 384–389.

5. A. Sorrenti, O. Illa, and R. M. Ortuno, *Chem. Soc. Rev.*, 2013, 42, 8200–8219.

6. T. P. J. Knowles and M. M. J. Buehler, *Nat. Nanotechnol.*, 2011, 6, 469–479.

7. E. Busseron, Y. Ruff, E. Moulin, and N. Giuseppone, *Nanoscale*, 2013, 5, 7098–140.

8. S. Gilead and E. Gazit, *Supramol. Chem.*, 2005, 17, 87–92.

9. R. Koopmans, *Advances in Chemical Engineering: Engineering Aspects of Self-Organising Materials (Volume 35)*, Academic Press (Elsevier), 2009.

10. X. Du, J. Zhou, J. Shi, and B. Xu, *Chem. Rev.*, 2015, 115, 13165–13307.

11. F. C. MacKintosh, J. Käs, and P. A. Janmey, *Phys. Rev. Lett.*, 1995, 75, 4425–4428.

12. G. F. Payne, E. Kim, Y. Cheng, H.-C. Wu, R. Ghodssi, G. W. Rubloff, S. R. Raghavan, J. N. Culver, and W. E. Bentley, *Soft Matter*, 2013, 9, 6019-6032.

13. S. R. Raghavan and J. F. Douglas, *Soft Matter*, 2012, 8, 8539-8546.

14. R. Dong, Y. Pang, Y. Su, and X. Zhu, *Biomater. Sci.*, 2015, 3, 937–954.

15. R. Li, C. C. Horgan, B. Long, A. L. Rodriguez, L. Mather, C. J. Barrow, D. R. Nisbet, and R. J. Williams, *RSC Adv.*, 2015, 5, 301–307.

16. C. Yan and D. J. Pochan, *Chem. Soc. Rev.*, 2010, 39, 3528–40.

17. V. Jayawarna, S. M. Richardson, A. R. Hirst, N. W. Hodson, A. Saiani, J. E. Gough, and R. V Ulijn, *Acta Biomater.*, 2009, 5, 934–43.

18. J. Raeburn, A. Zamith Cardoso, and D. J. Adams, *Chem. Soc. Rev.*, 2013, 42, 5143–56.

19. E. K. Johnson, D. J. Adams, and P. J. Cameron, *J. Mater. Chem.*, 2011, 21, 2024-2027.

20. C. Tomasini and N. Castellucci, *Chem. Soc. Rev.*, 2012, 42, 156–72.

21. J. P. Schneider, D. J. Pochan, B. Ozbas, K. Rajagopal, L. Pakstis, and J. Kretsinger, *J. Am. Chem. Soc.*, 2002, 124, 15030–7.

22. B. Ozbas, K. Rajagopal, J. P. Schneider, and D. J. Pochan, *Phys. Rev. Lett.*, 2004, 93, 268106.

23. M. Reches and E. Gazit, *Isr. J. Chem.*, 2005, 45, 363–371.

24. A. M. Smith, R. J. Williams, C. Tang, P. Coppo, R. F. Collins, M. L. Turner, A. Saiani, and R. V Ulijn, *Adv. Mater.*, 2008, 20, 37–41.

25. D. J. Adams, *Macromol. Biosci.*, 2011, 11, 160–173.

26. C. Berdugo, S. K. M. Nalluri, N. Javid, B. Escuder, J. F. Miravet, and R. V. Ulijn, *ACS Appl. Mater. Inter.*, 2015, 7, 25946–25954.

27. M. J. Serpe and S. L. Craig, *Langmuir*, 2007, 23, 1626–34.

28. T. Aida, E. W. Meijer, and S. I. Stupp, *Science*, 2012, 335, 813–817.

29. E. Krieg, M. M. C. Bastings, P. Besenius, and B. Rybtchinski, *Chem. Rev.*, 2016, 116, 2414–2477.

30. K. A. Houton, K. L. Morris, L. Chen, M. Schmidtmann, J. T. A. Jones, L. C. Serpell, G. O. Lloyd, and D. J. Adams, *Langmuir*, 2012, 28, 9797–806.

31. K. Liu, R. Xing, C. Chen, G. Shen, L. Yan, Q. Zou, G. Ma, H. Möhwald, and X. Yan, *Angew. Chemie Int. Ed.*, 2014, 54, 500 –505.

32. C. Xu and J. Kopeček, *Polym. Bull.*, 2006, 58, 53–63.

33. N. S. de Groot, T. Parella, F. X. Aviles, J. Vendrell, and S. Ventura, *Biophys. J.*, 2007, 92, 1732–1741.

34. S. Zhang, M. A. Greenfield, A. Mata, L. C. Palmer, R. Bitton, J. R. Mantei, C. Aparicio, M. O. de la Cruz, and S. I. Stupp, *Nat. Mater.*, 2010, 9, 594–601.

35. G. Fichman and E. Gazit, *Acta Biomater.*, 2014, 10, 1671–1682.

36. J. D. Hartgerink, E. Beniash, and S. I. Stupp, *Proc. Natl. Acad. Sci. U. S. A.*, 2002, 99, 5133–5138.

37. L. Deng, P. Zhou, Y. Zhao, Y. Wang, and H. Xu, *J. Phys. Chem. B*, 2014, 118, 12501–12510.

38. P. Marek, A. Abedini, B. Song, M. Kanungo, M. E. Johnson, R. Gupta, W. Zaman, S. S. Wong, and D. P. Raleigh, *Biochemistry*, 2007, 46, 3255–3261.

39. C. Wu, H. Lei, and Y. Duan, *Biophys. J.*, 2005, 88, 2897–2906.

40. K. M. Eckes, X. Mu, M. A. Ruehle, P. Ren, and L. J. Suggs, *Langmuir*, 2014, 30, 5287–5296.

41. J. D. Hartgerink, E. Beniash, and S. I. Stupp, *Science*, 2001, 294, 1684–1688.

42. S. R. Diegelmann, N. Hartman, N. Markovic, and J. D. Tovar, *J. Am. Chem. Soc.*, 2012, 134, 2028–2031.

43. L. Hsu, G. L. Cvetanovich, and S. I. Stupp, *J. Am. Chem. Soc.*, 2008, 130, 3892–3899.

44. M. S. S. de Samaniego and A. F. Miller, *Colloids Surfaces A Physicochem. Eng. Asp.*, 2008, 321, 271–274.

45. E. A. Appel, J. del Barrio, X. J. Loh, and O. A. Scherman, *Chem. Soc. Rev.*, 2012, 41, 6195–214.

46. D. J. Adams, L. M. Mullen, M. Berta, L. Chen, and W. J. Frith, *Soft Matter*, 2010, 6, 1971.

47. D. J. Adams, M. F. Butler, W. J. Frith, and M. Kirkland, *Soft Matter*, 2009, 5, 1856–1862.

48. L. Chen, S. Revel, K. Morris, L. C. Serpell, and D. J. Adams, *Langmuir*, 2010, 26, 13466–13471.

49. J. Raeburn, C. Mendoza-Cuenca, B. N. Cattoz, M. a. Little, A. E. Terry, A. Zamith Cardoso, P. C. Griffiths, and D. J. Adams, *Soft Matter*, 2015, 11, 927–935.

50. L. Chen, J. Raeburn, S. Sutton, D. G. Spiller, J. Williams, J. S. Sharp, P. C. Griffiths, R. K. Heenan, S. M. King, A. Paul, S. Furzeland, D. Atkins, and D. J. Adams, *Soft Matter*, 2011, 7, 9721–9727.

51. A. Aufderhorst-Roberts, W. J. Frith, M. Kirkland, and A. M. Donald, *Langmuir*, 2014, 30, 4483–4492.

52. A. Aufderhorst-Roberts, W. J. Frith, A. M. Donald, and R. Article, *Eur. Phys. J. E.*, 2014, 37, 1-11.

53. S. Bai, S. Debnath, N. Javid, P. W. J. M. Frederix, S. Fleming, C. Pappas, and R. V Ulijn, *Langmuir*, 2014, 30, 7576–7584.

54. O. Berger, L. Adler-Abramovich, M. Levy-Sakin, A. Grunwald, Y. Liebes-Peer, M. Bachar, L. Buzhansky, E. Mossou, V. T. Forsyth, T. Schwartz, Y. Ebenstein, F. Frolow, L. J. W. Shimon, F. Patolsky, and E. Gazit, *Nat. Nanotechnol.*, 2015, 10, 353–60.

55. K. Tao, E. Yoskovitz, L. Adler-Abramovich, and E. Gazit, *RSC Adv.*, 2015, 5, 73914–73918.

56. P. Kumaraswamy, S. Sethuraman, and U. M. Krishnan, *Soft Matter*, 2013, 9, 2684.

57. M. Wang, L. Du, X. Wu, S. Xiong, and P. K. Chu, *ACS Nano*, 2011, 5, 4448–4454.

58. J. Wu, A. Chen, M. Qin, R. Huang, G. Zhang, B. Xue, J. Wei, Y. Li, Y. Cao, and W. Wang, *Nanoscale*, 2014, 7, 1655–1660.

59. R. Orbach, I. Mironi-Harpaz, L. Adler-Abramovich, E. Mossou, E. P. Mitchell, V. T. Forsyth, E. Gazit, and D. Seliktar, *Langmuir*, 2012, 28, 2015–2022.

60. L. Pan, G. Yu, D. Zhai, H. R. Lee, W. Zhao, N. Liu, H. Wang, B. C.-K. Tee, Y. Shi, Y. Cui, and Z. Bao, *Proc. Natl. Acad. Sci. U. S. A.*, 2012, 109, 9287–92.

61. Q. Lu, S. Bai, Z. Ding, H. Guo, Z. Shao, H. Zhu, and D. L. Kaplan, *Adv. Mater. Inter.*, 2016, 3, 1500687 (1-6).

62. Y. Lin, Y. Qiao, P. Tang, Z. Li, and J. Huang, *Soft Matter*, 2011, 7, 2762–2769.

63. H. Cölfen and S. Mann, *Angew. Chem. Int. Ed. Engl.*, 2003, 42, 2350–65.

64. M. Lepere, C. Chevallard, J.-F. Hernandez, A. Mitraki, and P. Guenoun, *Langmuir*, 2007, 23, 8150–8155.

65. M. Berta, W. J. Frith, M. Kirkland, R. Holman, and P. Schuetz, *Annu. Trans. Nord. Rheol. Soc.*, 2013, 21, 273–280.

66. N. A. Dudukovic and C. F. Zukoski, *J. Chem. Phys.*, 2014, 141, 164905.

67. E. R. Draper, T. O. McDonald, and D. J. Adams, *Chem. Commun.*, 2015, 1, 8–10.

68. L. Deng and H. Xu, *Chinese Phys. B*, 2016, 25, 18701.

69. P. Prybytak, W. J. Frith, and D. J. Cleaver, *Interface Focus*, 2012, 2, 651–7.

70. X. Mu, K. M. Eckes, M. M. Nguyen, L. J. Suggs, and P. Ren, *Biomacromolecules*, 2012, 13, 3562–71.

71. W. J. Frith, *Philos. Trans. Ser. A*, 2016, 374.

72. X. Zhao, F. Pan, H. Xu, M. Yaseen, H. Shan, C. A. E. Hauser, S. Zhang, J. R. Lu, R. Ulijn, D. Woolfson, J. C. M. Van Hest, X. Zhao, F. Pan, H. Xu, M. Yaseen, and H. Shan, *Chem. Soc. Rev.*, 2010, 39, 3480.

73. D. J. Adams and P. D. Topham, *Soft Matter*, 2010, 6, 3707–3721.

74. S. I. Stupp, R. H. Zha, L. C. Palmer, H. Cui, and R. Bitton, *Faraday Discuss.*, 2013, 166, 9-30.

75. A. Baral, S. Basak, K. Basu, A. Dehsorkhi, I. W. Hamley, and A. Banerjee, *Soft Matter*, 2015, 11, 4944–4951.

76. R. V Ulijn, *Nat. News Views*, 2015, 295–296.

77. S. Fleming and R. V Ulijn, *Chem. Soc. Rev.*, 2014, 43, 8150–77.

78. M. Zelzer and R. V Ulijn, *Chem. Soc. Rev.*, 2010, 39, 3351–3357.

79. J. K. Gupta, D. J. Adams, and N. G. Berry, *Chem. Sci.*, 2016, 7, 4713–4719.

80. G. A. Silva, *Science*, 2004, 303, 1352–1355.

81. V. Yesilyurt, M. J. Webber, E. A. Appel, C. Godwin, R. Langer, and D. G. Anderson, *Adv. Mater.*, 2016, 28, 86–91.

82. J. B. Matson, C. J. Newcomb, R. Bitton, and S. I. Stupp, *Soft Matter*, 2012, 8, 3586-3595.

83. T. McDonald, A. Patrick, R. J. Williams, B. G. Cousins, and R. V Ulijn, in *Biomedical Applications of Electroactive Polymer Actuators Edited*, eds. F. Carpi and E. Smela, John Wiley & Sons Ltd., 2009, pp. 43–59.

84. B. D. Wall, S. R. Diegelmann, S. Zhang, T. J. Dawidczyk, W. L. Wilson, H. E. Katz, H.-Q. Mao, and J. D. Tovar, *Adv. Mater.*, 2011, 23, 5009–5014.

85. B. D. Wall, A. E. Zacca, A. M. Sanders, W. L. Wilson, A. L. Ferguson, and J. D. Tovar, *Langmuir*, 2014, 30, 5946–5956.

86. S. Semin, A. van Etteger, L. Cattaneo, N. Amdursky, L. Kulyuk, S. Lavrov, A. Sigov, E. Mishina, G. Rosenman, and T. Rasing, *Small*, 2015, 11, 1156–1160.

87. S. R. Diegelmann, J. M. Gorham, and J. D. Tovar, *J. Am. Chem. Soc.*, 2008, 130, 13840–13841.

88. Y. Liu, S. Hsu, F. Wu, H. Cheng, M. Yeh, and H. Lin, *Bioconjug. Chem.*, 2014, 25, 1794–1800.

89. L. L. Del Mercato, P. P. Pompa, G. Maruccio, A. Della Torre, S. Sabella, A. M. Tamburro, R. Cingolani, and R. Rinaldi, *Proc. Natl. Acad. Sci. U. S. A.*, 2007, 104, 18019–24.

90. M. Mizrahi, A. Zakrassov, J. Lerner-Yardeni, and N. Ashkenasy, *Nanoscale*, 2012, 4, 518–524.

91. H. A. M. Ardoña and J. D. Tovar, *Bioconjug. Chem.*, 2015, 26, 2290–2302.

92. H. Wang, C. Yang, M. Tan, L. Wang, D. Kong, and Z. Yang, *Soft Matter*, 2011, 7, 3897.

93. A. K. Das, A. R. Hirst, and R. V Ulijn, *Faraday Discuss.*, 2009, 143, 293–303.

94. R. Orbach, L. Adler-Abramovich, S. Zigerson, I. Mironi-Harpaz, D. Seliktar, and E. Gazit, *Biomacromolecules*, 2009, 10, 2646–51.

95. S. Awhida, E. R. Draper, T. O. McDonald, and D. J. Adams, *J. Colloid Interface Sci.*, 2015, 455, 24–31.

96. A. Baral, S. Roy, A. Dehsorkhi, I. W. Hamley, S. Mohapatra, S. Ghosh, and A. Banerjee, *Langmuir*, 2014, 30, 929–936.

97. X. Yu and M. V. Pishko, *Soft Matter*, 2011, 7, 8898-8904.

98. R. Huang, W. Qi, L. Feng, R. Su, and Z. He, *Soft Matter*, 2011, 7, 6222–6230.

99. S. R. Jadhav, B.-S. Chiou, D. F. Wood, G. DeGrande-Hoffman, G. M. Glenn, and G. John, *Soft Matter*, 2011, 7, 864–867.

100. S. Debnath, A. Shome, D. Das, and P. K. Das, *J. Phys. Chem. B*, 2010, 114, 4407–15.

101. M. Hughes, S. Debnath, C. W. Knapp, and R. V. Ulijn, *Biomater. Sci.*, 2013, 1, 1138-1142.

102. X. Tian, F. Sun, X.-R. Zhou, S.-Z. Luo, and L. Chen, *J. Pept. Sci.*, 2015, 21, 530–539.

103. A. Ghosh and J. Dey, *Langmuir*, 2009, 25, 8466–8472.

104. W. Helen, P. de Leonardis, R. V. Ulijn, J. E. Gough, N. Tirelli, and P. de Leonardis, *Soft Matter*, 2011, 7, 1732–1740.

105. J. Raeburn, G. Pont, L. Chen, and Y. Cesbron, *Soft Matter*, 2012, 8, 1168–1174.

106. K. Rajagopal, M. S. Lamm, L. A Haines-Butterick, D. J. Pochan, and J. P. Schneider, *Biomacromolecules*, 2009, 10, 2619–25.

107. X. R. Zhou, R. Ge, and S. Z. Luo, *J. Pept. Sci.*, 2013, 19, 737–744.

108. Y. Li, B. Li, Y. Fu, S. Lin, and Y. Yang, *Langmuir*, 2013, 29, 9721–9726.

109. N. A Dudukovic and C. F. Zukoski, *Langmuir*, 2014, 30, 4493–500.

110. Y. Lan, M. G. Corradini, R. G. Weiss, S. R. Raghavan, and M. A. Rogers, *Chem. Soc. Rev.*, 2015, 44, 6035–6058.

111. D. J. Pochan, J. P. Schneider, J. Kretsinger, B. Ozbas, K. Rajagopal, and L. Haines, *J. Am. Chem. Soc.*, 2003, 125, 11802–3.

112. C. Tang, R. V Ulijn, and A. Saiani, *Langmuir*, 2011, 27, 14438–14449.

113. D. W. P. M. Lowik, E. H. P. Leunissen, M. van den Heuvel, M. B. Hansen, J. C. M. van Hest, and D. W. P. M. Löwik, *Chem. Soc. Rev.*, 2010, 39, 3394–3412.

114. R. J. A. Hill, V. L. Sedman, S. Allen, P. Williams, M. Paoli, L. Adler-Abramovich, E. Gazit, L. Eaves, and S. J. B. Tendler, *Adv. Mater.*, 2007, 19, 4474–4479.

115. M. Reches and E. Gazit, *Nat. Nanotechnol.*, 2006, 1, 195–200.

116. M. Wallace, A. Z. Cardoso, W. J. Frith, J. A. Iggo, and D. J. Adams, *Chem. Eur. J.*, 2014, 20, 16484–16487.

117. J. Raeburn, T. O. McDonald, and D. J. Adams, *Chem. Commun.*, 2012, 48, 9355–7.

118. S. Boothroyd, A. Saiani, and A. F. Miller, *Biopolymers*, 2013, 101, n/a-n/a.

119. M. Reches and E. Gazit, *Science*, 2003, 300, 625–627.

120. Y. M. Abul-Haija and R. V. Ulijn, *Biomacromolecules*, 2015, 16, 3473–3479.

121. M. Rad-Malekshahi, M. Flement, W. E. Hennink, and E. Mastrobattista, *Microb. Cell Fact.*, 2014, 13, 987, 1482-1493.

122. D. J. Adams, K. Morris, L. Chen, L. C. Serpell, J. Bacsa, and G. M. Day, *Soft Matter*, 2010, 6, 4144–4156.

123. A. Aufderhorst-Roberts, W. J. Frith, and A. M. Donald, *Soft Matter*, 2012, 8, 5940.

124. A. Z. Cardoso, A. E. Alvarez Alvarez, B. N. Cattoz, P. C. Griffiths, S. M. King, W. J. Frith, and D. J. Adams, *Faraday Discuss.*, 2013, 166, 101–116.

125. L. Haines-Butterick, K. Rajagopal, M. Branco, D. Salick, R. Rughani, M. Pilarz, M. S. Lamm, D. J. Pochan, and J. P. Schneider, *Proc. Natl. Acad. Sci. U. S. A.*, 2007, 104, 7791–6.

126. M. a. Rogers, X. Liu, V. A. Mallia, and R. G. Weiss, *CrystEngComm*, 2015, 17, 8085–8092.

127. F. Tantakitti, J. Boekhoven, X. Wang, R. V. Kazantsev, T. Yu, J. Li, E. Zhuang, R. Zandi, J. H. Ortony, C. J. Newcomb, L. C. Palmer, G. S. Shekhawat, M. O. de la Cruz, G. C. Schatz, and S. I. Stupp, *Nat. Mater.*, 2016, 15, 469–476.

128. C. H. Görbitz, *Acta Crystallogr. Sect. B Struct. Sci.*, 2002, 58, 849–854.

129. C. C. H. Görbitz and F. Rise, *J. Pept. Sci.*, 2008, 14, 210–216.

130. C. H. Görbitz, *Chem. Commun.*, 2006, 22, 2332–2334.

131. C. H. Gorbitz, *Acta Cryst. B*, 2010, 66, 84–93.

132. L. Adler-Abramovich, D. Aronov, P. Beker, M. Yevnin, S. Stempler, L. Buzhansky, G. Rosenman, and E. Gazit, *Nat.*, 2009, 4, 849–854.

133. N. Amdursky, P. Beker, I. Koren, B. Bank-Srour, E. Mishina, S. Semin, T. Rasing, Y. Rosenberg, Z. Barkay, E. Gazit, and G. Rosenman, *Biomacromolecules*, 2011, 12, 1349–1354.

134. N. Hendler, N. Sidelman, M. Reches, E. Gazit, Y. Rosenberg, and S. Richter, *Adv. Mater.*, 2007, 19, 1485–1488.

135. A. Kholkin, N. Amdursky, I. Bdikin, E. Gazit, and G. Rosenman, *ACS Nano*, 2010, 4, 610–614.

136. N. Amdursky, E. Gazit, and G. Rosenman, *Adv. Mater.*, 2010, 22, 2311–2315.

137. M. Yemini, M. Reches, E. Gazit, and J. Rishpon, *Anal. Chem.*, 2005, 77, 5155–5159.

138. P. W. J. M. Frederix, G. G. Scott, Y. M. Abul-Haija, D. Kalafatovic, C. G. Pappas, N. Javid, N. T. Hunt, R. V. Ulijn, and T. Tuttle, *Nat. Chem.*, 2014, 7, 30–37.

139. Z. Yang and B. Xu, *Chem. Commun.*, 2004, 1, 2424–5.

140. Y. Zhang, Z. Yang, F. Yuan, H. Gu, P. Gao, and B. Xu, *J. Am. Chem. Soc.*, 2004, 126, 15028–15029.

141. Z. Yang, H. Gu, D. Fu, P. Gao, J. Lam, and B. Xu, *Adv. Mater.*, 2004, 16, 1440–1444.

142. I. Cherny and E. Gazit, *Angew. Chem. Int. Ed.*, 2008, 47, 4062–4069.

143. E. Gazit, *Chem. Soc. Rev.*, 2007, 36, 1263–1269.

144. V. Jayawarna, M. Ali, T. A. Jowitt, A. E. Miller, A. Saiani, J. E. Gough, and R. V Ulijn, *Adv. Mater.*, 2006, 18, 611–614.

145. T. Liebmann, S. Rydholm, V. Akpe, and H. Brismar, *BMC Biotechnol.*, 2007, 7, 88.

146. A. Mahler, M. Reches, M. Reches, S. I. A. Cohen, and E. Gazit, *Adv. Mater.*, 2006, 18, 1365–1370.

147. S. Sutton, N. Campbell, A. I. Cooper, M. Kirkland, W. J. Frith, and D. J. Adams, *Langmuir*, 2009, 25, 10285–10291.

148. D. J. Smith, G. A. Brat, S. H. Medina, D. Tong, Y. Huang, J. Grahammer, G. J. Furtmüller, B. C. Oh, K. J. Nagy-Smith, P. Walczak, G. Brandacher, and J. P. Schneider, *Nat. Nanotechnol.*, 2015, 11, 95–102.

149. J. Zhou, X. Du, N. Yamagata, and B. Xu, *J. Am. Chem. Soc.*, 2016, 138, 3813–3823.

150. Y. Gao, F. Zhao, Q. Wang, Y. Zhang, and B. Xu, *Chem. Soc. Rev.*, 2010, 39, 3425–33.

151. A. Maslovskis, J. Guilbaud, I. Grillo, N. Hodson, A. F. Miller, and A. Saiani, *Langmuir*, 2014, 30, 10471–10480.

152. R. Peltier, G.-C. Chen, H. Lei, M. Zhang, L. Gao, S. S. Lee, Z. Wang, and H. Sun, *Chem. Commun.*, 2015, 51, 17273–17276.

153. L. Szkolar, A. F. Miller, J. E. Gough, and A. Saiani, 2014, 28, 4609-46017.

154. X. Yan, F. Wang, B. Zheng, and F. Huang, *Chem. Soc. Rev.*, 2012, 41, 6042–65.

155. Y. Zhang, H. Gu, Z. Yang, and B. Xu, *J. Am. Chem. Soc.*, 2003, 125, 13680–13681.

156. Y. Gao, M. J. C. Long, J. Shi, L. Hedstrom, and B. Xu, *Chem. Commun.*, 2012, 48, 8404–6.

157. Y. Gao, Y. Kuang, X. Du, J. Zhou, P. Chandran, F. Horkay, and B. Xu, *Langmuir*, 2013, 29, 15191–15200.

158. Y. Gao, J. Shi, D. Yuan, and B. Xu, *Nat. Commun.*, 2012, 3, 1033-1040.

159. J. Rawson, A. C. Stuart, W. You, and M. J. Therien, *J. Am. Chem. Soc.*, 2014, 136, 17561–9.

160. J. H. Kim, M. Lee, J. S. Lee, and C. B. Park, Angew. Chem. Int. Ed., 2012, 51, 517–520.

161. P. D. Frischmann, K. Mahata, and F. Würthner, *Chem. Soc. Rev.*, 2013, 42, 1847–1870.

162. C. Chen, K. Liu, J. Li, and X. Yan, *Adv. Colloid Interface Sci.*, 2015, 225, 177–193.

163. J. H. Kim, D. H. Nam, Y. W. Lee, Y. S. Nam, and C. B. Park, *Small*, 2014, 10, 1272–1277.

164. L. Pereira, D. Gaspar, D. Guerin, A. Delattre, E. Fortunato, and R. Martins, *Nanotechnology*, 2014, 25, 11.

165. H. Cui, A. G. Cheetham, E. T. Pashuck, and S. I. Stupp, *J. Am. Chem. Soc.*, 2014, 136, 12461–12468.

166. M. Hughes, P. W. J. M. Frederix, J. Raeburn, L. S. Birchall, J. W. Sadownik, F. C. Coomer, I.-H. Lin, E. J. Cussen, N. T. Hunt, T. Tuttle, S. J. Webb, D. J. Adams, and R. V Ulijn, *Soft Matter*, 2012, 8, 5595-5602.

167. K. Joshi and S. Verma, *J. Pept. Sci.*, 2008, 14, 118–126.

168. K. Rajagopal, B. Ozbas, D. J. Pochan, and J. P. Schneider, *Eur. Biophys. J.*, 2006, 35, 162–9.

169. R. de la Rica and H. Matsui, *Chem. Soc. Rev.*, 2010, 39, 3499–509.

170. K. Ryan, J. Beirne, G. Redmond, J. I. Kilpatrick, J. Guyonnet, N.-V. Buchete, A. L. Kholkin, and B. J. Rodriguez, *ACS Appl. Mater. Inter.s*, 2015, 7, 12702–12707.

171. A. Lakshmanan, S. Zhang, and C. A. E. Hauser, *Trends Biotechnol.*, 2011, 30, 155–165.

172. A. S. Weingarten, R. V. Kazantsev, L. C. Palmer, M. McClendon, A. R. Koltonow, A. P. S. Samuel, D. J. Kiebala, M. R. Wasielewski, and S. I. Stupp, *Nat. Chem.*, 2014, 6, 1–7.

173. P. W. J. M. Frederix, R. V Ulijn, N. T. Hunt, and T. Tuttle, *J. Phys. Chem. Lett.*, 2011, 2, 2380–2384.

174. R. Vegners, I. Shestakova, I. Kalvinsh, R. M. Ezzell, and P. A. Janmey, *J. Pept. Sci.*, 1995, 1, 371–378.

175. K. Thornton, A. M. Smith, C. L. R. Merry, and R. V Ulijn, *Biochem. Soc. Trans.*, 2009, 37, 660–4.

176. Z. a. C. Schnepp, R. Gonzalez-McQuire, and S. Mann, *Adv. Mater.*, 2006, 18, 1869–1872.

177. A. J. Patil, R. Krishna Kumar, N. J. Barron, S. Mann, and R. K. Kumar, *Chem. Commun.*, 2012, 48, 7934–6.

178. E. Gazit, A. Mahler, and M. Reches, *WO Pat. WO/2007/043,048*, 2007, 61.

179. C. Tang, A. M. Smith, R. F. Collins, R. V Ulijn, and A. Saiani, *Langmuir*, 2009, 25, 9447–53.

180. H.-G. Braun and A. Z. Cardoso, *Colloids Surf. B. Biointer.*, 2012, 97, 43–50.

181. J. K. Kretsinger, L. a Haines, B. Ozbas, D. J. Pochan, and J. P. Schneider, *Biomaterials*, 2005, 26, 5177–86.

182. B. Ozbas, J. Kretsinger, K. Rajagopal, J. P. Schneider, and D. J. Pochan, *Macromolecules*, 2004, 37, 7331–7337.

183. T. Yucel and C. Micklitsch, *Macromolecules*, 2008, 41, 5763–5772.

184. B. Ozbas, K. Rajagopal, L. Haines-Butterick, J. P. Schneider, D. J. Pochan, and J. Darrin, *J. Phys. Chem. B*, 2007, 111, 13901–8.

185. P. Berndt, G. B. Fields, and M. Tirrell, *J. Am. Chem. Soc.*, 1995, 117, 9515–9522.

186. Y. C. Yu, P. Berndt, M. Tirrell, and G. B. Fields, *J. Am. Chem. Soc.*, 1996, 118, 12515–12520.

187. R. Matmour, I. De Cat, S. J. George, W. Adriaens, P. Leclère, P. H. H. Bomans, N. A. J. M. Sommerdijk, J. C. Gielen, P. C. M. Christianen, J. T. Heldens, J. C. M. van Hest, D. W. P. M. Lowik, S. De Feyter, E. W. Meijer, and A. P. H. J. Schenning, *J. Am. Chem. Soc.*, 2008, 130, 14576–14583.

188. D. W. P. M. Löwik, J. T. Meijer, I. J. Minten, H. van Kalkeren, L. Heckenmüller, I. Schulten, K. Sliepen, P. Smittenaar, and J. C. M. van Hest, *J. Pept. Sci.*, 2008, 14, 127–133.

189. K. L. Niece, C. Czeisler, V. Sahni, V. Tysseling-Mattiace, E. T. Pashuck, J. a Kessler, and S. I. Stupp, *Biomaterials*, 2008, 29, 4501–9.

190. S. Tsonchev, K. L. Niece, G. C. Schatz, M. A. Ratner, and S. I. Stupp, *J. Phys. Chem. B*, 2008,112,441–447.

191. H. Cui, M. Webber, and S. I. Stupp, *Pept. Sci.*, 2010, 94, 1–18.

192. I. W. Hamley, *Soft Matter*, 2011, 7, 4122–4138.

193. P. A Korevaar, C. J. Newcomb, E. W. Meijer, and S. I. Stupp, *J. Am. Chem. Soc.*, 2014, 136, 8540–3.

194. J. D. Tovar, R. C. Claussen, and S. I. Stupp, *J. Am. Chem. Soc.*, 2005, 127, 7337–45.

195. W. J. Frith, A. M. Donald, D. J. Adams, and A. Aufderhorst-Roberts, *J. Nonnewton. Fluid Mech.*, 2015, 222, 104–111.

196. T. Zuo-Xiu, Q. Meng, Z. Da-Wei, C. Yi, and W. Wei, *Chinese Phys. Lett.*, 2011, 28, 028702.

197. L. Chen, G. Pont, K. Morris, G. Lotze, A. Squires, L. C. Serpell, and D. J. Adams, *Chem. Commun.*, 2011, 47, 12071–12073.

198. Z. Zheng, J. Wang, P. Chen, M. Xie, L. Zhang, Y. Hou, X. Zhang, J. Jiang, J. Wang, Q. Lu, and G. Liang, *Nanoscale*, 2016, 8, 15142–15146.

199. G. Pont, L. Chen, D. G. Spiller, and D. J. D. Adams, *Soft Matter*, 2012, 8, 7797–7802.

200. C. Guo, Y. Luo, R. Zhou, and G. Wei, ACS nano 2012, 6, 3907–3918.

201. L. S. Birchall, S. Roy, V. Jayawarna, M. Hughes, E. Irvine, G. T. Okorogheye, N. Saudi, E. De Santis, T. Tuttle, A. A. Edwards, and R. V. Ulijn, *Chem. Sci.*, 2011, 2, 1349–1349.

202. K. L. Morris, L. Chen, J. Raeburn, O. R. Sellick, P. Cotanda, A. Paul, P. C. Griffiths, S. M. King, R. K. O'Reilly, L. C. Serpell, and D. J. Adams, *Nat. Commun.*, 2013, 4, 1480.

203. K. L. Niece, J. D. Hartgerink, J. J. J. M. Donners, and S. I. Stupp, *J. Am. Chem. Soc.*, 2003, 125, 7146–7.

204. H. A. Barnes, *Colloids Surfaces A Physicochem. Eng. Asp.*, 1994, 91, 89–95.

205. H. T. Davis, *Colloids Surfaces A Physicochem. Eng. Asp.*, 1994, 91, 9–24.

206. H.-S. Liao, J. Lin, Y. Liu, P. Huang, A. Jin, and X. Chen, *Nanoscale*, 2016, 8, 14814–14820.

207. N. Zanna, A. Merlettini, G. Tatulli, L. Milli, M. L. Focarete, C. Tomasini,Langmuir,2015,31, 12240-12250

208. A. Ghosh, M. Haverick, K. Stump, X. Yang, M. F. Tweedle, and J. E. Goldberger, *J. Am. Chem. Soc.*, 2012, 134, 3647–3650.

209. L. Chen, T. O. McDonald, and D. J. Adams, *RSC Adv.*, 2013, 3, 8714–8720.

210. N. Thota, Z. Luo, Z. Hu, and J. Jiang, *J. Phys. Chem. B*, 2013, 117, 9690–8.

211. R. G. Shrestha, K. Nomura, M. Yamamoto, Y. Yamawaki, Y. Tamura, K. Sakai, K. Sakamoto, H. Sakai, and M. Abe, *Langmuir*, 2012, 28, 15472–15481.

212. W. Hassouneh, E. B. Zhulina, A. Chilkoti, and M. Rubinstein, *Macromolecules*, 2015, 48, 4183–4195.

213. F. M. F. F. M. Menger and K. L. K. Caran, *J. Am. Chem. Soc.*, 2000, 122, 11679–11691.

214. L. A Estroff and A. D. Hamilton, *Chem. Rev.*, 2004, 104, 1201–1218.

215. M. de Loos, B. L. Feringa, and J. H. van Esch, *European J. Org. Chem.*, 2005, 2005, 3615–3631.

216. M. R. H. Krebs, K. R. Domike, D. Cannon, and A. M. Donald, *Faraday Discuss.*, 2008, 139, 265-274.

217. T. Yucel, C. C. M. Micklitsch, J. P. Schneider, and D. J. Pochan, *Macromolecules*, 2008, 41, 5763–5772.

218. I. Ramos Sasselli, P. J. Halling, R. V. Ulijn, and T. Tuttle, *ACS Nano*, 2016, 10, 2661–2668.

219. A. R. Hirst, I. a Coates, T. R. Boucheteau, J. F. Miravet, B. Escuder, V. Castelletto, I. W. Hamley, and D. K. Smith, *J. Am. Chem. Soc.*, 2008, 130, 9113–21.

220. S. Roy, N. Javid, P. W. J. M. Frederix, D. A. Lamprou, A. J. Urquhart, N. T. Hunt, P. J. Halling, and R. V Ulijn, *Chemistry*, 2012, 18, 11723–31.

221. B. Ding, Y. Li, M. Qin, Y. Ding, Y. Cao, and W. Wang, *Soft Matter*, 2013, 9, 4672-4680.

222. Y. Wang, Z. Zhang, L. Xu, X. Li, and H. Chen, *Colloids Surf. B. Biointer.*, 2012, 104C, 163–168.

223. A. Z. Cardoso, L. L. E. Mears, B. N. Cattoz, P. C. Griffiths, R. Schweins, and D. J. Adams, *Soft Matter*, 2016, 12, 3612–3621.

224. A. Pal and J. Dey, *Soft Matter*, 2011, 7, 10369–10376.

225. W. Edwards and D. K. Smith, *J. Am. Chem. Soc.*, 2013, 135, 5911–5920.

226. F. Delbecq, K. Tsujimoto, Y. Ogue, H. Endo, and T. Kawai, *J. Colloid Interface Sci.*, 2013, 390, 17–24.

227. L. Chen, K. Morris, A. Laybourn, D. Elias, M. R. Hicks, A. Rodger, L. Serpell, and D. J. Adams, *Langmuir*, 2010, 26, 5232–42.

228. C. Yan, A. Altunbas, T. Yucel, R. P. Nagarkar, P. Schneider, D. J. Pochan, J. P. Schneider, and D. J.

Pochan, *Soft Matter*, 2010, 6, 5143–5156.

229. K. L. Morris, A. Rodger, M. R. Hicks, M. Debulpaep, J. Schymkowitz, F. Rousseau, and L. C. Serpell, *Biochem. J.*, 2013, 450, 275–83.

230. V. Castelletto, C. M. Moulton, G. Cheng, I. W. Hamley, M. R. Hicks, A. Rodger, D. E. Lopez-Perez, G. Revilla-Lopez, and C. Aleman, *Soft Matter*, 2011, 7, 11405–11415.

231. A.-J. Avestro, M. E. Belowich, and J. F. Stoddart, *Chem. Soc. Rev.*, 2012, 41, 5881–95.

232. N. Javid, S. Roy, M. Zelzer, Z. Yang, J. Sefcik, and R. V. Ulijn, *Biomacromolecules*, 2013, 14, 4368–4376.

233. V. A. Mallia, P. Terech, and R. G. Weiss, *J. Phys. Chem. B*, 2011, 115, 12401–14.

234. J. H. Collier, J. S. Rudra, J. Z. Gasiorowski, and J. P. Jung, *Chem. Soc. Rev.*, 2010, 39, 3413–3424.

235. R. Feiner, L. Engel, S. Fleischer, M. Malki, I. Gal, A. Shapira, Y. Shacham-Diamand, and T. Dvir, *Nat. Mater.*, 2016, 15, 679–685.

236. L. Chen, S. Revel, K. Morris, C. S. L, D. J. Adams, L. C. Serpell, D. J. Adams, L. C. Serpell, D. J. Adams, L. C. Serpell, and D. J. Adams, *Langmuir*, 2010, 26, 13466–13471.

237. K. L. Morris, L. Chen, A. Rodger, D. J. Adams, L. C. Serpell, J. Adams, and L. C. Serpell, *Soft Matter*, 2015, 11, 1174–1181.

238. A. Brizard, R. Oda, and I. Huc, *Top. Curr. Chem.*, 2005, 256, 167–218.

239. L. A. Carpino and G. Y. Han, *J. Am. Chem. Soc.*, 1970, 92, 5748–5749.

240. L. A. Carpino and G. Y. Han, *J. Org. Chem.*, 1972, 37, 3404–3409.

241. L. Adler-Abramovich, M. Reches, V. L. Sedman, S. Allen, S. J. B. Tendler, and E. Gazit, *Langmuir*, 2006, 22, 1313–1320.

242. G. Demirel and F. Buyukserin, *Langmuir*, 2011, 27, 12533–12538.

243. Y. Su, X. Yan, A. Wang, J. Fei, Y. Cui, Q. He, and J. Li, *J. Mater. Chem.*, 2010, 20, 6734–6740.

244. R. Huang, W. Qi, R. Su, J. Zhao, and Z. He, *Soft Matter*, 2011, 22, 245609–7.

245. Y. Liu, Y. Cheng, H.-C. Wu, E. Kim, R. V Ulijn, G. W. Rubloff, W. E. Bentley, and G. F. Payne, *Langmuir*, 2011, 27, 7380–7384.

246. R. Hensel, R. Helbig, S. Aland, H. Braun, A. Voigt, C. Neinhuis, and C. Werner, Langmuir, 2013, 29, 1100-1112.

247. M. Wallace, J. A. Iggo, and D. J. Adams, *Soft Matter*, 2015, 11, 7739–7747.

248. E. R. Draper, E. G. B. Eden, T. O. McDonald, and D. J. Adams, *Nat. Chem.*, 2015, 7, 848–852.

249. M. Hughes, H. Xu, P. W. J. M. Frederix, A. M. Smith, N. T. Hunt, T. Tuttle, I. A. Kinloch, and R. V Ulijn, *Soft Matter*, 2011, 7, 10032–10038.

250. S. Ogi, T. Fukui, M. L. Jue, M. Takeuchi, and K. Sugiyasu, *Angew. Chemie Int. Ed.*, 2014, 53, 14363–14367.

251. P. a. Korevaar, S. J. George, A. J. Markvoort, M. M. J. Smulders, P. a. J. Hilbers, A. P. H. J. Schenning, T. F. a. De Greef, and E. W. Meijer, *Nature*, 2012, 481, 492–496.

252. S. Roy and R. V Ulijn, *Enzym. Polym.*, 2011, 237, 127–143.

253. S. S. Plotkin and J. N. Onuchic, *Understanding protein folding with energy landscape theory. Part I: Basic concepts.*, 2002, vol. 35.

254. K. A Dill and J. L. MacCallum, *Science*, 2012, 338, 1042–6.

255. S. L. Price, *Acta Crystallogr. B. Struct. Sci. Cryst. Eng. Mater.*, 2013, 69, 313–28.

256. J. H. Van Esch and J. H. van Esch, *Langmuir*, 2009, 25, 8392–4.

257. Z. Yang, G. Liang, M. Ma, Y. Gao, and B. Xu, *J. Mater. Chem.*, 2007, 17, 850-854.

258. A. Aggeli, M. Bell, N. Boden, J. N. Keen, P. F. Knowles, T. C. B. McLeish, M. Pitkeathly, and S. E. Radford, *Nature*, 1997, 386, 259–262.

259. T. Heuser, A. Steppert, C. Molano Lopez, B. Zhu, and A. Walther, *Nano Lett.*, 2014, 15, 2213–2219.

260. D. Berillo, B. Mattiasson, I. Y. Galaev, and H. Kirsebom, *J. Colloid Interface Sci.*, 2012, 368, 226–230.

261. E. R. Draper, L. L. E. Mears, A. M. Castilla, S. M. King, T. O. McDonald, R. Akhtar, and D. J. Adams, *RSC Adv.*, 2015, 5, 95369–95378.

262. C. Colquhoun, E. R. Draper, E. G. B. Eden, B. N. Cattoz, K. L. Morris, L. Chen, T. O. McDonald, A. Terry, P. C. Griffiths, L. C. Serpell, and D. J. Adams1,Nanoscale, 2014, 6, 13719-13725

263. J. Raeburn, B. Alston, J. Kroeger, T. O. McDonald, J. R. Howse, P. J. Cameron, and D. J. Adams, *Mater. Horizons*, 2014, 1, 241-246.

264. T. Muraoka, C. Y. Koh, H. Cui, and S. I. Stupp, *Angew. Chem. Int. Ed.*, 2009, 48, 5946–5949.

265. X. Li, Y. Gao, Y. Kuang, and B. Xu, *Chem. Commun.*, 2010, 46, 5364–6.

266. Y. Zhang and P. S. Cremer, *Curr. Opin. Chem. Biol.*, 2006, 10, 658–63.

267. J. S. Philo and T. Arakawa, *Curr. Pharm. Biotechnol.*, 2009, 10, 348–51.

268. R. L. Baldwin, *Biophys. J.*, 1996, 71, 2056–2063.

269. H. A. Lashuel, S. R. LaBrenz, L. Woo, L. C. Serpell, and J. W. Kelly, *J. Am. Chem. Soc.*, 2000, 122, 5262–5277.

270. A. Aggeli, M. Bell, L. M. Carrick, C. W. G. Fishwick, R. Harding, P. J. Mawer, S. E. Radford, A. E. Strong, and N. Boden, *J. Am. Chem. Soc.*, 2003, 125, 9619–9628.

271. M. R. Caplan, P. N. Moore, S. Zhang, R. D. Kamm, and D. A. Lauffenburger, *Biomacromolecules*, 2000, 1, 627–631.

272. N. L. Goeden-Wood, J. D. Keasling, and S. J. Muller, *Macromolecules*, 2003, 36, 2932–2938.

273. C. A. Dreiss, *Soft Matter*, 2007, 3, 956–970.

274. R. D. Wesley, C. A. Dreiss, T. Cosgrove, S. P. Armes, L. Thompson, F. L. Baines, and N. C. Billingham, *Langmuir*, 2005, 21, 4856–4861.

275. R. Vijay and P. L. Polavarapu, *J. Phys. Chem. A*, 2012, 116, 10759–69.

276. A. D. Martin, A. B. Robinson, and P. Thordarson, *J. Mater. Chem. B*, 2015, 3, 2277–2280.

277. S. M. M. Reddy, G. Shanmugam, and A. B. Mandal, *Org. Biomol. Chem.*, 2014, 12, 6181–9.

278. B. H. Ruessink and C. MacLean, *J. Chem. Phys.*, 1986, 85, 93.

279. I. O. Shklyarevskiy, P. Jonkheijm, P. C. M. Christianen, A. P. H. J. Schenning, D. Guerzo, J. Desvergne, E. W. Meijer, and J. C. Maan, 2005, 2108–2112.

280. E. R. Draper, O. O. Mykhaylyk, and D. J. Adams, *Chem. Commun.*, 2016, 52, 6934–6937.

281. T. Shimada, K. Megley, M. Tirrell, and A. Hotta, *Soft Matter*, 2011, 7, 8856-8861.

282. Z. Yang, G. Liang, and B. Xu, *Acc. Chem. Res.*, 2008, 41, 315–26.

283. A. R. Hirst, S. Roy, M. Arora, A. K. Das, N. W. Hodson, P. Murray, S. Marshall, N. Javid, J. Sefcik, J. Boekhoven, J. H. van Esch, S. Santabarbara, N. T. Hunt, and R. V Ulijn, *Nat. Chem.*, 2010, 2, 1089–1094.

284. J. Boekhoven, J. M. Poolman, C. Maity, F. Li, L. van der Mee, C. B. Minkenberg, E. Mendes, J. H. van Esch, and R. Eelkema, *Nat. Chem.*, 2013, 5, 1–5.

285. X.-D. Xu, C.-S. Chen, B. Lu, S.-X. Cheng, X.-Z. Zhang, and R.-X. Zhuo, *J. Phys. Chem. B*, 2010, 114, 2365–72.

286. W. Zheng, J. Gao, L. Song, C. Chen, D. Guan, Z. Wang, Z. Li, D. Kong, and Z. Yang, *J. Am. Chem. Soc.*, 2013, 135, 266–71.

287. I. Usov and R. Mezzenga, *Macromolecules*, 2015, 48, 1269–1280.

Chapter 2

2. Self-assembly of peptide-based low molecular weight hydrogels by a carbon dioxide pH-switch method

2.1. Abstract

A novel pH-switch method to form low molecular weight peptide hydrogels has been devised using carbon dioxide (CO_2) to acidify the water. A screening of different gelators with this new method allowed bulk hydrogel formation for most of the low molecular weight gelators (LMWG) tested with an apparent pK_a above 5.8. By using this method, when the gelator's apparent pK_a is in the region from 5.5 and 5.8 and the starting solution is not a structured phase, a peptide hydrogel membrane was formed instead of a bulk gel. The factors identified that determine the fate of gelation using this new method are the gelator apparent pK_a, the viscosity of the starting solution, the pH gradient during gelation, and concentration.

Furthermore, the unconventional hydrogel membrane formed with BrNapAV and the new pH-switch method revealed that the concentration, volume of sample, initial pH, exposure time to CO_2, and CO_2 pressure all have an impact on the mechanical properties, thickness, nanostructure, microstructure, and secondary structure of the hydrogel membrane. In the case of the BrNapAV gelator (apparent pK_a of 5.8), the resulting CO_2 hydrogel membrane at a final pH 6.4 had similar mechanical properties to an intermediate micellar phase formed when a BrNapAV solution at high pH (10.5) is gelled by a GdL pH-switch method to a final pH (4.0), below its apparent pK_a. This intermediate phase was not easily accessible with other gelation methods. Finally, the new CO_2 triggered method was investigated with regards to the self-assembly kinetics of gelation characteristics[1] and these were compared with glucono-δ-lactone (GdL) and HCl triggered gels[2] in order to examine the mechanical efficacy of each method.

2.2. Introduction

Peptide-based low molecular weight gelators have been shown to form hydrogels by different methods or self-assembly processes.[3–10] The methods used so far in the literature are described with detail in Chapter 1, Section 1.11, page 24. The control of hydrogelation, the process of forming hydrogels, is of paramount importance if the intention is to prepare more complex materials using simple components.[1,3,10] The present pH-witch methods are easy and simple to use. However, when a simple acid solution drops, such as HCl, are used to lower the pH and trigger the hydrogel formation, the hydrogels formed were shown to be heterogeneous.[2] These gels are dependent on difficult to control aspects of the self-assembly process, such as the mode of agitation and temperature changes.[23,47] The use of hydrolysis of glucono-δ-lactone (GdL) to lower the pH in water and trigger hydrogelation is a very versatile method to make more homogeneous hydrogels and study the pH-switch gelation process because the hydrolysis of GdL is a slow process.[2] Therefore, in this case, hydrogelation is a slow kinetic process typically lasting over 12 hours, which can be controlled by the amount of GdL added to the dissolved gelator solution. In spite the usefulness of this method, the method is still dependent on pouring some GdL powder over the solution and diffusion of the GdL powder over the solution. Therefore, we have focused this chapter on the development of a new CO_2 pH-switch gelation method, which would allow for a better hydrogelation control and homogeneity, while still being able to control the gelation spatially and at faster rates. This method is firstly introduced. Secondly, the new materials that can be formed with this same new method are characterised using a screening of different gelators (Fig. 2.1). Thirdly, the factors determining the formation of different types of hydrogels, only accessible with this new method are investigated. Following this, the new method is investigated with one particular kind of gelator, BrNapAV (Fig. 2.1) because of the unconventional behaviour found when this type of gelator is used in conjugation with the new method. Next, we have investigated the hypothesis, if this new pH-switch method does actually access an intermediary self-assembly state of all the previously studied pH-switch self-assembly methods used with modified-dipeptide gelators. Finally, the new method is then compared against existing pH-switch methods with regards to the self-assembly kinetic aspects of gelation.

Therefore, we start by the discussion of the important aspects of the self-assembly process (Section 2.2.1.); the known impact of the self-assembly kinetics for hydrogel formation (Section 2.2.2.); refresh the reader on the acidification of water by carbon dioxide (Section 2.2.3.), and then discuss our own results.

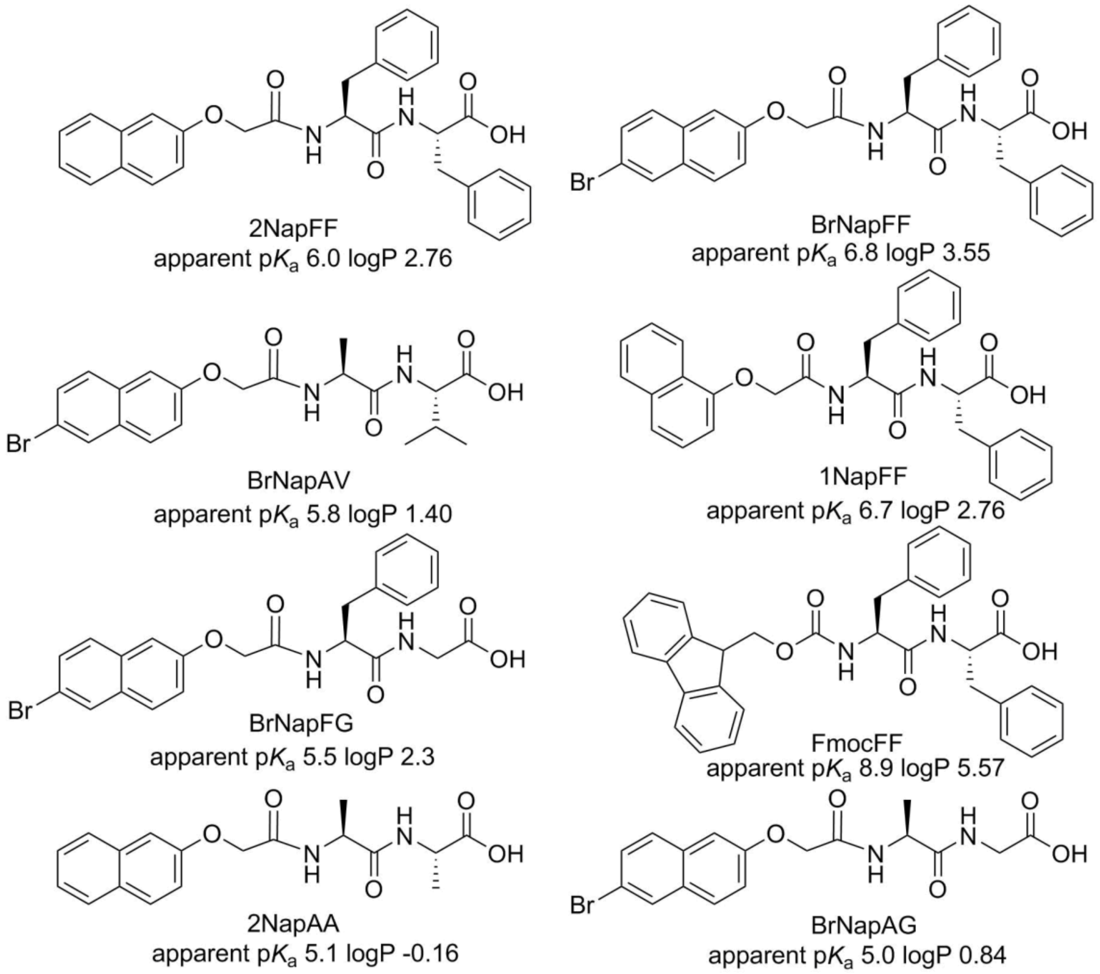

Fig. 2.1 – Structures of the gelators used in Chapter 2.

2.2.1. Different self-assembly processes or different gelators can form hydrogels with different properties

As described in Chapter 1, Section 1.6, using the same molecule-solvent system and different self-assembly pathways for the same gelator can result in hydrogels with different properties.[3–10] A number of self-assembling peptide-based gelators have been investigated with regards to the self-assembly pathway.[1,3,10] It has been found that a slight change in the self-assembling molecule (e.g. peptide sequence)[11–18] or the solvent conditions[4,19–23] results in a change in the properties of the hydrogel. For example, by changing the hydrophobicity and bulkiness of the gelator peptide sequence, Niece et al. were able to control the rate of gelation with the same assembly process.[24] Other groups have found that a change in solvent can alter the kinetics of the self-assembly pathway and so change the final hydrogel properties.[20,25–27] It is therefore important to understand how peptide hydrogels can be formed.

Supramolecular self-assembling systems can form hydrogels providing they can form one-dimensional structures that can entangle or cross-link with one another and trap water. These supramolecular structures that make the hydrogel are stabilised by non-covalent bonds (e.g. hydrogen bonds, π-π stacking, hydrophobic effects, van der Waals forces, electrostatic interactions). The self-assembly process that forms the hydrogels typically takes advantage of a change in solubility of the gelator used. For dipeptide-based gelators, the change in solubility can often be achieved by either the stabilisation of carboxylic groups with salt-switch and pH-switch methods, or by a structural change with an enzymatic-switch, or by a solubility change with solvent-switch methods (among other methods). These methods are described in Chapter 1, Section 1.12. The pH-switch method results in the transition from a solution of deprotonated gelator to a hydrogel. A pH-decrease changes the capacity to acquire charge in the carboxylic group, the acid/base properties of the gelator and other molecular features. In the case of the gelators studied in this Thesis, when the pH-switch method is used, this method works because it takes advantage of the transition from a deprotonated carboxylic group at high pH to a protonated carboxylic group at low pH. This transition changes the solubility from soluble to insoluble and allows the self-assembly of gelators to form an hydrogel.

In general, pH-switch methods discussed here involve a change from high pH to low pH. In a high pH solution, most *N*-protected dipeptide-based gelators behave as typical surfactants.[34–36] For example, it was shown recently by our group that the gelator 2NapFF (Fig. 2.1) forms micellar structures at 0.5 wt% when the pH is above its apparent pK_a.[37] The high pH solution phase of 2NapFF is studied in detail in Chapter 3. The transition from the high pH solution to a low pH solution is important to understand the pH-switch self-assembly processes for forming gels. Our group has found that the gelator's apparent pK_a and the final pH (pH$_f$) of the solution are important parameters in designing the final mechanical properties.[11] These gelators with high apparent pK_a can form gels at a higher final pH (as long as the pH is still below the apparent pK_a). Also, the lower the final pH (pH$_f$) of a hydrogel of *N*-protected dipeptide gelators studied by our group, the stiffer the gels are.[11] This is likely because there are more gelators with protonated carboxylic groups in solution. Additionally, protonated gelators with carboxylic groups can form structures. Stupp's research group has shown that by lowering the pH with HCl vapour, it is possible to form hydrogels of a peptide amphiphile system.[38] The use of a slower self-assembly process has proven to be advantageous in the case of the GdL pH-switch method.[2] The GdL pH-switch method uses the slow hydrolysis of GdL into gluconic acid to lower the pH, because of slow GdL reaction kinetics. With this method, our group was able to form more homogenous hydrogels from Fmoc-dipeptides as compared to when aqueous HCl was used. A homogeneous gel is here considered a transparent gel with no turbid regions. Also, the GdL pH-switch method allows the gelation process to be followed in more detail because it occurs more slowly. By analogy, using a slower gas triggered self-assembly process could also have similar advantages over the HCl vapour method. The literature shows that it is possible to control the final pH by means of carbon dioxide.[39,40] We note the group of Floren *et al*. have used high pressure CO_2 to induce hydrogelation of the native silk protein at 2 and 4 wt% for biomedical application.[41] Additionally, George and Weiss found that it is possible to form reversible organogels using the uptake of carbon dioxide (CO_2) by primary and secondary amines to trigger gelation.[42,43] This is not related to the pH, but rather the formation of carbamates. Recently, after the work here was completed, Angulo-Pachón et al. have used the sucrose-fuelled bacterial release of CO_2 to gel peptide amphiphiles.[44] Hence, using a slow gelation method might allow us to better understand modified-dipeptide gelators or make different hydrogels.

The study of the kinetics of the chemical processes, in this particular area of research, is related to the peptide hydrogel self-assembly kinetics.

2.2.2. Self-assembly kinetics of peptide-based low molecular weight hydrogels

In order to fully understand the self-assembly process, the gelation kinetics must be understood. The gelation kinetics is described by the rate of assembly and number of stages of the self-assembly process. In particular, peptide structure, additives, concentration changes of gelator species, temperature and salt concentrations can influence the gelation kinetics. Our group and others have investigated the gelation kinetics and attempted different strategies to control it.[1,2,28–33] We found that with a dipeptide gelator, BrNapAG (Fig. 2.1), the temperature at which we conducted a pH-switch self-assembly did not significantly change the final mechanical properties of the hydrogel.[1] The self-assembly in this case was kinetically trapped, independent of the temperature of process within the 15 to 45 °C region. However, for a different peptide-based gelator, MAX1 (Fig. 1.4c), the temperature and salt concentration were shown to directly influence the kinetic properties and the mechanical properties of the final hydrogel.[28,29] In the MAX1 hydrogel system, fast gelation kinetics was obtained by increasing the ionic strength with an increase of the salt concentration. The control of the gelation kinetics in this system regulated the stiffness of the hydrogels obtained because of an increase in the number of entanglements. Heuser *et al*. have used additives, which they called dormant deactivators and fast promoters, to regulate the stability of the self-assembly process. Therefore, they can tune the self-assembly kinetics from a period of minutes to days.[30] They are able to control the kinetics by implementing an internal feedback system of assembly and disassembly by means of the hydrolysis of ester-containing molecules to lower the pH (dormant deactivators) and basic buffers (promoters). Other forms of controlling the kinetics of self-assembly reside in the aging process of peptide gelators.[31,32] Therefore, gelation kinetics can depend on temperature, salt concentration, ionic strength, self-assembling competing molecules, and gel aging, impacting on the stiffness and number of entanglements, and eventually on the gel mechanical properties.

2.2.3. Acidification of water by carbon dioxide

Carbon dioxide can be used to lower the pH in water. The dissolution of CO_2 results in the formation of carbonic acid (H_2CO_3) which is converted into bicarbonate ($\mathrm{HCO_3^-}$) and carbonate ($\mathrm{CO_3^{2-}}$) species dependent on the pH.[45] Our hypothesis is that the formation of bicarbonate species in water lowers the solution pH to gradually protonate the gelator. When the number of uncharged gelator molecules increases, they may self-assemble and further form hydrogels. A way to represent the equilibrium of carbonate species in water is by a Bjerrum plot. This plot shows the equilibrium concentrations of carbon dioxide and the carbonate species as a function of the pH in solution (Fig. 2.2). In terms of H^+ availability, the higher the aqueous CO_2, the more it reacts with water to make carbonic acid. The carbonic acid may loose its protons to form bicarbonate and carbonate, therefore shifting the H^+ balance in water to higher proton values and lower pH.

The equilibrium constants can be used to calculate the final pH of a solution at a given pressure and temperature of CO_2.[46] However, in our hydrogel systems these equations are not completely valid as the system includes the gelator and NaOH.

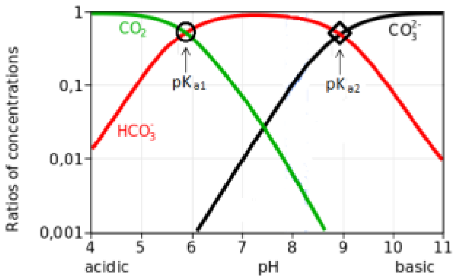

Figure 2.2 – Bjerrum plot of the carbonate system. pH at each of the proportions of carbonate species (modified from Zeebe *et al.*[39]). The circle and the diamond indicate pK_{a1} = 5.86 and pK_{a2} = 8.92 of carbonic acid respectively.[39]

2.3. Results and Discussion

2.3.1. Introducing the new pH-switch method for preparation of peptide-based low molecular weight hydrogels

Here, we have used a new low pressure CO_2 triggering process with peptide-based gelators and then compared this method with existing pH-switch methods. The gelators used here were in-house synthesised *N*-protected dipeptides (see Materials and Methods, 2.5.1). They were chosen because they have a range of apparent pK_a's, hydrophobicities (Fig. 2.1). Additionally, we have combined this new CO_2 triggered process with the GdL method to form hydrogels in a two-step process.

All self-assembly methods described here begin by diluting the required amount of gelator in double distilled water (ddH_2O) and NaOH (or D_2O and NaOD for Fourier Transform Infrared Spectroscopy (FTIR) experiments) at a specific initial pH (pH_i), typically pH 10.5 (unless mentioned otherwise). This pH_i has to be above the pK_a of the gelator we intend to form a hydrogel.[11] Throughout this Chapter, this starting state is referred to as the solution phase (or just solution).

To form a gel, the pH of this solution phase is changed. The use of a mineral acid to lower the pH is the simplest method that is used to form a hydrogel (Fig. 2.3a). The HCl vapour and aqueous HCl methods rely on diffusion of a saturated gas phase of HCl or the addition of 1.1 molar equivalents of 1M HCl solution into the gelator high pH solution, respectively (Fig. 2.3a). As mentioned above, the GdL method uses the slow hydrolysis of GdL into gluconic acid to lower the pH. In this method, the high pH solution is transferred to a vial with a pre-weighed amount of GdL and the closed vial incubated at room temperature (20 ± 2 °C) for 24 hours (Fig. 2.3b). The newly devised pH-switch method is based on CO_2 acidification of the high pH gelator solution by connecting a carbon dioxide gas source (i.e. CO_2 gas cylinder) to a reaction chamber containing an open vial (Fig. 2.3c). In a pressure-controlled setup, a CO_2 gas cylinder with a pressure regulator is used as the CO_2 inlet (Fig. 2.3c). For all quantitative experiments, the CO_2 cylinder was used as a CO_2 inlet. The sample

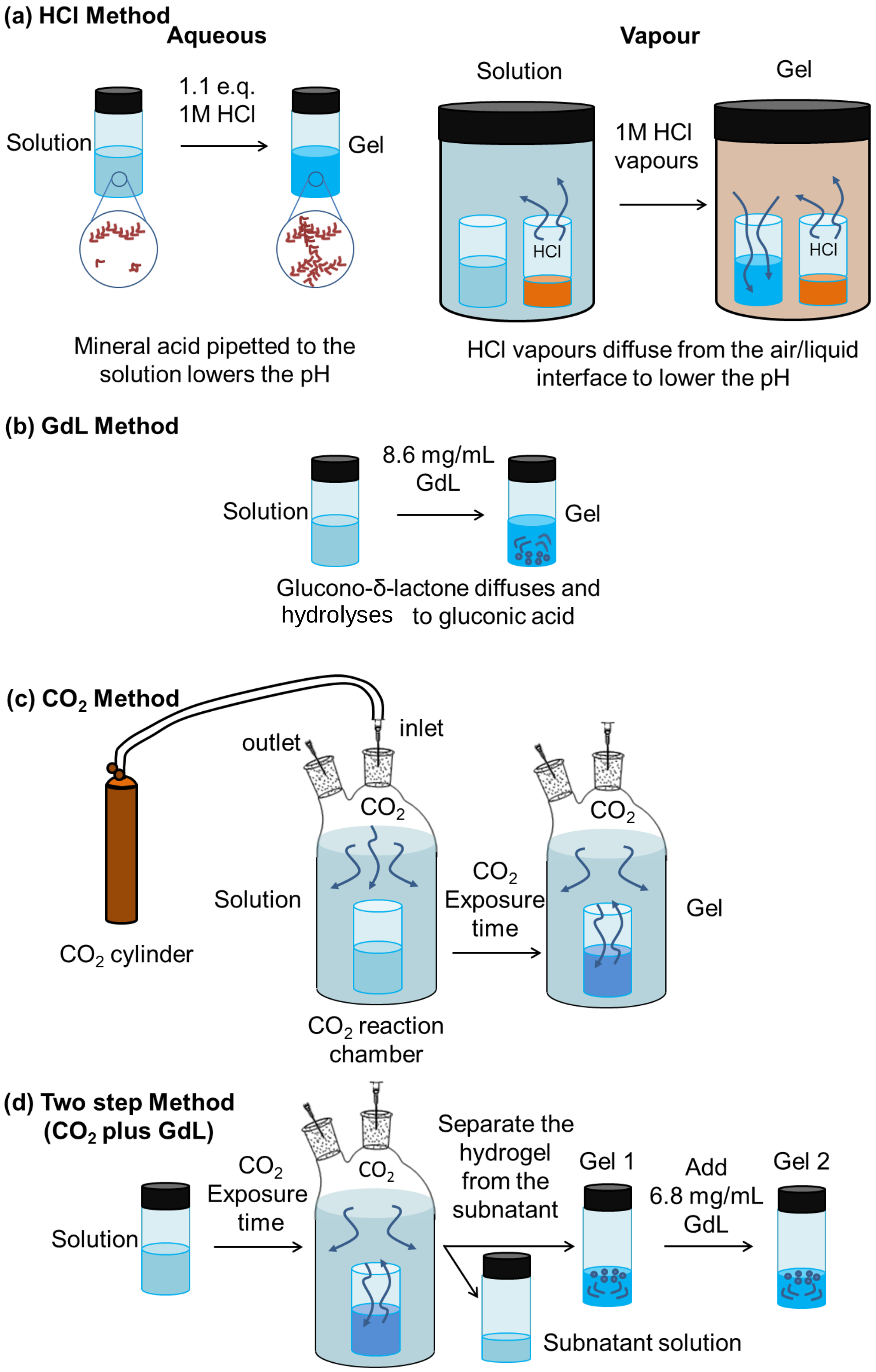

Figure 2.3 – Experimental setups of the different self-assembly methods used in this Chapter: (a) HCl method with either aqueous or vapour phase; (b) GdL method; (c) CO_2 method; (d) two-step method (CO_2 plus GdL).

reservoir can be made without a high-pressure chamber by using an outlet to maintain a pressure similar to the atmospheric pressure inside the vial. In this project, the pressure of CO_2 used (pCO_2) was near atmospheric pressure conditions ($pCO_2 = 3.5 \cdot 10^{-4}$ atm) and at room temperature. Additionally, this new method can be combined with the existing GdL method. In Fig. 2.3d, a new two-step self-assembly method is illustrated. This self-assembly process uses a double pH-switch method. In the first step, the solution is exposed to CO_2 for a set period of time (typically 3 hours) and then a pre-weighed amount of GdL is added to the transferred CO_2 hydrogel. This method allows us to compare the effect of CO_2 in self-assembly and compare the CO_2 method with the GdL method.

In all of these methods (Fig. 2.3), it is important to note that the solution is not stirred, nor is the temperature changed during the self-assembly process. As mentioned in Chapter 1, several groups have found that agitation and changes in temperature do affect the self-assembly process.[23,47] Also, the pressure indicated in this Chapter is the selected pressure at the outlet of gas cylinder and not the actual pressure at the reaction chamber as a needle outlet is placed with a 1 mm gauge. Therefore, the pressure in the reaction chamber will be slightly above the atmospheric pressure.

According to tabulated pCO_2 and pH tables, a slightly acid solution (pH = 5.65) is expected for a pure aqueous solution (without the gelator) at atmospheric pressure.[48] This suggests that the final solution pH could be controlled by the partial pressure of CO_2 in an improved experimental setup. Based on our previous research, a gelator with an apparent pK_a above the pH_f (final pH) should form a strong hydrogel with G′ and G″ above 1×10^4 Pa and 1×10^2 Pa, respectively.[11]

Carbon dioxide has the potential to acidify an aqueous solution. Hence, a new method was found and developed for triggering low molecule weight peptide gelators using CO_2. Subsequently, this new method described here is screened with different gelators.

2.3.2. Screening of different gelators with the new CO_2 self-assembly method for peptide-based low molecular weight hydrogels

Here, we have used carbon dioxide to lower the pH of a diluted solution from pH 10.5 (indicated as high pH, i.e. above the apparent pK_a of all gelators) of a range of gelators with different apparent pK_a. A range of gelators with a variety of hydrophobicity were synthesised (see Materials and Methods, Section 2.5.1, page 80). The gelators selected are composed of an *N*-protecting group and two amino acids (Fig. 2.1). All of these gelators have been previously shown to be able to form bulk hydrogels at 0.5 wt% with the GdL pH-switch method.[11,23,49] These gelators were used to test the CO_2 gelation method (Fig. 2.3c). When these gelators were triggered by a GdL pH-switch method, they form fibrillar self-assembled nanostructures in the hydrogel.[11,23,49] The nanostructures typically formed in these hydrogels are the result of self-assembly by hydrophobic interactions, hydrogen bonding, π-π stacking.[11,23,49] β-sheet structures were reported to be formed in the hydrogels of FmocFF.[50,51]

Table 2.1 – Properties of the CO_2 triggerd hydrogels using different gelators ordered by apparent pK_a. The apparent pK_a and predicted logP of gelators in Fig. 2.1. The gelator acronym indicates the protective group and the amino acid groups. The apparent pK_a were obtained from previous work,[12,23,49] logP was calculated from online programme molinspiration calculator.[87] The type of hydrogel formed was classified based: passing or failing the inversion vial test or a visible phase separation into a membrane gel and a subatant. The final pH recorded was a difficult measurement to make because the pH of the samples would change once the vials were opened to test the pH and drive the pH into a new re-equilibrated state based on the pressure of CO_2, therefore this was done as soon as a plateu appeared in the measurements within 1 minute of putting the probe in the sample. Average rheological properties of 2NapFF bulk hydrogels, BrNapAV membrane hydrogel, BrNapFG membrane hydrogels, 2NapAA solution and BrNapAG solution triggered by the CO_2 method. These results are taken from strain-sweeps at 0.5 % strain and frequency of 10 rad/s. In all cases, the same self-assembly process was used (2 hours CO_2 exposure of 1.25 atm and gelator concentration 5 mg/mL). Those with error are the standard deviation of the mean (n=3). n.a. stands for not available because of out of range measurement values. Membrane hydrogels are highlighted in green.

Gelator	**apparent pK_a**	**logP**	**Hydrogel formed**	**Final pH**	**G' (Pa)**	**G'' (Pa)**	**breakage strain (%)**
FmocFF	8.9	5.57	Bulk Hydrogel	8.3	1140	224	n.a.
BrNapFF	6.8	3.55	viscous solution, Non-Newtonian	6.0	5.8	0.9	251
1NapFF	6.7	2.76	Bulk Hydrogel	7.4	216	71	70
2NapFF	6.0	2.76	Bulk Hydrogel	6.7	99 ± 34	18 ± 18	33 ± 11
BrNapAV	5.8	1.40	Membrane hydrogel	6.4 ± 0.4	424 ± 228	57 ± 27	36 ± 13
BrNapFG	5.5	2.30	Membrane hydrogel	6.0 ± 0.2	102 ± 35	16 ± 5	20 ± 5
BrNapAG	5.0	0.84	No hydrogel	n.a.	3 ± 2	1 ± 1	3 ± 3
2NapAA	5.1	-0.16	No hydrogel	n.a.		n.a	

All of the gelators shown in Fig. 2.1 were triggered by the CO_2 pH-switch method (Fig. 2.3c), to assess whether different structures effects would be formed if using a different method. The final pH, type of gel and mechanical properties of the gels formed are shown in and Table 2.1. Gelators 2NapFF, 1NapFF and FmocFF formed bulk hydrogels. Fig. 2.4a shows the behaviour of 2NapFF and the inversion vial test. However, the typical inversion vial test was not adequate to show the macroscopic behaviour of BrNapAV and BrNapFG because they did not form a bulk gel or a complete liquid. Gelators BrNapAV and BrNapFG form a phase separated hydrogel membrane above a liquid phase. The unexpected behaviour of these two gelators is shown for BrNapAV in Fig. 2.4b. Furthermore, gelators 2NapAA and BrNapAG were not able to form hydrogels. In the case of BrNapAV, a second step was used to further lower the pH by adding GdL and modify the mechanical properties of the membrane hydrogel, which resulted in a stiffer hydrogel shown in Fig. 2.4c. The HCl vapour method (Fig. 2.3a, vapour) was used with BrNapAV for comparison purposes (Fig. 2.4d). BrNapFF did not form either a stable hydrogel that could pass the inversion vial test or a membrane, although it appeared more viscous (investigated in more detail in Section 2.3.2.1). FmocFF and 1NapFF formed slightly turbid bulk hydrogels. Gelator 2NapAA formed small needle crystals deposited in the bottom of the vial (with the same lattice parameters as previously found by crystallography experiments[49]), shown in Fig. 2.4e.

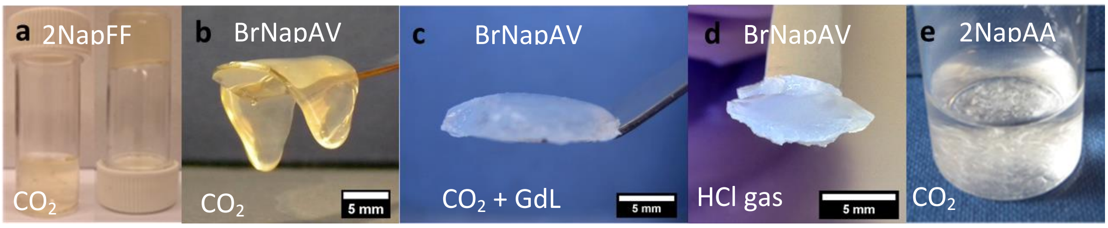

Figure 2.4 – Different behaviours in hydrogel formation when a different gelator or a different self-assembly process are used (a, b and e show data for structurally similar gelators but with different pK_a) or a different self-assembly process (b, c and d) is used in aqueous solution. Gelators shown here are: (a) 2NapFF (pK_a 6.0); (b, c and d) BrNapAV (pK_a 5.8); and (e) 2NapAA (pK_a 5.1). Solutions (a), (b), (c) and (e) were triggered from high pH with the CO_2 method (Fig. 2.3c) at 1.25 atm for 2 hours. Additionally, BrNapAV sample (c) passed an additional step in the self-assembly process as 16 mg of glucono-δ-lactone was added to the sample to attain pH 4 (Fig. 2.3d). In sample (d) the BrNapAV hydrogel at 0.5 wt%, $pH_f = 2.2$ was formed using an HCl gas phase method for 3 hours (Fig. 2.3a).

The mechanical properties of the hydrogels are defined by the structural features, and are usually tailored for a particular industrial application.[52,53] Despite forming different macroscopic hydrogels (i.e. bulk and membrane hydrogels), both kinds of gelators were compared with a plate-plate rheology measuring system. The CO_2

triggered hydrogels were transferred with a spatula onto a sandblasted plate-plate system, while the gels made with the other methods where formed directly between the two plates. In all cases, hydrogels were kept for 5 minutes after the gelation time between plates before starting the measurement. This allows for the relaxation of the hydrogel network between the plates, therefore excluding any strain artefacts resulting from lowering the top plate. Table 2.1 shows the measured mechanical properties of CO_2 triggered hydrogels and solutions in terms of storage modulus (G′), loss modulus (G″) and breakage strain for the transparent gelators. To full characterise the hydrogels mechanically, recovery measurements were attempted on these gels. However, we realised that in this case the recovery represents both the hydrogel recovery, because of molecular recombination, and recovery related to shear alignment. Therefore, this was not analysed here. Formation of shear aligned structures was reported when a large strain amplitude oscillatory force is applied in a polymer system of poly(ε-caprolactone)[54] and in block copolymer systems.[55]

The screening of different gelators with the CO_2 self-assembly method identified that gelators with apparent pK_a above 5.8 formed bulk gels (with exception of BrNapFF); gelators with apparent pK_a between 5.8 and 5.5 formed membrane gels and gelators with apparent pK_a below 5.0 did not form gels. In order to understand the reasons why these different types of gelation occurred, the factors influencing CO_2 gelation are discussed.

2.3.3. Factors determining formation of bulk or membrane hydrogels

The resulting phase after the CO_2 trigger was applied suggests that this kind of gelation is dependent on the apparent pK_a and the final pH (Table 2.1). This has proven to be the case with the GdL method.[56] The pH_f was dependent on the pressure of CO_2 used and the time the sample was exposed to CO_2. Once the CO_2 supersaturation in solution and the bicarbonate reactions had reached a dynamic equilibrium, extending the exposure time after the equilibrium was reached should not change the mechanical properties of the hydrogel. Therefore, for a fixed starting phase of each of these gelators at 0.5 wt%, we could see that the fate of the solution transition depends on the gelator apparent pK_a, and possibly, the final pH (Table 2.1). Gelators with apparent pK_a between 5.5 and 5.8 formed a membrane hydrogel. This appears to be related with the fact that the final pH for the membrane gelators is between 6.0 and 6.4, approximately half a unit above the value reported for a CO_2

acidified water solution without a gelator pH = 5.65.[48] The pH_f for each of the gelators tested here was obtained with an pH_i of approximately 10.6 and with a $p(CO_2)$ = 1.25 atm applied for 2 to 3 hours. Gelators BrNapAV and BrNapFG both have an apparent pK_a near the water acidification pH under similar conditions as those studied here and these were the only two gelators found to form the membrane hydrogels. Below the apparent pK_a of 5.5, no gels were formed, as in the cases of 2NapAA and BrNapAG (Table 2.1). Therefore, to form membrane gels using this method, we suggest that it is required to choose a gelator with an apparent pK_a between 5.5 and 5.8 and the pH_f achieved by $p(CO_2)$ at near atmospheric pressure to be half a pH unit above the pK_a of $[CO_2]$. Gelators with an apparent pK_a above 5.8 formed bulk gels and gelators with apparent pK_a below 5.5 did not form any gel.

The new CO_2 method allows for the formation of hydrogel membranes happens under the conditions studied here, when gelator's apparent pK_a is between 5.8 and 5.5. One possible reason to explain this could be because the apparent pK_a of the gelators that form hydrogel membranes is close to the $pK_{a,1}$ of CO_2 = 5.65 (Fig. 2.2). This could be because the bicarbonate species under the conditions studied, favour only a kinetic stability and formation of a structured gel. All of these might only be able to occur when CHO_3^- and CO_2 are the dominant species at that pH, temperature and pressures chosen in this study.

Since all gelators tested with apparent pK_a above 5.8 formed bulk gels, with exception of BrNapFF (apparent pK_a = 6.8), which formed a viscous solution, while the pH_f was 6.0, we decided to investigate this gelator further.

2.3.3.1. High viscous solutions at high pH with the CO_2 method

With the analysis above, BrNapFF should form a bulk gel, having an apparent pK_a of 6.8 above the $pH_f = 5.8 \pm 0.3$ for this specific gelator. In fact, BrNapFF formed a highly viscous, shear thinning solution of viscosity (η) 0.291 ± 0.002 Pa.s at a shear stress of 0.1 Pa (see Fig. 2.5, G' and G" < 10 Pa and breakage strain of approximately 100%) before the addition of CO_2. This result suggests that there are structures formed under this conditions, which is in agreement with previous measurements conducted by our group (Chapter 3).[37] The gelator transition with CO_2 results in a small increase in viscosity at low shear stress and there is a further increase of an already high viscosity at high pH, 0.190 ± 0.002 Pa.s, at shear stress of 0.1 Pa (Fig. 2.5), when compared with solutions of other gelators. The high pH solution appears to have already large assemblies because the solution is birefringent (Fig. 2.5, inset). This behaviour might be because the pre-assembled BrNapFF micellar system formed at the start (white circles, Fig. 2.5) has already a structure that is detected by a viscosity significantly above water viscosity. These are not prone to form hydrogels with CO_2.

In line with these results, we hypothesise that we require both an apparent pK_a between 5.8 and 5.5, the pH_f near this apparent pK_a and an initial phase with a viscosity below 0.29 Pa.s, based on the BrNapFF exceptional case.

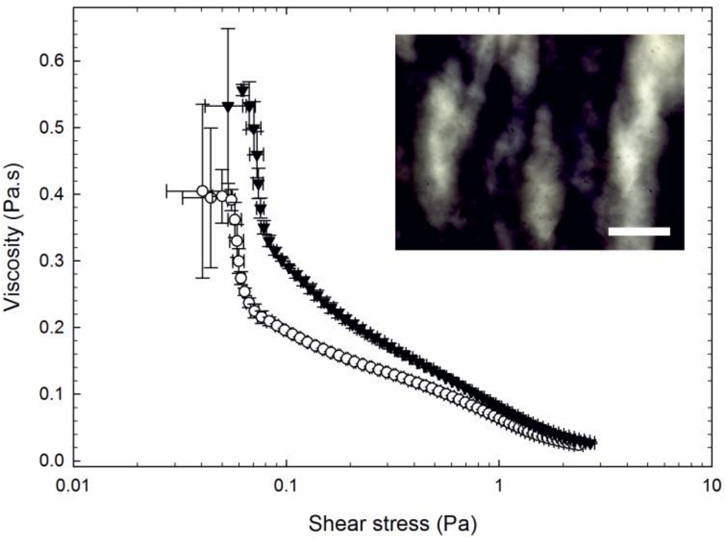

Figure 2.5 – Viscosity plot for BrNapFF as function of shear stress at pH 10.5 (white) and after use of the CO_2 method (black), data collected after 3 hours and $p(CO_2)$ = 1.25 atm. The inset shows an optical microscopy image of BrNapFF at high pH under cross-polarised lenses, the scale bar is 20 µm.

Since the BrNapAV and BrNapFG hydrogel membranes are formed in the top region of the vial while the bottom of the vial was not gelled, we decided to investigate the pH gradient with dyes instead of the pH meter to better image the phenomena with similar diffusion to the actual gelation with CO_2.

2.3.3.2. Effect of CO_2 gas in the pH gradient of water

In order to understand how the pH is changed in our system, experiments with different volumes of water at high pH were left to equilibrate under the same conditions used for CO_2 gelation (with $p(CO_2)$ = 1.25 atm) at room temperature. These results show that as expected, with a larger sample volume, the longer time it takes to reach the full solution equilibrium. NaOH aqueous solutions of 1, 2 and 5 mL with $pH_i = 10.6 \pm 0.4$ were lowered to $pH_f = 6.5 \pm 0.1$ with CO_2 at near to atmospheric pressure for 3 hours. For a fixed volume of 10 mL, time-lapse pictures of a ddH_2O solution with a universal indicator dye (colour change at pH 7) are shown in Fig. 2.6.

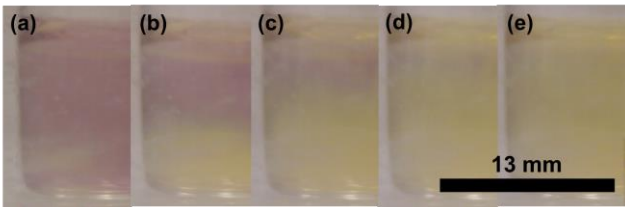

Figure 2.6 - Carbon dioxide acidification of a ddH_2O solution with universal indicator over a 3 hour period under an atmosphere of carbon dioxide (generated using dry ice in a separate reservoir). Photographs (a-e) were selected approximately at every 36 minute period over a 3 hour period. Purple indicates the solution pH is above pH 7 and yellow indicates the solution pH is below pH 7.

The results indicate that there is a gradual pH gradient formed upwards from the bottom of the solution without the presence of the peptide. This further develops into a full diffusion through the whole solution, with the low pH front coming from the bottom to the top solution. There is also a slight acidification at the top of the sample. Both effects might be due to the difference in density of the carbonic acid and water (carbonic acid has a density of 1.668 $g.cm^{-3}$, slightly higher than water).[57] This behaviour is expected to be dependent on the convection and diffusion rates in different directions of the vial. Therefore, the physical shape of the vial may influence these effects. It is important to note that the full acidification of 10 mL of ddH_2O in the CO_2 reaction chamber depicted in Fig. 2.3c takes 3 hours to obtain a pH below 7 (Fig. 2.6). Nonetheless, in the peptide systems studied here, the additional restriction of the CO_2 diffusion in solution upon self-assembly is likely to influence the solution pH gradient.

The next step was to identify the additional complexity of the gelation gradient when a dissolved gelator is added to a basic aqueous solution acidified by the CO_2 method. We then followed the self-assembly gradient in the 1NapFF bulk gelation.

2.3.3.3. Measurement of the gelation gradient in CO_2 bulk gel of 1NapFF

A CO_2 gelation was carried out in the presence of 1NapFF in the same conditions. It was found that a hydrogel gradually forms from the air-liquid interface downwards into the bulk (Fig. 2.7). This images showed the turbidity change over time during CO_2 atmosphere gelation of 1NapFF at (a) 2 hours, (b) 3 hours, (c) 4 hours and (d) 6 hours (at atmospheric pressure with a dry ice source). The final pH was 7.4 and the hydrogel passed the inversion vial test at 3 hours, 4 hours, and 6 hours. This property suggests potential applications could be outlined for setups where phase transitions and different diffusion rates are required in the same hydrogel sample.

This result shows that with the CO_2 method, the time to achieve an water equilibrium at pH below 7 (pH_f 6.5) in 10 mL is 3 hours, while here only at 6 hours a aqueous solution of 0.5 wt% 1NapFF reached the full gelation equilibrium at pH_f 7.4. Both experiments were conducted at room temperature with exposure to 1.25 bar of CO_2.

2.3.3.4. Importance of gelator apparent pK_a and solution pH_f on bulk gelation

The visual inspection of 1NapFF indicates a similar behaviour to 2NapFF and FmocFF. Although all of these formed bulk gels that passed the inversion vial test, the pH_f of 1NapFF bulk gel was 7.4, above the apparent pK_a of 6.7. This indicates that for the CO_2 gels, the measured final pH was not a good indicator of the final properties. The measured pH_f of the solutions formed by the CO_2 method were in same region or slightly above the apparent pK_a of these three gelators (all apparent p$K_a \geq 6.0$).[12,23,49] These results suggest that these three gelators undergo a gradual gelation process starting at the liquid-air interface. Despite the pH_f in the bulk of the hydrogel being above or similar to the apparent pK_a, the local pH near the liquid-air interface may well be near or below the apparent pK_a of the gelator, therefore triggering the gelation at the interface first. Cooperative self-assembly effects[58] may allow the gradual assembly from the interface into the bulk despite the pH in the bulk still being one pH unit above the apparent pK_a of the gelator. So, the apparent pK_a is better at predicting the most likely type of CO_2 gelation outcome than the final pH under the conditions studied here using the CO_2 gelation method.

Following these experiments, we focused our efforts on better comprehending this new self-assembly process and the resulting hydrogels in the case of BrNapAV membrane hydrogels. This choice of this gelator relied on the formation of stable hydrogel membranes, therefore this was a good case to study this behaviour.

2.3.4. The case of BrNapAV CO_2 hydrogel membrane

2.3.4.1. pH gradient for membrane hydrogels

The first stage in characterising the gelator behaviour was to determine the onset of pH change with this new self-assembly method. The pH change was monitored with a pH probe near the liquid-air interface, as in Figure 2.8 (solid line), probe on the first 6 mm from the interface and at the bottom bulk of the solution (dotted line), from a depth of 10 mm to 16 mm from the liquid-air interface.

As the CO_2 gaseous reservoir was connected to the vial chamber, the solution pH decreases from pH_i of 10.1. The pH on the top of the vial decreases gradually to pH 7.0 from the opening of the CO_2 valve (Fig. 2.8, before left arrow), while when the pH probe is placed at the bottom of the vial the onset of the pH decrease takes 3 min from opening the CO_2 gas valve (Fig. 2.8, after lelf arrow). Both appear to decrease in tandem after 11 min (Fig. 2.8, right arrow). The final pH of the solution (6.2) reached approximately the apparent pK_a of the gelator BrNapAV (5.8). Note that the decrease in pH was faster at the top of the vial when compared to the bottom of the vial, in the same initial self-assembly period. This effect agreed with the formation of a membrane hydrogel exclusively at the top of the vial.

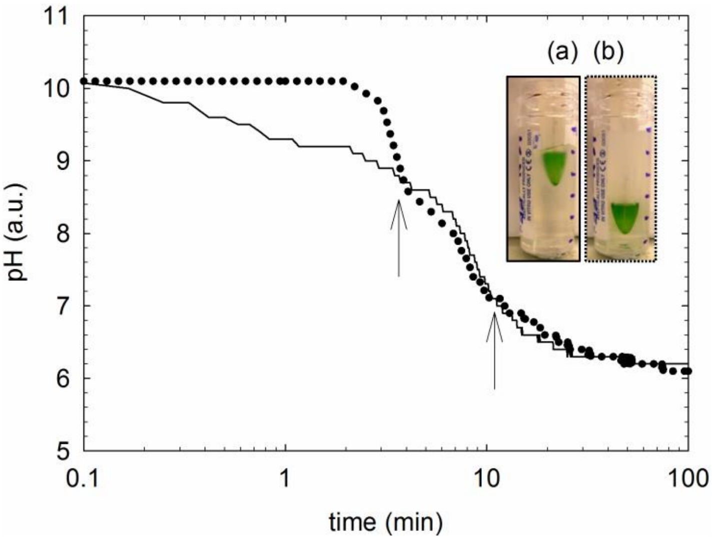

Figure 2.8 – pH measurement during the exposure of the pre-gelator solution of BrNapAV (pH_i = 10.1) for the first hour. The pH_f of both the top (solid line) and the bottom (dotted line) probe measurements indicated an equilibrium pH_f of approximately 6.2 after 2 hours. The inset image shows the pH probe at the top of the vial (a) and at the bottom of the vial (b) during the CO_2 self-assembly process. The time axis is shown on a log scale.

The pH 6.2 in the bottom part of the sample did not lead to gel formation. This effect could be explained by both a difference in the speed of pH decrease between the top and bottom of the vial and by a difference in the equilibrium of carbon dioxide species formed at the bottom of the vial as opposed to the top of the vial. Several reports suggest that salts are able to stabilise by screening the charges of gelator molecules from solutions at high pH.[24,28,37,59–64] Here, the speed of pH decrease at the top of the vial was consistent with the initial observation in Fig. 2.6, where the pH drops at the liquid/air interface first.

The next step was to optimise and identify the typical hydrogel membrane mechanical properties, which are unconventional according to literature.

2.3.4.2. Mechanical properties of membrane hydrogels

The typical BrNapAV hydrogel membrane strain and frequency sweep rheological measurements at a frequency of 10 rad/s and strain of 0.5 % are shown in Fig. 2.9. Fig. 2.9a shows a strain-independent region till 1 % strain. At 0.5 % strain, the G' and G" are 270 Pa and 75 Pa, respectively. The cross-over point is at 50 % strain with G' = G" = 18 Pa. This cross-over point is significantly higher than the cross-over points reported previously for BrNapAV hydrogels formed by the GdL method to a lower final pH (all between 1 % to 10 % strain, see Fig. 11 from Chen et al.[56]) The frequency sweep shows significant frequency dependence above 10 rad/s (Fig. 2.9b).

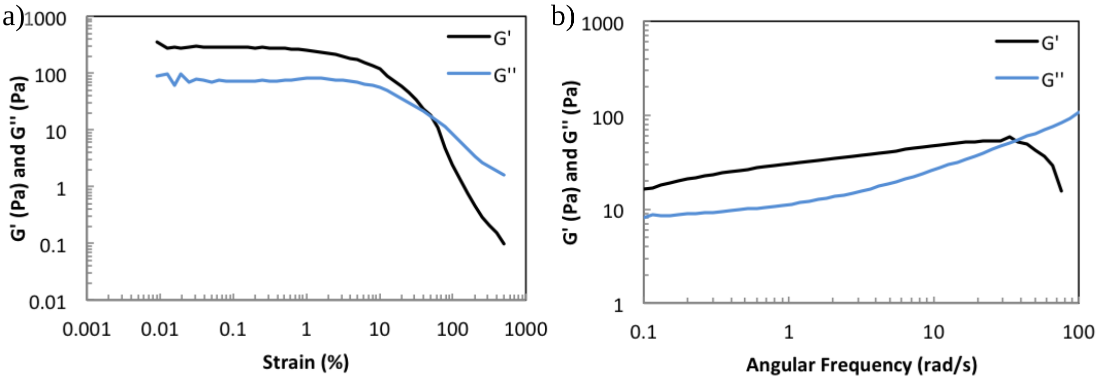

Fig. 2.9 – Rheological profile of a 0.5 wt% BrNapAV hydrogel membrane at 25 °C: (a) strain-sweep of 1 hour of CO_2 exposure time at 1.25 bar pressure, measured at frequency of 10 rad/s; (b) frequency-sweep of 3 hours of CO2 exposure at 1.25 bar pressure, measured at strain of 0.5 %.

The variation in mechanical properties of BrNapAV hydrogel membranes across a specific range were investigated for various parameters: concentration (c), pH_i, volume (V), CO_2 exposure time, and CO_2 pressure ($p(CO_2)$). Since the type vial and temperature might also be important, whilst each of the parameters was varied separately, the same kind of vial was used and temperature was maintained (± 2°C).

2.3.4.2.1. Effect of concentration on the mechanical properties

The mechanical properties of the hydrogel membranes formed by BrNapAV were studied over a range of gelator concentrations from 1 wt% to 0.5 wt%. The measurement of the membrane formed from the 1 wt% solution revealed a G' ≅ 100 Pa and G" ≅ 40 Pa from strain-sweeps at 0.5 % strain and frequency of

10 rad/s. This more concentrated hydrogel membrane had similar mechanical properties from this set of conditions: c = 1 wt%, V = 2 mL, pH$_i$ 10.0, exposed to the carbon dioxide for 12 hours, from a dry ice reservoir. The subnatant (the non-gelled part of the solution) was removed from the gelation vial and was found to have a pH of 7.5 – 6.2. We hypothesise that this pH varies following the removal of the subnatant, because of slight differences in room temperature and gelation time.

The membranes formed with the new CO$_2$ method with 0.5 wt% BrNapAV had similar mechanical properties to the 1.0 wt% with the same exposure time, volume and initial pH tested. This is likely because the other parameters were not optimised.

2.3.4.2.2. Effect of volume on the mechanical properties

The optimal volume to form the membrane with greatest depth with vials used was found to be 4 mL (we tested a range from 1 to 6 mL).

2.3.4.2.3. Effect of initial pH on the mechanical properties

The third condition for optimisation was pH$_i$ of the pre-gelator solution, found to be optimal at pH 8. Table 2.2 summarises the final mechanical properties for hydrogel membranes formed with a pH$_i$ in the range from 10 to 7 (with fixed initial conditions: concentration = 1 wt%, RT = 20 ± 1 °C, V = 4 mL, exposure time 3 hours from a dry ice reservoir).

Table 2.2 – Mechanical properties as a function of initial pH of BrNapAV hydrogels. Breakage strain is defined here the crossover point between G' and G". These results are taken from strain-sweeps at 0.5 % strain and frequency of 10 rad/s, with increasing time of exposure to CO$_2$ to reach the specified final pH. The green line were the best optimized pH conditions to obtain the hydrogel membranes with the highest breakage strain.

Initial pH (± 0.10)	**Final pH (± 0.10)**	**G′ (Pa)**	**G″ (Pa)**	**Breakage strain (G′ = G′) %**
10.00	6.18	16	6.5	20 %
9.00	7.68	490	70	31 %
9.00 (subnatant)	7.44	14	2.2	63 %
8.00	6.89	300	30	80 - 90 %
7.00	6.16	100	10	50 %

The data in Table 2.2 indicate that the self-assembly process with a pH$_i$ 8 could result in a hydrogel membrane with exceptionally high breakage strain. Strain sweeps revealed that these gels were significantly less affected by strain as compared to gels formed by other pH-switch methods.[56] The breakage strain (the cross-over point between G′ and G″) obtained with the hydrogel membranes was in the range of 80 – 90. This high breakage strain suggests that the hydrogel network is made of different type of entanglements or crosslinks between the formed fibre network from those formed by other pH-switch methods.[3] Typically, with the CO_2 gelation method, the breakage strain occurs at 20 – 90 % (Table 2.1). This was higher than gels formed, for example, using GdL pH-switch method (strain below of 10 %).[12,23,49] This result correlated with the observed membrane flexibility shown in Fig. 2.4b. As a result, these gels were significantly easy to transfer and manipulate without visible damage. The G′ and G″ of hydrogel membranes were up to two orders of magnitude below the bulk hydrogels obtained by the GdL method, formed at a final lower pH.[12,23,49] The final hydrogel membrane pH (approximately $pH_f = 6.0$) was similar to the apparent pK_a for the gelator BrNapAV. Interestingly, the pH_f measured was slightly above the estimated pH for a solution without gelator at 1 atm (pH 5.65).[48] Analysis of the sample with pH_i 10.0 and Vl = 4 mL formed a weak membrane, however another solution starting at pH 10.0 and Vl = 2 mL formed a self-sustained hydrogel membrane. This was possibly due to the 3 hours fixed CO_2 exposure time, which was not enough to form a hydrogel of a 4 mL volume, starting pH 10.0. As the pH_i was decreased, the breakage strain increases with a maximum at pH 8.0 (Table 2.2). The initial pH of 8.0 was the ideal pH for obtaining hydrogels with highest breakage strain using the new CO_2 method with BrNapAV, therefore it was taken as starting pH in the following studies.

2.3.4.2.4. Effect of exposure time to CO_2 on the mechanical properties

Following these findings, we investigated the mechanical properties as a function of exposure time to CO_2 with a gas cylinder set at a fixed pressure of 1.25 atm (Fig. 2.10). Based on our above method optimisation, the volume was kept at 4 mL, pH_i 8.0, BrNapAV concentration of 1 wt%. In Figure 2.10a, it was shown that both the G′ and G″ increased with time (in the viscoelastic region) to a plateau of approximately G′ = 335 Pa and G″ = 66 Pa from 3 hours. The breakage strain changes from a varying region with a mean of 80% below 3 hours to a narrower region 25 – 70 % (Fig. 2.10b, black). The crossover point reaches an equilibrium value of 40 Pa at 12 hours (Fig. 2.10b, white). The membranes formed with the CO_2 method were found to have significantly lower G′ and G″ compared to gels formed using GdL pH-switch method.[12,23,49] The explanation is that the pH_f affects the G′ and G″ of the gel membranes (as shown above) since it has previously been shown for the GdL method.[12,23,49] The mechanical properties of gels formed using the CO_2

method could be adjusted to some degree by varying the CO_2 exposure time (Fig. 2.10a and 2.10b), although the mechanical properties never increased to the values observed for gels formed using GdL (which are on the order of G′ approximately 10 kPa at the same concentration but at low pH after overnight incubation). Figure 2.10c and 2.10d show the mechanical properties as a function of the pressure of CO_2.

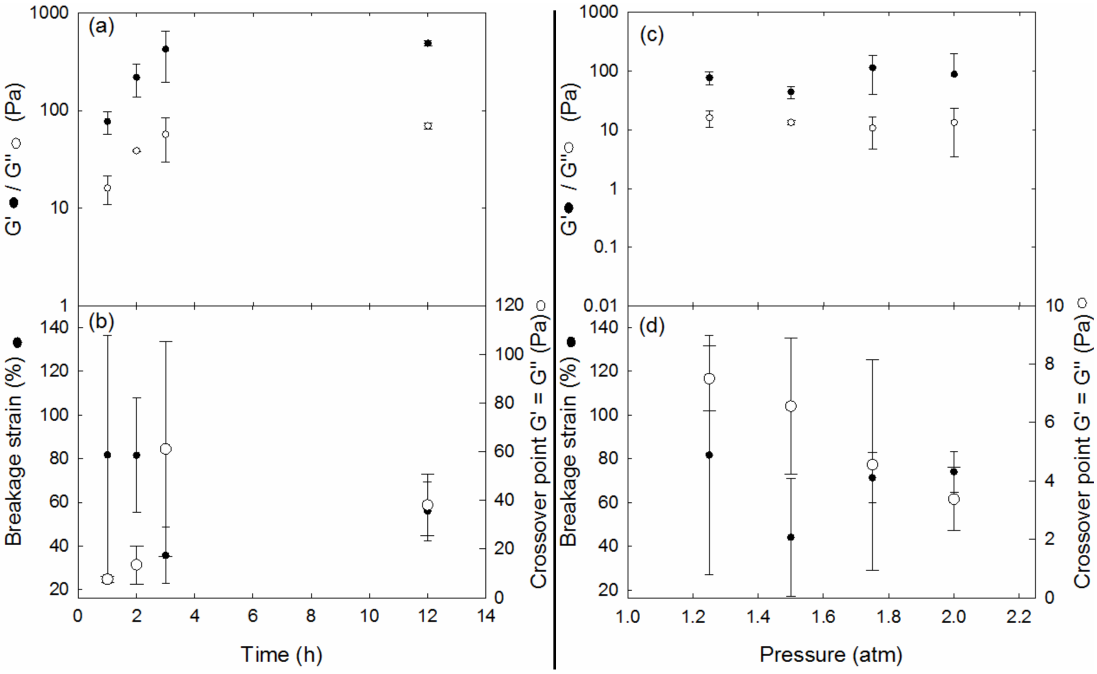

Figure 2.10 – Mechanical properties measured from strain sweeps of a hydrogel membrane of BrNapAV at frequency of 10 rad/s and strain of 0.5 %: (a) G′ (black symbols) and G″ (white symbols); (b) the breakage strain (%, black symbols) and crossover point moduli at G′=G″ (Pa, white symbols) as a function of exposure time of CO_2. (c) G′ (black symbols) and G″ (white symbols); (d) the breakage strain (%, black) and crossover point moduli at G′=G″ (Pa, white) as a function of pressure of CO_2. Each measurement represents an average value over 3 samples. Error bars are the standard deviation of the mean (SDM).

2.3.4.2.5. Effect CO_2 pressure on the mechanical properties

The choice of p(CO_2) does not appear to influence substantially the G′ or G″ in the range studied here (Fig. 2.10c and 2.10d). The breakage strain appears to go from a varying value between 25 – 130 % to approximately 70 ± 10 % for higher pressures (Fig. 2.10d, black). The average crossover point of the membranes decreases with an increase of pressure (Fig. 2.10d, white). This result suggests that the faster kinetics of gelation could allow more entanglements to be formed, because the breakage strain becomes narrower and the G′ = G″ crossover point occurs at lower values with increasing time (Fig. 2.10b) and pressure (Fig. 2.10d). Therefore the gels break at a lower shear stress once triggered by higher pressures or for longer exposure times.

Hence, the CO_2 method allows the breakage strain could be adjusted to some degree by varying the pressure of CO_2 used, however, G' and G'' couldn't be changed (Fig. 2.10c and d). During these experiments, it was noted that the thickness of the membrane hydrogels varied with the applied pressure of CO_2 and exposure time. This observation indicated that the measurements of the membrane mechanical properties just discussed, had to be made with a variable choice of plate to plate distance, adjusted based on the hydrogel thickness.

2.3.4.3. Thickness of the hydrogel membrane

After the CO_2 self-assembly process was completed, the hydrogel membranes were transferred to the horizontal inert surface of the rheometer plate-plate measurement system. Thickness measurements were made indirectly by gradually lowering the top plate of the rheometer plate-plate system before each measurement. At the point where the top plate touched the hydrogel membrane, the gap thickness of the plate-plate geometry was registered. The average thickness obtained as a function of $p(CO_2)$ and CO_2 exposure time is shown in Fig. 2.11a and 11b, respectively.

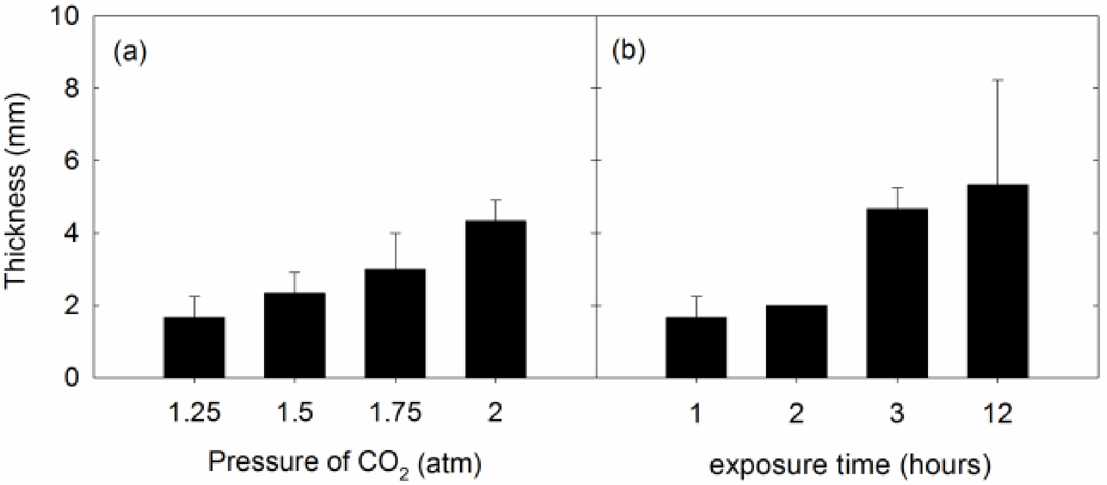

Figure 2.11 – Mean thickness for BrNapAV membrane hydrogels obtained over three measurements as a function of (a) CO2 pressure (with time = 1 h) and (b) exposure time (with p(CO2) = 1.25). The error bars represent the standard deviation taken from three measurements.

The CO_2 method using BrNapAV allows the thickness of the hydrogel membranes can be increased slightly with an increase in pressure or with an increase in the exposure time as shown in Fig. 2.11. The first result is expected because with a higher pressure, the depth of the fast kinetic carbonic acid formation and the rate of pH decrease is increased. The second result is in agreement with a cooperative self-assembly process (discussed below). It is possible that after gelation is initiated, the higher number of molecules that diffuses and pass by convection mechanism near the gelation front, at the top of the solution, could gradually become self-assembled in this phase. In order to investigate if this was indeed the case, a set of experiments were done to understand the final concentration of the hydrogel/solution phase.

2.3.4.4. Concentration heterogeneity on the hydrogel membrane

Since the sample of 0.5 or 1.0 wt% BrNapAV formed membranes only in a specific region of the solution, it was thought that investigating the actual concentration of the membrane could reveal the mechanism of hydrogel membrane formation or if it played a role in the unconventional gel formation. Two attempts at quantifying the peptide concentration using freeze-drying to remove the water of the sample and a second attempt using TGA analysis to quantify the were not conclusive, and this investigation was not pursued further.

To further characterise the BrNapAV hydrogel membranes we studied their structure by microscopy techniques.

2.3.4.5. Nanostructure and microstructure of the hydrogel membrane

To further comprehend the morphology of these hydrogels, scanning electron microscopy (SEM) and laser scanning confocal microscopy (LSCM) were used to investigate the final assembled state (Fig. 2.12). The SEM preparation used a dried sample on top of a pre-cleaned diced silicon wafer with the use of a blotting and drying method (Fig. 2.12, 2nd row, see Materials and Methods, Section 2.5.4 below).

The LSCM used a Nile blue staining method (Fig. 2.12, top row). In order to understand if the CO_2 process formed a completely different or similar nanostructure and microstructure to that of the other pH-triggered methods, the BrNapAV hydrogel membrane was investigated here in comparison with other methods. The microscopy images of the BrNapAV at the starting stage of self-assembly process and by different pH-switch methods are shown in Fig. 2.12.

In Fig. 2.12d.1, the LSCM image shows the hydrated state of BrNapAV hydrogel membrane microstructure, with water pockets and fibre network bundles. Fig. 2.12d2 shows the typical dense nanofibre network of an open-air dried sample in a silicon wafer. Nanofibre size or thickness was measured perpendicularly from the sides of a high contrast line of a curved line. The average nanofibre thickness was found to be $\phi = 22 \pm 8$ nm (n=100, by SEM). These fibres are densely packed upon drying.

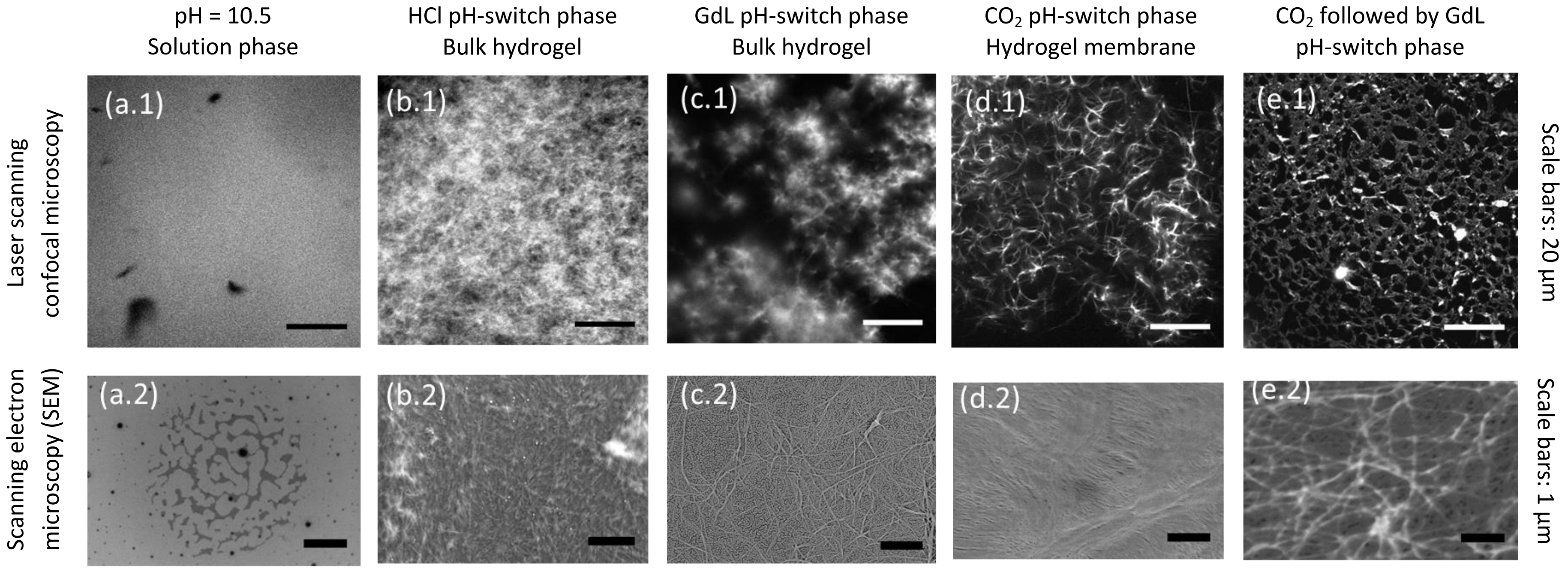

Figure 2.12 – Structural characterisation of BrNapAV at 0.5 wt% in different phases by LSCM image (1) and SEM imaging (2). The images were taken from (a) high pH – solution phase; (b) HCl pH-switch phase; (c) GdL pH-switch phase; (d) CO_2 pH-switch phase; and (e) a hydrogel membrane formed by the CO_2 pH-switch method followed of addition of 16 mg/mL of GdL. The nanostructural features of solution or hydrogel membranes of BrNapAV are visible in the SEM image (2), while microscale features such as fibre bundles, entanglements, branching and hooks are visible in the hydrated LSCM image (1). No coatings were applied to any of these images. All LSCM have a 20 µm scale bar. SEM images 2 have a scale bar of 1 µm.

They show flexible features from the SEM data and rheological data. The membrane hydrogel undergoes a quicker macroscopic drying (under 1 day for 2 mL of sample) when compared with the drying from the GdL method (over a week for 2 mL of sample). This outcome in drying a CO_2 hydrogel membrane and drying a GdL hydrogel suggests that the water is kept in the hydrogel membranes not as effectively as the water trapped with the GdL method (Fig. 2.12c). This further extends the result[61] concerning the presence of structures at this transition pH (pH_f = apparent pK_a) for some gelator systems because a weakly cross-linked microstructure is expected to align more upon drying when compared to a strongly cross-linked microstructure.[54,55] The SEM images of dried samples prepared with the GdL triggered method (Fig. 2.12c.2) show fibres more randomly oriented when compared with the dried samples of the CO_2 triggered method (Fig. 2.12d.2). However, the LSCM images of the same samples in the wet state both show no aligned features (Fig. 2.12 c1 and d1).

To conclude, LSCM is a more useful technique to identify the actual hydrogel network and bundle features, however it lacks in resolution. This technique showed hydrogel membranes of BrNapAV formed with the new CO_2 method have a nanofibre network with water pockets and no alighted features. Dried samples suggest a fibre thickness of 22 ± 8 nm. The images and drying effects of the BrNapAV hydrogel appears to form a structure with more flexible network than the HCl or the GdL methods alone. However, using the GdL method after the CO_2 method formed a structure that dries with similar random orientation features as the GdL only structures. The LSCM images of the GdL only or GdL plus CO2 method appear to be of higher contrast and larger mesh size than the CO_2 only image.

Furthermore, secondary structure characteristics were investigated by FTIR.

2.3.4.6. Secondary structure of the hydrogel membrane

Fourier Transfer Infrared Spectroscopy was conducted for BrNapAV with the GdL method previously by our group.[56] The spectrum showed characteristic peaks at 1718 cm^{-1} (broad), 1628 cm^{-1} (narrow), 1679 cm^{-1} (narrow) and another at 1645 cm^{-1} (narrow). The peak at 1718 cm^{-1}, was assigned to the terminal carboxylic group. The peaks at 1679 cm^{-1} and 1628 cm^{-1} were assigned to be a beta-sheet structure.[65,66] The final peak at 1645 cm^{-1} was assigned to a random coil or from the -C=C- stretching of the naphthalene-ring.[65,66] Figure 2.13 shows the FTIR spectra of following three states of self-assembly: (1) high pH solution, (2) CO_2 pH-switch membrane – intermediate gelation, (3) GdL method (only), (4) HCl method, and (5) two-step self-assembly (CO_2 plus GdL) to allow us to compare the previous results from our group with greater depth.[56]

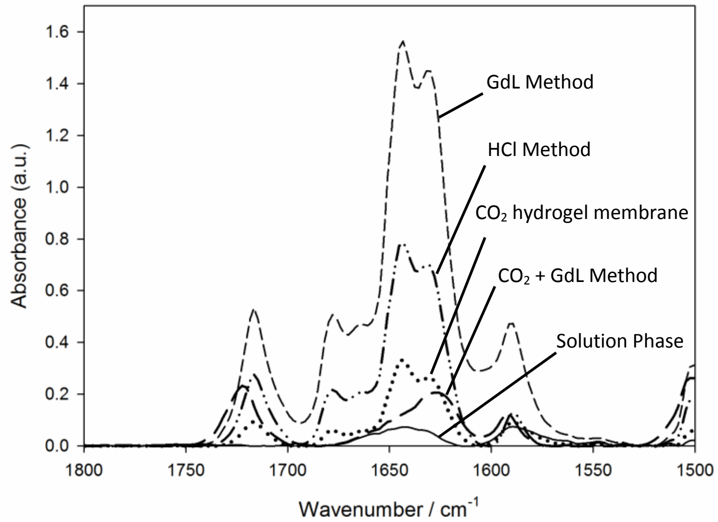

Figure 2.13 - FTIR of BrNapAV under different self-assembly processes: (1) solution phase – pD = 10.9 (solid line); (2) CO_2 hydrogel membrane – pD_f = 6.2 (dotted line); (3) GdL Method – pD_f = 3.8 (thin dashed line); (4) HCl Method – pD_f = 3 (dot-dashed line); and (5) two-step self-assembly – CO_2 plus GdL Method (thick dashed line). Each of these spectral measurements are averages of 3 repeated measurements and all data was baseline corrected (see Materials and Methods Section 2.5.7, below).

According to the data summarized by Pelton *et al.*[67] and Barth *et al.*[68] with peak assignments for protein samples in D_2O, it is possible to suggest secondary structural features to each FTIR spectrum. However, the peak assignments should be considered only a preliminary assignment as it has been noticed in the recent literature that these assignments are based on studies conducted for large proteins[65,66], as it is explained below. A study of the FTIR spectrum of BrNapAV as function of pD was reported previously by our group.[56] In the context of proteins, the amide I and amide II region are mostly used for peak assignment.[67,68] The solution phase has a single peak at 1643 cm^{-1}, which suggests that the structural arrangement is aperiodic (random oriented structures). This result we should consider the hypothesis of randomly packed micelles in the solution phase. The analysis of the FTIR spectrum of the CO_2 triggered membrane suggests that there is transition from the (1) solution phase (Fig. 2.13, solid line) to the CO_2 triggered membrane phase (Fig. 2.12, dotted line). Once the CO_2-triggered membrane is formed, there is a coexistence of β-sheet structure and randomly oriented structures (dotted line). This assignment was conducted on the basis of the single peak of 1629 cm^{-1}

corresponding to β-sheet structure and the broad shoulder from 1640 cm^{-1} to 1680 cm^{-1} corresponding to randomly oriented structures.[67,68] The single peak suggests the existence of a parallel β-sheet structure, however the previously reported procedures for peak assignment to parallel or anti-parallel β-sheet structure have been conducted on large proteins with intramolecular packing.[65,66] In this system, the peptide sequence has only two amino acids and the suggested packing is intermolecular. Therefore, the vibrational frequencies visible in the FTIR could result in different modes because of the smaller size of the peptide and a precise secondary structure assignment is currently not possible without further study.[66]

In order to understand the two-step gelation method (CO_2 plus GdL), two additional samples were prepared. One sample prepared only with the GdL method (dashed line) and another sample with the HCl Method (dotted-dashed line). These samples both suggest that at low pD (below the apparent pK_a of the gelator) the gelator assembles in a preferential β-sheet structure (1631 cm^{-1} and 1678 cm^{-1}) and some randomly packed structures (1643 cm^{-1}). This result agrees with previous reports on BrNapAV.[56] A final state at pH 3.4 formed by the CO_2 plus GdL method (which forms stiffer self-assembled membranes) resulted in the presence of only one narrower and higher intensity peak at 1627 cm^{-1}, which suggests β-sheet structure (Fig. 2.13, thick dashed line). Surprisingly, the region assigned to randomly oriented structures (1640 cm^{-1} to 1680 cm^{-1}) and the shoulder peak of the β-sheet features present in the GdL method (used alone, Fig. 2.13, thin dashed line) are not present in this two-step self-assembled system (Fig. 2.13, thick dashed line). It would be expected that in the two-step process, the transition of the structures after the final step (GdL addition, 24 hours) would also self-assemble or re-assemble the already formed assemblies by the carbonate species (CO_2 process, 3 hours). However, this transition to a lower pH occurs over a longer period of time and the carbonate species may re-equilibrate with the lower partial pressure of CO_2 in the atmosphere, possibly giving place to a preferable transition from the carbonate self-assembled gelator molecules to mostly protonated gelator molecules. Thus, the FTIR spectra of the two-step process do not show the randomly packed peak or the shoulder of β-sheet features. However, as noted above, the CO_2 triggered BrNapAV hydrogel membrane shows the two peaks of the randomly packing region and the shoulder of the β-sheet features. Additionally, the peak at 1720 cm^{-1} indicates an increase in protonation of the carboxylic group from the solution phase, to the CO_2 membrane hydrogel phase and ultimately to the low pD phases (DCl, GdL and CO_2 plus GdL phases). This is in agreement with our hypothesis for the CO_2 self-assembly in Section 2.2 and Wallace *et al.* results of the GdL self-assembly transition by multinuclear NMR spectroscopy.[69]

In conclusion, the secondary structure analysis by FTIR showed all hydrogels formed by the pH-switch methods tested demonstrated the following: once the pH is decreased, the samples transition from no secondary structures in the solution phase to β-sheet structures in the self-assembled hydrogels. However, using only the CO_2 method, random packing is also present in the structures. In addition, when a GdL method is used after the CO_2 method, the randomly packed features are not found by the FTIR spectra.

Considering that the GdL gelation method transitions the BrNapAV pH from high (pH 10.5) to low pH (3.5 – 4), it is interesting that since the CO_2 hydrogel membranes have a final pH (6.4), then the hydrogel formed by GdL should go through the same kinetic state as the final state of the CO_2 hydrogel membranes. In other words, the final state of the CO_2 hydrogels is an intermediary state of the GdL self-assembly process. Therefore, we decided to investigate by rheology, whether the final mechanical properties of the CO_2 are equivalent to the intermediary mechanical properties during the GdL gelation.

2.3.5. Intermediary self-assembly state of all pH-controlled self-assembly systems

A time-sweep of 0.5 wt% BrNapAV with 8.6 mg/mL GdL with repeat frequency-sweeps at 0.5 % strain at each time point was run to clarify if the hydrogel membranes (formed by the CO_2 method) are in the same structural phase as the early stages of self-assembly by the GdL method. The rheology results presented above for 0.5 wt% BrNapAV hydrogel membranes indicated mechanical properties at a frequency of 10 rad/s and 0.5 % strain of $G' = 270$ Pa and $G'' = 75$ Pa (Fig. 2.9). These are equivalent to the mechanical properties found here for 0.5 wt% BrNapAV hydrogels by 8.6 mg/mL GdL at the same frequency and strain between 22.8 – 50 minutes (Fig. 2.14a, dashed lines and Fig. 2.14b). Precisely, at 30.4 minutes, G' and G'' are 203 and 79 Pa, respectively, at a frequency of 10 rad/s and 0.5 % strain.

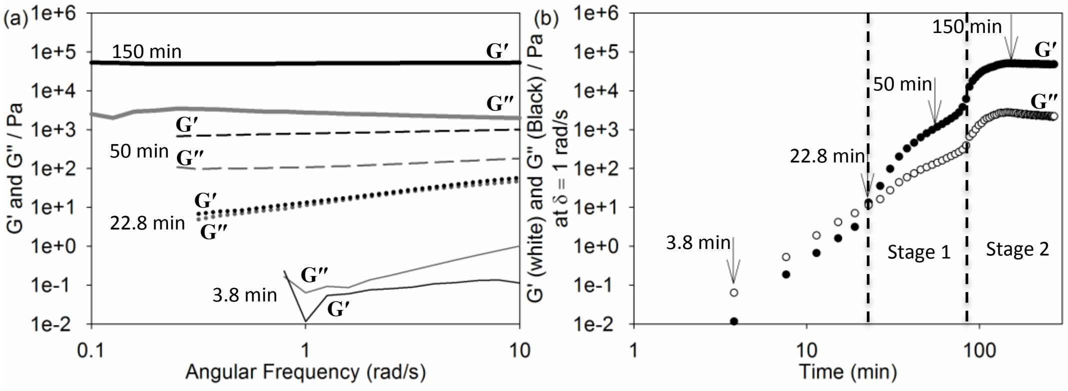

Figure 2.14 – Kinetics of hydrogel formation of BrNapAV 5 mg/mL with 8.6 mg/mL GdL recorded by a time dependent frequency-sweep measurement at 0.5 % strain. The plot (a) shows a selection of frequency sweeps at 3.8 (solid lines), 22.8 (dotted lines), 50 (thin dashed lines) and 150 minutes (thick dashed lines), with G′ (black) and G″ (grey). The plot (b) shows the values of G′ and G″ as function of time at frequency of 1 rad/s. The arrows in (b) indicate the times at which each of the frequency-sweeps on (a) were selected.

These values are equivalent to those found for BrNapAV hydrogel membranes (Table 2.2 and Fig. 2.9). In the case of the GdL self-assembly method (Fig. 2.3b), the pH is gradually decreased. At a certain time point (dependent of the pH_i and the amount of GdL used), the pH of the sample reaches the apparent pK_a of the gelator. From the Henderson-Hasselbach equation it can be read that at a pH = pK_a, half of the gelator is protonated and another half is deprotonated. This intermediate stage (pH = apparent pK_a) appears to be clearly visible when a reduced amount of GdL is used (2.94 mg/mL) in a previous publication from our group,[56] where we have shown that BrNapAV self-assembles in a two step process, in agreement with the result shown here in Fig. 2.14b. Therefore, the self-assembled state where the pH is close to the apparent $pK_a = 5.8$ is an intermediary state of the GdL self-assembly method.

In the GdL method (Fig. 2.3), the hydrolysis of GdL changes the pH from values above the apparent $pK_a = 5.8$ (pH 10.5 at t = 0 min) to values below the apparent pK_a (pH = 3.5 – 4 at t > 60 minutes). The G′ and G″ values shown in the transition region at 22 minutes (Fig. 2.14a and 2.14b) by the use of time-lapsed frequency-sweep rheology measurement (see Methods Section 2.5.3) shows transitions from a frequency-dependent viscous solution (below 22 minutes) to a frequency-independent hydrogel (above 50 minutes). The pH measurements of the CO_2 hydrogel membrane indicate a final pH close to the apparent pK_a (above 30 minutes in Fig. 2.8). The discrepancies in the time-domain are most certainly because of the different kinetics of each method to reach equilibrium. There is a lag time between these two measurements because of the different influence of diffusion and kinetics of CO_2 conversion to carbonate species and the influence of GdL hydrolysis to lower the pH of the solution. In the pH measurements shown in Fig. 2.8, the region where the pH approaches the apparent pK_a is described in the literature as a pH-lead, which precedes the self-assembly response.[30] The mechanical properties of the hydrogel membranes formed by the CO_2 method could not be probed over time easily with the rheometer, because it was both unsafe to set up a CO_2 triggered system in our rheometer and unfeasible to transfer only the portion of the solution phase that becomes a hydrogel membrane. The self-assembly response of BrNapAV hydrogelation triggered by GdL was measured by rheology with a parallel plates system (see Methods Section 2.5.3, below). These results are in strong agreement with the intermediary transition region found in the CO_2 method to be the intermediary phase of the GdL method because of the similarities in the mechanical properties and pH of these two states.

Following these findings, it was found by time-lapsed rheological measurements at fixed temperatures in a parallel project in our group, that the GdL-triggered self-assembly process is independent of temperature (in the range of 15 – 55 °C) for a similar gelator BrNapAG.[1] Thus, in the case of these class of gelators, the final hydrogel phase is a kinetically trapped state.[1] In other words, the self-assembly process can be made faster or slower by an increase or decrease in temperature without compromising the final hydrogel mechanical properties. Additionally, those results showed that self-assembly of modified-dipeptide hydrogels is a kinetically trapped state, instead of a thermodynamic in these particular dipeptide-based hydrogel cases. These results suggest that the transitions to the hydrogel state at low pH (using pH-switch methods) may all go through an intermediate kinetically controlled state or starting structured phase, which can only be accessed using the CO_2 gelation method, for example, in the case of BrNapAV (results in Fig. 2.14, two-step process) and BrNapFF (results in Fig. 2.5, higher viscosity state).

To understand the effect of different kinetic self-assembly processes on the mechanical properties of BrNapAV hydrogels formed by pH-switch methods, we investigated the self-assembly control by comparing and contrasting the mechanical properties, nano- and micro-structural properties and the secondary structural properties of these different hydrogels.

2.3.6. Kinetics and self-assembly control

In this Section, the structural and mechanical characterisation of the BrNapAV (Fig. 2.1, page 41) are discussed for the solution phase, the BrNapAV hydrogel phase triggered by the HCl method, GdL method, CO_2 method and two-step (CO_2 plus GdL). This informs on the kinetic steps from the self-assembly by pH-switch.

All methods start from dissolution at pH 10.5, this was the first phase investigated.

2.3.6.1. BrNapAV solution phase

In pursuit of this study, our group gathered some evidence by scanning electron microscopy in a recent publication that the initial diluted solution of BrNapAV at 0.5 wt% was non-irregular structures.[37] In the same publication, similar gelator 2NapGF showed at 0.5 wt% and pH 11.7 a mixture of spherical micellar structures and worm-like structures. Here, It was identified that the BrNapAV solution at 0.5 wt% is just below the reported critical micellar concentration (cmc) for BrNapAV, 0.51 ± 0.02 wt%.[11] Now, we have also found that the formation of some structure at this concentration is likely because through ^{1}H-NMR spectroscopy experiments. In these, we found that, at pH 10.5, the solution phase has 50 ± 1 % mobile gelator at 0.5 wt% and 91 ± 8 % mobile gelator at 0.1 wt% from the total amount of BrNapAV expected in the vial. This indicates that at 0.5 wt% in the ^{1}H-NMR spectroscopy measurement timescale, half of the molecules are static and half of the molecules are mobile. As the amount detectable can be dependent on the NMR experimental timescale, the developed method was above this threshold, see the Methods Section 2.5.9. Additionally, I have measured that the mobile BrNapAV has a mean diffusion of $2.83 \pm 0.07 \times 10^{-10}$ m^2/s (on the experimental time scale, see Methods Section). This means that the average of free gelator molecules and gelator molecules exchanging with the micellar aggregates have this value as average characteristic diffusion. The Laser Scanning Confocal Microscopy (LSCM) images of BrNapAV at 0.5 wt% do not reveal any micellar systems at length-scales above 1 µm (Fig. 2.12 a.1). However, the dried/blotted samples in a silicon wafer are not conclusive (Fig. 2.12 a.2), SEM experiments had already shown that there are some structures at 0.5 wt%.[37] Interestingly, also at 0.5 wt%, TEM images at early time points of BrNapAV, after the onset of GdL gelation, also show what appears to be a transition from proto-filaments or aggregates to elongated structures with increasing fibre diameter possibly due to lateral association.[56] This result is in agreement with a more detailed micellar phase study of 2NapFF conducted in Chapter 3. Here, it was found that BrNapAV at high pH has a G′ and G″ both below 1 Pa (Table 2.3).

Table 2.3 – Mechanical properties of gels formed from 0.5 wt% BrNapAV using different self-assembly methods. The G′ and G″ are average values taken from three measurements in the linear viscoelastic region of the strain sweeps with a frequency of 10 rad/s. All measurements were conducted at 25 °C and the gels were formed at a room temperature of approximately 22 °C. The asterisk (*) indicates the measurement was not possible as the properties of the solution phase were very near the detection limits of the rheometer. The frequency independent column indicates if the G′ and G″ are frequency independent in the typical viscoelastic region for peptide hydrogels. The error is the standard deviation.

			Strain Sweep (σ) at frequency of 10 rad/s		
Self-assembly Process	**Gelator Concentration (wt%)**	**G′ and G″ Freq. Independent**	**G'**	**G''**	**Break Strain %**
Solution pH_i 10.50	0.5	no	0.4 ± 0.2	0	n.a.
Solution pH_i 10.50	1	no	0.9 ± 0.4	0	0.6
CO_2 Method $p(CO_2) = 1.25$ atm; t = 2h	0.5	no	60 ± 13	16 ± 2	1.2
CO_2 Method $p(CO_2) = 1.25$ atm; t = 2h	1	no	204 ± 9	29 ± 1	12.6
GdL Method GdL = 1.0 mg/mL apparent $pK_a = pH$	0.5	n.a. [*]	63 ± 1	13 ± 1	0.4
CO_2 Method $p(CO_2) = 1.25$ atm t = 2h plus GdL Method [GdL]= 6.8 mg/mL	1	yes	11021 ± 495	1014 ± 17	4.4
GdL Method [GdL]= 6.8 mg/mL	1	yes	68214 ± 409	2103 ± 75	0.7
Liquid HCl Method 10 uL of 1M HCl - pH_i 10.5	1	yes	30443 ± 705	1066 ± 39	0.7
Gas HCl Method 10 uL of 1 M HCl - pH_i 8.5	1	yes	8950 ± 17	418 ± 6	3.0

No turbidity was observed by UV-Vis spectroscopy measured at 400 nm for both concentrations 0.5 and 0.1 wt% (Materials and Methods, Section 2.5.10). This turbidity measurement by UV-Vis suggests that at these concentrations there are no large aggregates in detectable amounts. Therefore, the size of the dried down spherical structures observed by SEM is 989 nm is an artefact (Table 2.4). This result cannot be trusted for this water-dependent and ionic bound structure, because of drying effects on the aggregates (e.g. increase in concentration, collapse of the structure in vacuum).

SEM measurements could not reveal the size of the solution spherical aggregates as the sample was possibly changed with drying artefacts. Additionally, the size measurement of fibrillar structures of hydrogels can just be regarded as a close approximate value of the fibre size in solution for some self-assembly systems. The size measurements by dried microscopy samples may only relate to the actual solution and hydrogel phase depending on the strength of the intermolecular bonds in vacuum and sample preparation procedures. Cryo-TEM, wet-AFM and neutron/x-ray scattering techniques can bypass the addition of drying artefacts, however they are not readily available and may depend on sample preparation conditions.[70] However, other features of the solution or hydrogel can be understood from dried down techniques,[71] i.e. stiffness of the fibres (as discussed in Chapter 5).

2.3.6.2. BrNapAV triggered by the HCl method

A nanofibrous gel can be formed quickly by adding HCl aliquots to the micellar phase (Fig. 2.3a). This method, as in all pH-switch methods, protonates the carboxylic groups of the gelator and allows elongated self-assembly and lateral packing to form a hydrogel network (Fig. 2.12b). The HCl hydrogels have approximately a $G' = 30$ kPa and $G'' = 1$ kPa when formed by a liquid method and $G' = 9$ kPa and $G'' = 0.4$ kPa when formed by a gas phase method (the methods are described in Materials and Methods Section 2.6.2. and a summary of the mechanical properties is shown in Table 2.3). Inspection of a dried BrNapAV hydrogel through SEM suggests a nanofibre size of 33 ± 10 nm. The bundle size and the mesh size were measured by LSCM, since this measurement is near the microscope resolution lower limit and it depends on the fluorophore staining ability and objective,[72] it is not expected to be quantitative in our system. The bundle size is defined similarly to the nanofibre size but obtained from LSCM images, at the microscale, in the aqueous state, measured perpendicularly to the fibre direction, across the high contrast, stained area. The mesh size is defined as the average distance between the fibre bundles at the microscale in the aqueous state, measured through the unstained region in LSCM images. Through LSCM, aqueous measurements indicate a bundle size of 0.84 ± 0.30 μm or below, a mesh size of 6.2 ± 6.9 μm and a persistence length of approximately 50 μm (Table 2.4). Fergg *et al.* have reported on LSCM size measurements in hydrogel fibre-like features up to 1 μm in diameter and mesh size.[73] The mesh size and bundle size were established by measuring these lengths over 100 times in each of 5 images. All mesh size and persistence length size measurements resulted values above 1 μm, therefore applicable for quantitative characterisation in this study (Table 2.4). For reasons discussed above, all nanoscale measurements conducted by SEM should be regarded only as indicative of the actual size of the structure in solution and an indication of the comparative size between different methods.

In Table 2.4, it is interesting to note that the mesh size measurements of the HCl triggered hydrogel (6.2 ± 6.9 μm) have a significantly high standard deviation when compared with the GdL triggered hydrogels (1.4 ± 0.34 μm). These results agree with the previous reports of a more homogeneous hydrogel network obtained with GdL method when compared with the HCl gelation method.[2]

Table 2.4 – Structural shape, diameter, bundle size, mesh size (determined using ImageJ[74]) and persistence length (determined using FiberApp[71]) measurements determined by analysis of the SEM and LSCM images (Fig. 2.11). FTIR results are summarized here for comparison. (†) This results can only be used for comparison purposes as the results are near the LSCM detection limit between 0.4 – 1 μm calculated for the experimental setup used here.[72] (‡) These results agree with the results reported recently by our group, which indicate that the BrNapAV hydrogel shrinks on gelation.[69] The main values and errors are obtained from the average and standard deviations, respectively, of over 100 structures.

Self-assembly Method		**high pH**	**CO_2 (3 hours)**	**GdL (24 hours)**	**Two-step CO_2 (3 hours) and GdL (8.6 mg/mL, 24 hours)**	**HCl liquid (24 hours)**
Nanoscale (SEM)	Structural shape	non-irregular structures	possibly worm-like micelles	nanofibres	nanofibres	nanofibres
	Diameter (nm)	989 ± 519	22 ± 8	28 ± 13	64 ± 13	33 ± 10
Microscale (LSCM)	Bundle size † (μm)	n.a.	0.48 ± 0.093	0.52 ± 0.16	1.5 ± 0.68	0.84 ± 0.30
	Mesh size ‡ (μm)	n.a.	3.8 ± 2.1	1.4 ± 0.34	2.2 ± 1.2	6.2 ± 6.9
	Persistence Length (nm)	n.a.	8226 ± 821	41 420 ± 2286	7889 ± 143	50 070 ± 24
FTIR	Secondary Structure	no secondary structure	β-sheet and random packing	β-sheet	β-sheet and random packing	β-sheet

2.3.6.3. BrNapAV triggered by the GdL Method

The GdL method allows a more homogeneous hydrogel microstructure across macroscopic length scales.[2] It also enables a close monitoring of gelation because the process is slower compared to the HCl method.[2] In the case of the GdL method (Fig. 2.3c), as the pH slowly reaches the apparent pK_a of the gelator, an increasing fraction of the gelator molecules becomes protonated and change conformation gradually from no apparent structure or randomly packed amorphous structures to β-sheet-like structures (FTIR results, Fig. 2.13). A transition from flexible to stiffer structure is suggested by the FiberApp analysis of the microscopy images[71] (Fig. 2.12) in Table 2.4 (higher persistence length is correlated with stiffer fibres) and measured by mechanical properties (Fig. 2.14). The BrNapAV hydrogelation by the GdL method resulted in gels with approximately G′ = 50 kPa and G″ = 3 kPa, slightly above the corresponding HCl method (G′ = 30 kPa and G″ = 1 kPa) at approximately the same pH_f of 4. The nanofibre diameter, bundle size, mesh size and persistence length all appeared slightly smaller than the HCl counterpart (Table 2.4, above). In the time-lapsed frequency-sweep rheology measurements, it can be seen that there is an increase in the absolute values and transition from an initial frequency dependence to independence of G' and G" (Fig. 2.14) at the pH region where the pH is equal to the apparent pK_a of the gelator (pH 5.8 measured by pH probe). This result is a transition from a micellar solution, through a transient phase, into a typical hydrogel network.

2.3.6.4. BrNapAV triggered by the CO_2 Method

Our hypothesis of the hydrogel membrane equivalence to an intermediary state in the GdL self-assembly process is confirmed here by further rheology and microscopy experiments. It is suggested this occurs because the negative charges on the carboxylic groups of BrNapAV are likely to be present on the micellar structures and prevent them from abrupt collapse into larger packed bundles.[1,69] However, due to its structural anisotropy, the elongated structures can stack with a relatively large lateral packing distance when triggered by the CO_2 method. These domains can reach from hundreds of nanometres to micrometres in size. Image analysis by the FiberApp software[71] shows a persistence length of the order of 7–9 μm by LSCM images (discussed below). This range of self-assembly at the microscale is related to the hierarchical self-assembly of hundreds nanometres. This final phase of the CO_2 method or intermediate phase (Fig. 2.4d) does not have similar properties as an HCl gaseous trigger (Fig. 2.4b). The typical mechanical properties at 25 °C and 0.5 wt% BrNapAV triggered by the CO_2 method are G′ = 50 – 200 Pa and G″ = 10 – 30 Pa in shear and frequency independent regions (Table 2.4 and Fig. 2.9). A typical 0.5 wt% BrNapAV hydrogel membrane strain-sweep and frequency-sweep with one or three hours gelation time and 1.25 bar CO_2 is shown in Fig. 2.9. However, the breakage strain can go from 12.6 % with a 2 hours trigger (highest value of this dataset, Table 2.4) to 90 % when the conditions are optimized (Fig. 2.10b, black). On the other hand, the HCl gas trigger was G′ = 9000 Pa and G″ = 400 Pa under similar measurement conditions (Table 2.4), but the breakage strain is a low 3 %. We hypothesise that the CO_2 hydrogel exceptional case happens primarily because a negatively charged structured micellar phase is formed. However, G′ and G″ are almost two orders of magnitude below the HCl counterpart because the pH_f of the solution with the HCl gas phase trigger goes far below the apparent pK_a (it is difficult to control the pH_f using this method. The pH_f of the HCl method is reached quickly as HCl is a strong acid. Therefore it strongly depends on how much HCl diffuses into the solution, directly influenced by the type of vial and time the sample is left in the saturated HCl atmosphere).

Unlike the HCl method, the CO_2 method allows a tuning of the pH_f between pH 7 and pH 5.5. The final equilibrium phase with 0.5 wt% BrNapAV achieved by the CO_2 method is also achieved by the GdL method with a small amount of GdL, 1 mg/mL (Table 2.4). This lead to the hypothesis that the phase obtained by the membrane hydrogel with the CO_2 method is equivalent to the intermediate phase that the GdL or HCl gelation process go through before they reach their maximum in mechanical properties and low pH state (Table 2.4).

The final state of the BrNapAV triggered by the CO_2 method forms possibly elongated micelles with a diameter of 22 ± 8 nm (possibly overestimated by drying artefacts), a bundle size smaller than 1 μm (not accessible by LSCM), a mesh size of 3.8 ± 2.1 μm and a persistence length of approximately 8 ± 1 μm (Table 2.4). The mesh size decrease from the CO_2 triggered hydrogels to the GdL hydrogels, agrees with the recently reported shrinkage of the hydrogel upon gelation.[69] The average diameter of the structures is smallest when compared with the other methods (Table 2.4). This suggests that there may be a fibre diameter dependence on the pH_f of the self-assembly process used.

2.3.6.5. BrNapAV triggered by the two-step (CO_2 plus GdL) method

When the pH is further changed to values below the apparent pK_a, the gelator should become mostly protonated (only about 20 ± 10 % deprotonated),[69] the elongated structures can gradually pack with their nearest neighbours with close lateral packing (Table 2.4). This further gelation, achieved with the two-step process, forms nanofibres of 64 ± 13 nm, an average bundle size of 1.5 ± 0.68 μm and 2.2 ± 1.2 μm mesh size structures at the microscale (Table 2.4 and Fig. 2.11e). Therefore, gelation changes from the solution phase into an intermediate CO_2 triggered phase to a final GdL hydrogel phase, with closer lateral packing (bundle size, Table 2.4) and higher persistence length (Table 2.4). The persistence length is a measure of the stiffness of the material.[81] Here, we obtained the highest persistence length for the GdL and the HCl methods alone (> 40 μm). However, the hydrogel formed with the CO_2 method followed by the GdL method (two-step method) appears to have fibres with a persistence length similar to the CO_2 method alone (Table 2.4). This suggests that the higher mechanical properties of the two-step process when compared to the CO_2 method alone are an effect of the microstructure (e.g. number of crosslinks and entanglements) rather than the stiffness of the individual fibres. The lower the pH of the solution, the higher will be the number of entanglement points, non-covalent cross-links and larger will be the mesh size because of higher order self-assembly. This last point was shown to be the case in a parallel study by multinuclear NMR spectroscopy conducted in our group.[82]

This is also observed by LSCM. A slight increase is measured in the BrNapAV bundle size from the CO_2 method alone to when the GdL, HCl and the two-step processes are used (Table 2.4). However these values are near the resolution limit of the instrument, and are not conclusive. However, it was already shown by Chen et al. by TEM self-assembly evolution images of BrNapAV at 0.5 wt%, in the presence of 14.2 mg/mL of GdL, there the fibre diameter increases from 12.0 nm to 25.4 nm.[56] Here, The mesh size increases from both the CO_2 method (with a large standard deviation) and the GdL method to the two-step process and the HCl method (determined by LSCM).

The two transitions, (1) from the non-irregular structures to possibly worm-like structures and (2) from possibly worm-like micelles to nanofibre structured hydrogel are part of a self-assembly process which allows kinetic control (and depends on the amount of GdL).[2] Adams et al. showed for a similar modified-dipeptide gelator FmocLG, that there is a step-wise transition from aggregates at high pH to peptide fibres at low pH from rheology data, this links with the findings of a two-step process with pH-switch method found here for BrNapAV.[2] In the same work, it was shown by fluorescence spectra that this self-assembly is driven by π-π stacking. The worm/nanofibre diameter, persistence length and bundle thickness increases as the semi-protonated elongated structures change to mostly protonated nanofibres. It is remarkable that this class of materials, as shown in Table 2.4, has a range of G' and G" up to 3 orders of magnitude using these different self-assembly processes, from approximately 1 – 200 Pa (solution phase and CO_2 method phase) to 10^4 Pa (GdL, HCl and two-step methods, hydrogel phase). The mechanical analysis shown in Table 2.4 also suggests a more brittle hydrogel is formed upon addition of the GdL to the CO_2 triggered membrane, because the breakage strain percentage is higher in the CO_2 case. All other methods or the starting solutions have a lower breakage strain. It is perhaps most interesting to see that the addition of GdL still allows a gradual transition to a fully bulk hydrogel phase, similar to the direct application of GdL to a solution at high pH (Table 2.4). The mechanical properties of these post-treated membranes are similar to those formed using GdL alone. Interestingly, adding GdL to the top of a CO_2-triggered hydrogel membrane resulted in the formation of a more rigid gel (Fig. 2.4c) when compared with the CO_2-triggered method (Fig. 2.4b), however the persistence length of the individual fibrils appears to be maintained (Table 2.5). This result suggests that the entanglement points and the microstructure of the hydrogel may be the main cause of the higher mechanical strength. A more brittle hydrogel membrane is formed with addition of only GdL or HCl when compared with the CO_2 method alone (Table 2.4). The nanostructure (observed by SEM) and hydrated microstructure (observed by LSCM) indicate that the fibre network consists of thicker fibres with larger water pockets in the fibrous mesh structure as shown in Fig. 2.12. The SEM images of BrNapAV triggered with the two-step process (Fig. 2.12 e.2) show a fibre thickness of 64 ± 13 nm. The apparent increase in thickness of the fibres (from 16 ± 10nm with the CO_2 method) may indicate that there is a structural packing change associated with lowering the pH. There could also be a contribution from the evaporation of water both from the time required to self-assemble with the two-step process (above 12 hours, measured after approximately 24 hours). The drying effects should not be negligible in such a long period of gelation. However, the relative thickness increase could be related to how much the fibres bundle on the hydrated material. Addition of either aqueous HCl to a solution at high pH or exposure to HCl vapour both result in different hydrogel phases as compared with any of the methods described above (Table 2.4 and Table 2.5).

In summary, these results show the impact of different self-assembly processes in the final hydrogel structure and properties, as reported for other peptide gelators.[3] The kinetic aspects of each method were described. The new CO_2 method is shown to follow a similar kinetic pathway to other pH-switch methods, however the CO_2 method reaches a final equilibrium structure different than what can be achieved using other pH-switch methods. The new method allows accessing a final equilibrium state that is likely to be an intermediary state of the other pH methods that go from pH above the apparent pK_a to a pH well below the apparent pK_a.

2.4. Conclusions

The carbon dioxide pH-switch method can be used to as a hydrogelation trigger for modified-dipeptide self-assembly and can be combined with other pH-switch methods. The pathway of hydrogelation can be controlled by the pK_a of carbonic acid with the use of gaseous CO_2. The screening of different gelators with the new method showed that some gelators with an apparent pK_a well above the carbonic acid pK_a (> 5.8) also form bulk hydrogels. However, the CO_2 pH-switch method additionally permits a hydrogel membrane formation under specific conditions of gelator apparent pK_a, between 5.5 and 5.8. Therefore, the new method works when the apparent pK_a of the gelator is above or close to the pK_a of the carbonic acid and the solution is not a structured phase at high pH. Thus, the factors identified to be determining of bulk of hydrogel membrane hydrogel formation are the gelator apparent pK_a, the viscosity of the starting solution, the pH gradient during gelation, and concentration.

A focus study of BrNapAV hydrogel membranes formed with the new CO_2 pH-switch method showed that the speed of pH-gradient, in different parts of the vial, may have an effect on the outcome of hydrogel membrane formation. Typical hydrogel membranes have a G' and G" of 270 Pa and 75 Pa, respectively, from a strain-sweep, in a strain-independent region, at 0.5 % strain and 10 rad/s. The cross-over point can be significantly higher (from 10 % to 80 % strains) than the cross-over points reported previously for BrNapAV hydrogels formed by the GdL method to a lower final pH (all between 1 % to 10 % strain).[56] The concentration, volume of sample, initial pH, exposure time to CO_2, and CO_2 pressure all have an impact on the mechanical properties, thickness, nanostructure, microstructure, and secondary structure of the hydrogel membrane.

The previously studied pH triggers (vapour and aqueous HCl,[83] or GdL[2], as well as other recently reported hydrolysis of anhydrides[84]) are only able to form a bulk hydrogel. The CO_2 triggered method is also able to form bulk hydrogels and can additionally form hydrogel membranes with some gelators. All CO_2 triggered hydrogels are weaker than HCl and GdL triggered gels formed with the same gelator. Nonetheless, they break at higher strains, above 10 %. This higher breakage strain allows easier physical manipulation. The CO_2 pH-switch method can only switch to a maximum final pH of approximately pH 5.5 within a maximum of cylinder $p(CO_2)$ = 2 atm (i.e. with the pressure chamber and temperature used here). Additionally, it requires CO_2, either from a reservoir containing dry ice or pressure regulated gas cylinder for better control over the final properties and the rate of gelation.

Although the kinetic pathway is not the sole determinant of the final rheological properties, the different GdL pathways (i.e. GdL only or a two-step process with CO_2 plus GdL) form different nanostructures, different fibre stiffness and form hydrogels with different mechanical properties. The two step process, with a preceding CO_2 gelation step, forms hydrogels with potentially thicker nanofibres and bundles (SEM, Table 2.5), lower persistence length (less stiff, measured by imaging software, in Table 2.5), a similar mesh size and lower G′ than the GdL method alone (Table 2.4).

The CO_2 method permits: (1) the control of a gradual pH change from the liquid-air interface; (2) a reproducible pH_f; (3) the combination with other methods; (4) the formation of a transparent hydrogel membrane and (5) the manipulation of the hydrogel without breakage. In addition, (6) when this method is used in combination with other methods, such as GdL, it is possible to adjust further the mechanical properties and the nanostructure. This happens within a significant change in G′ from tenths to thousands of Pascal and with a breakage strain from 80 % from to 10 %. For comparison, the typical optimized CO_2 method used with BrNapAV has a G′ = 270 Pa, G″ = 75 Pa and breakage strain from 10 % to 80 %. The sequential two-step process with CO_2 followed by GdL formed hydrogels with G′ = 12 kPa, G″ = 0.5 kPa and strain break of 10 %.

The kinetic experimental results using BrNapAV suggest that, during the transitions to the hydrogel state at low pH (using pH-switch methods), all similar gelators are likely to go through an intermediate kinetically controlled state or starting structured phase. This state can only be accessed using the CO_2 gelation method, for example, in the case of BrNapAV (results in Fig. 2.14, two-step process) and BrNapFF (results in Fig. 2.5, higher viscosity state).

Results presented in this Chapter show that distinct self-assembly processes allow for a broad range in the final material properties and control of the structure of supramolecular hydrogels.[3] The use of the new CO_2 acidification method to trigger modified-dipeptide gel formation may allow for novel applications in the biomedical setting where CO_2 is already used in low quantities.[41,86] The CO_2 pH-switch method could potentially be used to trigger gelation in a minimally invasive intervention using hydrogels in the human body, regulated by the CO_2 diffusion rate and equilibrium constants of carbonate species. This method may have other advantages in the biomedical or lubricant industries because of its range of rheological control.

2.5. Materials and Methods

2.5.1. Materials

All gelators were synthesised as described previously.[11,51] The gelators used in this chapter were synthesised by Dave J. Adams, Jaclyn Raeburn and a portion of the 2NapFF used here by myself. The final dipeptides used have a purity > 98% as determined by ^{1}H-NMR spectroscopy. Carbon dioxide was purchased from BOC and used as received. Diced silicon wafer, aluminium stubs, black tape, and 400 mesh hexagonal copper grids were purchased from Agar Scientific. All other materials were purchased from Sigma-Aldrich and used as received. Millipore water was used throughout (resistivity = 18 mΩ.cm).

2.5.2. Preparation of Hydrogels

All hydrogels are formed by preparing a starting solution of the gelator diluted at high pH, followed by the application of a hydrogel triggering method. In this Chapter, the hydrogels studied were formed by one of the following methods: HCl method, a GdL method, a CO_2 method and a two-step (CO_2 plus GdL) method described below.

- **Preparation of the starting solution**

An amount of gelator, typically 0.5 wt% or 1.0 wt%, was diluted in ddH_2O with 1.2 molar equivalent of NaOH with stirring for 12 hours to obtain a clear starting solution at pH 10.5 (unless otherwise noticed). Solutions with a lower starting pH were used when mentioned, by adding a reduced amount of NaOH (approximately 1 molar equivalent) and adjusted with more NaOH during the stirring process, instead of adjusting at the end with HCl. This was done to avoid the presence of irreversible formed aggregates at the addition of HCl.

All gelators were tested at 0.5 wt% in the Section 2.3. The optimisation of the hydrogel membranes steered the full characterisation of BrNapAV with different methods (Section 2.4) to be conducted on 1 wt% hydrogels (unless stated otherwise).

- **Preparation of HCl hydrogels**

Aqueous version

To a starting solution at pH 10.5 was added dropwise 1.1 eq. of 1M HCl and allowed to gel for 12 hours before characterisation (Fig. 2.3a).

Vapour version

The vial cap of the starting solution was removed and the vial placed in a large jar with a second vial with 4 mL of 1M HCl. The jar was closed and the HCl vapours allowed diffuse to the starting solution for 3 hours before characterisation (Fig. 2.3a).

- **Preparation of GdL hydrogels**

The starting solution was pipetted to a vial with 8.6 mg/mL of glucono-δ-lactone (GdL) and left to gel for approximately 24 hours before characterisation (Fig. 2.3b).

- **Preparation of CO_2 hydrogels**

CO_2 acidification of the starting solution of the gelator was conducted in a reaction chamber with an inlet of CO_2 from either a cylinder (for pressure regulation) or a dry ice reservoir (Fig. 2.3c). A dry ice reservoir was only used for initial experimental tests of gelation inversion vial tests with different gelators, shown in Fig. 2.4a, Fig. 2.6 and Fig. 2.7. All quantification of mechanical properties where conducted with CO_2 triggered gels by the cylinder pressure regulated system. A needle outlet was placed in the reaction chamber to equalise the pressure with the atmospheric pressure during the experiment. The pressure selected in the CO_2 cylinder was from 0.25 to 1.00 atm above the atmospheric pressure, to result in reaction chamber pressures of 1.25 to 2.00 atm. The samples were left for typically 3 hours in the reaction chamber at the selected pressure, unless stated otherwise. For experiments over 3 hours, the pressure gauge may require adjustment if the cylinder pressure is near the outlet pressure selected. After the CO_2 exposure time, samples were removed and the vials were closed. In the case of the hydrogel membrane formation with this method, the subnatant was removed with a needle syringe 0.9 mm gauge (BD Microlance, REF 301300).

- **Preparation of two-step (CO_2 plus GdL) hydrogels**

This method was tested only on the BrNapAV 1.0 wt% hydrogel membrane. The preparation of the two-step hydrogels described here is a combination two methods. The CO_2 method was used first, with a gas cylinder at 1.25 atm for 3 hours. The hydrogel membranes were formed first by the CO_2 method described above and then transferred to a separate surface to be separated from the subnatant (removed with a syringe). This was followed by the pouring of 16 mg of GdL to approximately 2mL sized hydrogel membranes (GdL method). The diffusion and hydrolysis of GdL was allowed to take place for approximately 24 hours.

Rheology measurements of these hydrogels were conducted on hydrogel membranes which has the second step formed directly in the Rheometer plate-plate system. The FTIR measurement of this hydrogel was made of a hydrogel membrane aged approximately 24 hours and then transferred to the FTIR liquid cell system.

2.5.3. Rheology

All rheological experiments were performed using an Anton Paar Physica MCR101 or a MCR301 rheometer, both previously calibrated within one month or prior to each measurement for measurements close to the torque of the instrument. All strain sweeps and frequency sweeps of the carbon dioxide hydrogel membranes were carried out using the sandblasted plate-plate geometry. Parallel plates were used for the time-dependent frequency sweep analysis. A solution or hydrogel was prepared as described in section 2.5.2 (above) and immediately transferred to the rheometer where it was sandwiched between the plate-plate measuring system (PP50/S or PP25/S, depending on the size of the hydrogel intended for measurement, 50 mm or 25 mm denote the diameter of the top plate probe). A sandblasted plate was used in order to eliminate artefacts arising from wall slip.[52] The plate gap used was 1 mm, unless stated otherwise. Before each measurement, rheometer plate surfaces were washed with ethanol and distilled water. Viscosity measurements were conducted with 75 mm and 1 ° angle cone-plate geometry with a 0.05 mm gap, a shear rate from 0.1 to 100 s^{-1}, a sampling rate of 20 points/decade, a normal force of 0 N at 25 °C and 61 measurement points were recorded.

For the initial analysis of the mechanical properties in Table 2.1, 2NapFF, 2NapAA and BrNapAG were measured in a cup and vane system was used instead of the plate-plate geometry because of the difficulty in removing the sample from the vial without mechanically destroying it. In this case, the samples (2 mL) were formed directly in 7 mL Sterilin cups at room temperature before the measurements. The measurement with the vane was conducted by mounting the Sterilin cup on the rheometer and lowering the vane so that it was immersed in the sample.

2.5.4. Scanning Electron Microscopy (SEM)

SEM images were recorded using a Hitachi S-4800 FE-SEM at 3 KeV. Diced silicon wafers or TEM copper grids were used to probe the gels. Hydrogel or solution samples were prepared as described in Section 2.5.2.

Typically, the most simple method to probe a sample for SEM consists of cutting or scooping a piece of the hydrogel with a blade/spatula onto a pre-cleaned diced silicon wafer (cleaned with ethanol and acetone in a sonicator and then dried under nitrogen) and allowing it to dry. An alternative sample preparation method, was used here in all SEM images unless stated otherwise. This method consists of first placing a pre-cleaned sliced silicon piece or a copper mesh grid (where mentioned) typically used for transmission electron microscopy in the bulk of the hydrogel for 30 minutes. This is then carefully removed with tweezers into an aluminium foil reservoir and air-dried for 1 hour. Only in the case of examining the two-step hydrogel case the copper grid version appeared most representative of the sample. The images shown in Fig. 2.12 were all obtained from samples prepared with the bulk hydrogel probing in silicon method with exception of the two-step processed samples in Fig. 2.12e.2 (used copper grid) because the way the sample was prepared would not allow a clear representation of the stiff millimetre sized hydrogel membrane if the diced silicon was used. This occurs because the shaper of the hydrogel membrane being smaller than the diced silicon.

This probing of a bulk gel method gave reproducible and simple to characterize the peptide fibres, avoiding most drying artefacts due to a lower amount of sample and avoiding changes in dilution of the sample and possibly changes in structure by drying. All hydrogel samples were imaged both with the copper grid as well as the in silicon version of the method, resulting in similar results.

No coatings were applied to the gels. To avoid charging, a low voltage SEM was used (0.5 to 1KeV) at a 1.5 to 3 mm distance with the deceleration mode (i.e. deceleration Voltage = 2 KeV, from 3 to 1 KeV).

2.5.5. Laser Scanning Confocal Microscopy (LSCM)

Observations with the LSCM from the low to high magnifications were carried out with oil emersion lenses from Zeiss for the higher magnifications (62 and 100 times). All lenses were carefully cleaned with ethanol before use. LSCM images were obtained on a Zeiss LSM510 and a Plan-Apo 100x (1.4 NA oil) objective. Nile blue fluorescence was excited with a 633 nm Helium Neon laser and emission detected between 638 and 758 nm using a pinhole diameter of 1 Airy unit (approximately 0.8 μm resolution). The samples (e.g. hydrogel membrane) were prepared as described in Section 2.5.2 with the additional inclusion of 0.001 M Nile blue in the initial ddH_2O to make the solution phase (pipetting a selected amount from a 0.01 M stock solution). The solution phase samples were poured instead of pipetted after the gelator is diluted. The final one-step CO_2 hydrogel membrane was poured on a cell culture dish (Greiner bio-one). The two-step self-assembly processed hydrogel membrane was sectioned and imaged to avoid handling artefacts due to the contact with the tweezers. Typical shown images were selected from a range of over 50 images captured of multiple samples (minimum 3 samples) and measured for this study. The images were analysed using the Zeiss AIM software (Zeiss, Jena, Germany), ImageJ software[74] and FiberApp software.[71] Size measurements such as bundle size and mesh size were measure by ImageJ using several straight-line distance measurements using the image contrast to identify where these features were in the image. The mesh size was measured as the average distance between the fibres. Averages were obtained over 100 measurements per image were conducted on at least 5 images. Persistence length was measured by an algorithm implemented by the authors of the FiberApp software based on the tangent over a length scale along the fibre path.

2.5.6. Optical Microscopy

Optical Microscopy was carried out using a Nikon Eclipse Microscope and image analysis was done with ImageJ.[74] Solutions and hydrogels were prepared as described in Section 2.5.2. They were poured to a microscope slide and examined in the bright field and under cross-polarizers.

2.5.7. FTIR Spectroscopy

A Bruker Tensor 27 spectrometer at a resolution of 2 cm^{-1}, averaging over 64 scans from 4000 cm^{-1} to 800 cm^{-1} was used to make these experiments. The hydrogels were prepared with D_2O, NaOD and DCl for these experiments as described above in Section 2.5.2 (above) for the non-deuterated analogues.

2.5.8. TGA and Freeze-drying to find concentration

Samples were prepared as described in Section 2.5.2. As prepared samples were transferred with a spatula to aluminium sample pans (TA Instruments) and placed on the stainless steel bail (TA Instruments). The sample plus holder were placed on the sample holder of a TA Instruments Q5000IR TGA to be analysed. The sample and pan weight have to be reweighed. The programmed mode of operation consisted on a 5°C/min ramp to 150°C.

To calculate the final concentration, two corrections were made to the obtained values from the freeze-drying and TGA weight measurements. The first correction included the addition of NaOH and HCl, while the second correction included the expected weight losses on the hydrogel preparation. The first correction in the calculation introduced a reduction in the final membrane weight accounting for NaOH and HCl added to adjust the pH, assuming an approximate final membrane weight of 0.6 mL. The second correction was found necessary as a result of control experiments which found a loss of gelator molecules in the preparation process, described below. These corrections included a maximum weight loss of 0.12 wt%, when starting with a 1 wt% gelator using both techniques. This was found using control samples with the gelator diluted in solution at high pH.

2.5.9. ^{1}H-NMR Spectroscopy

Solutions and hydrogels were prepared as described in Section 2.5.2 (above) with the deuterated analogues (D_2O and NaOD). ^{1}H-NMR Spectroscopy was used to characterize the solution phase. A 500 MHz Bruker Avance-III HD equipped with an 11.74 T magnet and a liquid nitrogen cooling system was used for all experiments. A common ^{1}H-NMR experiment with 30 degrees flip angle was used to obtain the spectra. The total number of scans was 16 and the acquisition time per scan was 3 minutes for each measurement at 25 °C, except when mentioned. Aliquots of 0.5 mL of each solution were transferred to a NMR tube (NE-ML5-8, NEW ERA Enterprises). All measurements were conducted at 25 °C.

The ^1H-NMR spectroscopy integrals were calibrated against a known amount of ethanol sealed in a capillary in D_2O (approximately 6 µL Ethanol in 1 mL D_2O solution) and sealed with a PTFE tape. The capillary was calibrated with 8 mg/mL L-alanine solution in H_2O. Before each measurement, the reference capillary was inserted with a PTFE holder into the NMR tube with the 2NapFF solution. Additionally, a common solvent suppression experiment using pre-saturation and spoil gradient under the same conditions was conducted and used for the quantification analysis.

Diffusion experiments were carried out under appropriate conditions with a pulsed field gradient-NMR spectroscopy as previously used in our group.[82] The relaxation delay was set to 25 seconds so that the diffusion measurement reflects the diffusion of the low molecular weight gelators here studied. Samples of L-alanine and L-valine were used to calibrate our measurements to literature values for the diffusion of these amino acids in water at 25 °C.

2.5.10. Turbidity measurement by UV-Vis Spectroscopy

Samples were prepared as described in Section 2.5.2. The background was measured for a sample with ddH_2O in the cuvette. Each sample was poured into a quartz cuvette if it was a solution or weak viscous gel. If the sample was a gel, it was prepared in the cuvette. After the sample was in the cuvette, a standard measurement was initiated. The turbidity of the sample was evaluated by measuring the absorption intensity at 400 nm. If the intensity at 400 nm was above the signal-to-noise ratio of the control sample (ddH_2O), then the sample was said to be turbid.

2.6. References

1. A. Z. Cardoso, A. E. Alvarez Alvarez, B. N. Cattoz, P. C. Griffiths, S. M. King, W. J. Frith, and D. J. Adams, *Faraday Discuss.*, 2013, 166, 101–116.
2. D. J. Adams, M. F. Butler, W. J. Frith, and M. Kirkland, *Soft Matter*, 2009, 5, 1856–1862.
3. J. Raeburn, A. Zamith Cardoso, and D. J. Adams, *Chem. Soc. Rev.*, 2013, 42, 5143–56.
4. R. C. Hayward and D. J. Pochan, *Macromolecules*, 2010, 43, 3577–3584.
5. S. Ogi, T. Fukui, M. L. Jue, M. Takeuchi, and K. Sugiyasu, *Angew. Chemie Int. Ed.*, 2014, 53, 14363–14367.
6. A. R. Hirst, S. Roy, M. Arora, A. K. Das, N. W. Hodson, P. Murray, S. Marshall, N. Javid, J. Sefcik, J. Boekhoven, J. H. van Esch, S. Santabarbara, N. T. Hunt, and R. V Ulijn, *Nat. Chem.*, 2010, 2, 1089–1094.
7. D. J. Adams, K. Morris, L. Chen, L. C. Serpell, J. Bacsa, and G. M. Day, *Soft Matter*, 2010, 6, 4144–4156.
8. L. Cademartiri and K. J. M. Bishop, *Nat. Mater.*, 2015, 14, 2–9.
9. S. L. Price, *Acta Crystallogr. B. Struct. Sci. Cryst. Eng. Mater.*, 2013, 69, 313–28.

10. B. Ding, Y. Li, M. Qin, Y. Ding, Y. Cao, and W. Wang, *Soft Matter*, 2013, 9, 4672.

11. L. Chen, S. Revel, K. Morris, L. C. Serpell, and D. J. Adams, *Langmuir*, 2010, 26, 13466–13471.

12. D. J. Adams, L. M. Mullen, M. Berta, L. Chen, and W. J. Frith, *Soft Matter*, 2010, 6, 1971-1980.

13. E. F. Banwell, E. S. Abelardo, D. J. Adams, M. A. Birchall, A. Corrigan, A. M. Donald, M. Kirkland, L. C. Serpell, M. F. Butler, and D. N. Woolfson, *Nat. Mater.*, 2009, 8, 596–600.

14. P. W. J. M. Frederix, G. G. Scott, Y. M. Abul-Haija, D. Kalafatovic, C. G. Pappas, N. Javid, N. T. Hunt, R. V. Ulijn, and T. Tuttle, *Nat. Chem.*, 2014, 7, 30–37.

15. A. L. Rodriguez, C. L. Parish, D. R. Nisbet, and R. J. Williams, *Soft Matter*, 2013, 9, 3915–3919.

16. H. A. M. Ardoña, K. Besar, M. Togninalli, H. E. Katz, and J. D. Tovar, *J. Mater. Chem. C*, 2015, 3, 6505–6514.

17. H. Cui, A. G. Cheetham, E. T. Pashuck, and S. I. Stupp, *J. Am. Chem. Soc.*, 2014, 136, 12461–12468.

18. E. Gazit, *Nat. Chem.*, 2014, 7, 14–15.

19. D. M. Zurcher and A. J. McNeil, *J. Org. Chem.*, 2015, 80, 2473–2478.

20. J. Raeburn, C. Mendoza-Cuenca, B. N. Cattoz, M. a. Little, A. E. Terry, A. Zamith Cardoso, P. C. Griffiths, and D. J. Adams, *Soft Matter*, 2015, 11, 927–935.

21. P. Jonkheijm, P. van der Schoot, A. P. H. J. Schenning, E. W. Meijer, P. Van Der Schoot, and A. P. H. J. Schenning, *Science*, 2006, 313, 80–83.

22. K. Flanagan, J. Walshaw, S. L. Price, and J. M. Goodfellow, *Protein Eng.*, 1995, 8, 109–16.

23. J. Raeburn, G. Pont, L. Chen, and Y. Cesbron, *Soft Matter*, 2012, 8, 1168–1174.

24. K. L. Niece, C. Czeisler, V. Sahni, V. Tysseling-Mattiace, E. T. Pashuck, J. A. Kessler, and S. I. Stupp, *Biomaterials*, 2008, 29, 4501–9.

25. P. a Korevaar, C. J. Newcomb, E. W. Meijer, and S. I. Stupp, *J. Am. Chem. Soc.*, 2014, 136, 8540–3.

26. L. Chen, J. Raeburn, S. Sutton, D. G. Spiller, J. Williams, J. S. Sharp, P. C. Griffiths, R. K. Heenan, S. M. King, A. Paul, S. Furzeland, D. Atkins, and D. J. Adams, *Soft Matter*, 2011, 7, 9721–9727.

27. Y. Lan, M. G. Corradini, R. G. Weiss, S. R. Raghavan, and M. A. Rogers, *Chem. Soc. Rev.*, 2015, 44, 6035–6058.

28. B. Ozbas, J. Kretsinger, K. Rajagopal, J. P. Schneider, and D. J. Pochan, *Macromolecules*, 2004, 37, 7331–7337.

29. B. Ozbas, K. Rajagopal, J. P. Schneider, and D. J. Pochan, *Phys. Rev. Lett.*, 2004, 93, 268106.

30. T. Heuser, A. Steppert, C. Molano Lopez, B. Zhu, and A. Walther, *Nano Lett.*, 2014, 15, 2213–2219.

31. A. Baral, S. Basak, K. Basu, A. Dehsorkhi, I. W. Hamley, and A. Banerjee, *Soft Matter*, 2015, 11, 4944–4951.

32. E. R. Draper, T. O. McDonald, and D. J. Adams, *Chem. Commun.*, 2015, 1, 8–10.

33. J. S. Foster, J. M. Żurek, N. M. S. Almeida, W. E. Hendriksen, V. A. A. le Sage, V. Lakshminarayanan, A. L. Thompson, R. Banerjee, R. Eelkema, H. Mulvana, M. J. Paterson, J. H. van Esch, and G. O. Lloyd, *J. Am. Chem. Soc.*, 2015, 137, 14236–14239.

34. L. A. Estroff and A. D. Hamilton, 2004, 104, 1201–1218.

35. K. Holmberg, *Curr. Opin. Colloid Interface Sci.*, 2001, 6, 148–159.

36. R. Vijay and P. L. Polavarapu, *J. Phys. Chem. A*, 2012, 116, 10759–69.

37. L. Chen, T. O. McDonald, and D. J. Adams, *RSC Adv.*, 2013, 3, 8714–8720.

38. J. D. Hartgerink, E. Beniash, and S. I. Stupp, *Science*, 2001, 294, 1684–1688.

39. R. E. . Zeebe and D. Wolf-Gladrow, *CO_2 in Seawater: Equilibrium, Kinetics, Isotopes*, Elsevier B.V, 2001.

40. K. Adamczyk, M. Prémont-Schwarz, D. Pines, E. Pines, and E. T. J. Nibbering, *Science*, 2009, 326, 1690–4.

41. M. L. Floren, S. Spilimbergo, A. Motta, and C. Migliaresi, *Biomacromolecules*, 2012, 13, 2060–2072.

42. M. George and R. G. Weiss, *Langmuir*, 2002, 18, 7124–7135.

43. M. George and R. G. Weiss, *J. Am. Chem. Soc.*, 2001, 123, 10393–10394.

44. C. A. Angulo-Pachón and J. F. Miravet, *Chem. Commun.*, 2016.

45. C. E. Housecroft and A. G. Sharpe, *Inorganic Chemistry*, Prentice-Pearson-Hall, 2nd edn., 2005.

46. P. Y. Bruce, *Organic Chemistry*, University of California, Santa Barbara, 2007.

47. W. Helen, P. de Leonardis, R. V. Ulijn, J. E. Gough, N. Tirelli, and P. de Leonardis, *Soft Matter*, 2011, 7, 1732–1740.

48. N. N. Greenwood and A. Earnshaw, *Chemistry of the Elements (2nd ed.). Butterworth–Heinemann*, Butterworth–Heinemann, 1997.

49. K. A. Houton, K. L. Morris, L. Chen, M. Schmidtmann, J. T. A. Jones, L. C. Serpell, G. O. Lloyd, and D. J. Adams, *Langmuir*, 2012, 28, 9797–806.

50. A. M. Smith, R. J. Williams, C. Tang, P. Coppo, R. F. Collins, M. L. Turner, A. Saiani, and R. V Ulijn, *Adv. Mater.*, 2008, 20, 37–41.

51. C. Tang, A. M. Smith, R. F. Collins, R. V Ulijn, and A. Saiani, *Langmuir*, 2009, 25, 9447–53.

52. S. Sathaye, A. Mbi, C. Sonmez, Y. Chen, D. L. Blair, D. J. Pochan, J. P. Schneider, and D. J. Pochan, *Wiley Interdiscip. Rev. Nanomed. Nanobiotechnol.*, 2014, 2, 1–59.

53. V. Breedveld, A. P. Nowak, J. Sato, T. J. Deming, and D. J. Pine, *Macromolecules*, 2004, 37, 3943–3953.

54. R. Krishnamoorti and E. P. Giannelis, *Macromolecules*, 1997, 30, 4097–4102.

55. R. G. Larson, K. I. Winey, S. S. Patel, H. Watanabe, and R. Bruinsma, *Rheol. Acta*, 1993, 32, 245–253.

56. L. Chen, K. Morris, A. Laybourn, D. Elias, M. R. Hicks, A. Rodger, L. Serpell, and D. J. Adams, *Langmuir*, 2010, 26, 5232–42.

57. R. C. Reid, J. M. Prausnitz, and B. E. Poling, *The Properties of Gases & Liquids*, McGraw-Hill, Boston, 4th edn., 1987.

58. A. R. Hirst, I. A. Coates, T. R. Boucheteau, J. F. Miravet, B. Escuder, V. Castelletto, I. W. Hamley, and D. K. Smith, *J. Am. Chem. Soc.*, 2008, 130, 9113–21.

59. R. L. Baldwin, *Biophys. J.*, 1996, 71, 2056–63.

60. S. Roy, N. Javid, P. W. J. M. Frederix, D. A. Lamprou, A. J. Urquhart, N. T. Hunt, P. J. Halling, and R. V Ulijn, *Chemistry*, 2012, 18, 11723–31.

61. L. Chen, G. Pont, K. Morris, G. Lotze, A. Squires, L. C. Serpell, and D. J. Adams, *Chem. Commun.*, 2011, 47, 12071–12073.

62. S. Roy, R. V Ulijn, N. Javid, J. Sefcik, and P. J. Halling, *Langmuir*, 2012, 28, 16664–16670.

63. A. Cayuela, S. R. Kennedy, M. L. Soriano, C. D. Jones, M. Valcárcel, and J. W. Steed, *Chem. Sci.*, 2015, 6, 6139–6146.

64. Y. Zhang and P. S. Cremer, *Curr. Opin. Chem. Biol.*, 2006, 10, 658–63.

65. S. Awhida, E. R. Draper, T. O. McDonald, and D. J. Adams, *J. Colloid Interface Sci.*, 2015, 455, 24–31.

66. X. Mu, K. M. Eckes, M. M. Nguyen, L. J. Suggs, and P. Ren, *Biomacromolecules*, 2012, 13, 3562–71.

67. J. T. Pelton and L. R. McLean, *Anal. Biochem.*, 2000, 277, 167–76.

68. A. Barth and C. Zscherp, *Q. Rev. Biophys.*, 2002, 35, 369–430.

69. M. Wallace, J. A. Iggo, and D. J. Adams, *Soft Matter*, 2015, 11, 7739–7747.

70. R. Mammadov, A. B. Tekinay, A. Dana, and M. O. Guler, *Micron*, 2012, 43, 69–84.

71. I. Usov and R. Mezzenga, *Macromolecules*, 2015, 48, 1269–1280.

72. N. S. Claxton, T. J. Fellers, and M. W. Davidson, in *Encyclopedia of Medical Devices and Instrumentation*, John Wiley & Sons, Inc., Hoboken, NJ, USA, 2006, vol. 1979, pp. 1–37.

73. F. Fergg, F. J. Keil, and H. Quader, *Colloid Polym. Sci.*, 2001, 279, 61–67.

74. W. S. S. Rasband, *U. S. Natl. Institutes Heal. Bethesda, Maryland, USA*.

75. C. Ligoure and S. Mora, *Rheol. Acta*, 2013, 52, 91–114.

76. C. A. Dreiss, *Soft Matter*, 2007, 3, 956–970.

77. J. T. Padding and E. S. Boek, *Europhys. Lett.*, 2004, 66, 756–762.

78. O. Radulescu, P. D. Olmsted, J. P. Decruppe, S. Lerouge, J.-F. Berret, and G. Porte, *Europhys. Lett.*, 2003, 62, 230–236.

79. T. Mitchison and M. Kirschner, *Nature*, 1984, 312, 237–42.

80. C. Chassenieux and L. Bouteiller, *Rheology. Supramolecular Chemistry: From Molecules to Nanomaterials.*, John Wiley & Sons, Ltd, Chichester, UK, 2012.

81. S. Ezrahi, E. Tuval, and A. Aserin, *Adv. Colloid Interface Sci.*, 2006, 128–130, 77–102.

82. M. Wallace, D. J. Adams, and J. A. Iggo, *Soft Matter*, 2013, 9, 5483–5491.

83. B. M. Rabatic, R. C. Claussen, and S. I. Stupp, *Chem. Mater.*, 2005, 17, 5877–5879.

84. E. R. Draper, L. L. E. Mears, A. M. Castilla, S. M. King, T. O. McDonald, R. Akhtar, and D. J. Adams, *RSC Adv.*, 2015, 5, 95369–95378.

85. T. Li, M. Kalloudis, A. Z. Cardoso, D. J. Adams, and P. S. Clegg, *Langmuir*, 2014, 30, 13854–60.

86. D. Buenger, F. Topuz, and J. Groll, *Prog. Polym. Sci.*, 2012, 37, 1678–1719.

87. www.molinspiration.com, *Cheminformatics Molinspiration Ulica*.

Chapter 3

3. Peptide supramolecular gelator solution phase

3.1. Abstract

The investigation of the solution phase of the 2NapFF gelator at 25 °C and pH 10.5 was carried out with surface tension, ^{1}H-NMR spectroscopy, rheology, conductivity, UV-Vis spectroscopy, optical microscopy and laser scanning confocal microscopy (LSCM). A tentative model for phase diagram of the 2NapFF solution phase suggests a range of micellar transformations with an increase in concentration from free-surfactant, spherical aggregate phase, worm-like micellar phase and packed worm-like micellar phase. This solution behaviour is similar to some surfactants.[1,2] The main 2NapFF solution phase above a concentration of 0.5 wt% was found to be the worm-like micellar phase. However, in this phase, if the temperature is increased from 15 °C to 45 °C, the ^{1}H-NMR spectroscopy suggested that the sample can go from a more densely packed micellar phase to a more mobile micellar phase. The identified critical micellar concentration or critical aggregation concentrations of 17 gelators solution phase suggested that this information could be used to predict the possibility of a set of gelators solutions to form hydrogels above a particular concentration. This prediction is possible because the 2NapFF results shown a correlation between the presence of densely packed micellar structures in the solution phase and the formation of strong hydrogels. Also the minimum gelation concentration for 2NapFF is in between the first and the second critical micellar concentrations.

Disclaimer: This chapter was written with a significant portion of the results presented in our recent publication Cardoso *et al*. Soft Matter 2016, although not exclusively with those results.

3.2. Introduction

The first step in hydrogel preparation is typically dissolving the gelator in water. Here, we refer to the resulting solution as the solution phase. For the preparation of gels by a pH-switch (Chapter 2, Fig. 2.3) or salt-switch (Chapter 4, Section 4.2), this solution is prepared by dissolving the gelator at an alkaline pH.[3,4] In order to dissolve the gelator, the initial pH is necessarily above its apparent pK_a. Hence, the carboxylic group at the *C*-terminus of the gelator's peptide sequence is deprotonated and forms polar interactions with water. Hence, the gelator is solubilised. The apparent pK_a of the peptide gelators used in this study are between 5.0 and 8.9 (Chapter 2, Table 2.1). Thus, in high pH conditions (pH ≈ 10.5), they are deprotonated and negatively charged.[5–7] In the field of peptide supramolecular hydrogels, the solution phase itself has generally received little attention, as research has mostly focused on the final hydrogel properties. However, in some cases, solution phase properties were found related to hydrogel properties. One case is the gelator's critical micellar concentration (cmc) link with the apparent pK_a.[8] Accordingly, the link between higher hydrophobicity (lower solution cmc) and higher apparent pK_a of a gelator permits the prediction of the pH at which a gel is formed. In other words, if the solution hydrophobicity is higher or the cmc is lower, then the higher it will be the pH we can get a hydrogel made from N-protected dipeptide gelators. Therefore, understanding in greater detail the solution phase of a gelator may reveal important features of hydrogel formation.

The general structure of the peptide-based supramolecular gelators studied here is a peptide sequence (e.g. with both hydrophilic and hydrophobic regions) with a hydrophobic *N*-protecting group. These structural features are typical of surfactants. However, the surfactant character of peptide-based gelators is, in most cases, not taken into account in discussing self-assembly. The amino acids used in this study have hydrophobic side chains or no side chains (glycine).

Surfactants in water form nanostructures that can be classified as micellar phases. The formation of structures is dependent on monomer solubility. Several factors,

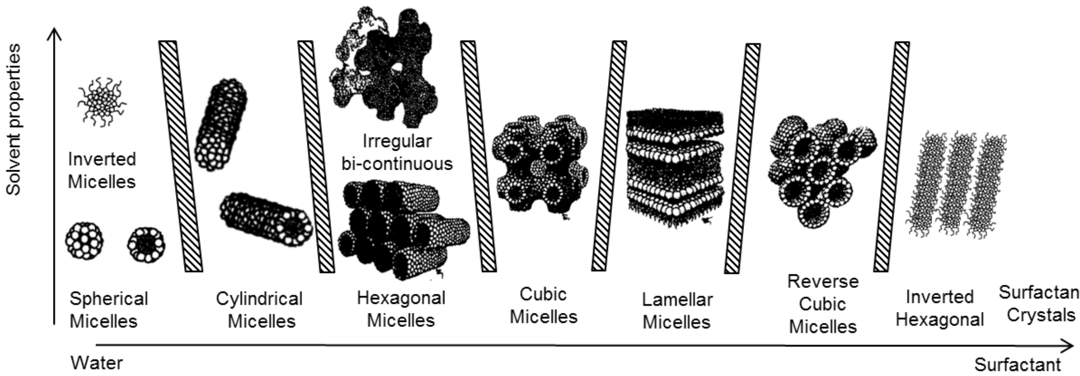

Figure 3.1 – Schematic Phase diagram of a simple surfactant in a water system, adapted from Davis *et al.*[2] The dashed regions illustrate the transition regions between the adjacent phases. The micellar phases are drawn in a concentration axis from low concentration (left) to high concentration (right) of surfactant molecules. The y-axis represents micellar variations dependent on the solvent properties (i.e. water). Reprinted with permission Elsevier Limited.

such as the size of the hydrophobic (or hydrophilic) regions of the tail (or head) group or the hydrophobicity of each of these groups, can influence the kind of micellar structure the surfactant forms.[2] Israelachvili developed a mathematical model to predict the main nanostructures formed depending on the packing parameter (PP) of the surfactant.[9] The surfactant concentration is also a key factor to control the surfactant structure formed. Figure 3.1 (adapted from Davis *et al.*) shows a typical phase diagram as a function of concentration.[2] Similarly to the concentration dependent structure, the PP is a predictive tool that postulates that a surfactant molecule in water has a specific set of structural parameters, therefore forms a specific structure at low concentrations. The PP is the ratio between the hydrocarbon tail volume (V_T) and the product of the optimum head group area (a_0) and the critical hydrocarbon length (l_C), in Equation 3.1.

$$Packing\ Parameter\ (PP) = \frac{V_T}{a_0\, l_C} \qquad \text{Equation 3.1}$$

According to equation 3.1, the nanostructures formed by surfactants with PP values below 1/3 should be spherical micelles or an isotropic solution of the surfactant monomer. Above this PP value, the nanostructures formed can have cylindrical, hexagonal, cubic, among other micellar phases.[9]

Upon dissolving a surfactant in water, the liquid-air interface saturates and a small amount of surfactant in water forms an isotropic solution of surfactant monomers.[2] With further addition of surfactant molecules to the solution, these could form micellar structures (e.g. spherical micelles or worm-like micelles) above a concentration called the critical micellar concentration (cmc_1). In some cases, some surfactants have a second cmc (cmc_2).[10–14] In these cases, the surfactant molecules form another structural micellar re-arrangement (Fig. 3.1). Some surfactants could form cylindrical micelles or worm-like micelles above the cmc_1.[15] In the past 15 years, multiple and exclusive phases have been identified for each surfactant: e.g. hexagonal, ribbon-like, star-like, amongst others.[15] The micellar systems are not only influenced by concentration but also by temperature, salts and other additives that change the solvation of the surfactant structures formed.[2] Similar results have been confirmed recently for peptide hydrogels.[7,16,17] However, the low molecular weight gelators used in this study are significantly different in structure to typical surfactants. The most common surfactants (e.g. sodium dodecyl sulphate, SDS) have a carbon tail (hydrophobic) and a charged group (hydrophilic). The peptide gelators used in our study are typically rich in hydrophobic groups also across the peptide backbone and have a negatively charged carboxylic group at high pH (hydrophilic). The significantly different molecular structure of peptide gelators in a basic solution cannot be described by the use of the PP described above to predict their behaviour in solution.[9]

A range of methods can be used to characterise surfactants (Fig. 3.2). As mentioned above, cmc is a key parameter to identify the surfactant behaviour.

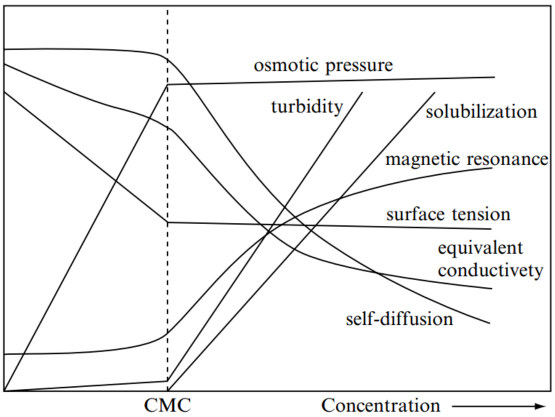

Figure 3.2 – Schematic of the measurement of some physical properties of solutions of a micelle-forming surfactant as function of the concentration. Redrawn from K Holmberg, B Jönsson, B Kronberg, B Lindman, Surfactants and polymers in aqueous solution, 2nd edition (1998) John Wily and Sons Ltd., reprinted in Oct 1, 2002, reproduced with permission.

Recent research suggests that the pre-gelation phase of protected dipeptide gelators is a surfactant system.[3,4,8] Our group has identified the cmc for a range of these gelators[8] and assigned the solution phase state to the formation of either free-flowing solutions or viscous solutions.[3,4] These behaviours were ascribed to the formation of spherical aggregates and worm-like micelles, respectively.[3,4] For example, 2-naphthalene-diphenylalanine (2NapFF, Fig. 3.3), at high pH and at a concentration of 0.5 wt% forms a viscous solution and this was identified as a worm-like micellar phase.[3] Furthermore, we have found that these worm-like micelles can be aligned at high pH.[18] It is then possible to gel the aligned solutions with a salt-switch method.[18] These solutions result in hydrogel formation when calcium is added. Further explanation of this process is given in Chapter 4. These naphthalene-protected dipeptides have a similar behaviour to peptide-amphiphiles (PAs), formed by the linkage of oligopeptides with an alkyl tail. Both form structures at high pH and hydrogels following the addition of salts.[19–24] It has been suggested that PAs form worm-like micelles in solution.[25] Finally, Wallace at al. found by NMR spectroscopy measurements that the aqueous solution of 2NapFF at 0.5 wt% at pH 10 has a larger mesh size that the 1.0 wt% solution.[26]

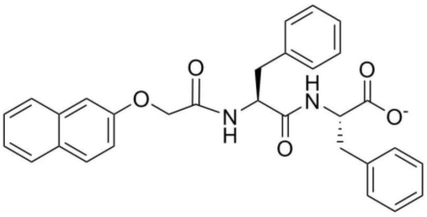

Figure 3.3 – Molecular structure of deprotonated 2-naphthalene-diphenylalanine (2NapFF).

Within this Chapter, in order to clarify the behaviour of 2NapFF in solution, the characterisation of the phase diagram of 2NapFF at 25 °C and pH 10.5 over a concentration range of 0.001 to 1.0 wt% is discussed.[3,4] A range of techniques, such as rheology, spectroscopy, microscopy and conductivity measurements, were used to the study of the 2NapFF solution phase. Following this, the phase diagram is explored at other temperatures by ^{1}H-NMR spectroscopy. Finally, the common surfactant features of this class of dipeptide gelators were evaluated in an exploratory study of 17 related gelators investigating their solution phase properties at 0.1 and 0.5 wt%.

3.3. Results and Discussion

To examine the solution phase of peptide gelators, focus is given to 2NapFF as it has been shown to form worm-like micelles at 0.5 wt%.[3,4] This gelator has been extensively investigated by our group and shown to be able to form hydrogels with a variety of methods.[3,8] As highlighted in Chapter 2, the gelator BrNapAV was also shown to form worm-like micelles but only under specific conditions, with CO_2 and a final pH (pH_f) close to its apparent pK_a. 2NapFF can form gels at one of the lowest reported minimum gelator concentration (mgc, 0.02 wt%) as determined by the inversion vial test.[27] In this test, vials with different gel concentrations are simply turned upside down and if the sample does not flow and fall, the sample is said to be a gel. The lowest of these concentrations is the mgc. Thus, a mgc of 0.02% for 2NapFF means that water is trapped in the hydrogel phase up to a 99.98 wt% Furthermore, 2NapFF hydrogels have shown some of the highest mechanical properties reported for naphthalene dipeptide gelators.[8] The high apparent $pK_a = 6.0$ of 2NapFF allows gelation at pH_f values below pH = 6.0, a high value when compared with less hydrophobic gelators.

3.3.1. The 2NapFF solution phase transition concentrations

Firstly, the critical micellar and aggregation concentrations (cmc and cac) of the 2NapFF solution phase (Fig. 3.3) were investigated. These concentrations are the transition points between different micellar phases.

3.3.1.1. Tensiometry to identify the transition concentrations

Tensiometry is a commonly used technique to study the cmc of a surfactant. A high throughput Kibron Delta-8 Surface Tensiometer using a Du Nouy-Padday method (maximum pull on a rod) measured the surface tension in 6 parallel measurements (Fig. 3.4a).

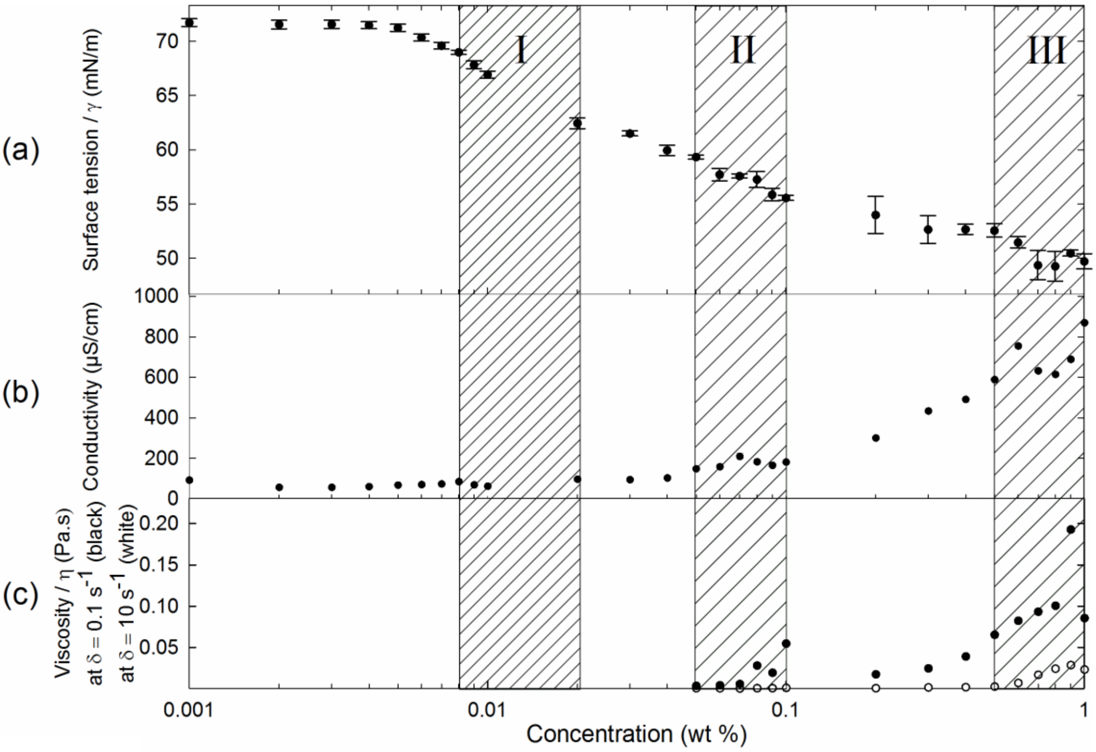

Figure 3.4 – Characterisation of 2NapFF solution micellar states at pH 10.5 ± 0.5 by (a) surface tensiometry, (b) conductivity and (c) viscosity at shear rate of 0.1 s^{-1} (closed symbols) and 10 s^{-1} (open symbols). The concentration is plotted in a logarithmic scale. Each hatched region represents three different micellar transitions of the peptide solutions at high pH identified by the changes in the measured properties. The error bars represent the standard deviation of three measurements.

For this peptide gelator, the results obtained with tensiometry were not conclusive to identify the cmc. After the first starting plateau at the surface tension of water, the surface tension decreases, indicating the gelators are assembling at the liquid-air interface (Fig. 3.4a). However, a second plateau is not present through this measurement for this particular gelator. The transition point to the second plateau would indicate the 1st cmc (cmc_1). Only the air to water partition coefficient (K_{aw}) could be obtained from the transition from the first plateau to the decreasing surface tension (0.005 ± 0.0005 wt%). The K_{aw} is the ratio of the concentration of the gelator in the air by the concentration of the gelator in the water. This ratio indicates the difference in solubility of the compound in these two phases. The value of K_{aw} is proportional to the ratio between the number of molecules found in the bulk and the number of molecules found in the interface. The surface tensiometry is insufficient in this case to characterise the cmc of the 2NapFF solution phase. Surface tensiometry is a surface dependent method and together with the unconventional properties at the interface of some gelators, compared with a typical surfactant, may explain the different results obtained here for 2NapFF.[28] Therefore, a bulk measurement, such as solution conductivity, was selected to evaluate the cmc of 2NapFF. The conductivity of 2NapFF solutions across the same range of concentrations used in the tensiometry measurements is shown in Fig. 3.4b. A detailed analysis reveals a transition typical of a cmc in the concentration range from 0.008 to 0.04 wt% as indicated by a significant reduction in the rate of increase in conductivity with increasing concentration in the same range (Fig. 3.5a).

3.3.1.2. Conductivity to identify the transition concentrations

Contrary to the surface tension data, the conductivity data transitions for 2NapFF are typical for some surfactants' cmc transitions (Fig. 3.5a,b). For example, they are similar trends to our control experiment with SDS (Fig. 3.5c,d).[29] The exchange rate of OH^- with the electrode surface is reduced and the diffusion of OH^- slows down, as the micellar structures become the dominant species in solution.[27] The transition shown in Fig. 3.5a agrees with the surface tension result of micellar structure formation above 0.005 wt% (conresponding to K_{aw}). SDS at different concentrations was here measured by conductivity to validate this technique to identify the cmc_1 and cmc_2 in a demanding concentration region. The conductivity data for SDS shows a first transition, identified by other techniques to be from free-surfactant to spherical micellar structures.[29] In SDS, this is followed by a second transition from spherical micelles to worm-like micelles. These are the first two transitions in this system and a series of more complex transitions that can occur (Fig. 3.1). The conductivity data obtained here for 2NapFF shows a first transition at a concentration from 0.008 to 0.02 wt%, region I in Fig. 3.4. A second transition is shown in Fig. 3.5b, from 0.05 to 0.1 wt%, with a peak at 0.07 wt%. This transition is indicated as the region II in Fig. 3.4. This first and second transition can be assigned to a cmc$_1$ and a cmc$_2$, respectively. Linear fits to the data allowed an accurate quantification of the cmc, described below in the discussion of the 2NapFF phase diagram.

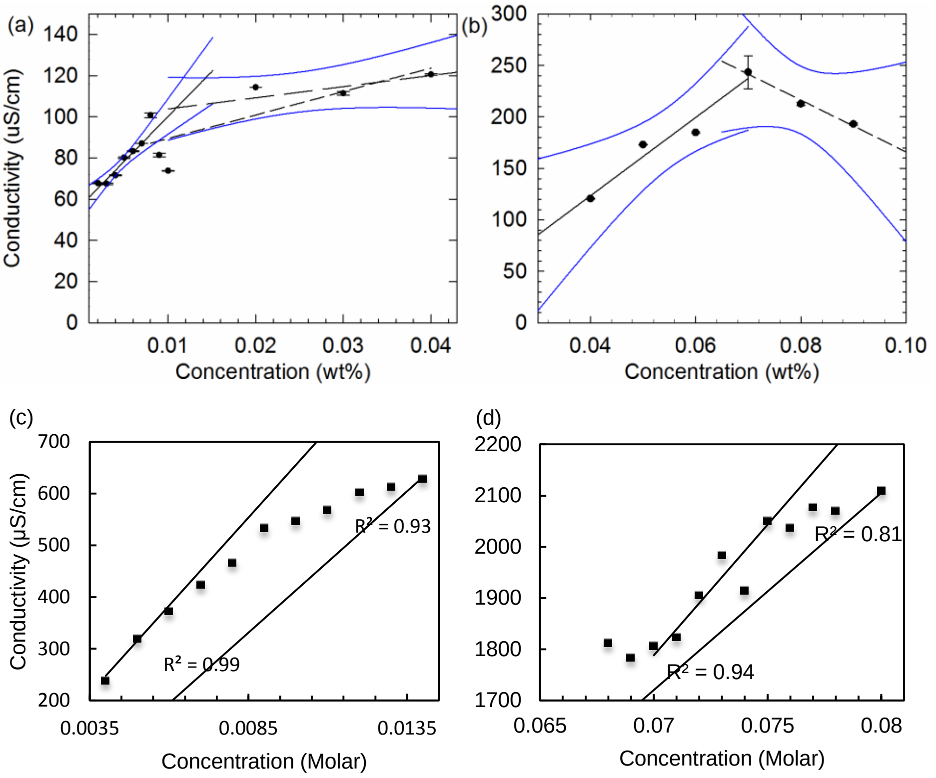

Figure 3.5 – Detailed analysis of the conductivity data as a function of concentration for 2NapFF at a pH 10.6 ± 0.2 (a, b) and SDS (c, d) at a temperature of 22.4 ± 0.7 °C. (a) Analysis of the first change in the rate of increase in conductivity, with linear regression fits to the regions between 0.002 and 0.007 wt% (solid line), 0.008 to 0.04 wt% (short dashed line) and 0.008 and 0.04 wt%, excluding 0.009 and 0.01 wt% (long dashed line). The first (solid line) and last (long dashed line) interval were used for obtaining cmc$_1$ = 0.011 ± 0.004 wt% (0.222 ± 0.075 mM). (b) Analysis of the second change in the rate of increase in conductivity with linear regression fits to the regions 0.04 to 0.07 wt% (solid line) and 0.07 to 0.09 wt% (dashed line). These fits were used to obtain a cmc$_2$ = 0.069 ± 0.015 wt% (1.39 ± 0.302 mM). For (a and b), all blue curves are delimiting the 95 % confidence intervals used for evaluating both cmc. The error bars represent the standard deviation of three measurements. (c, d) Conductivity measurements as a function of SDS concentration allow the findings of cmc$_1$ = 0.0086 ± 0.0010 mM and cmc$_2$ = 0.073 ± 0.003 mM, equivalent to literature values.[29]

3.3.1.3. Viscosity to identify the transition concentrations

As the conductivity transitions occur at low concentration, only the second transition was detectable by rheological measurements. The rheology measurements at low shears (0.1 s^{-1}) show a change in viscosity between 0.08 and 0.1 wt% (Fig. 3.4c, closed symbols). This agrees with the second transition suggested by conductivity. At high shear rates (10 s^{-1}), the viscosity only significantly increases above 0.5 wt% (Fig. 3.4c, open symbols). This mechanical response was described previously for similar systems as shear alignment.[25] Here, it occurs for low and high shear rates from 0.1 to 0.5 wt%. From 0.5 to 1.0 wt% a plateau appears. These rheological features are in agreement with our conductivity data top concentration range and suggest a structural arrangement is formed in the concentration range from 0.5 wt%

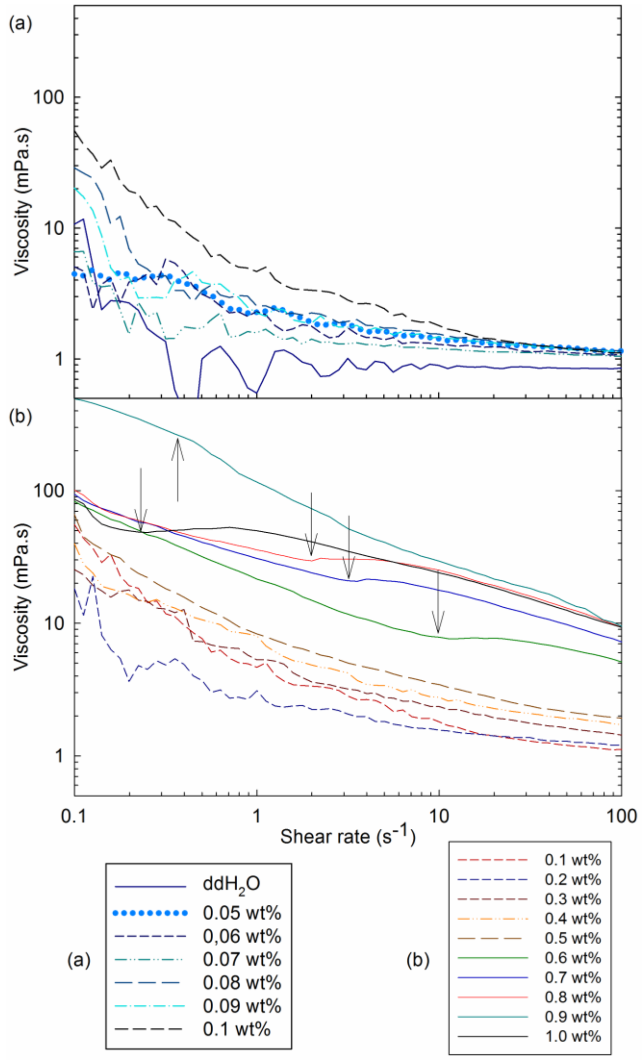

Figure 3.6 - Viscosity measurements for 2NapFF pre-gelation solution phase. (a) Subset of results for ddH$_2$O and concentrations between 0.05 and 0.1 wt% and (b) subset of results for concentrations between 0.1 and 1.0 wt% and ddH$_2$O. The arrows indicate the transition to a shear banding period in between the shear thinning regions.

to 1.0 wt%, indicated as region III in Fig. 3.4. For clarity in Fig. 3.6, the fully raw viscosity data between 0.05 and 1.0 wt% was plotted separately for lower (a) and higher concentration (b). From the viscosity data (supported by the microscopy data shown subsequently), in the region from 0.6 to 1.0 wt%, the micellar structures become increasingly strongly entangled. In this concentration region, a narrow plateau or slightly increase in viscosity is visible in between the overall shear thinning behaviour (Fig. 3.6). One interpretation for this plateau in viscosity is to assign it to a shear banding behaviour. Shear banding is a localized deformation that develops in a broad range of ductile materials. In this case, shear banding could occur because the solution flow close to the top plate of the rheometer measuring system becomes separate and at a different speed to the flow of the solution close to the bottom plate, therefore given the impression of a constant viscosity in a narrow region of shear rates (Fig. 3.6). At low shear rates, the sample first shows shear thinning behaviour. In Fig. 3.6b, a steady increase in absolute viscosity is shown as the concentration of 2NapFF increases from 0.2 wt% to 0.8 wt%. From 0.8 to 1.0 wt%, only a minor increase in viscosity occurs at high shear rates, above 10 s^{-1}, when compared with low shear rates. The lateral packing of different gelators and bundling have been associated to the formation of hierarchical structures.[32,33] In those works, it was speculated through cryo-scanning electron microscopy (cryo-SEM) imaging of nanostructures of a similar peptide gelator, that the increase in fibre size or bundling may be associated with the formation of hierarchical structures.[33] In their cryo-SEM images, it appeared that gelation to a lower pH lead to aggregation of fibrils or smaller bundles into larger bundles at later stages with pH-switched gelation. In their case, the network formed was of a denser network with rod-like interconnections. The further change in structure with increasing concentration is also influencing the mesh size.[26,27,34–36] Here, a decrease in mesh size, strongly bound entanglement points, stiffer fibres, larger bundles, among others, could possibly result in a significant increase in the viscosity. In Fig. 3.6, the viscosity at low shear rates has exceptional jumps at 0.9 wt% and 0.1 wt%. The 0.9 wt% overshoot increase in viscosity is likely associated with a structural or linkage change, among others (as suggested below using the microscopy images in Fig. 3.13).[31] This is sometimes referred to as bundling, which causes the micelles to relax the stress more slowly because the bundling adds further relaxation modes to the network.[31] Relaxation modes are shear-dependent breaking points in the structure. With an increase in concentration from 0.1 – 0.2 wt% to 0.5 wt%, the viscosity increases. This could be due to an increase in the number of worm-like micelles, increase in the length of the micellar structures or the degree of crosslinking.

3.3.1.4. Frequency and strain sweep rheology to identify the transition concentrations

Following the initial viscosity analysis, a full rheological characterization of the 2NapFF micellar solutions was attempted with a series of frequency-sweeps (Fig. 3.7 to Fig. 3.9) and strain-sweeps (Fig. 3.10 to Fig. 3.12) at fixed strain (0.5 %) and fixed frequency (10 rad/s), respectively, in the concentration range from 0.001 wt% to 1.0 wt%. The rheometer is near its lower torque limits below a concentration of 0.3 wt% under a 0.5 % strain and below a concentration of 0.04 wt% under a 10 rad/s frequency. The torque limitation and proximity to the water viscosity did not allow us to use strain-sweep, frequency-sweep and viscosity measurements to interpret conclusively the solution rheological features below these concentrations (0.3 wt% frequency-sweeps and 0.04 wt% strain-sweeps). However, at some strains (0.5 %) in the frequency-sweeps at 10 rad/s (Fig. 3.9) and at some frequencies (10 rad/s) in the strain sweep at 1 % (Fig. 3.12), the measurements did allow us to pick up readings of storage modulus (G′) and loss modulus (G″) across the concentration region tested 0.001 wt% to 1.0 wt%.

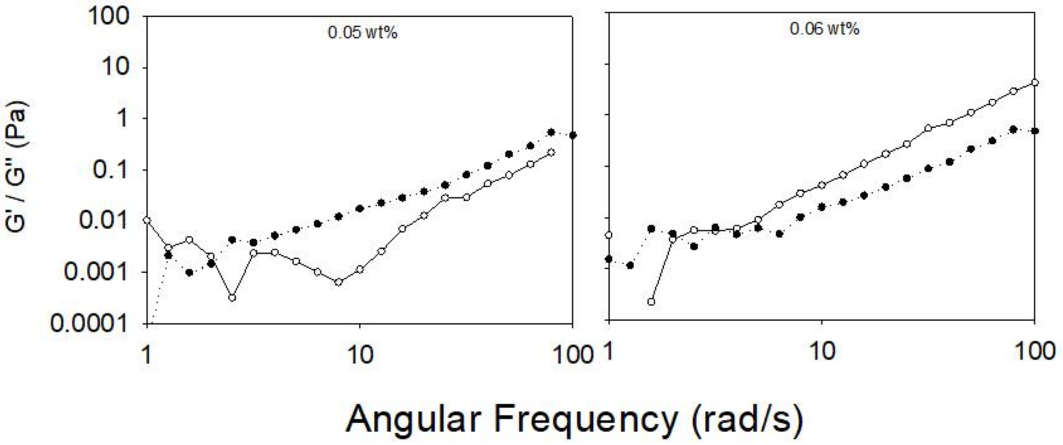

Figure 3.7 – Frequency sweeps, at a strain of 0.5 %, of solutions of 2NapFF at 0.05 wt% and 0.06 wt% at pH 10.5. The storage modulus (G′, filled circles) and loss modulus (G″, empty circles) are plotted as function of the angular frequency. Each plot was only measured once with each point based on an average obtained from 40 repeat measurements within 5% tolerance, with all data collected with 10 points per decade. The set of measurements at the torque limits from 0.001 wt% to 0.04 wt% are shown in the appendix (Fig. 3.25).

In this case, the rheometer feedback measuring system was in the threshold of acceptability for most measurements and close to the torque limit (5 mN.m) at concentrations below a concentration of 0.3 wt% (frequency-sweeps) and

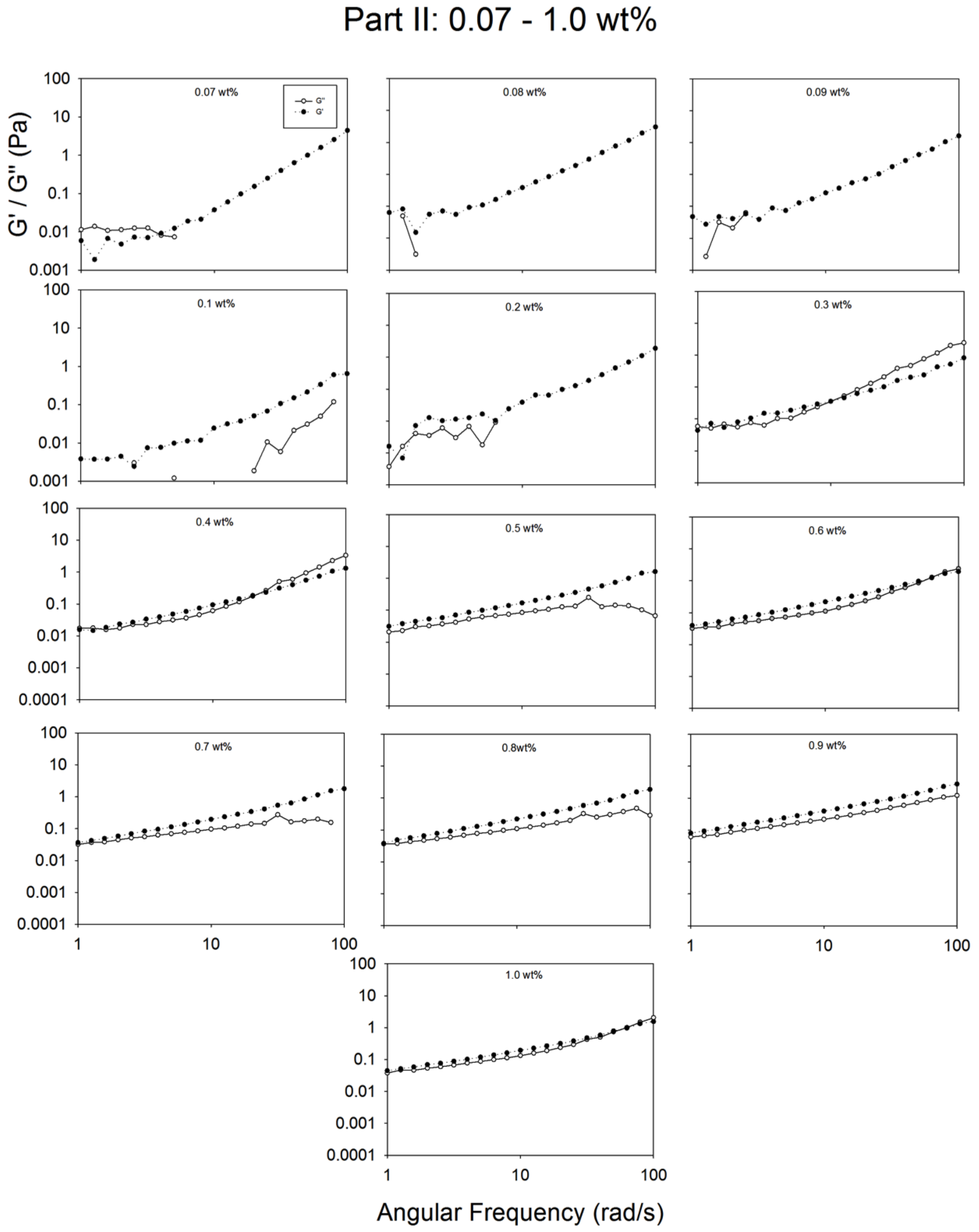

Figure 3.8 – Frequency sweep, at a strain of 0.5 %, of solutions of 2NapFF from 0.07 wt% up to 1.0 wt% at pH 10.5. The storage modulus (G′, filled circles) and loss modulus (G″, empty circles) are plotted as function of the angular frequency. Each plot was only measured once with each point based on an average obtained from 40 repeat measurements within 5% tolerance, with all data collected with 10 points per decade. Some points are omitted because the rheometer could not pick up the G″ under those measurement conditions.

below 0.04 wt% (strain-sweeps). It is likely that other strain-sweep and frequency-sweep conditions could be changed to avoid being in the torque limits for the less concentrated solutions, for example, at higher fixed strains or frequencies. However, our initial rational for the choice of strain and frequency conditions was to have a comparative platform with the conditions adequate to measure the corresponding hydrogels (studied in Chapter 4) as well as compare with previous research.[8]

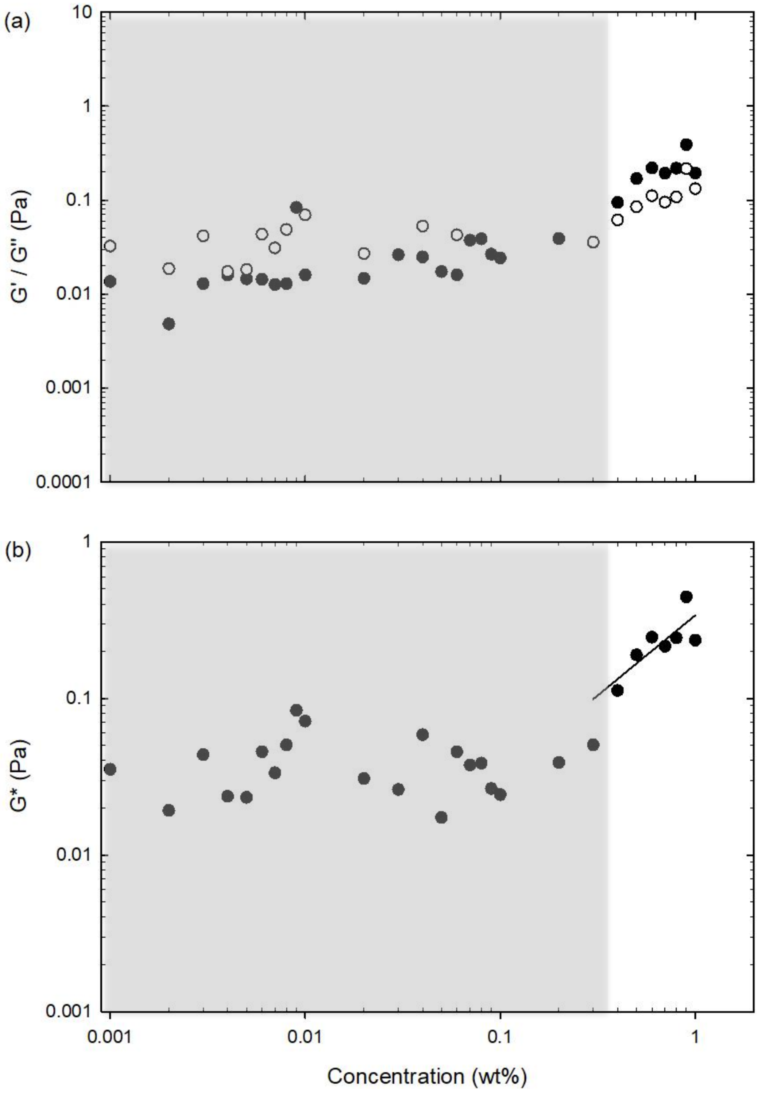

Figure 3.9 – Summary of frequency sweeps analysis of 2NapFF solutions from 0.001 wt% up to 1.0 wt% at pH 10.5 with stain of 0.5 % and frequency of 10 rad/s. Readings of absolute values were taken from the frequency of 10 rad/s of the solution frequency-sweep plots. Shear modulus (G′, black) and loss modulus (G″, white) are plotted against concentration (a) and the corresponding complex modulus (G*) is also plotted against concentration (b). A power exponent of 1.03 was obtained from the fit to the concentration region from 0.3 to 1.0 wt%. The grey area is in the rheometer torque limits.

Analyses of G′ and G″ from the frequency sweeps at a frequency of 10 rad/s, shown in Fig. 3.9a, and calculation of the complex modulus (G*). In Fig. 3.9b, obtained from the frequency-sweep measurements above, there is a possibly that the increase of G* from 0.1 wt% to 0.5 wt% is related with the second cmc assigned to the conductivity data (cmc_2 = 0.05 – 0.1 wt%). Also, it is possible that the plateau observed in G* from 0.5 wt% to 1.0 wt% is related to the critical aggregation concentration (cac) suggested also from the plateau observed in the conductivity in the same region and the increasing viscosity data (Fig. 3.6).

Equivalent analyses of the strain sweep data (obtained at a frequency of 10 rad/s) suggest only one transition (cac = 0.5 wt%, when this data is combined with microscopy data). The strain sweeps are shown in Fig. 3.10 and Fig. 3.11 and the analyses of the G′ and G″ with these strain-sweeps are shown in Fig. 3.12.

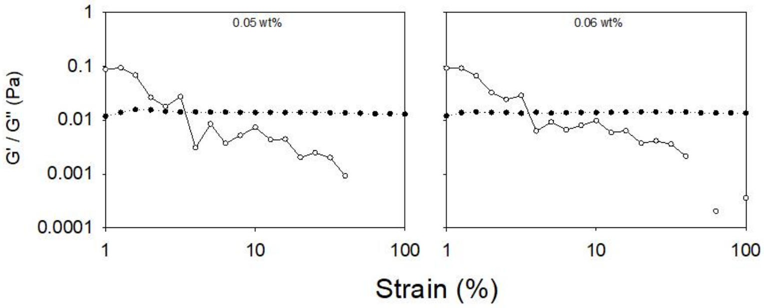

Figure 3.10 – Strain Sweeps, at a frequency of 10 rad/s, of solutions of 2NapFF at 0.05 wt% and 0.06 wt% at pH 10.5. The storage modulus (G′, filled circles) and loss modulus (G″, empty circles) are plotted as function of the strain applied. The full set of measurements at the torque limits from 0.001 wt% to 0.04 wt% are shown in the appendix (Fig. 3.26).

In is important to note for the comparison with the hydrogel phase, in Chapter 4, both plots of the strain-sweep and the frequency sweep have given exponent coefficient of 1.03 and 1.04, respectively, for the G* to concentration dependence.

3.3.1.5. Cross-polarised optical and confocal microscopy to identify the transition concentrations

Birefringence is the optical property observed in a material when the polarization and direction of light affects the refractive index of the material. Anisotropic materials are birefringent because they have aligned domains.[25,37] Solution phases of 2NapFF samples from 0.5 to 1.0 wt% are birefringent under cross-polarized light (Fig. 3.13a). At these concentrations, the results concur with the formation of a hierarchical structure, possibly bundles of worm-like micelles. These birefringent domains are approximately 100 μm to over 1 mm in fibre length and this effect increases with concentration. A network of worm-like structures was identified by confocal microscopy using a Nile blue staining technique (Fig. 3.13b) for concentrations above 0.1 wt%. In Fig. 3.13, the image of 2NapFF at 1.0 wt% shows an increase in the microstructural packing of the network of worm-like micellar structures as compared to lower concentrations. The contrast of structures-to-background of this raw image (1.0 wt%) is higher than the ones with 0.3, 0.5 wt% and 0.1 wt%. In the 0.05 and 0.1 wt% images, spherical aggregates appear to be present in the solution,

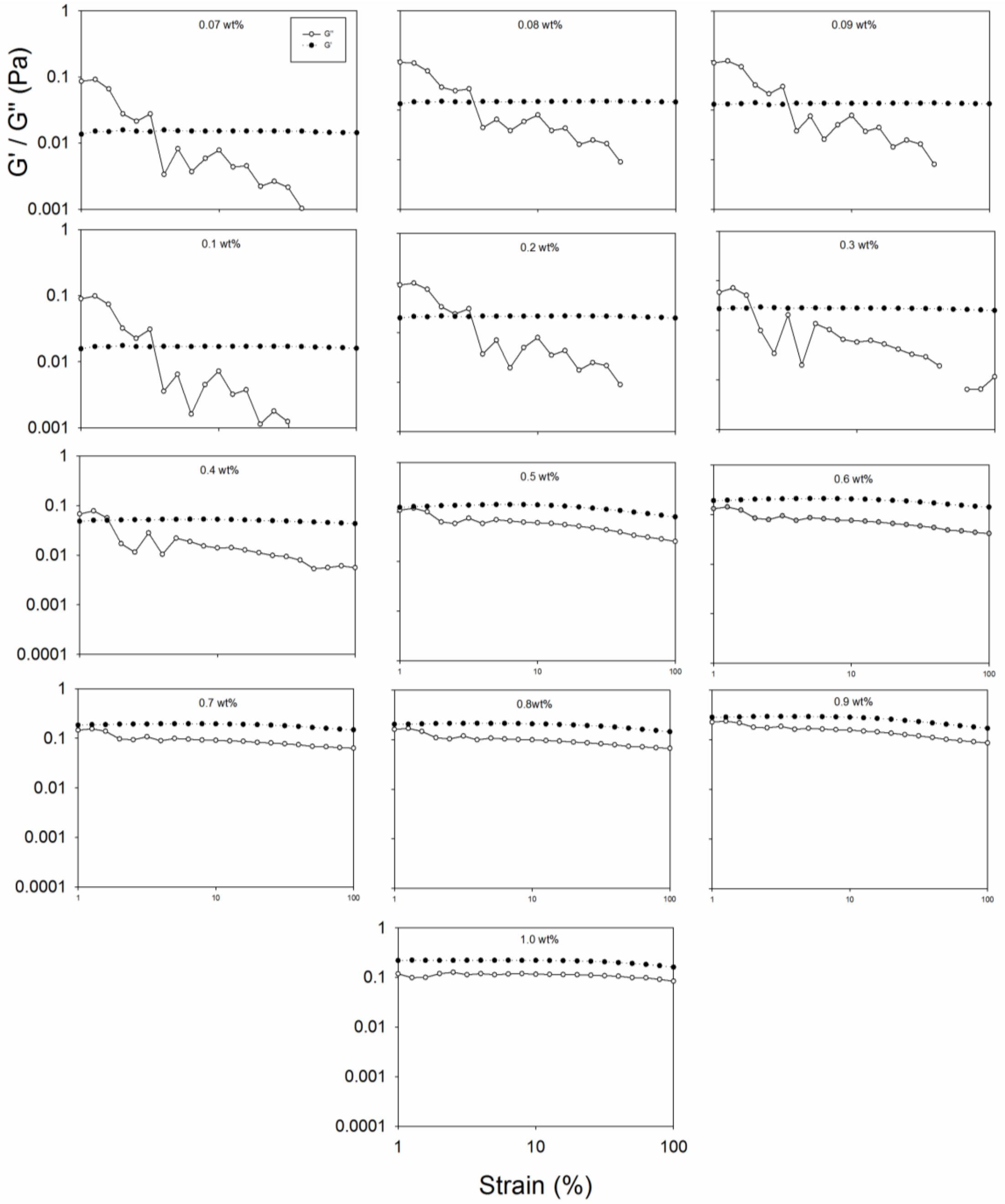

Figure 3.11 – Strain Sweeps, at a frequency of 10 rad/s, of solutions of 2NapFF from 0.07 wt% up to 1.0 wt% at pH 10.5. The storage modulus (G′, filled circles) and loss modulus (G″, empty circles) are plotted as function of the stain applied. Some points are omitted because the rheometer could not pick up the G″ under those measurement conditions.

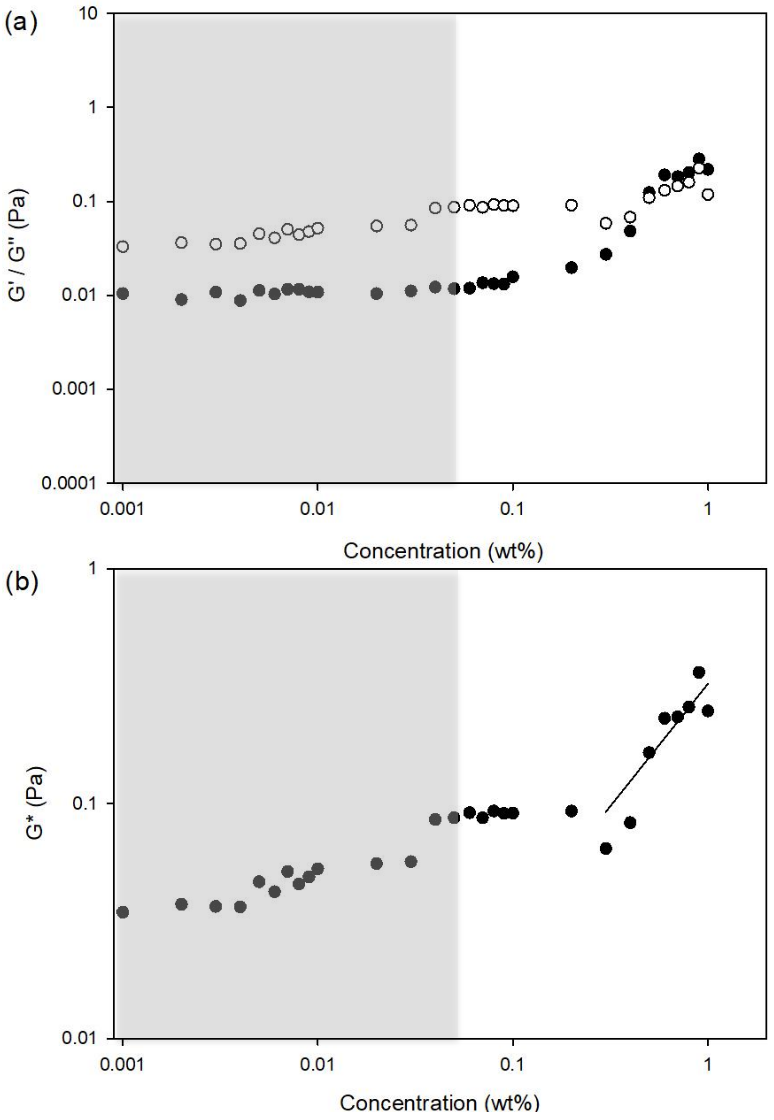

Figure 3.12 – Strain Sweeps analysis of solutions of 2NapFF solutions from 0.001 wt% up to 1.0 wt% at pH 10.5 with frequency of 10 rad/s and 1 % strain. Readings of absolute values were taken from the 1 % strain of the solution strain sweep plots. Shear modulus (G′, black) and loss modulus (G″, white) are plotted against concentration (a) and the corresponding complex modulus (G*) is also plotted against concentration (b). A power exponent of 1.04 was obtained from the fit to the concentration region from 0.3 to 1.0 wt%. The grey area is in the rheometer torque limits.

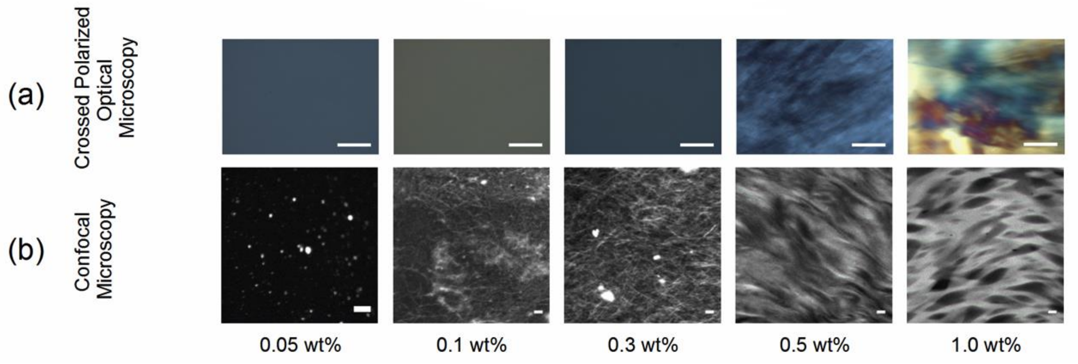

Figure 3.13 – Microscopy images of 2NapFF at pH 10.5 ± 0.5 and approximately 25 °C with concentrations of 0.05, 0.1, 0.3, 0.5 and 1.0 wt%: (a) cross-polarised optical microscopy (scale bar: 500 µm) and (b) confocal microscopy measurements in Nile blue staining (scale bar: 20 µm).

but the resolution of the images is not sufficient to interpret the nature of these structures. We hypothesise that at these concentrations of 2NapFF the Nile blue in solution has no suitable hydrophobic regions to bind with 2NapFF and so suggest the spherical structures in the images are Nile blue aggregates.

3.3.1.6. ^{1}H-NMR and UV-Vis spectroscopy to identify the transition concentrations

^{1}H-NMR spectroscopy is a non-invasive magnetic resonance technique used here to characterise and identify the micellar phases. Even with the concentration detection limits of the technique, it was still possible to determine and study the phase transitions at concentrations from 0.05 to 1.0 wt%, because of the proton resonance sensitivity to the molecular environment. Under optimised conditions (see Section 3.6.3), we can measure the change in the chemical shift of each proton of 2NapFF as a function of concentration (Fig. 3.14a) and quantify the percentage detectable by solution state NMR spectroscopy (Fig. 3.14b). Since the assigned aromatic naphthalene peaks show the greatest change in chemical shift of all 2NapFF protons, the peak corresponding to the proton in position-7 of the naphthalene aromatic ring was selected to monitor the changes in chemical shift and to calculate the percentage of 2NaphFF NMR detectable. The chemical shifts of the naphthalene protons move significantly upfield when the concentration increases from 0.1 wt% up to 0.5 wt%, which implies that aggregation is occurring. The chemical shift becomes constant

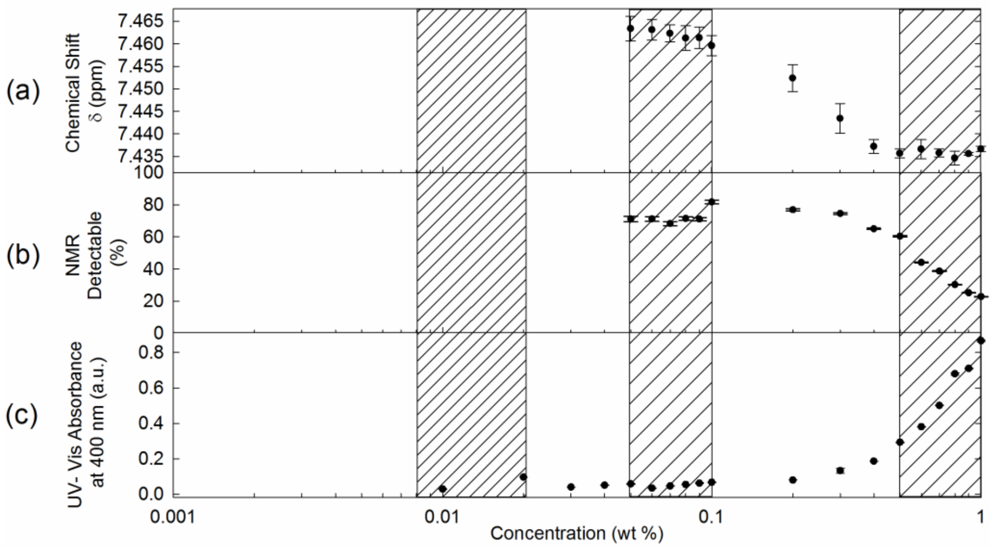

Figure 3.14 – ^{1}H-NMR (a and b) and UV-Vis spectroscopy (c) analysis of 2NapFF micelle solutions. The chemical shift (a) and quantification of NMR detectable percentage (b) were measured at the 7th proton in the 2NapFF naphthalene group.

above 0.5 wt%, while the percentage NMR detectable continues to decrease. This data indicates a phase change between 0.05 wt% to 0.1 wt%, in agreement with our conductivity and microscopy data.

Complementarily, UV-Vis spectroscopy measurements were used to investigate the phase transitions in the 2NapFF solution phase (Fig. 3.14c). The results showed that only above 0.1 wt% does the turbidity gradually increase up to a concentration of 0.4 wt%, after which there is a rapid increase from 0.5 to 1.0 wt%. This result supports the hypothesis suggested by the confocal microscopy data that in the concentration region from 0.1 to 1.0 wt%, the worm-like structures bundle into larger, possibly hierarchical, structures which scatter significantly.

All these attempts to understand the cmc's, cac and the present literature results can be summarised with a phase diagram under the set of conditions studied.

3.3.2. Phase Diagram of 2NapFF solution at pH 10.5 and 25 °C

Taking all of the data from the techniques presented above into account, distinct solution phases and transition regions can be identified. First, the 2NapFF molecules initiate the self-assembly at the liquid-air interface at a concentration of 0.005 wt% ± 0.0005 wt% (0.101 ± 0.010 mM). Secondly, based on a time-lapsed cryo-TEM of similar peptide gelators 2NapFG[3] and FmocLG[38] where spherical micelles are present at high pH, an educated guess can be made on the structures formed here with 2NapFF. In this second transition, a transient spherical micellar structures form and become the dominant phase after the 1st cmc (cmc_1) at 0.011 ± 0.004 wt% (0.222 ± 0.075 mM). This value is amongst the lowest reported in the surfactant database of the USA national standard reference data system.[1] Very similar peptide hydrogel systems have similarly low cmc_1 as it is shown in the appendix Table 1 from Du et al review.[32] The first transition (cmc_1) was difficult to obtain with more accuracy because of the limited sensitivity of the available techniques at these concentrations. Based both on the cryo-TEM studies mentioned above and SANS parallel study I have collaborated with,[54] it is likely that we have a sphere-to-worm-like transition on a 2nd cmc because the SANS data suggests that at 0.3 wt% there are two phases present, one that can be fitted to a worm-like model and a second that can not be discriminated which could be the spherical micellar phase.[54] Therefore, with an increase in concentration, the spherical micellar structures could self-assemble to form elongated worm-like micellar structures. This transition is assigned to a 2nd cmc

(cmc_2) at 0.069 ± 0.015 wt% (1.39 ± 0.302 mM). These two cmc values were estimated based on an in-depth analysis of conductivity measurements as discussed above (Fig. 3.5a and 3.5b). At approximately 0.08 wt%, the viscoelastic nature of the solution phase observed in the frequency- and strain-sweep rheological data suggests the initial formation of elongated worm-like micellar structures (after the 2nd cmc). At the start of this phase, this micellar phase is expected to coexist with the previous phase because of the maximum observed in the rheology measurements and the ^{1}H-NMR spectroscopy transition (Fig. 3.14a and Fig. 3.14b). At 0.5 wt% (10.1 mM), the worm-like micellar structures become dominant in the solution and they entangle as the concentration is increased further. These entanglements form micellar networks with increasing viscosity (Fig. 3.6) and higher levels of packing (Fig. 3.14c). This is in agreement with the conductivity data and the assignment of a critical aggregation concentration (cac) at 0.5 wt%. With further increase in concentration, more compact assemblies of worm-like micellar structures are formed. Hence, the data is consistent with three transitions: (1) free molecule to spherical micellar phase (cmc_1), (2) spherical micellar phase to worm-like micellar phase (cmc_2); and (3) worm-like micellar phase to a bundled worm-like micellar phase (cac). A schematic of the phase diagram at 25 °C is shown in Figure 3.15.

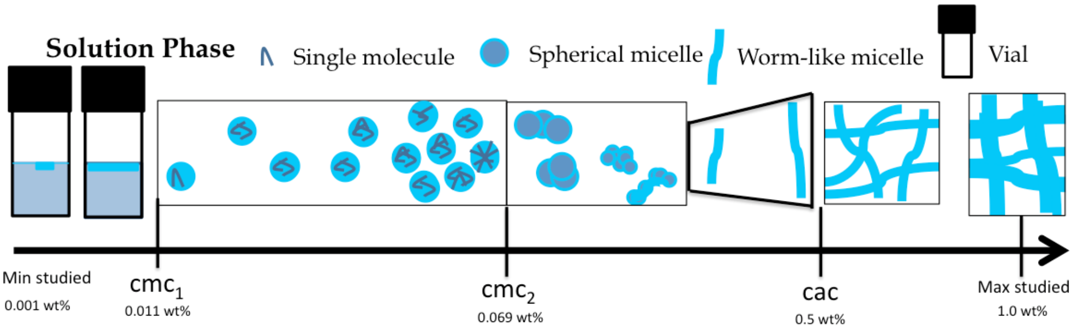

Figure 3.15 – Proposed scheme of the phase diagram of 2NapFF at 25 °C and pH 10.5 including the transition concentrations found by our experiments and the model structures.

3.3.3. Temperature-dependent transitions of 2NapFF by ^{1}H-NMR for concentrations between 0.05 and 1.0 wt%

The analysis of the phase diagram of the 2NapFF solution phase by means of different techniques proved challenging because each technique may not completely or accurately represent the nature of the phenomena we intend to measure. ^{1}H-NMR spectroscopy was found to be a robust, readily available and easily reproducible technique. A limitation is the requirement of a signal-to-noise ratio of 1/1000 that could only be guaranteed above a concentration of 0.04 wt% and under a particular set of experimental conditions (Section 3.5). Following its use at 25 °C, a temperature-variable ^{1}H-NMR spectroscopy was used to access the phase diagram of 2NapFF at a range of temperatures from 15 to 45 °C.

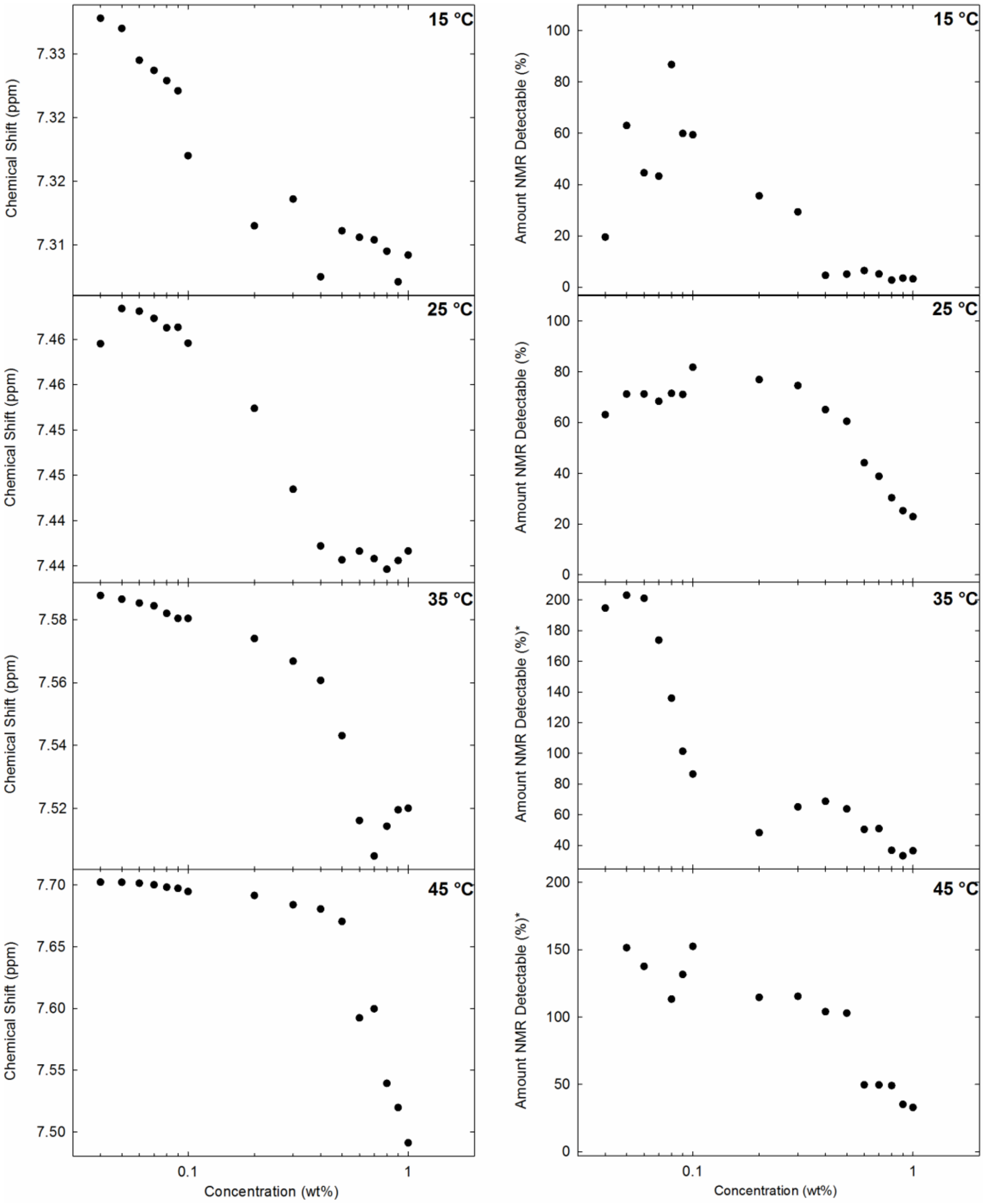

Figure 3.16 – ^{1}H-NMR spectroscopy studies: chemical shift and amount of 2NapFF detectable at pH 10.5, at 15, 25, 35 and 45 °C for the concentration range from 0.04 to 1.0 wt%. These results were calculated using the NMR spectroscopy peak from the 7th proton of the naphthalene group and were calibrated against a pre-calibrated ethanol reference capillary. Note that the graphs of the amount NMR detectable signal with 35 and 45 °C have different scales on the y-axis to accommodate values out of the expected range.

Samples of 2NapFF from 0.04 to 1.0 wt% in H_2O were placed in a ^{1}H-NMR tube with a reference capillary containing a calibrated amount of ethanol in D_2O (see Section 3.5 for further details). It is important to note that the 2NapFF micellar phase was only in the H_2O solution around the capillary. Therefore, the results were comparable with our data obtained with other techniques. The temperature was controlled using a thermostatted probe with a liquid nitrogen source and a heating coil. Each set of results for each sample at a specific concentration consisted of (1) the chemical shifts for each proton of 2NapFF and (2) quantification of the amount of 2NapFF detected, as a percentage of the total amount. As explained above, the proton of the naphthalene group in position-7 was also used here to look at the change in molecular environment of the 2NapFF. The change in chemical shift of this proton and the percentage of 2NapFF detectable at pH 10.5 is plotted against concentration (from 0.04 to 1.0 wt%) in Fig. 3.16, at 15, 25, 35 and 45 °C. A 5% error is expected in all the integrations of ^{1}H-NMR spectra from statistics of the data shown above (Fig. 3.14b). ^{1}H-NMR spectroscopy studies of the solution phase at different temperatures allowed us to draw an extended picture of the 2NapFF phase diagram (Fig. 3.18). These analyses consisted in evaluating where the transition points and plateau regions were found for each temperature. The amount NMR detectable is calibrated by identifying the peak area of a known amount of L-alanine (standard), at 25 °C, considering this corresponds to 100% visible with the same NMR method (Section 3.5.3). Hence, the amount NMR detectable is taken qualitatively for samples measured at temperatures above 25 °C. This is likely the reason why the normalized percentage is above 100 % for these temperatures. For future research, it is advisable that standards at different temperatures have to be calibrated as well if qualitative data is required.

Micellar solutions can undergo phase transitions with a temperature change,[39] since the hydrophobicity and hydrogen bonding change the energy of scission of the micellar structures.[40] Figure 3.17a shows the chemical shift as function of temperature at concentrations 0.1, 0.5 and 1.0 wt%. The overall trend shows that the chemical shift increases linearly with temperature for 0.1 and 0.5 wt%. This indicates that the molecular environment of 2NapFF becomes less hydrophobic with an increase in temperature. However, the increase in concentration, to 1.0 wt%, reduces the temperature dependence of the chemical shift (Fig. 3.17a, dashed line).

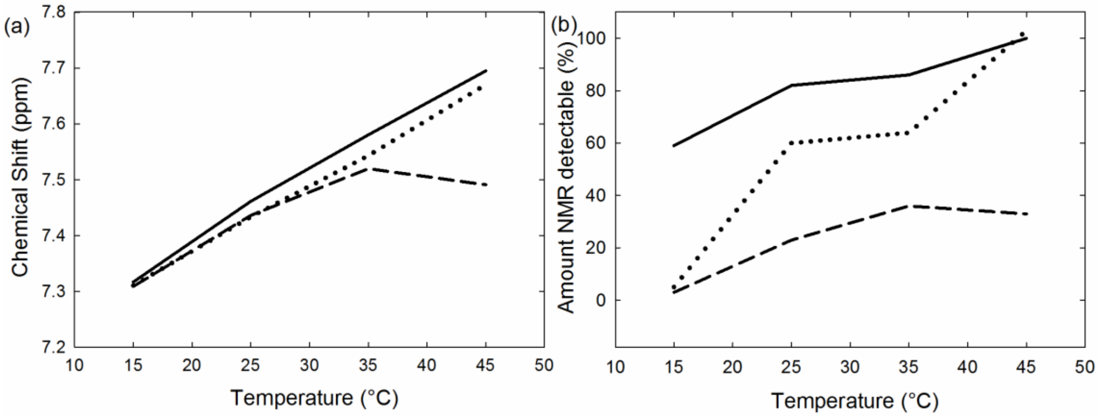

Figure 3.17 – Temperature dependent ^{1}H-NMR spectroscopy studies. Chemical shift (a) and amount NMR detectable (b) are plotted as function of temperature at 0.1 wt% (solid line), 0.5 wt% (dotted line) and 1.0 wt% (dashed line).

Equally, the percentage of 2NapFF detectable by NMR spectroscopy decreases with increasing concentration. The micellar phases appear to be more stable at 0.1 and 1.0 wt% across this concentration range and not at 0.5 wt% (Fig.17b, dotted line). The percentage detectable of 0.5 wt% increases from approximately 0 % to 100 % as temperature increases. It is observable that the 1.0 wt% has a broad range of stability as opposed to the 0.5 wt% or 0.1 wt% in Fig. 3.17a and Fig. 3.17b.

3.3.4. Phase Diagram of 2NapFF solution from 15 °C to 45 °C

The analyses of the changes in chemical shift and percentage of 2NapFF detectable by ^{1}H-NMR spectroscopy with temperature and concentration, shown in Fig. 3.16, allowed us to suggest an initial phase diagram for 2NapFF from 0.04 wt% to 1 wt% and 15 °C to 45 °C in Fig. 3.18. If the chemical shift is in the downfield plateau range (higher values of chemical shift) then the assignment was a free worm-like micellar structure; if is in the upfield plateau range (lower values of chemical shift), then the structure assigned was a densely-packed worm-like micellar structure; else if the chemical shift was in a transition region it was a transition (Fig. 3.18).

This 2D phase diagram shows a schematic representation of the micellar phases across a range of concentrations and temperatures. A transition from fully packed worm-like micelles to free worm-like micelles and spherical micelles is possible with a change in temperature from 15 to 45 °C, in the concentration range of 0.2 to 0.5 wt%. A temperature-stable phase is present in the concentration range from 0.9 and 1.0 wt%. This result indicates that the solution phase formulation in this range of concentration and temperature impacts the starting structure.

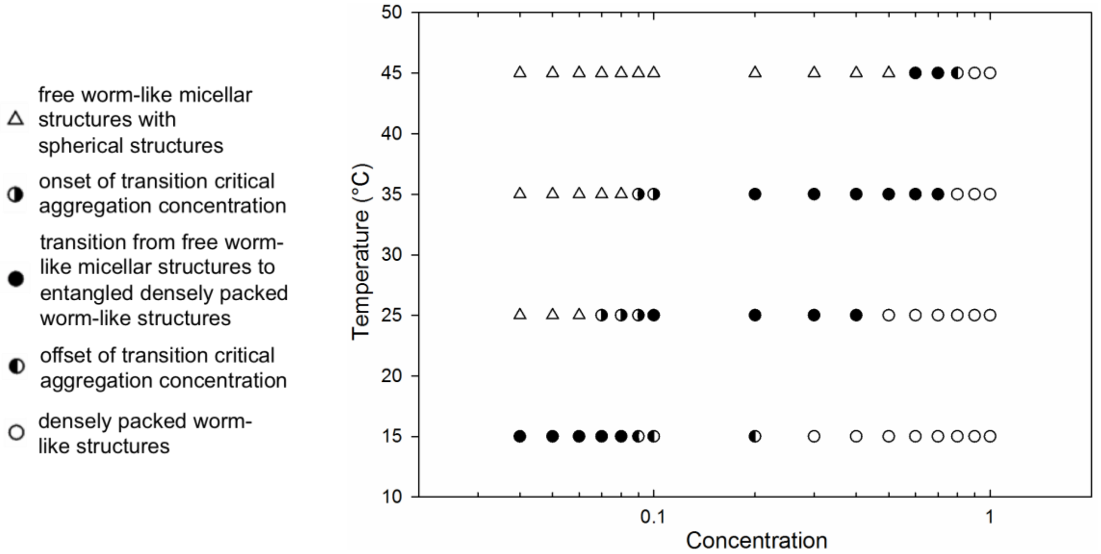

Figure 3.18 – 2NapFF phase diagram based on ^{1}H-NMR spectroscopy measurements at 15, 25, 35 and 45 °C. In this concentration and temperature range, only two micellar phases could be clearly distinguished and a transition phase, possibly: (1) free worm-like micellar structures with spherical structures (empty triangles), (2) densely packed, bundled worm-like structure (empty circles) and (3) the transition from less entangled and free worm-like structures to entangled densely packed worm-like structures (filled and half-filled circles). The concentration axis is on a log-scale.

This physical change in the solution phase could potentially be used for the controlled release of an active component in food, agriculture, health and beauty commercial products, which require a phase transition for their functionality.[39,41–43] The property of temperature stability could represent a step forward in creating product which can maintain their function across a range of climatic conditions.[44,45] These features could therefore reduce the costs of modifying products to adapt to the temperature conditions, which is a major drawback for current nanotechnological applications.[44,45] Accurate knowledge of the stability or dynamic instability range of the 2NapFF solution phase can allow for the application of this type of surfactant in advanced formulation of products in countries with different ambient temperature requirements. In this domain, further studies in temperature-controlled self-assembly may reveal new avenues in peptide supramolecular material design. Formulation of stable surfactants in the range from 15 to 45 °C appears to be interesting for biomedical, agricultural or food related applications.[45–49] For example, recently Scott *et al.* have shown that some unprotected tripeptides can form emulsifiers with temperature stabilities between 50 to 80 °C.[50]

With these results focused on 2NapFF gelator, we investigated if we would identify similar gelator solution features when this gelator is compared with 16 other gelators.

3.3.5. Solution phase of other peptide-based low molecular weight gelators

An investigation of the solution phase properties of 17 gelators with experimental techniques such as ^{1}H-NMR spectroscopy, dynamic light scattering, surface tension and turbidity was carried out to test the hypothesis formulated based on the results of 2NapFF. It was expected to achieve an overall perspective of the solution phase properties for each gelator based only on a single or few non-invasive measurements. If these were in agreement with our 2NapFF detailed study and agreed between them, these would allow predictions to be made regarding their solution phase. This study allowed us to categorise the in-house designed gelators into different classes of solution behaviour, which could be useful if the solution phase properties are found to be connected with the hydrogel properties (discussed in Chapter 4). Figure 3.23 shows the molecular structure of 2NapFF analogues based on the linkage of substituted 2-naphthalenes with a series of dipeptides and the tetrahydronapFF gelator (2-((5,6,7,8-tetrahydronaphthalen-2-yl)acetyl)phenylalanylphenylalanine).

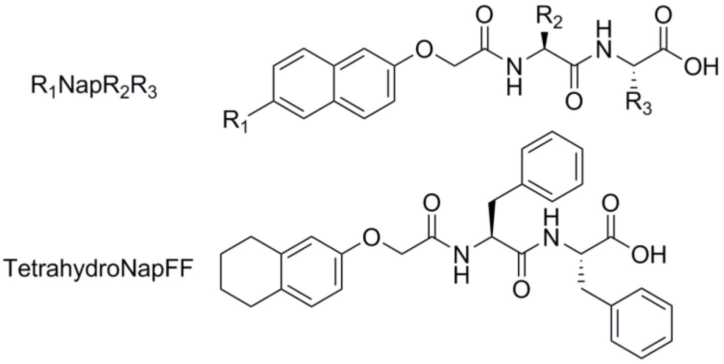

Figure 3.23 – Molecular structure of 2-Napthalene-dipeptides and the structure of tetrahydronapFF. The acronym of naphthalene-dipeptides has the following form: $R_1NapR_2R_3$, with the substituents shown in Table 3.1.

An initial analysis of some of these gelators (Fig. 3.23 and Table 3.1) by surface tension transitions was previously conducted by our group.[8] Here, a list of gelators, selected from our group library of compounds, was analysed by surface tensiometry: tetrahydroNapFF, 3MeO-NapFF, 2NapYF, 7MeO-FV, BrNapAF and 2NapVV (Table 3.2). These findings have not previously been reported and therefore allow a further interpretation of the most hydrophobic gelators of our group's gelator library.

Table 3.1 – Acronym, apparent pK_a, predicted logP and substituents on the corresponding structure of Fig. 3.23 for the gelators studied. The apparent pK_a's shown here were obtained from our previous work only,[5–7] logP values were calculated using the online programme MolinspirationTM calculator.[51] The gelators are listed in descending LogP order.

Gelator	**apparent pK_a at 0.5 wt%, 25 °C**	**logP**	**R_1**	**R_2**	**R_3**
BrNapFF	6.8	3.55	Br	Ph	Ph
2NapFF	6.0	2.76	H	Ph	Ph
ArFF	-	2.76	-	Ph	Ph
3MeO-NapFF	-	2.35	3MeO	Ph	Ph
BrNapFG	5.5	2.30	Br	Ph	H
2NapYF	-	2.28	H	Ph-4-(OH)	Ph
7MeO-FV	-	2.11	7MeO	Ph	$CH(CH_3)_2$
BrNapAF	-	2.07	Br	CH_3	Ph
2NapFV	6.5	2.08	H	Ph	$CH(CH_3)_2$
CN-NapFV	6.1	1.81	CN	Ph	$CH(CH_3)_2$
BrNapAV	5.8	1.40	Br	CH_3	$CH(CH_3)_2$
2NapVV	6.8	1.40	H	$CH(CH_3)_2$	$CH(CH_3)_2$
CN-NapFG	5.0	1.25	CN	Ph	H
BrNapAG	5.0	0.84	Br	CH_3	H
BrNapAA	4.9	0.63	Br	CH_3	CH_3
2NapAV	4.2	0.62	H	CH_3	$CH(CH_3)_2$
2NapAA	5.1	-0.16	H	CH_3	CH_3

2NapFF surface tension data was previously reported.[8] However, we have conductivity results (Fig. 3.15), which strongly indicate that our previous reported data for the cmc of 2NapFF, 0.5 wt%, corresponds to a critical aggregation concentration (cac) instead of a cmc. This transition is likely to be from less bundled worm-like micelles to entangled/packed worm-like micelles (shown in Fig. 3.13 by LSCM with an increase in bundling size and contrast). This transition is also expected to change the surface tension in a similar way to a cmc. Here, additional techniques (e.g. conductivity and LSCM) proven useful to identify the concentration of the transition and narrow down the possible nature of the transition. Looking closely to Table 3.2, 2NapFF has actually the lowest transition detected, so probably this is why our surface tension measurements did not work for this gelator. However, for all other 16 gelators the surface tension results showed two clear plateaus, the first one related to the apparent air-water partition coefficient (K_{aw}) and the second related to the cmc$_1$, cmc$_2$ or cac as speculated based on the amount ^{1}H-NMR detectable. This new results for 2NapFF and new tensiometry data for all 16 other gelators are shown in Table 3.2.

Table 3.2 – Tensiometry data, molecular weight and apparent pK_a at 0.5 wt% and 25 °C for the gelators studied (listed by logP in decreasing order). †Apparent pK_a and the surface tension results reported previously by our group.[52] ‡ - cmc value obtained by conductivity in Section 3.3 and cross-sectional area (A_S) and apparent air-water partition coefficient (K_{aw}) values obtained by a new surface tension measurement. n.d. – not determined; n.a. – not available; *Assignment confirmed by ^{1}H-NMR measurements.

Gelator	**M_w (g/mol)**	**apparent pK_a at 0.5 wt% 25 °C†**	**Transition concentration (wt%)**	**Type of transition**	**A_S(Å^2)**	**K_{aw} (1/a.u.)**
BrNapFF[†]	575.45	6.8	0.04 ± 0.01	cmc$_1$	602 ± 140	85.7 ± 2.0
2NapFF[†‡]	496.55	6.0	0.011 ± 0.004	cmc$_1$	63 ± 1.5	157.9 ± 0.9
Ar-FF	500.59	n.a.	0.030 ± 0.002	cmc$_1$	56 ± 2	567.4 ± 69
3MeO-NapFF	526.58	n.a.	0.327 ± 0.034	n.d.	58 ± 1.5	69 ± 7.4
BrNapFG[†]	485.33	5.5	0.53 ± 0.06	cac*	101 ± 10	108 ± 6.5
2NapYF	512.55	n.a.	0.53 ± 0.02	cmc$_1$*	39 ± 1.2	22 ± 0.7
7MeO-FV	478.54	n.a.	0.792 ± 0.008	cac/cmc$_2$*	48 ± 0.9	28 ± 0.7
BrNapAF	499.35	n.a.	0.237 ± 0.007	n.d.	44 ± 1.3	38 ± 2.4
2NapFV[†]	448.51	6.5	0.75 ± 0.1	cac*	70.4 ± 0.7	71.9 ± 6.9
CN-NapFV[†]	473.52	6.1	0.81 ± 0.1	cac*	57.5 ± 1.2	66.5 ± 3.2
BrNapAV[†]	451.31	5.8	0.51 ± 0.02	cac/cmc$_2$*	41.5 ± 2	13.2 ± 0.8
2NapVV	400.47	6.8	1.99 ± 0.01	cac*	47 ± 2	9 ± 0.3
CN-NapFG[†]	431.44	5.0	0.9 ± 0.02	cac/cmc$_2$*	55.5 ± 0.6	56 ± 0.1
BrNapAG[†]	409.23	5.0	0.67 ± 0.01	cac*	39 ± 3	6.8 ± 0.8
BrNapAA[†]	423.26	4.9	1.1 ± 0.2	cac*	45 ± 2	5.55 ± 0.3
2NapAV[†]	372.41	4.2	2.65 ± 0.1	cac*	25.5 ± 2.3	65.5 ± 0.5
2NapAA[†]	344.36	5.1	2.85 ± 0.1	n.d.	43 ± 0.8	5.45 ± 0.5

The transition concentration in Table 3.2 refers to the surface tension transition from a decreasing surface tension to a plateau region. Only in the case of the 2NapFF, this presented a challenge and only the conductivity measurements were representative. All of the gelators studied are able to form hydrogels with at least one methodology (e.g. pH-switch or salt-switch methods). As noted earlier in the Chapter, the minimal gelation concentration (mgc) is the characteristic concentration from which the gelator can form a hydrogel. From Table 3.2 it is possible to see that the general trend for the molecular weight and apparent pK_a (at 0.5 wt% and 25 °C) is to decrease with a decrease in logP. The cmc values measured suggest that some are in fact cmc_2 or critical aggregation concentration (cac) because they are at concentrations significantly above the reported mgc,[8] while others are indeed cmc_1.

The 2NapFF case (above in Section 3.3) showed the difficulty in classifying the transition between micellar phases. Further evidence of this difficult assignment process is confirmed by correlations with the corresponding hydrogel phase shown in the next chapters (Chapter 4). In this case, the mgc is significantly below the measured cmc_2 value, the region between this mgc value and cmc_2 is a transition region from possibly spherical micellar structures to worm-like structures, capable of forming a hydrogel (Chapter 4). Additionally, we have found that the surface tension measurement may not reveal the cmc value conclusively with these peptide-based surfactants, as the actual cmc occurs at a significantly lower concentration for 2NapFF (Section 3.3). In the case of 2NapFF, the concentration region of possibly spherical micellar structures at 25 °C is also significantly smaller when compared with the worm-like micellar region. Therefore, in the gelators for which the cmc determined by surface tension is significantly above the mgc, it is most certainly not the cmc_1 but rather a cmc_2 or a critical aggregation concentration (cac), as was pointed out in Table 3.2 with type of aggregation. Furthermore, the cmc_1 is expected to be close to the mgc because the formation of a hydrogel requires a suitable worm-like microstructure.[53] A list of the mgc's used to evaluate the type of transition was reported by Chen *et al*.[8] The case of 2NapFF studied above indicated that the previously measured surface tension transition was in fact a cac. The analysis of these gelators' reported transition concentrations and mgc's suggests the hypothesis that these surface tension transitions relate to cac, if the difference between the mgc and the transition concentration is above 0.4 wt%, while if it is below this value, the transition is likely to represent a cmc_1 or cmc_2 (Table 3.2). Therefore, most of the previously reported cmc are potential cac (with the exception of BrNapFF).

^{1}H-NMR spectroscopy was used to clarify the presence of structures at 0.1 wt% and 0.5 wt% of the 17 gelators studied. In Fig. 3.24, the percentage ^{1}H-NMR detectable as a function of the predicted logP is shown. These results are listed for each of the 17 gelators in Table 3.3. The percentage ^{1}H-NMR detectable at 0.1 wt% and 0.5 wt% and suggestions of structures at each of these concentrations (also shown in Table 3.3) is based on ^{1}H-NMR detectable amount and the difference between that concentration and the cmc$_1$, cmc$_2$ or cac. Gelator solutions above the cmc$_1$ are expected to have a percentage of NMR detectable below 100 %. Most of these results are in agreement with the surface tension interpretation, except for BrNapAF, whose measured surface tension transition is at a concentration of 0.237 ± 0.007 wt%. Therefore, BrNapAF at 0.5 wt% was expected to be below 100 % NMR detectable and this is not the case here. A possible explanation for this is that a rapid exchange occurs between micellar structures and the water at 0.5 wt% therefore appear as 100 % NMR detectable. The transition in surface tension could still occur at 0.237 ± 0.007 wt%. In the cases of BrNapFG, 2NapFV, CN-NapFG, BrNapAG, BrNapAA, 2NapAV and 2NapAA, the presence of NMR detectable structures at 0.1 wt% confirms that the surface tension transitions listed in Table 3.2 above this value are a cac or cmc$_2$. The case of 2NapYF confirms that the surface tension transition at 0.53 ± 0.02 wt% is likely to be a cmc$_1$ because at 0.5 wt% the sample is approximately 100 % NMR detectable (Table 3.3).

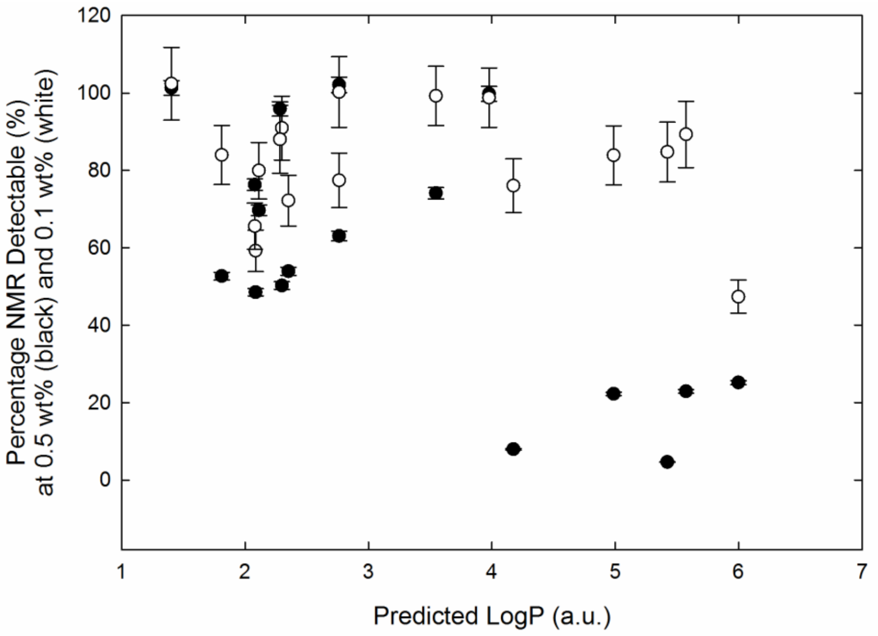

Figure 3.24 – Percentage of gelator NMR detectable as a function of predicted logP for solutions of 0.5 wt% (black) and 0.1 wt% (white), calculated from online programme Molinspiration^{TM} calculator.[51] The gelators studied are listed in order of predicted logP in Table 3.1.

The process of classifying the micellar transitions requires a combined interpretation of the percentage of gelator NMR detectable and proximity of the surface tension transition to the concentrations investigated:

(0) Below 70 % NMR detectable and a concentration above cmc_2 or cac (WLM = entangled worm-like micelles).

(1) Below 100 % NMR detectable and a value close to the surface tension transition (SM - spherical micelle; free-worm-like micelles – free-WLM – or elongated worms that are not entangled);

(2) Just near to 100% NMR detectable and a value below the surface tension transition (FM - free molecules or SM – spherical micelles); and

(3) 100% NMR detectable and far below the surface tension transition (FM - free molecules).

Table 3.3 – Percentage NMR detectable and structural assignment of micellar phase for the 17 gelators and their respective predicted LogP. The micellar phase abbreviations are as follows: FM – free molecules; SM – spherical micelles; and WLM – worm-like micelles.

Gelator	**logP**	**NMR Detectable 0.5 wt% (%)**	**Suggested Structures**	**NMR Detectable 0.1 wt% (%)**	**Suggested Structures**	**Indicative of cmc below 0.1 wt%**
BrNapFF	6.0	25 ± 0.5	WLM	47 ± 4	free WLM	yes
2NapFF	5.6	23 ± 0.5	WLM	90 ± 9	free WLM	yes
TetrahydroNap-FF	5.4	5 ± 0.1	WLM	42 ± 4	free WLM	yes
3MeO-NapFF	5.0	22 ± 0.4	WLM	84 ± 8	SM or free WLM	yes
BrNapFG	4.2	8 ± 0.2	WLM	76 ± 7	SM or free WLM	yes
2NapYF	4.0	100 ± 0.2	SM and free WLM	99 ± 8	FM	no
7MeO-FV	3.5	74 ± 1.5	FM and SM	99 ± 8	FM	no
BrNapAF	2.8	102 ± 2	FM and SM	100 ± 9	FM	no
2NapFV	2.8	63 ± 1.2	WLM	76 ± 7	SM or free WLM	yes
CN-NapFV	2.4	54 ± 1.1	WLM	72 ± 7	SM or free WLM	
BrNapAV	2.3	50 ± 1	WLM	91 ± 8	FM	no
2NapVV	2.3	96 ± 1.9	FM and SM	88 ± 9	FM and SM	yes
CN-NapFG	2.1	70 ± 1.4	FM and SM	90 ± 7	SM or free WLM	yes
BrNapAG	2.1	49 ± 1	FM and SM	59 ± 5	SM or free WLM	yes
BrNapAA	2.1	76 ± 1.5	FM	66 ± 6	SM or free WLM	yes
2NapAV	1.8	53 ± 1	SM	84 ± 8	FM and SM	yes
2NapAA	1.4	101 ± 1.9	FM	102 ± 9	FM	no

These results for the 16 extra gelators studied here were shown follow same trends as we found for 2NapFF in the previous sections. These results suggested that knowing

^{1}H-NMR quantitative information and the phase transitions of the particular gelator of interest, it is possible to suggest solution phases have worm-like micellar structures form modified-dipeptide when the study is complemented by microscopy or scattering techniques. The most effective way to identify the phase transitions is by surface tension or by conductivity measurements, if the surface tension is not available or the transitions are not clear.

3.4. Conclusion

The phase diagram of 2NapFF was fully characterised at pH 10.5 and 25 °C. For this study, conductivity, microscopy and rheology proved fundamental for the understanding of the phase diagram. With the conductivity, spectroscopy and microscopy results from this thesis and complementary SANS data done in colaboration[54] for 2NapFF solutions at pH 10.5 we found a $cmc_1 = 0.011 \pm 0.004$ wt% (0.222 ± 0.075 mM) and a $cmc_2 = 0.069 \pm 0.015$ wt% (1.39 ± 0.302 mM). Confocal microscopy, cross-polarised microscopy and a viscosity increase from 0.1 – 0.2 wt% to 0.5 wt% could be indicating an increase in the number of worm-like structures or the degree of cross-linking. Strain and frequency sweeps in the region from 0.3 wt% to 1 wt% show a best fit for an exponential function with coefficients of 1.03 and 1.04, respectively, for the relation between G* and concentration. Confocal microscopy shows an increase in microstructural packing of the worm-like micellar network. The full characterisation of 2NapFF at pH 10.5 and 25 °C is consistent with three transitions: (1) free molecule to spherical micellar phase (cmc_1), (2) spherical micellar phase to worm-like micellar phase (cmc_2); and (3) worm-like micellar phase to a bundled worm-like micellar phase (cac = 0.5 wt%).

A temperature dependent phase diagram was obtained for the worm-like micellar region between 15 °C to 45 °C. The 2NapFF gelator can form hierarchical structures in the solution phase, which can be modified structurally by increasing the temperature. The understanding of these features of peptide-based gelators allows control over transitions in the solution phase properties depending on concentration and temperature. These transitions could be instrumental in the application of these materials.

A screening study of 16 other gelators showed that low molecular weight modified-dipeptide systems at concentrations of 0.1 wt% and 0.5 wt% could be in any of the four phases: a free-flowing molecular phase, a spherical aggregate micellar phase, a worm-like micellar phase or a packed worm-like micellar phase. The measured transitions by surface tension or conductivity and quantification measurements by ^{1}H-NMR spectroscopy are only sufficient to suggest if the sample is either a micellar phase, free molecules or a transition between the two based on complementary microscopy and SANS observations. The presence of worm-like micelles can only be confirmed if either the surface tension or conductivity measurements are conclusive, SANS data is available and in agreement with microscopy and typical rheological features of worm-like micelles at that particular concentration.[54] Literature suggests that access to a cryo-TEM or wet-AFM (Chapter 5) allow the determination and confirmation of the peptide-based micellar type, structural features and dimensions.[37] However, the transition regions and structural information of each micellar phase can be identified for 2NapFF solutions at pH 10.5. The presence of worm-like micelles in the concentration region between the cmc_2 and the cac was confirmed. These findings are likely to allow some degree of prediction on the fate of gelation, gel or no gel, for that same gelator solution at specific concentrations and temperatures for which the phase diagram shows worm-like micellar structures.

3.5. Materials and Methods

All gelators were synthesised as described previously.[17, 23] All other chemicals were purchased from Sigma-Aldrich and used as received. In this work, the majority of the gelators was synthesised by Dave J. Adams and Jaclyn Raeburn, while a small portion of the BrNapAV, BrNapFF and 2NapFF used in this Thesis was synthesised by myself.

3.5.1. Pre-gelator solution preparation

Stock solutions of the gelators with a specified concentration were prepared by dissolving the gelator powder in doubly distilled H_2O and adding approximately 1.2 equivalents of 1M NaOH per gelator to obtain a starting solution at a pH of 10.5. The 1M NaOH solution was freshly prepared and filtered through a 0.2 µm syringe (Minisart RL 15, Sartorius Stedim) before use. The stock solution pH was adjusted with this NaOH solution and measured with a FC200 pH probe (HANNA Instruments) with a (6 mm x 6 mm) conical tip. The stated accuracy of the pH measurements is ± 0.1. The basic solution was then stirred for 24 hours to yield a clear solution with a pH of 10.5.

Solutions were initially prepared by dilution of the stock solutions. However, for low concentrations of this gelator (below 0.1 wt%), we observed that there are some micellar structural differences depending on the preparation method: either diluting from a more concentrated sample or dissolving at that concentration. Thus, for all measurements each sample at any concentration was freshly prepared at that concentration.

3.5.2. Surface Tension

The surface tension measurements were performed on a high throughput Kibron Delta-8 Surface Tensiometer which uses a Du Nouy-Padday method (maximum pull on a rod). The results were analysed by the Delta-8 Manger software. The pre-gelation samples were prepared as described above, and the dilutions were first performed using an Eppendorf epMotion 5072 for a preliminary scan. Subsequently the solutions were prepared directly at the required concentrations (as described above) to obtain the data shown here. For the robotic system, 200 μL of the concentrated gelator solution was transferred onto the first column of a standard Nunclon 96-well plate. A series of concentrations were prepared by sequential dilution of the gelators using pH 10.5 water across the plate, with the concentration being decreased by a dilution factor for each column using a transfer-and-mix protocol. Finally, 50 μL samples of each concentration were transferred to the detection plate for measurement. All measurements were conducted at 18 °C. The averaged result and standard deviation were calculated from 4 separate samples.

3.5.3. ^{1}H-NMR Spectroscopy

^{1}H-NMR Spectroscopy was used to characterise the solution micellar transitions. A 500 MHz Bruker Avance-III HD equipped with an 11.74 T magnet and a liquid nitrogen cooling system was used for all experiments. A common ^{1}H-NMR experiment with 30 degrees flip angle was used to obtain the spectra. The total number of scans was 16 and the acquisition time per scan was 3 minutes for each measurement at 25 °C, except when mentioned. Aliquots of 0.5 mL of each solution were transferred to a NMR tube (NE-ML5-8, NEW ERA Enterprises).

The ^{1}H-NMR spectroscopy integrals were calibrated against a known amount of ethanol sealed in a capillary in D_2O (approximately 6 μL ethanol in 1 mL D_2O solution) and sealed with a PTFE tape. The capillary was calibrated with 8 mg/mL $_L$-alanine solution in H_2O. Before each measurement, the reference capillary was inserted with a PTFE holder into the NMR tube with the gelator solution. Additionally, a common solvent suppression experiment using pre-saturation and spoil gradient under the same conditions was conducted and used for the quantification analysis.

If the conditions are quantitative and a good signal-to-noise ratio (over 1000), it is possible to use the chemical shift and the integration of a proton resonance frequency to estimate both the molecular environment (i.e. hydrophobicity near the protons investigated) and the degree of mobility (all at relaxation delay of 1 s). The molecular environment of the gelator was estimated by the chemical shift of the proton on the position-7 of the naphthalene ring (or the 4 protons in the position 6 and 7 of the Tetrahydro-naphthalene in the case of TetrahydroNapFF). The degree of mobility was evaluated by the relative intensity of the CH_2 protons of the phenylalanine groups to estimate the average amount of detectable gelator indirectly by the corresponding number of mobile protons in the sample with the same frequency. Triba *et al*. have showed that micellar transitions in lipids can be detected by analysis of the chemical shifts and relative integrations between two components.[46] Thus, if the 2NapFF is in dynamic equilibrium, there is a probability of each molecule either being free-flowing in solution and a complementary probability of it being self-assembled as part of a possible micellar structure. The on-off ratio can be defined as the number of self-assembled molecules divided by the number free molecules. If this ratio is high, we expect that the molecules are forming micellar structures. However, the quantification is independent on the relaxation delay used for the measurement for the low concentrations studied (relaxation delay of 1 s). The molecules will be detectable if they exchange with the solvent in the timescale of the experiment. Thus, in this case, we expect to see less of the detectable amount of surfactant only if the molecules are forming structures and they exchange with the solvent at a slower rate than the relaxation delay. Therefore, quantification should be treated with caution when being used to confirm the presence of structural features in solution. The LMWG being a surfactant in the solution phase could be just partially detectable, however the dominant phase could still be the one of spherical or worm-like micellar structures if the exchange with the solvent is quicker than the measurement timescale.

3.5.4. Rheology

Dynamic rheological experiments were performed using an Anton Paar Physica MCR301 rheometer. The rheometer was calibrated for inertia and motor every 5 days or immediately before each measurement for the solution phase measurements in order to obtain accurate measurements in the low viscosity and low torque region. These calibrations resulted in improved instrument resolution at low torque. All measurements were conducted at 25 °C. The solution phase measurements of 2NapFF, strain and frequency-sweep measurements were conducted in a cone-plate system (Anton Paar CP50-1), used to improve sensitivity of the viscoelastic solutions and samples were poured to the stage to minimize mechanical artefacts, samples were stabilized in the cone-plate system for 30 minutes before each measurement. The frequency-sweep measurements were measured at a constant strain of 0.1 % for the solution phase (to capture the network features). This choice of parameters was based on the attempt to be in the viscoelastic region and having data obtained with similar parameters used in the visco-elastic region of the hydrogel analysis in Chapter 4, whilst still being able to conduct the measurement in a sensible time and investigate the material properties of the bulk and not just the surface.[47] No time restrictions were made on the time needed to reach each measurement point (instrumental average over 40 recordings). To ensure the frequency measurements were carried out in the linear viscoelastic regime, strain-sweep measurements were performed at a static frequency of 10 rad/s. The results showed no significant variation in the storage modulus (G') and the loss modulus (G'') measured by frequency-sweeps between a strain of 0.1 and 0.5 %. For each sample, G', G'', the complex modulus (G^*) or viscosity (η) were measured as appropriate.

3.5.5. Conductivity

Samples were prepared as described in Section 3.5.1. The instrument was calibrated with double distilled water at 25.0 ± 0.1 °C and conductivity of KCl solutions were used to confirm the accuracy of the instrument (± 2%) with literature values. The measurements were performed using a PCE – PHD 1 conductivity probe with temperature compensation (PCE Instruments). The probe was rinsed 5 times with ddH_2O before each measurement.

3.5.6. UV-Vis spectroscopy

Samples were prepared as described above and poured in to a quartz cuvette. Each measurement was performed using a NanoDrop 2000c UV-Vis Spectrophotometer (Thermo Scientific).

3.5.7. Optical microscopy

Optical Microscopy was carried out using a Nikon Eclipse Microscope and image analysis was done with ImageJ.[55] Samples were prepared as described in section 3.5.1. They were poured onto a microscope slide and examined in the bright field and under cross-polarizers.

3.5.8. Laser scanning confocal microscopy

Confocal microscopy images were obtained on a Zeiss LSM510 and a Plan-Apo 100x (1.4 NA oil) objective. Nile Blue fluorescence was excited with a 633 nm Helium Neon laser and emission detected between 638 and 758 nm using a pinhole diameter of 1 Airy unit (approx. 0.8 μm resolution). The 2NapFF samples were prepared as described previously for any gelator with the additional aliquot of a Nile blue solution to make a final 0.001 M Nile blue (pipetting a selected amount from a 0.01 M Nile blue stock solution). Typical pictures selected of over the 50 captured were chosen and measured for this study. The images were analysed using the Zeiss AIM software (Zeiss, Jena, Germany) and ImageJ software.[55]

3.6. Appendix

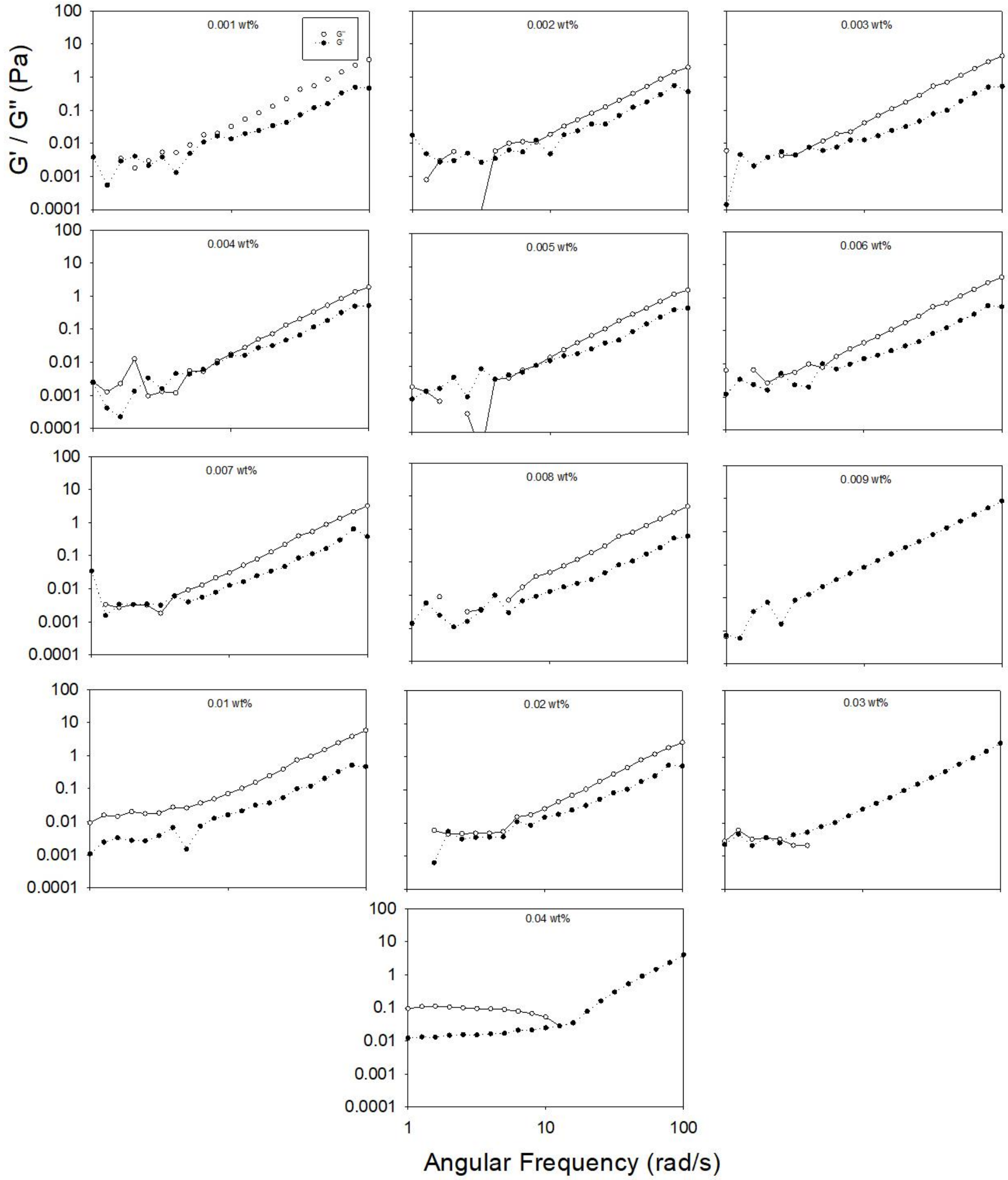

Figure 3.25 – Frequency sweeps, at a strain of 0.5 %, of solutions of 2NapFF from 0.001 wt% till 0.04 wt% at pH 10.5 near the torque limits of the rheometer. The storage modulus (G′, filled circles) and loss modulus (G″, empty circles) are plotted as function of the angular frequency. Each plot was only measured once with each point based on an average obtained from 40 repeat measurements within 5% tolerance, with all data collected with 10 points per decade. Some points are omitted because the rheometer could not pick up the G″ under those measurement conditions.

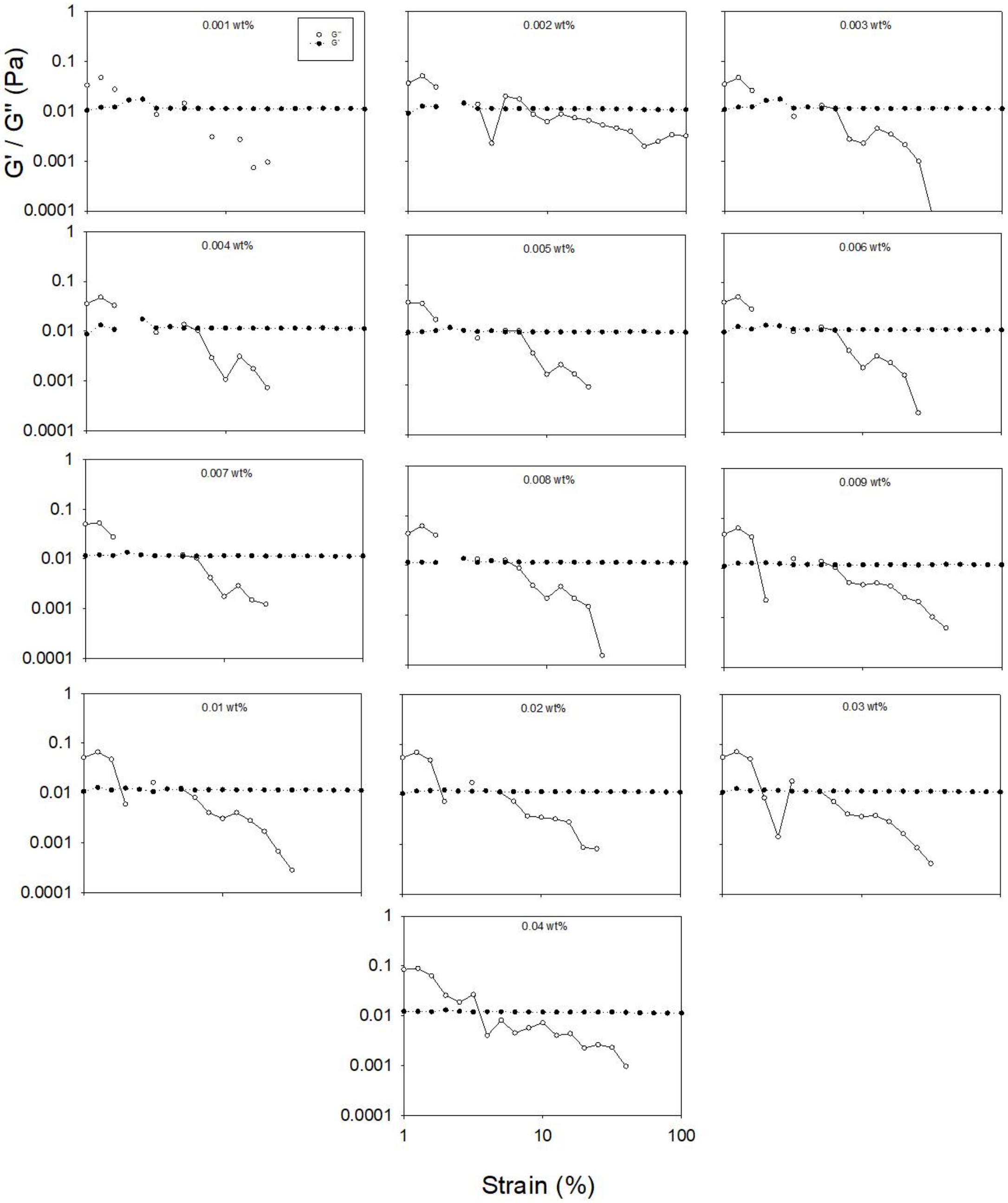

Figure 3.26 – Strain Sweeps, at a frequency of 10 rad/s, of solutions of 2NapFF from 0.001 wt% to 0.04 wt% at pH 10.5 near the torque limits of the rheometer. The storage modulus (G′, filled circles) and loss modulus (G″, empty circles) are plotted as function of the strain applied. Some points are omitted because the rheometer could not pick up the G′ or G″ under those measurement conditions.

3.7. References

1. P. Mukerjee and K. Mysels, *Critical micelle concentrations of aqueous surfactant systems*, 1971, vol. 61.

2. H. T. Davis, *Colloids Surfaces A Physicochem. Eng. Asp.*, 1994, 91, 9–24.

3. L. Chen, T. O. McDonald, and D. J. Adams, *RSC Adv.*, 2013, 3, 8714–8720.

4. L. Chen, G. Pont, K. Morris, G. Lotze, A. Squires, L. C. Serpell, and D. J. Adams, *Chem. Commun.*, 2011, 47, 12071–12073.

5. K. A. Houton, K. L. Morris, L. Chen, M. Schmidtmann, J. T. A. Jones, L. C. Serpell, G. O. Lloyd, and D.

J. Adams, *Langmuir*, 2012, 28, 9797–806.

6. D. J. Adams, L. M. Mullen, M. Berta, L. Chen, and W. J. Frith, *Soft Matter*, 2010, 6, 1971.
7. J. Raeburn, G. Pont, L. Chen, and Y. Cesbron, *Soft Matter*, 2012, 8, 1168–1174.
8. L. Chen, S. Revel, K. Morris, L. C. Serpell, and D. J. Adams, *Langmuir*, 2010, 26, 13466–13471.
9. J. Israelachvili, *Colloids Surfaces A Physicochem. Eng. Asp.*, 1994, 91, 1–8.
10. M. Miura and M. Kodama, *Bull. Chem. Soc. Jpn.*, 1972, 45, 428–431.
11. A. González-Pérez, J. Czapkiewicz, G. Prieto, and J. R. Rodríguez, *Colloid Polym. Sci.*, 2003, 281, 1191–1195.
12. L. Magnus Bergström, *Curr. Opin. Colloid Interface Sci.*, 2016, 22, 46–50.
13. D. Danino, L. Abezgauz, I. Portnaya, and N. Dan, *J. Phys. Chem. Lett.*, 2016, 7, 1434–1439.
14. L. M. Bergström, A. Tehrani-Bagha, and G. Nagy, *Langmuir*, 2015, 31, 4644–4653.
15. P. Alexandridis and U. Olsson, 1998, 7463, 2627–2638.
16. B. Ozbas, J. Kretsinger, K. Rajagopal, J. P. Schneider, and D. J. Pochan, *Macromolecules*, 2004, 37, 7331–7337.
17. G. Pont, L. Chen, D. G. Spiller, and D. J. D. Adams, *Soft Matter*, 2012, 8, 7797–7802.
18. M. Wallace, A. Z. Cardoso, W. J. Frith, J. A. Iggo, and D. J. Adams, *Chem. - A Eur. J.*, 2014, 20, 16484–16487.
19. J. D. Hartgerink, E. Beniash, and S. I. Stupp, *Science*, 2001, 294, 1684–1688.
20. J. D. Hartgerink, J. R. Granja, R. A. Milligan, and M. R. Ghadiri, *J. Am. Chem. Soc.*, 1996, 118, 43–50.
21. P. A. Korevaar, C. J. Newcomb, E. W. Meijer, and S. I. Stupp, *J. Am. Chem. Soc.*, 2014, 136, 8540–3.
22. E. T. Pashuck and S. I. Stupp, *J. Am. Chem. Soc.*, 2010, 132, 8819–8821.
23. J. D. Tovar, R. C. Claussen, and S. I. Stupp, *J. Am. Chem. Soc.*, 2005, 127, 7337–45.
24. S. Cavalli, F. Albericio, and A. Kros, *Chem. Soc. Rev.*, 2010, 39, 241–263.
25. S. Zhang, M. a Greenfield, A. Mata, L. C. Palmer, R. Bitton, J. R. Mantei, C. Aparicio, M. O. de la Cruz, and S. I. Stupp, *Nat. Mater.*, 2010, 9, 594–601.
26. M. Wallace, D. J. Adams, and J. A. Iggo, *Soft Matter*, 2013, 9, 5483–5491.
27. D. J. Adams and P. D. Topham, *Soft Matter*, 2010, 6, 3707–3721.
28. T. Li, M. Kalloudis, A. Z. Cardoso, D. J. Adams, and P. S. Clegg, *Langmuir*, 2014, 30, 13854–60.
29. J.-S. Kim, C.-K. Kim, P.-S. Song, and K.-M. Lee, *J. Colloid Interface Sci.*, 1981, 80, 294–296.
30. Z. Lin, J. J. Cai, L. E. Scriven, and H. T. Davis, *J. Phys. Chem.*, 1994, 98, 5984–5993.
31. C. A. Dreiss, *Soft Matter*, 2007, 3, 956–970.
32. X. Du, J. Zhou, J. Shi, and B. Xu, *Chem. Rev.*, 2015, 115, 13165–13307.
33. W. J. Frith, A. M. Donald, D. J. Adams, and A. Aufderhorst-Roberts, *J. Nonnewton. Fluid Mech.*, 2015, 222, 104–111.
34. W. Wang and S. A. Sande, *Polym. J.*, 2015, 47, 302–310.

35. A. Aufderhorst-Roberts, W. J. Frith, M. Kirkland, and A. M. Donald, *Langmuir*, 2014, 30, 4483–4492.

36. R. G. Weiss and P. Terech, *Molecular Gels*, Springer Netherlands, Dordrecht, 2006.

37. R. Mammadov, A. B. Tekinay, A. Dana, and M. O. Guler, *Micron*, 2012, 43, 69–84.

38. L. Chen, J. Raeburn, S. Sutton, D. G. Spiller, J. Williams, J. S. Sharp, P. C. Griffiths, R. K. Heenan, S. M. King, A. Paul, S. Furzeland, D. Atkins, and D. J. Adams, *Soft Matter*, 2011, 7, 9721–9727.

39. S. J. Holder and N. a. J. M. Sommerdijk, *Polym. Chem.*, 2011, 2, 1018.

40. K. Rajagopal, A. Mahmud, D. a. Christian, J. D. Pajerowski, A. E. X. Brown, S. M. Loverde, and D. E. Discher, *Macromolecules*, 2010, 43, 9736–9746.

41. S. R. Jadhav, B.-S. Chiou, D. F. Wood, G. DeGrande-Hoffman, G. M. Glenn, and G. John, *Soft Matter*, 2011, 7, 864–867.

42. H. Boulaiz, P. Alvarez, and A. Ramirez, *Int. J. Mol. Sci.*, 2011, 12, 3303–3321.

43. S. Debnath, S. Roy, and R. V Ulijn, *J. Am. Chem. Soc.*, 2013, 135, 16789–16792.

44. B. Goldenbogen, N. Brodersen, A. Gramatica, M. Loew, J. Liebscher, A. Herrmann, H. Egger, B. Budde, and A. Arbuzova, *Langmuir*, 2011, 27, 10820–10829.

45. B. Hack, H. Egger, J. Uhlemann, M. Henriet, W. Wirth, A. W. P. Vermeer, and D. G. Duff, *Chemie Ing. Tech.*, 2012, 84, 223–234.

46. T. R. Cuadros and J. M. Aguilera, *Food Biophys.*, 2015, 10, 487–499.

47. N. A. Peppas, P. Bures, W. Leobandung, and H. Ichikawa, *Eur. J. Pharm. Biopharm.*, 2000, 50, 27–46.

48. M. J. Bassetti, J. S. Moore, and D. J. Beebe, in *2nd Annual International IEEE-EMBS Special Topic Conference on Microtechnologies in Medicine and Biology. Proceedings (Cat. No.02EX578)*, IEEE, 2002, 410–413.

49. G. A. Silva, *Science (80)*, 2004, 303, 1352–1355.

50. G. G. Scott, P. J. McKnight, T. Tuttle, and R. V. Ulijn, *Adv. Mater.*, 2016, 1381-1386.

51. www.molinspiration.com, *Cheminformatics Molinspiration Ulica*.

52. L. Chen, S. Revel, K. Morris, C. S. L, D. J. Adams, L. C. Serpell, D. J. Adams, L. C. Serpell, D. J. Adams, L. C. Serpell, and D. J. Adams, *Langmuir*, 2010, 26, 13466–13471.

53. J. Raeburn, A. Zamith Cardoso, and D. J. Adams, *Chem. Soc. Rev.*, 2013, 42, 5143–56.

54. A. Z. Cardoso, L. L. E. Mears, B. N. Cattoz, P. C. Griffiths, R. Schweins, and D. J. Adams, *Soft Matter*, 2016, 12, 3612–3621.

55. W. S. S. Rasband, *U. S. Natl. Institutes Heal. Bethesda, Maryland, USA*.

Chapter 4

4. Linking the 2NapFF micellar phase with the corresponding hydrogel phase

4.1 Abstract

It was found that the 2NapFF peptide hydrogel phase is structurally connected to the corresponding solution phase. This allows prediction of the final properties of the calcium-hydrogels (Ca-hydrogels) from the starting conditions of the corresponding peptide surfactant solutions studied in Chapter 3, based on consideration of the solution phase diagram and self-assembly process. These results showed that the 2NapFF solutions could form Ca-hydrogels in a concentration from 0.02 wt% to 1.0 wt%, corresponding to three orders of magnitude in complex modulus. It was also found that the presence of worm-like micelles in the solution phase is linked to mechanically stronger Ca-hydrogels. The gelation by addition of the calcium salt shifts the worm-like micellar concentration region and changes the microstructure to increase packing. In the worm-like micellar region, the concentration is an exponentially dependent on the complex modulus (mechanical strength) with a 1.99 exponential coefficient, typical for cross-linked networks and biopolymer gels.[1]

4.2 Introduction

Peptide hydrogels can be formed with various methods (Chapter 1). The properties of the hydrogels are a result of their non-covalent hierarchical self-assembly, from supramolecular structures to a macroscopic viscoelastic material. It was shown in Chapter 2 that BrNapAV could form an intermediate state of worm-like self-assembled structures with carbon dioxide, when compared to the low pH hydrogels (Fig. 2.13, Section 2.4.4.). Furthermore, the initial phase formed upon dissolution of 2NapFF above its apparent pK_a is a micellar phase (Chapter 3). These types of solutions of peptides can form surfactants.[2–4] 2NapFF can form hydrogels when a calcium salt is added to a solution at a pH above its apparent pK_a (6.0).[5,6] This gelator can also form gels at a pH below this value, as was investigated previously by our group.[7] Other oligopeptide systems such as peptide-amphiphiles[8] also form worm-like micelles,[9] which can also be stabilised with calcium salts.[10] Further details on the behaviour and characteristics of peptide-hydrogels are discussed in Chapter 1.

The aim of this Chapter is to investigate whether the resultant Ca-triggered hydrogels are correlated with the 2NapFF micellar phases studied in Chapter 3. The hypothesis is that the properties of the Ca-hydrogels can be predicted from the properties of the initial 2NapFF surfactant solutions. If correct, this understanding would allow the final properties to be determined by the choice of starting conditions based on consideration of the solution phase diagram and self-assembly process. Here, the self-assembly process is fixed to the addition of two molar equivalents of calcium nitrate to 2NapFF (Section 4.5.1).

4.3 Results and discussion

4.3.1 Hydrogel state characterisation

Following from the assignment in Fig. 3.15, Chapter 3, of the phase diagram for micellar solutions of 2NapFF from 0.001 wt% to 1.0 wt%, in this Chapter we attempt to correlate the features of the starting solution phase with final hydrogel properties formed by the addition of calcium salts. Our group has studied a variety of salts to trigger gelation and the divalent cation Ca^{2+} was shown to induce the formation of the strongest salt-switch hydrogels at 0.5 wt%.[6,5] In this Chapter, the 2:1 salt to peptide ratio was kept constant from previous studies, where it was found to form the strongest hydrogels with this optimised ratio.[5]

4.3.1.1 Identification of the minimum gelation concentration and phase transition

The ability of 2NapFF solutions to form a hydrogel upon addition of Ca^{2+} was first evaluated by the inversion vial test. It was used here as a preliminary test to identify gels, if it passes the inversion vial test. Self-supporting hydrogels were formed between 0.03 and 1.0 wt% (Fig. 4.1). Below 0.01 wt%, the solutions did not form self-supporting hydrogels on addition of calcium nitrate. At 0.02 wt%, the sample partially passes the inversion vial test (Fig. 4.1) and oscillatory rheology suggests a weak hydrogel with storage modulus, G′ (16 Pa), an order of magnitude above the loss modulus, G″ (1.6 Pa). Further details of the hydrogels mechanical properties are discussed below. The minimum gelation concentration (mgc) of 2NapFF is assigned to a concentration of 0.02 wt%. Interestingly, this value is just above the solution phase cmc_1 (0.011 ± 0.0037 wt%), identified in Chapter 3.

Typically, gels are formed where cross-linked one directional structures are present, such as in the case of an entangled worm-like micelle phase, a phase here existent

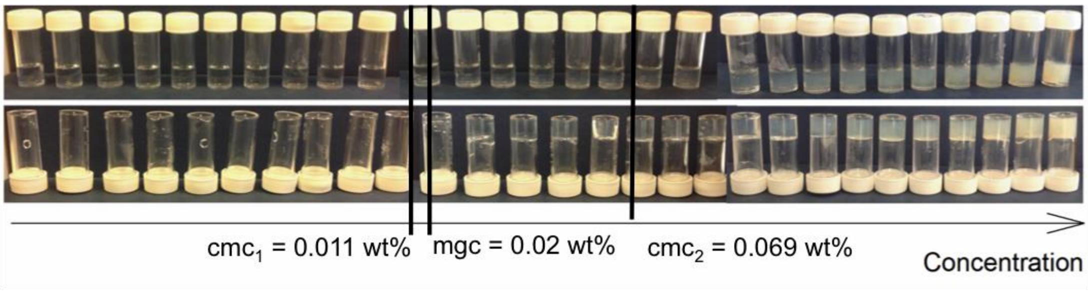

Figure 4.1 - Inversion vial test for 2NapFF solutions on addition of calcium nitrate at a molar ratio of 2:1 calcium to 2NapFF; the samples are 2NapFF concentrations of, from left to right, 0.001, 0.002, 0.003, 0.004, 0.005, 0.006, 0.007, 0.008, 0.009, 0.01, 0.02, 0.03, 0.04, 0.05, 0.06, 0.07, 0.08, 0.09, 0.1, 0.2, 0.3, 0.4, 0.5, 0.6, 0.7, 0.8, 0.9 and 1.0 wt%. In the top row, the samples are standing in the upright position and in the bottom row, the samples are inverted. The vertical lines indicate the corresponding concentrations indicated below.

above cmc_2.[11–15] Here, at concentrations just below the cmc_2, gels are also formed (Fig. 4.1). As shown in Chapter 3, between cmc_1 and cmc_2, possibly both spherical micelles and some worm-like micelles exist and, only from the cmc_2 are worm-like micelle dominant. This result points towards actual structural transformations when the calcium salt is added and the gelation is not merely a result of “locking in” the micellar structures, as was first suggested by our group.[5] “Locking in” is defined by a self-assembly stabilisation between the gelator carboxylic group, negatively charged, and the salts, positively charged, with the formation of ionic bonds. Ulijn *et al*. recently reported using data from prism-based computational modelling of one self-assembled fibre that the nanostructures of peptide-based low molecular weight gelators may well be in either a kinetically trapped state or a thermodynamic minimum.[16] Our experimental results agree with their predictions, which suggest that a combination of thermodynamics and kinetics can govern the metastable state of peptide hydrogels.[17] Sphere-to-worm micellar transitions with increasing concentration have been observed previously, for example in aqueous solutions of cetyltrimethylammonium bromide (CTAB).[18] Armes *et al*. have also investigated block-copolymer systems which show sphere-to-worm and worm-to-vesicle morphological transitions with a small change in block-copolymer structure.[19,20] Here, we appear to be in the presence of a sphere-to-worm transition between the cmc_1 and cmc_2, when salt is added to the solutions to form gels. The presence of spherical structures at high pH in this concentration region between the cmc_1 and cmc_2 is based on (1) the presence of these two phase transitions by conductivity measurements (Fig. 3.5, Section 3.3.1.2.), (2) SANS data suggesting there are two phases in a pD 10.5, 0.3 wt%, 2NapFF solution, worm-like phase and a spherical micellar phase (suggesting a spherical phase could precede the worm-like phase at lower concentrations)[21] and (3) cryo-TEM from similar gelators at high pH and during pH decrease showing spherical micellar phases, as discussed in Chapter 3.[6,22] The presence of worm-like structures at the hydrogel phase is verified with microscopy and suggested by the inversion vial test and rheology measurements.

4.3.1.2 Frequency and strain sweep rheology of 2NapFF hydrogels

Based on the results of the inversion vial tests (Fig. 4.1) and findings from other groups as described above, we decided to investigate in detail the mechanical properties of 2NapFF Ca-hydrogels with concentrations in the range from 0.001 wt% to 1.0 wt%. Fig. 4.2 and Fig. 4.3 show the frequency-sweep data of 2NapFF in this concentration range at a 0.5 % strain, which is in the linear viscoelastic region (LVR) for the hydrogels formed. The mechanical strength of a material can be represented by the complex shear modulus, G* ($|G^*| = |G' + i\ G''|$). G′ is a measure of the elasticity of the sample, the in-phase or solid-like component and G″ measures the damping of the oscillations, the out-of-phase or liquid-like component.[23] The complex shear modulus describes the storage and dissipation in constant amplitude while the sample is in an oscillating strain field.[24] This parameter was used to compare the mechanical properties of the solution state with the properties of the hydrogel state. A summary of these frequency-dependence results at a strain of 0.5 % is shown as a function of storage modulus (G′) and loss modulus (G″) in Fig. 4.4a and in terms of G* in Fig. 4.4b.

The frequency-sweep results below 0.02 wt% in Fig. 4.2 show an irregular the behaviour characteristic when the torque is below the acceptable 5 μN.m. These were shown here for comparison purposes with the other data sets only. Below this concentration, G′ and G″ are low and below the rheometer detection limit at 0.5 % strain. As shown in the inversion vial image in Fig. 4.1, these were liquid samples. At 0.02 wt%, in the low shear rate region, G′ and G″ are frequency-independent, with G′ one order of magnitude above G″, which indicates the formation of a weak gel (Fig. 4.2). This agrees with our observation of mgc at this concentration (Fig. 4.1). At high frequencies in some cases, such as 0.02 and 0.06 wt%, the data shows an hydrogel slippage artefact, with only a detectable G″, cross-over of G″ and G′ or no data collected. Above 0.02 wt%, the G′ and G″ both gradually increase with an increase in concentration from approximately 10 Pa (G′) and 1 Pa (G″), to approximately 100 kPa (G′) and 10 kPa (G″) at 1.0 wt% respectively (Fig. 4.3 and Fig. 4.4a). This shows an exceptional four orders of magnitude increase in mechanical properties over a two orders of magnitude increase in concentration (Fig. 4.4). Here, tan δ (the damping factor, calculated by G″ divided by G′) is 0.13 ± 0.03 across the concentration range from 0.05 to 1 wt%, which suggests that the gel networks have similar microstructural features linked with their viscoelastic behaviour, e.g. elasticity or response to deformation. Further details of the structural sizes of the networks are given below and in Chapter 5 from microscopy results.

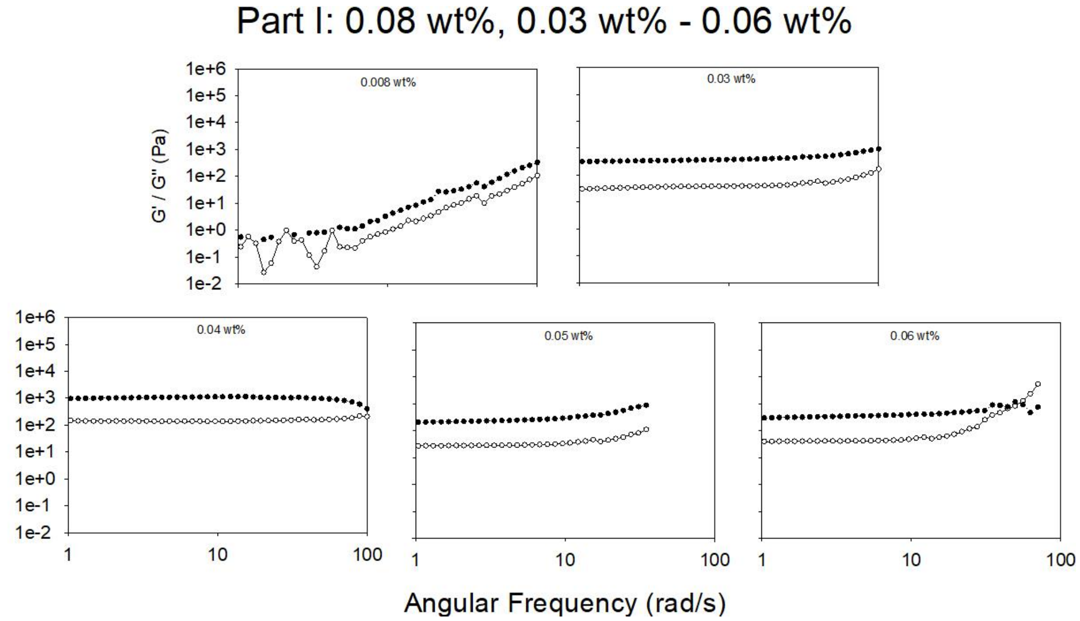

Figure 4.2 – Frequency sweeps, at strain of 0.5 %, of Ca-hydrogels of 2NapFF from 0.001 wt% up to 0.06 wt% at pH 10.5 and 25 °C. In all cases, the closed symbols represent G´ and the open symbols refer to G″. Some data is not detected, out-of-range, possibly because of hydrogel slippage artefacts. The set of measurements at the torque limits from 0.001 wt% to 0.03 wt% are shown in the appendix (Fig. 4.15).

Despite a relatively constant tan δ across the concentration range, the number of cross-links in the network increases with an increase in concentration. In Fig. 4.4b, the increase in G* with increasing 2NapFF concentration appears to have three concentration dependent regions. In the first region, from 0.001 wt% to 0.01, no gels are formed and the mechanical properties are close to those of water. In the second region, from 0.02 wt% to 0.09 wt%, weak gels are formed, after a sudden increase in G* from the previous concentration region. In the third region, from 0.1 to 1.0 wt%, the increase in G* can be fitted with an exponential equation of the form $y = a + b\ e^{c}$.

The frequency-sweep measurements have a best fit to a power exponential with an exponential coefficient of 1.99. This equation was used to fit the similar supramolecular polymerization of the biological inner cell network (F-Actin filaments Gels).[1] In this work, Mackintosh *et al*. fitted the mechanical properties for

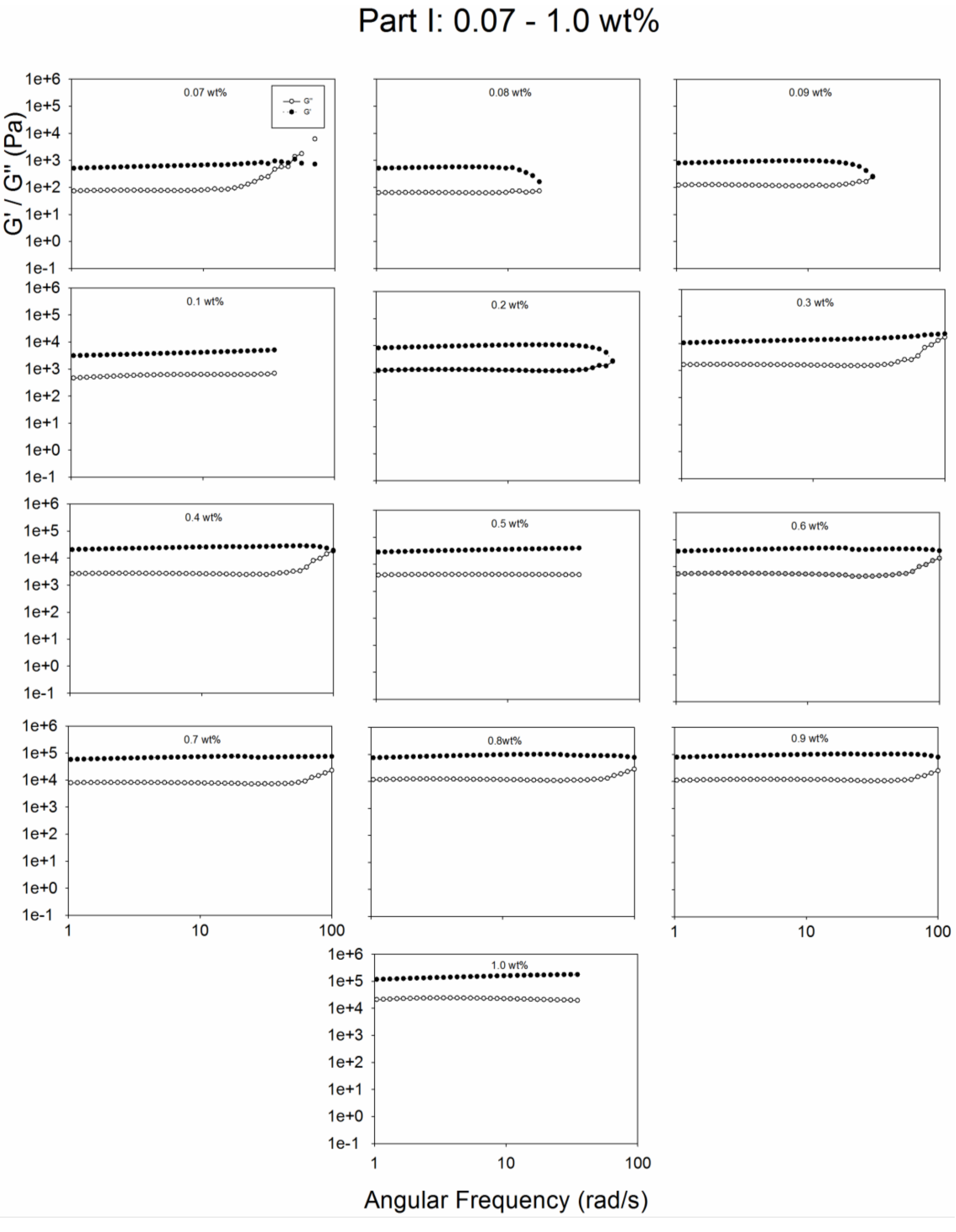

Figure 4.3 – Frequency sweeps, at strain of 0.5 %, of Ca-hydrogels of 2NapFF from 0.07 wt% up to 1.0 wt% at pH 10.5 at 25 °C. In all cases, the closed symbols represent G´ and the open symbols refer to G″. Some data is not detected, out-of-range, possibly because of hydrogel slippage artefacts.

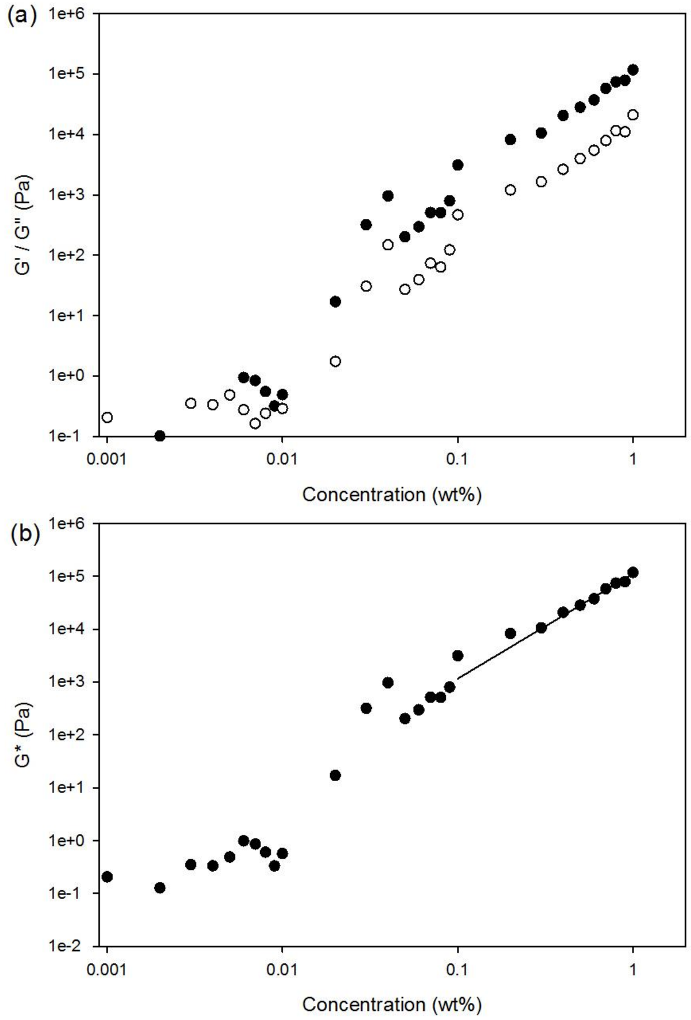

Figure 4.4 – Summary of frequency sweeps analysis of Ca-Hydrogels of 2NapFF from 0.001 wt% up to 1.0 wt% at pH 10.5, with 0.5 % strain, 10 rad/s frequency and 25 °C. Readings of absolute values were taken from the frequency of 10 rad/s of the solution frequency sweep plots. The exponential power fit coefficient obtained here in the region from 0.1 and 1.0 wt% was 1.99. In all cases (a), the closed symbols represent G′ and the open symbols refer to G″. In (b), G* is the complex modulus. Both axes are in the Log-scale.

F-actin gels, which scale with concentration, to this exponential equation with c ≈ 2.2. An exponential factor significantly above 2 is typical of colloidal gels, while with c ≈ 2, the system can be described as typical cross-linked networks and biopolymer gels. For 2NapFF hydrogels, an exponent of 1.99 was found for the concentration region between 0.1 to 1.0 wt%, with an $R^2 > 98$ %. This result is in agreement with Mackintosh *et al*. findings and suggests the presence of a cross-linked network typical of biopolymer gels.[1]

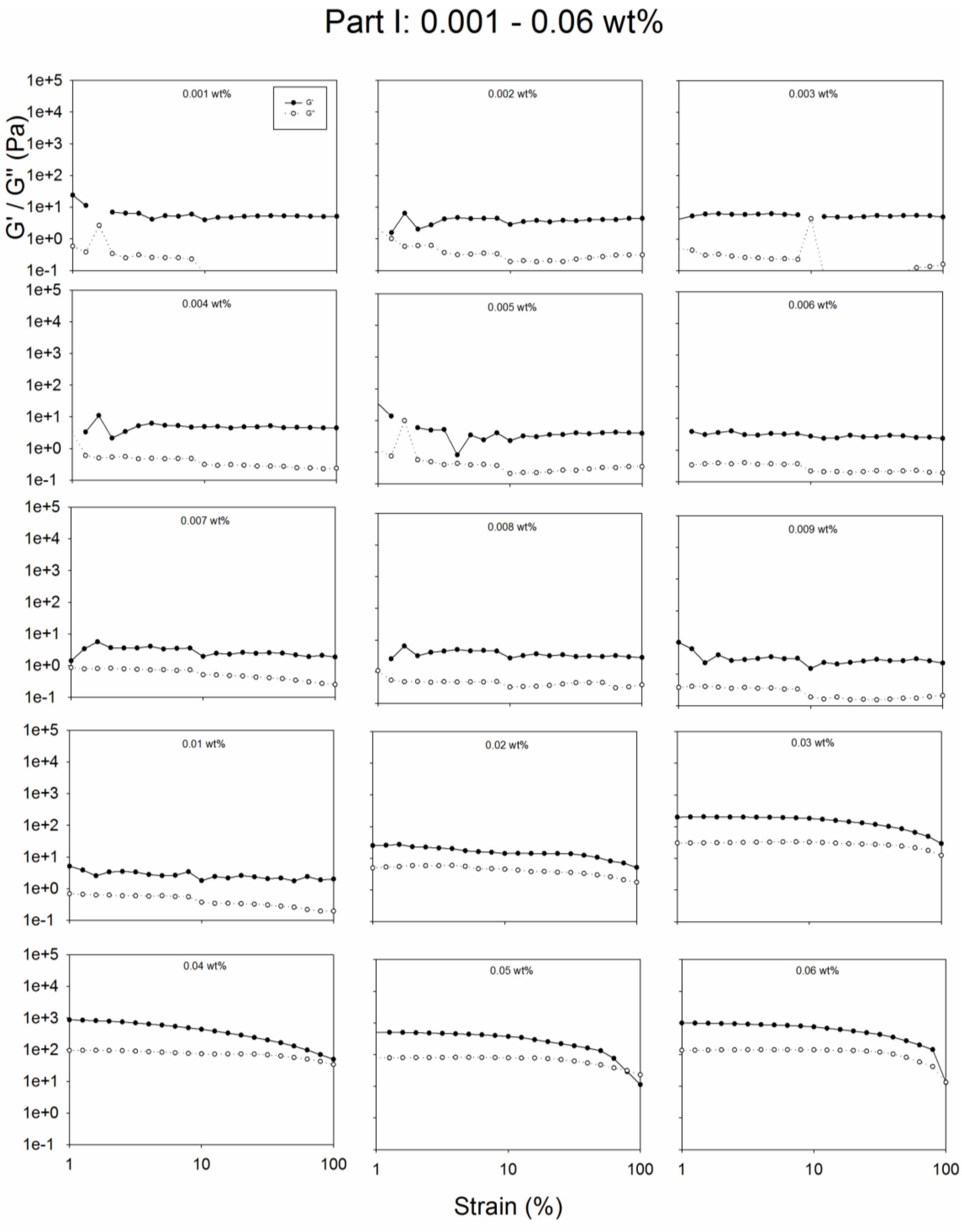

Figure 4.5 – Strain sweeps, at frequency of 10 rad/s, of Ca-hydrogels of 2NapFF from 0.001 wt% up to 0.06 wt% at pH 10.5 at 25 °C. In all cases, the closed symbols represent G´ and the open symbols refer to G″. Some points are omitted because the rheometer could not pick up the G´ or G″ under those measurement conditions.

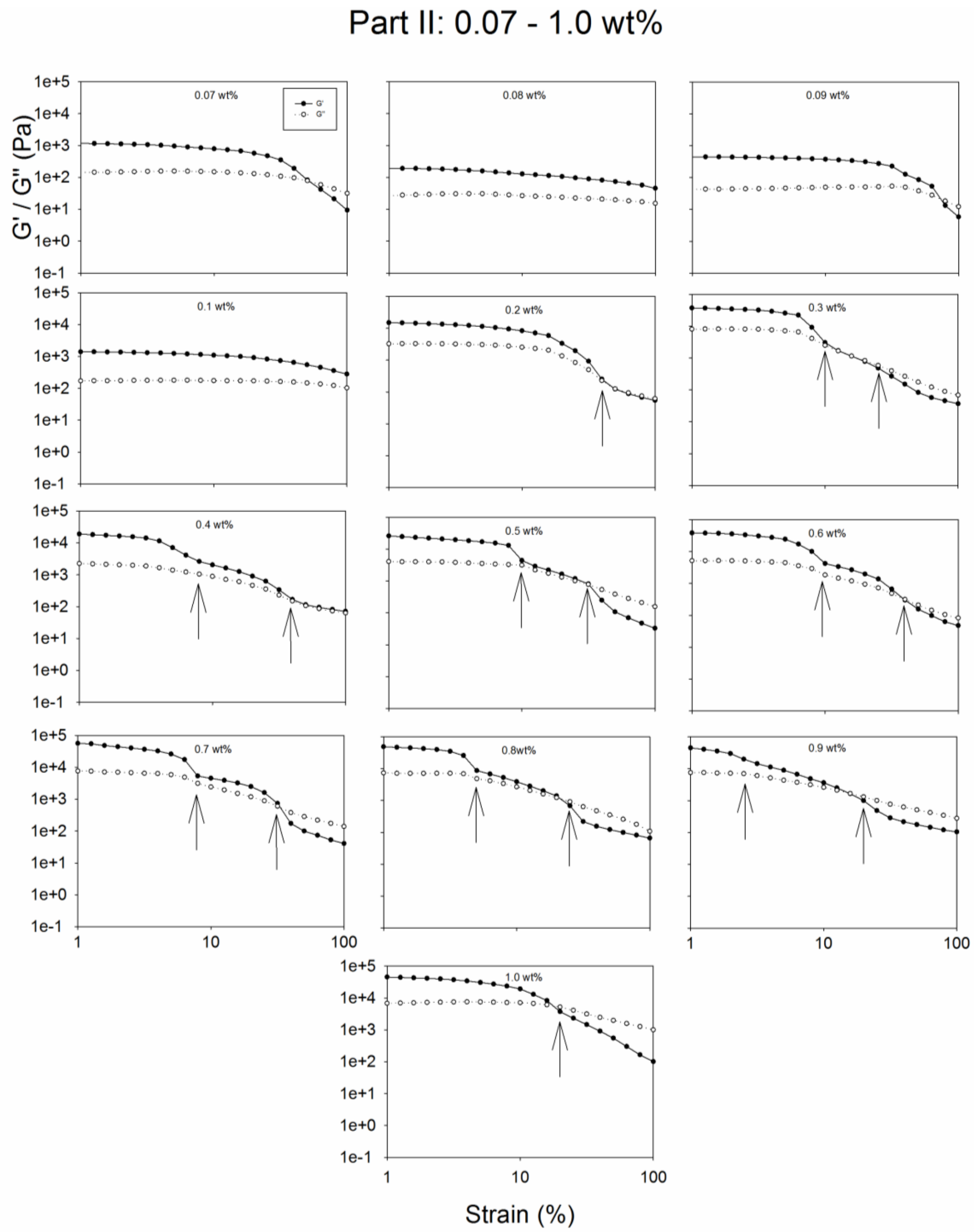

Figure 4.6 – Strain sweeps, at frequency of 10 rad/s, of Ca-hydrogels of 2NapFF from 0.07 wt% up to 1.0 wt% at pH 10.5 at 25 °C. In all cases, the closed symbols represent G´ and the open symbols refer to G″. The arrows indicate transitions in the strain-dependent G´ and G″.

Complementary to the frequency-sweep results, Fig. 4.5 and Fig. 4.6 show the strain-sweep data of 2NapFF at a frequency of 10 rad/s in the same concentration range studied above and a summary of these strain-sweep results is shown in Fig. 4.7.

The strain-sweep results showed a similar three-stage change in G* with an increase in concentration (Section 4.6, Appendix, Fig. 4.15). At lower concentrations, between 0.001 and 0.01 wt%, the samples are in a viscous liquid state (Fig. 4.5). At intermediary concentrations, between 0.01 and 0.1 wt%, the samples are hydrogels with increasing G´ and G˝ (Fig. 4.5 and 4.6). In this concentration range, an elasticity effect is visible for higher strains, above 10 % a decrease in the G´ and G˝, with G´ getting closer to G˝ indicates a transition from a hydrogel to a viscous liquid. However, in the third stage of higher concentrations, between 0.1 and 1.0 wt%, the results for high strains (above 10 %) show at least two kinds of network packing present, possibly because of the chical packing of the fibres. This can be observed by identifying three distinct strain dependent behaviours emergent with increasing concentration (Fig. 4.6, transitions delimited by the arrows). A first low strain (< 10 %) behaviour, shows the network is mostly strain-independent above 0.1 wt% (Fig. 4.6). On the other hand, the strain-sweep results in the concentration region between 0.3 wt% to 1.0 wt% show that near 10 % strain, G′ converges with G″ to make them approximately equal, typical of viscoelastic solutions (Fig. 4.6, arrow at the lowest strain value).[25] The mid shear rate behaviour is followed by a divergence of G′ from G″ towards lower values (Fig. 4.6, arrow at the highest strain value). This can be interpreted as a breakage point in the viscoelastic solution, which makes G′ progressively lower than G″ with the increase in strain. This effect was amplified with the increase in concentration of 2NapFF hydrogels, likely because of an increase in the number of nanofibres promotes more entangled domains that can break at higher length scales at progressively lower shears to relax the network.

4.3.1.3 2NapFF hydrogel recovery properties

The recovery properties of the hydrogels were investigated with a triple oscillatory shear measurement (See Materials and Methods, Section 4.5.2). The recovery results suggest that the supramolecular polymers restructure in the first 30 minutes (Fig. 4.7a). At later times, all samples that form hydrogels at 0.05 wt% and above remain constant up to 3 hours (Fig. 4.7b). A summary of the results is shown in Fig. 4.8, illustrating that at all the concentrations of 2NapFF, calcium hydrogels recover up to 100 % after a 100 s period of 100 % strain, when compared to their properties before the high strain region. These features are typical of supramolecular polymer systems and have also been previously reported for peptide gelators by our

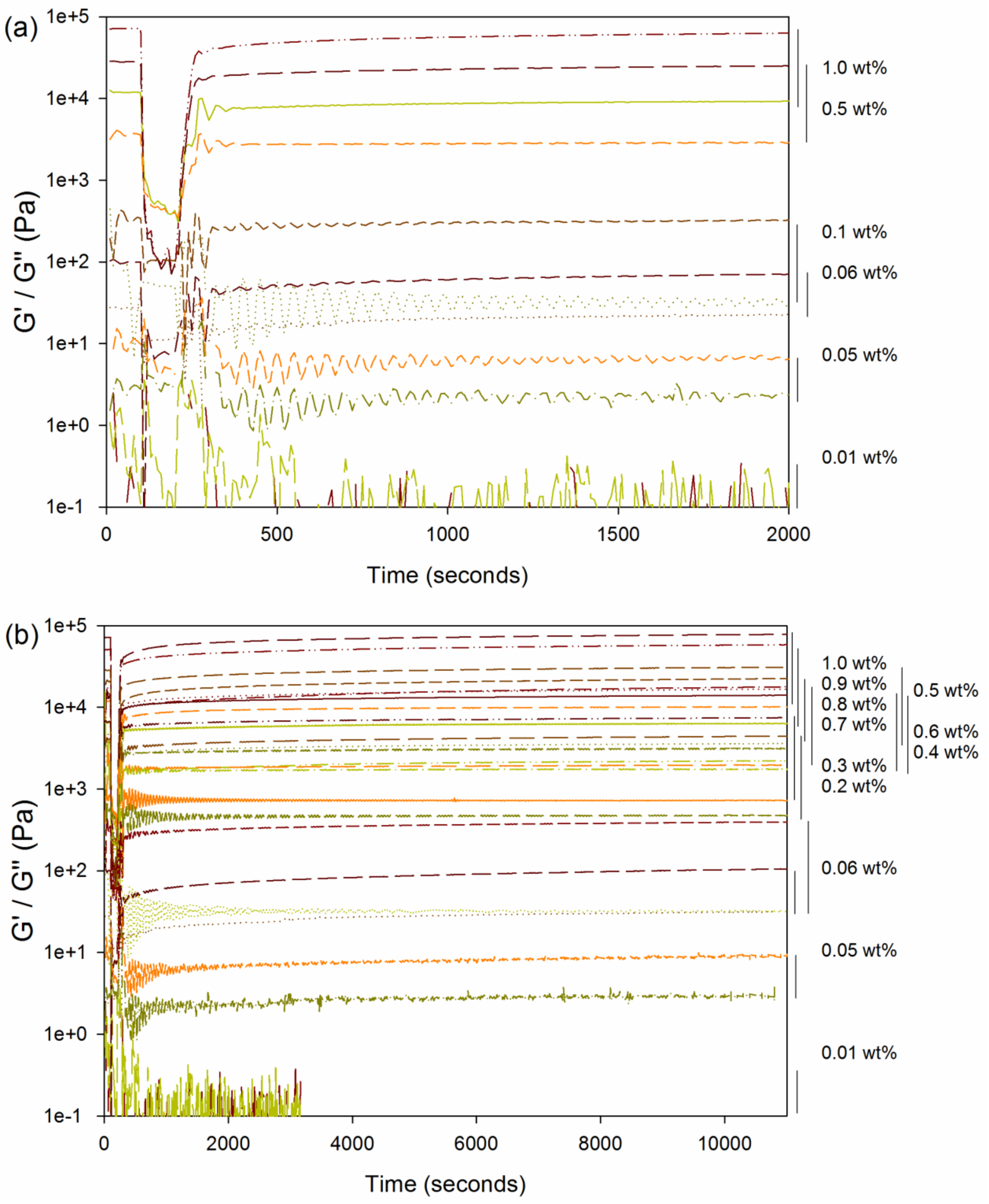

Figure 4.7 – Triple oscillation recovery tests (as described in Materials and Methods Section 4.5.2) for 2NapFF Ca^{2+} hydrogels formed with 2:1 Ca^{2+}/gelator ratio across a range of concentrations from 0.01 to 1.0 wt% at 25 °C. On the right side of the graph, a schematic legend shows a line guide between the G′ (top side of all lines) and G″ (bottom side of all lines) for each concentration. The recovery results are plotted for a selected number of samples at early time points, the first 33 minutes (a) and over a longer period of time, 3 hours (b). All hydrogels show full recovery (0.05 wt% and above).

and other groups.[6,26] In some cases, the recover percentage exceeds 100 % because the shear alignment features contribute to an apparent increase in G′ and G″.[25]

In analogy with the results of Pochan's group,[26] here we see the break in connectivity of the hydrogel is also linked to the rupture of the self-assembled network. The elasticity of the hydrogel allows its quick recovery, in the first few minutes after the cessation of the high shear. This quick recovery has been mentioned in drug delivery hydrogel studies for animal model trials as beneficial for the effective release of a drug with the designed profile of release (i.e. pharmacokinetics).[27]

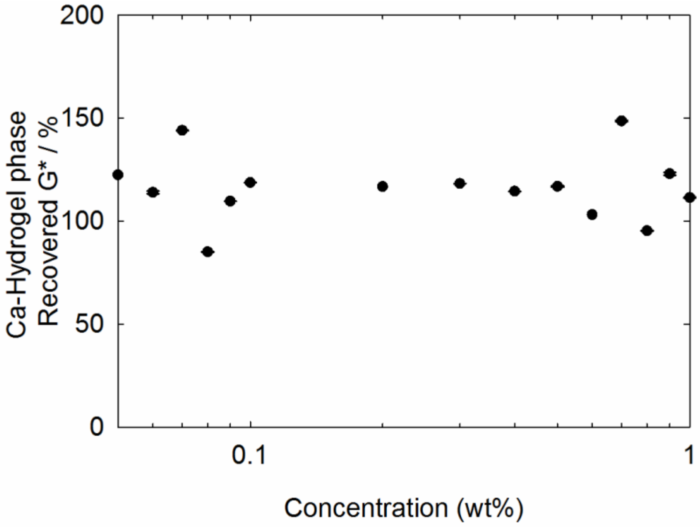

Figure 4.8 – Recovery percentage for the G* of the Ca-hydrogel phase at 20 thousand seconds (or at plateau) after cessation of high strain (100%), when compared with the starting G* at the low shear of 0.5 % and 25 °C. The recovery protocol is described in the Materials and Method Section 4.5.2.

4.3.1.4 Powder x-ray diffraction of 2NapFF hydrogels

There has been a growing discussion in the peptide materials field about the degree of crystallinity in the kinetically trapped hydrogels. Techniques such as imaging through cryo-TEM, electron diffraction through TEM and fibre x-ray crystallography suggest that there are common periodicities in different directions of self-assembled fibres that constitute the structure of hydrogels.[28–30] Therefore, this indicates that there are crystal-like features. However, the mechanical properties of these materials suggest a non-crystalline phase is present (Fig. 4.6). Figure 4.9 shows the powder x-ray diffraction (pXRD) for 2NapFF hydrogels dried after 24 hours (xerogels). The xerogels measurements show a broad peak at approximately 4.710 ± 0.075 nm (Fig. 4.9) which is in the same region as crystal structures of similar *N*-protected dipeptides obtained through fibre XRD and transmission electron microscopy.[29,31,32] Here, the broadness of this peak indicates the structure is semi-crystalline.

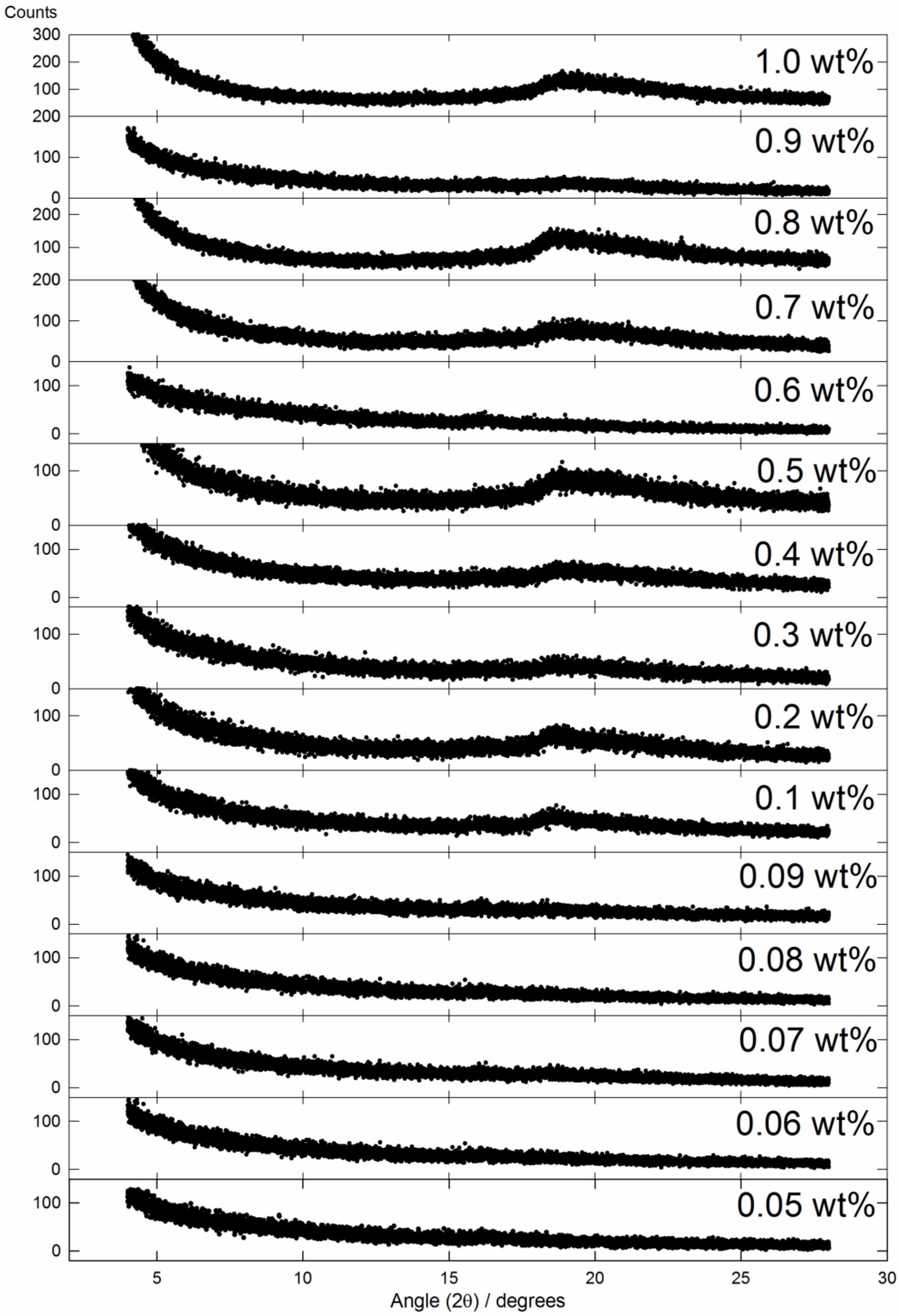

Figure 4.9 – Powder X-ray Diffraction (pXRD) data for dried gels (xerogels) formed from 2NapFF after addition of $Ca(NO_3)_2$. Gels were allowed to form for 24 hours before a sample was removed and dried for pXRD measurements. From bottom to top, the concentration of 2NapFF increases. An average peak of 4.710 ± 0.075 nm can be obtained from the samples from 0.1 to 1.0 wt% (within the error being the instrument resolution). The y-axis is plotted in different scales, because the intensity depends on the amount of material in the x-ray beam for a fixed amount of time (60 min).

In conclusion, our pXRD results suggest by analogy that the hydrogels may have both crystal-like properties because of the similarity to peaks obtained for crystals of similar gelators and amorphous material properties because of the broadness of the peak in the pXRD.

An average peak of 4.710 ± 0.075 nm can be obtained from the samples from 0.1 to 1.0 wt% (Fig. 4.10). Here, this measured distance is shown in the pXRD as a broad diffraction peak indicative of an amorphous structure. Interestingly, if we plot the peak position obtained with 3 significant digits (Software X'Pert MDP) as function of concentration, it is possible to set the measurements into two groups (Fig. 4.10). One group at a low concentration range, with the first three peaks with a position above the overall average of 4.72 nm and a second group for the following peaks (above 0.3 wt%) below 4.72 nm. However, it is important to note that the instrument-measured resolution is 0.075 nm and below 0.1 wt%, no features could be identified. At present, the results could be interpreted in one of two ways.

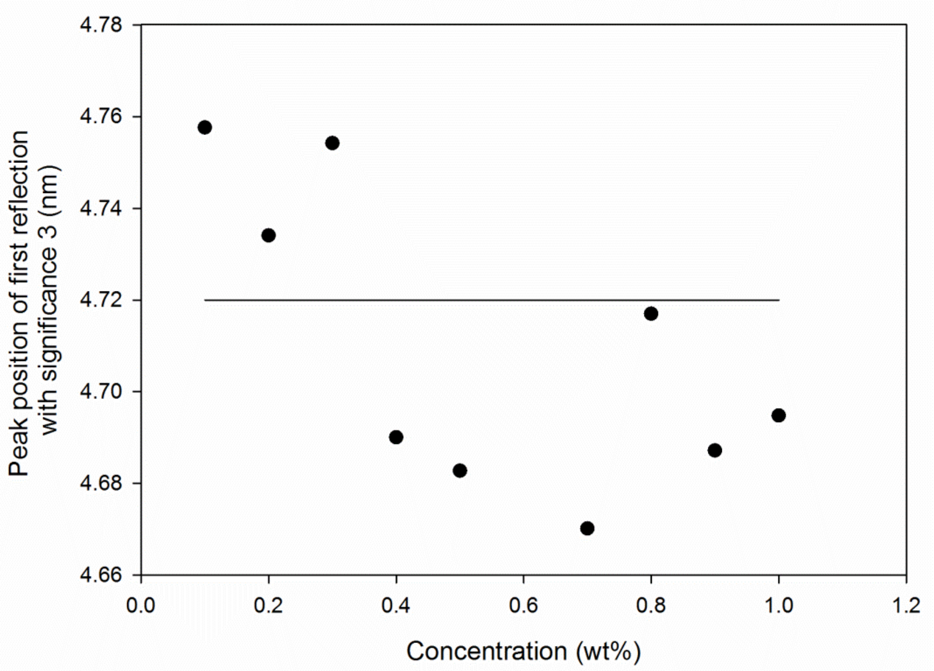

Figure 4.10 – Analysis of powder X-ray scattering peak of Ca-hydrogels 2:1 molar ratio of Ca^{2+} to 2NapFF. The peak position was obtained (Software X'Pert MDP) as function of concentration. The line is the average value of the 1st peak position for each concentration. The instrument resolution is 0.075 nm.

First, these peaks could result solely from the drying of the hydrogels and therefore, not be indicative of the aqueous phase. This would be supported by the fact that these peaks are not present if we measure a thin aqueous film of hydrogel in the pXRD (results not shown). This first interpretation cannot be refuted by the absence of peaks in the aqueous hydrogel phase at the range of concentrations studied here because this type of sample will have a reduced number of fibres in the path of the X-ray beam, therefore the scatters may not be sufficient to result in a measurement. The second interpretation is that, since this peak appears in the same region as the main meridional reflection of fibre diffraction patterns and crystals obtained with similar gelators,[29,31,32] the peak could represent the average distance in the fibre axis of the aqueous state. However, these are xerogels, which have dried overnight at open air, therefore their structure could be transformed.[33]

It is important to note that the distance of 4.72 nm obtained here is slightly above the results obtained for the small angle neutron scattering (SANS) data fit to a flexible cylinder model found for the radius of the Ca-hydrogel through of 3.7 ± 0.3 nm.[21] This SANS result suggests that further SANS experiments on dried and wet-hydrogels may reveal the nature of this scattering intensity features found in both data. At present, this 4.72 nm is likely to be the size of the primary worm-like assembled structures once the calcium is added to the solution.

4.3.2 Rheology correlations between the solution phase and the Ca-hydrogel phase

The damping factor, tan δ (or phase lag), is a measurement of the relative contribution of elasticity to viscosity under the conditions measured.[24] Peptide hydrogels of concentration 0.5 wt% or above have viscoelastic behaviour with a tan δ close to 0.1. These hydrogels do not show a zero-shear viscosity, hence these indicate a solid structure at rest.[25] If tan δ is below 1, the sample is a typical gel, while the closest to 1 or above, the more liquid-like the sample is relative to solid-like behaviour. In Fig. 4.11a, the tan δ values measured for the solution phases of 2NapFF are plotted against the tan δ values for the corresponding solutions after the addition of calcium salt. This graph shows that tan δ is concentration dependent in the solution phase and concentration independent in the hydrogel phase. This agrees with a lower energy minimum for the kinetically trapped hydrogels relative to the corresponding solution phase.

In Fig. 4.11b, the G* of the solution phase is plotted against G* of the corresponding hydrogel phase. The samples can be grouped into three regions (Fig. 4.11b), as observed for the hydrogel phase in Section 4.3.1. In the first region, the micellar solutions have a G* below 17 mPa. No hydrogel is formed on addition of calcium nitrate in this concentration range. In the second region, the solution phase has a G* between 15 to 20 mPa. These solutions form weak hydrogels on addition of calcium nitrate. Finally, there is a third concentration region where the solutions have a G* between 20 mPa to 400 mPa, which forms strong hydrogels, with a G* of between 13 – 40 kPa (Fig. 4.11b). Overall, these results show a G* range of four orders of magnitude between the formation of weak and strong hydrogels. This range of properties is preceded by a solution phase with a smaller range of less than two orders of magnitude in G*. Furthermore, the results show that above the cmc_1, 2NapFF can form hydrogels. However, only above the cmc_2 (Chapter 3), in this case the worm-like micellar region, do the strongest hydrogels form. Thus, the solution phase of 2NapFF is likely structurally connected with the hydrogel phase.

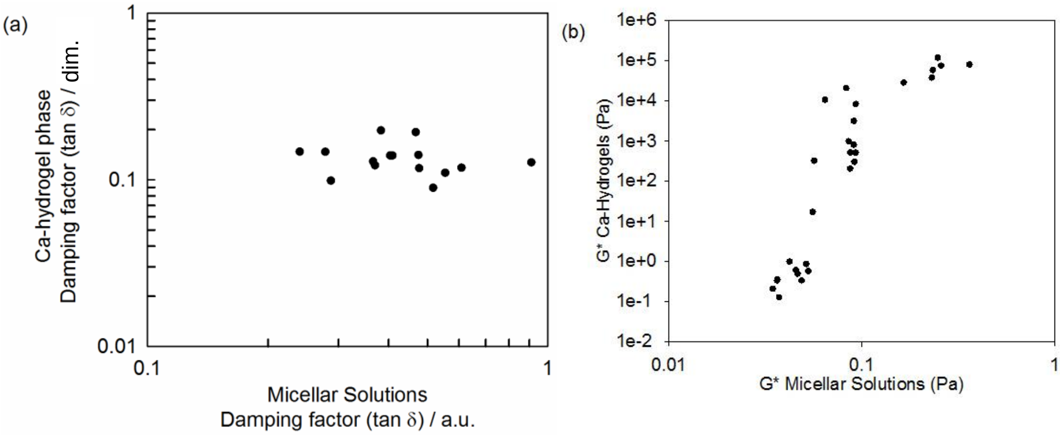

Figure 4.11 – Mechanical correlation for 2NapFF solutions and hydrogels formed on addition of calcium nitrate at 2NapFF concentrations of 0.001, 0.002, 0.003, 0.004, 0.005, 0.006, 0.007, 0.008, 0.009, 0.01, 0.02, 0.03, 0.04, 0.05, 0.06, 0.07, 0.08, 0.09, 0.1, 0.2, 0.3, 0.4, 0.5, 0.6, 0.7, 0.8, 0.9 and 1.0 wt%. (a) Correlation between the tan δ of 2NapFF solutions and the corresponding tan δ of 2NapFF hydrogels, all obtained from frequency sweeps in the strain-independent region from 0.05 to 1.0 wt%. Each measurement point is averaged over 40 consecutive measurements of G′ and G″ of the solution phase and hydrogel phase, by the rheometer with a tolerance calibrated below 5 %; dim. stands for dimensionless. (b) Correlation between G*’s of the solution and the hydrogel phase from 0.001 wt% to 1.0 wt%. Axes are all plotted in logarithmic scale.

Ideally, we would investigate the transformations between the solution phase between cmc_1 and cmc_2 to comprehend if any structural reorganisation is occurring upon calcium salt addition. Unfortunately, the low concentrations here prevent the use of several techniques (e.g. ^{1}H-NMR spectroscopy, confocal microscopy, FTIR) that are frequently used to investigate the molecular assembly of such dipeptides. In this case, a cryo-Transmission Electron Microscopy (cryo-TEM) could result in further support to the sphere-to-fibre transformation upon gelation.[34] However, this instrumentation was not accessible to us at the present time.

4.3.3 Molecular structure correlations between the solution phase and the Ca-hydrogel phase

In order to understand if a molecular transition could be present in the case of 2NapFF between the cmc$_1$ and cmc$_2$ and also to characterise the molecular packing structure, FTIR spectra were collected in D_2O (Section 4.6, Appendix, Fig. 4.16 and Fig. 4.17, for the complete data set of the solution and hydrogel phase, respectively). The baseline corrected data for both the solution and hydrogel phase is summarised in Fig. 4.12 for selected concentrations of 0.05 wt%, 0.1 wt% and 0.5 wt%.

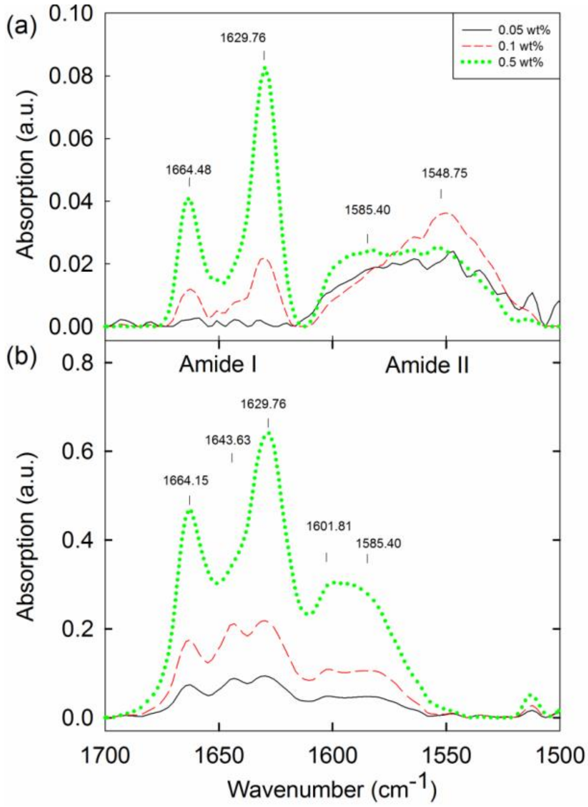

Figure 4.12 – FTIR spectra of (a) 2NapFF solutions at high pD 11.5 ± 0.5 (0.05 to 0.5 wt%) and (b) the corresponding hydrogels (0.05 to 0.5 wt%) up to the lower limits of detection. For the complete data set for the solution and gel phase, see Fig. 4.13 and Fig. 4.14. All data in this Figure was baseline corrected in OPUS 7.0 software with the baseline concave rubberband correction method.

The data for the solution phase below 0.1 wt% (Fig. 4.12a) did not show the presence of ordered molecular packing. Between 0.1 and 1.0 wt%, peaks at 1629 cm^{-1} and

1664 cm^{-1} were observed (Fig. 4.12a). In the case of the corresponding hydrogels, peaks at 1629 cm^{-1} and 1664 cm^{-1} are also present across the concentration range from 0.01 to 1.0 wt% (Fig. 4.12b). These peaks suggest the presence of β-sheet structure at both the solution phase and the Ca-hydrogel phase.[12,35] These are similar peaks to dipeptide gelators with a protective 9-fluorenylmethyloxycarbonyl group (Fmoc).[28,36] Overall, the molecular structure appears preserved with the transition from solution phase to hydrogel phase for concentrations above 0.3 wt% (Section 4.6, Fig. 4.16 and Fig. 17). However, for concentrations below 0.3 wt%, a distinct peak is visible at 1643 cm^{-1} in the hydrogel, which is not present in the solution. These IR results imply that there is possibly a molecular packing and structural transformation, at least between 0.1 wt% and 0.3 wt% when the solution phase is triggered to form a hydrogel. From data for polypeptides, these peaks would be assigned to β-sheets (1629 cm^{-1}) and random coil structures (1643 cm^{-1}),[37] although our group highlighted previously that it is not clear if such direct assignment is possible for dipeptides.[12,35,38] In addition, peaks at 1548 cm^{-1} and 1585 cm^{-1} in the solution state, and at 1585 cm^{-1} and 1602 cm^{-1} in the hydrogel state can be associated with different naphthalene and phenylalanine packing.[37,39]

4.3.4 Microstructure correlations between the solution phase and the Ca-hydrogel phase

To further compare the solution and gel phases, we investigated the hydrogels by microscopy. Optical microscopy did not show any visible structures, either under bright field or cross-polarised light (data not shown). Confocal microscopy (with Nile blue staining) showed that the hydrogels are formed of hierarchical nanofibre structures (Fig. 4.13).

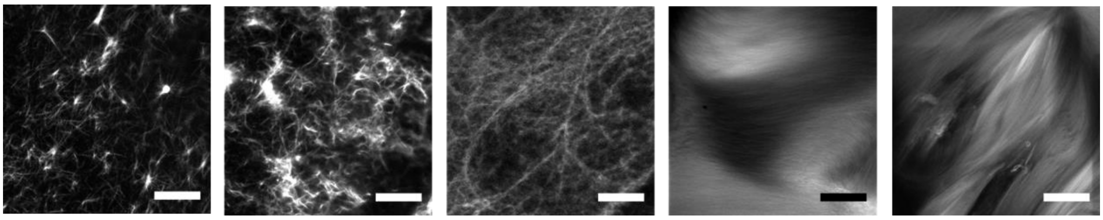

Figure 4.13 – Confocal Micrographs of aqueous 2NapFF calcium nitrate hydrogels at concentrations of 0.05, 0.1, 0.3, 0.5 and 1.0 wt% (left to right), with 0.0002 M Nile Blue staining, after 24 hour incubation at RT (22 °C) the solutions were gelled with 0.02 M $Ca(NO_3)_2$. Images were taken after 4 days of incubation in sealed confocal glass dishes. All scale bars are 20 μm.

These results suggest that the worm-like micellar structures previously observed in the solution phase now become hierarchically packed into large bundles of highly entangled nanofibres with high persistence length (at the microscopic level, over millimetre range). As stated in Chapter 3, confocal microscopy has a lower limit of resolution of the order of 0.7 – 1.0 μm, depending on the experimental conditions and material interactions with the dye. Here, we could not collect any meaningful data below 0.05 wt%.

Here, it was obtained by pXRD an average periodicity in the dried hydrogel of 4.7 nm (Fig. 4.10). At 1.0 wt%, an average mesh size of $\xi = 10 \pm 5$ μm was measured by confocal microscopy (Fig. 4.13). These results and further structural analysis are discussed in Chapter 5 with the use of atomic force microscopy (AFM), SEM and fibre image analysis software.

The conclusions of this Chapter results are summarised in Fig. 4.14, which shows the structures and mechanical properties correlations between solution phases and hydrogels phases formed by 2NapFF gelator.

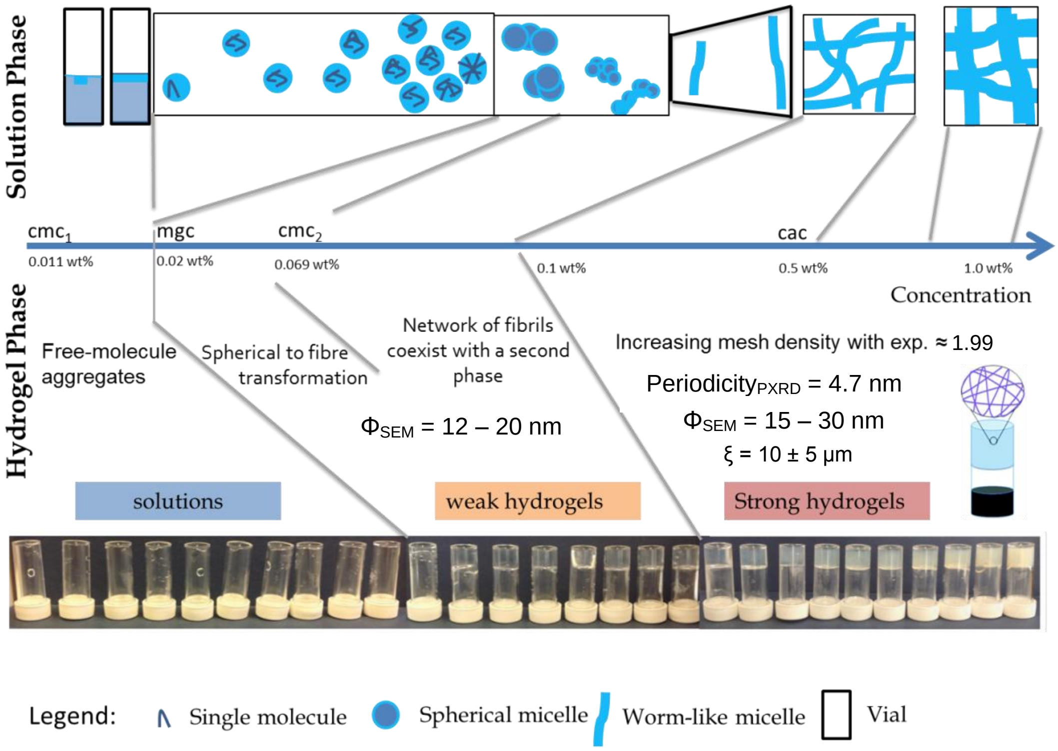

Figure 4.14 – Scheme of the link between solution phase and hydrogel phase. A summary of the confocal microscopy and SEM (Chapter 5) results is shown for the Ca-hydrogel phase.

4.4 Conclusions

A link between the solution phase properties and the hydrogel properties was found for 2NapFF with the Ca-switch methods across a concentration range from 0.001 to 1.0 wt%. The molecular packing present in the solution phase is already the characteristic β-sheet aggregates also measured for the Ca-hydrogel phase, for concentrations above 0.3 wt%. However, for lower concentrations, a sphere-to-worm transition occurs between the cmc_1 and cmc_2 as well as possible molecular packing transformations. The concentration in the worm-like micellar region of 2NapFF is correlated with the complex modulus by an exponential function with a 1.99 coefficient, this is typical for cross-linked networks and biopolymer gels.[1] In Chapter 5, further detailed wet-atomic force microscopy (wet-AFM), scanning electron microscopy (SEM) and imaging analysis were used to further investigate the structural features of the solutions and hydrogels at different length scales.

4.5 Materials and Methods

4.5.1 Preparation of Salt-triggered Calcium Nitrate hydrogels

These pre-gelation solutions were prepared by the method described in Chapter 3, Section 3.5.1, To trigger gelation, aliquots of a $Ca(NO_3)_2$ solution (either 20 mg/mL or 200 mg/mL) were added to dissolve the peptide, by pipetting 5 uL aliquots on top of the peptide solution, such that the final ratio of calcium ions to peptide was 2:1. The samples were left to stand for an incubation period of 24 hour at a room temperature of 22 °C. No dilutions were performed to prepare samples at different concentrations. Each sample was directly prepared at a specific concentration.

4.5.2 Rheology

Dynamic rheological experiments were performed using an Anton Paar Physica MCR301 rheometer. The rheometer was calibrated for inertia and motor adjustment every 5 days or immediately before each measurement for the solution phase measurements in order to obtain accurate measurements in the low viscosity and low torque region, on recommendation by the manufacturer. These calibrations resulted in improved instrument resolution at low torque. All measurements were conducted at 25 °C. For the hydrogels, strain and frequency-sweep measurements were conducted in a vane-cup measurement system (Anton Paar ST10-4V-8.8/97.5) and samples were prepared in a plastic Sterlin cup (7 mL volume) and incubated at ≈ 22 °C for 24 hours before each measurement. The frequency-sweep hydrogel measurements were conducted at a constant strain of 0.5 %. The frequency-sweep measurements showed no significant variation in the storage modulus (G′) and the loss modulus (G″) between a strain of 0.1 and 0.5 %. The choice of 0.5 % strain was based on the attempt to be in the viscoelastic region for the Ca-hydrogel systems, whilst still being able to conduct the measurement in a practical time and investigate the material properties of the bulk and not just the surface.[40] No restrictions were made on the time needed to reach each measurement point (instrumental average over 40 recordings). To ensure the frequency measurements were carried out in the linear viscoelastic regime, strain-sweep measurements were performed for the hydrogels at a static frequency of 10 rad/s. For each sample, G′, G″ and the complex modulus (G*) were measured as appropriate.

Recovery measurements were conducted using a triple oscillation program of 0.5 % strain for 100 seconds, 100 % strain for 100 seconds and then recovery at 0.5 % strain recorded until a plateau was reached (which was monitored over 3 hours). All recovery measurements were conducted at a frequency of 0.5 rad/s.

4.5.3 Laser scanning confocal microscopy

Confocal microscopy images were obtained on a Zeiss LSM510 and a Plan-Apo 100x (1.4 NA oil) objective. Nile Blue fluorescence was excited with a 633 nm Helium Neon laser and emission detected between 638 and 758 nm using a pinhole diameter of 1 Airy unit (approx. 0.8 μm resolution). The hydrogel membrane was prepared as described previously, including a 0.001 M Nile Blue in the initial solution (pipetting a selected amount from a 0.01 M stock solution). Typical images selected from more than 50 images captured were chosen and measured for this study. The images were analysed using the Zeiss AIM software (Zeiss, Jena, Germany) and ImageJ software[41].

4.5.4 Fourier transform infrared spectroscopy (FTIR)

A Bunker Tensor 27 spectrometer at a resolution of 2 cm^{-1}, averaging over 64 scans from 4000 cm^{-1} to 800 cm^{-1} was used to conduct these experiments. The hydrogels were prepared with D_2O, NaOD and DCl for these experiments as described in Section 4.5.1.

4.5.5 Powder X-ray Scattering

2NapFF xerogels were prepared by open air drying over 2-5 days a scooped amount from prepared hydrogel (2 mL total volume) prepared as described above in Section 4.5.1. Samples were analysed in an Xpert-Pro diffractrometer system in high throughput transmission aluminium stage with a minimum step size of 0.01 ° with θ from 4° to 28°.

4.6 Appendix

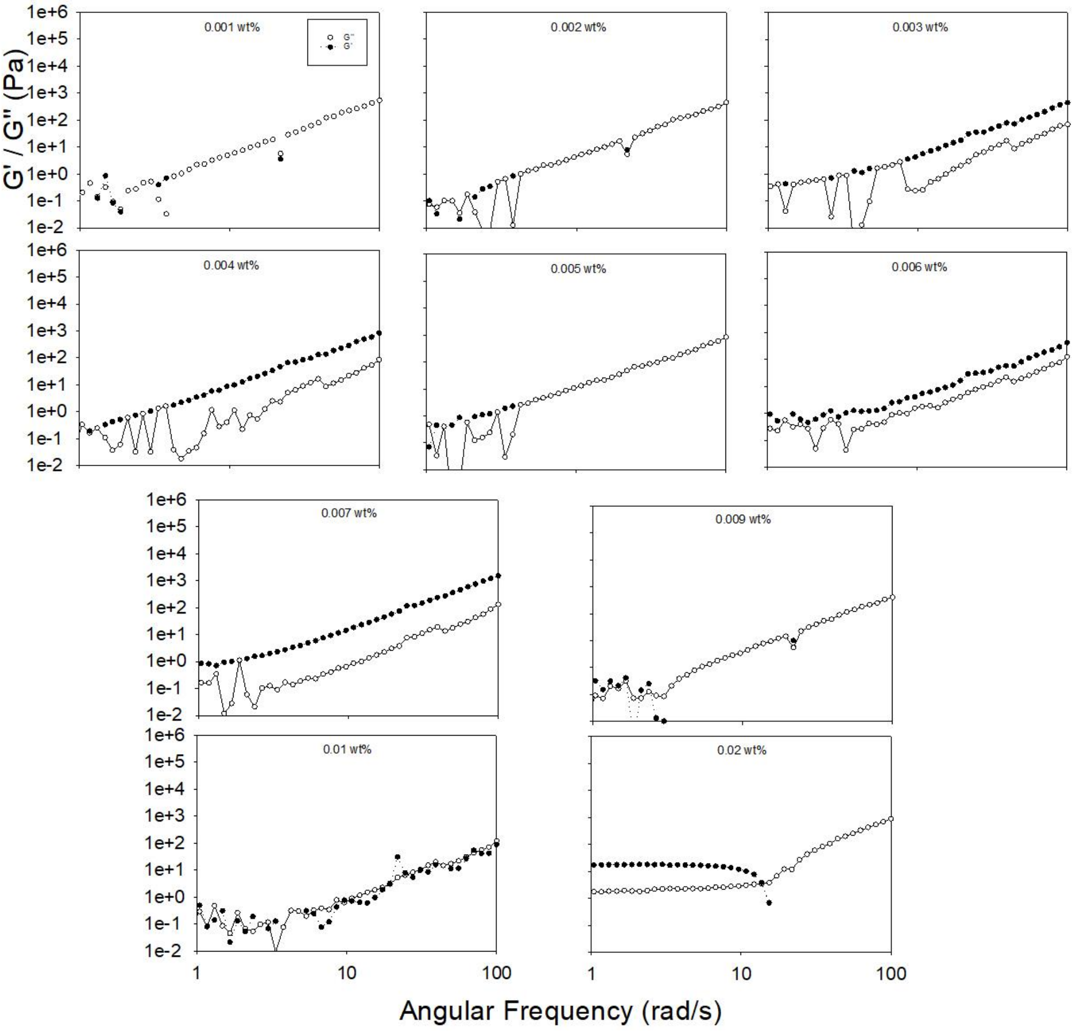

Figure 4.15 – Frequency sweeps, at strain of 0.5 %, of Ca-hydrogels of 2NapFF from 0.001 wt% up to 0.007 wt% and from 0.09 wt% till 0.02 wt% at pH 10.5 and 25 °C. In all cases, the closed symbols represent G´ and the open symbols refer to G″. Some data is not detected, out-of-range, possibly because of hydrogel slippage artefacts.

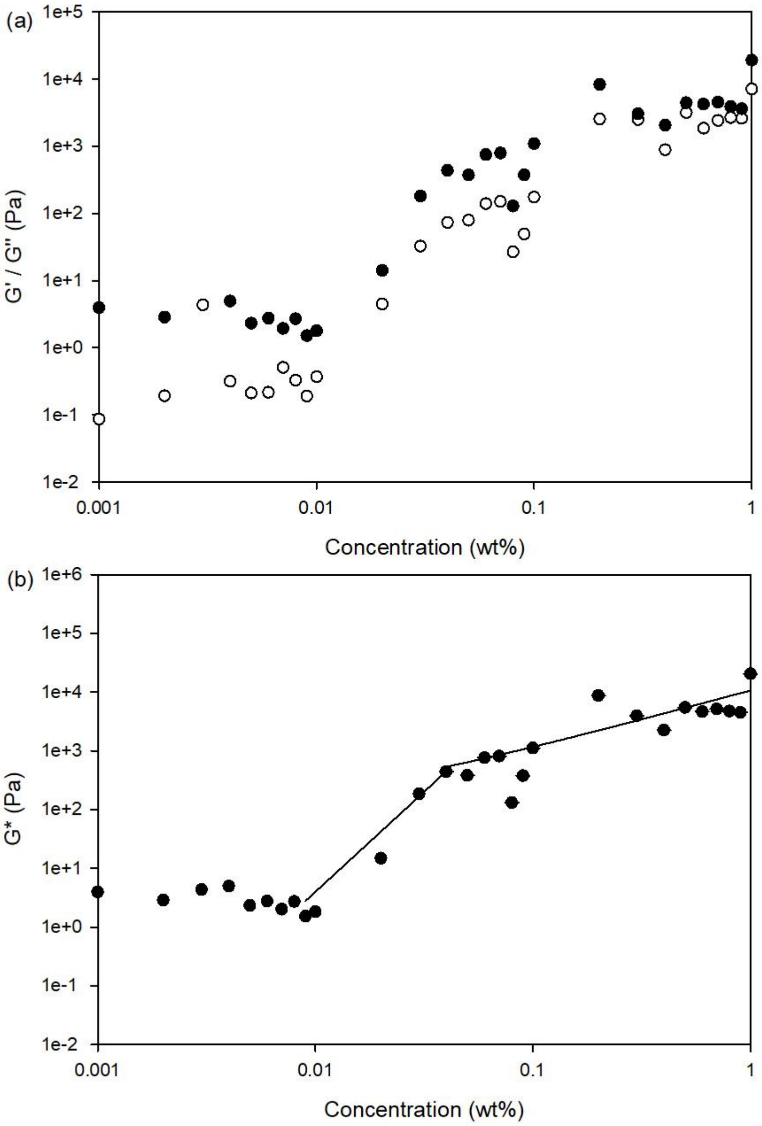

Figure 4.16 – Summary of strain sweeps analysis, at frequency of 10 rad/s and strain 1%, of Ca-Hydrogels of 2NapFF from 0.001 wt% up to 1.0 wt% at pH 10.5 and 25 °C. Readings of absolute values were taken from 1 % strain of the solution strain sweep plots. In (a) the closed symbols represent G´ and the open symbols refer to G″. A concentration dependent exponential fits are obtained in the region from 0.009 to 0.04 wt% with a $R^2 > 99$ %, while in the region from 0.04 to 1.0 wt%, the $R^2 = 0.18$, therefore not representative in this region. A power exponent of 3.40 and 6.77 were fitted to the concentration regions from 0.009 - 0.04 wt% and 0.04 - 1.0 wt%, respectively. Both axes are on a log-scale.

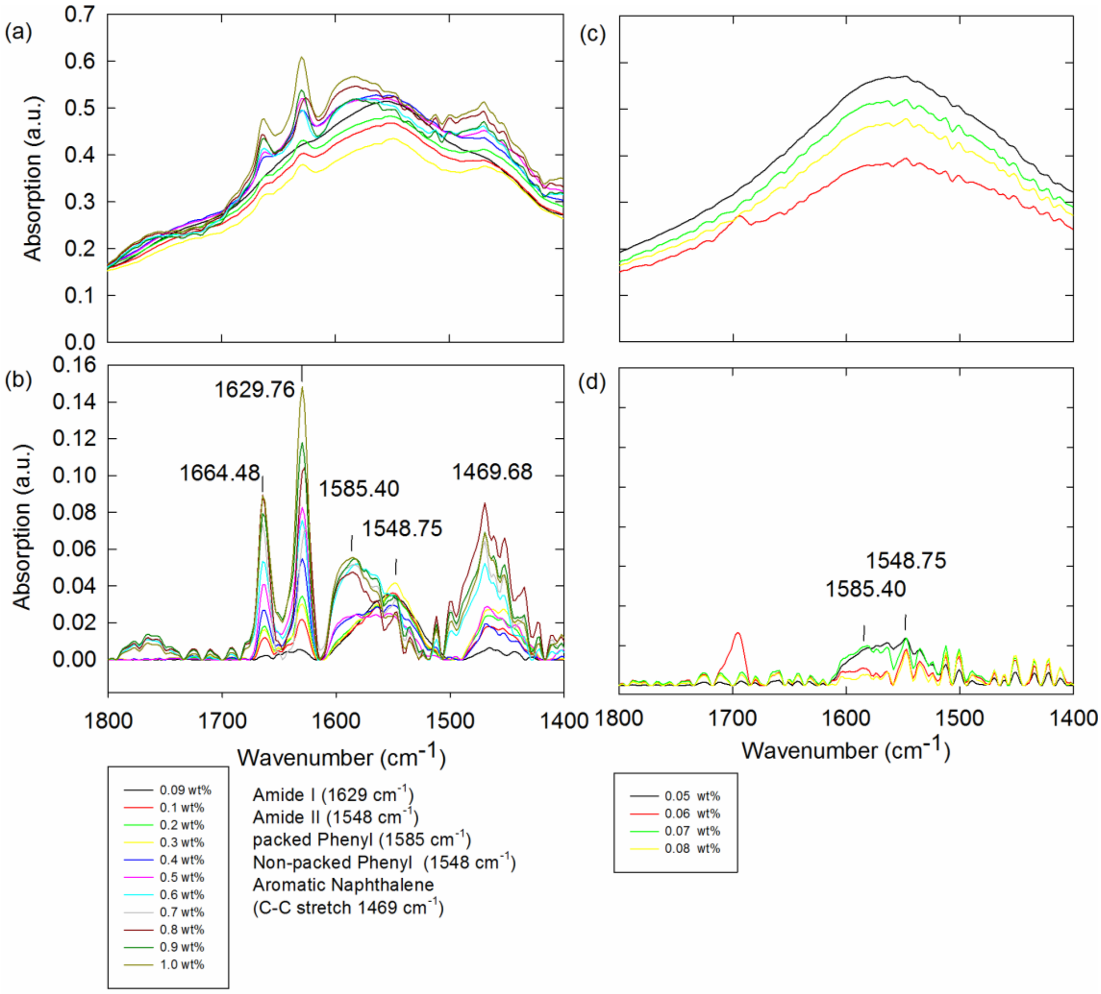

Figure 4.17 – FTIR of 2NapFF Micellar Solutions in a liquid-cell system as a function of concentration at pD 11.5 ± 0.5 in D_2O for high ((a) and (b)) and low ((c) and (d)) concentration region with air background subtracted ((a) and (c)) and with baseline correction with baseline concave rubberband model ((b) and (d)). In (a) and (c), the spectra were collected with only the air and CaF_2 windows as background absorption, thus a broad peak with a maximum at 1550 cm^{-1} appears due to residual water in this region. In (b) and (d), a baseline correction option in OPUS 7.0 software (baseline concave rubberband correction method) was used to suppress the broad water peak influence in the spectra.

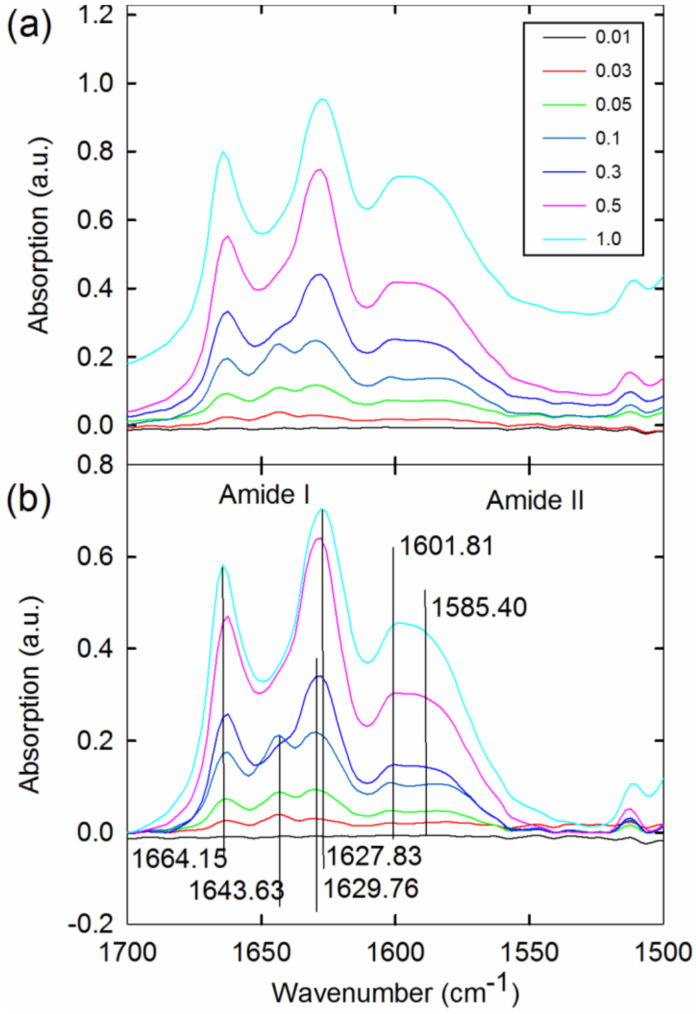

Figure 4.18 – FTIR spectra of (a) 2NapFF Ca-hydrogels at high pD 11.5 ± 0.5 without the baseline correction and (b) with the baseline correction option in OPUS 7.0 software (baseline concave rubberband correction method).

4.7 References

1. F. C. MacKintosh, J. Käs, and P. a. Janmey, *Phys. Rev. Lett.*, 1995, **75**, 4425–4428.

2. G. G. Scott, P. J. McKnight, T. Tuttle, and R. V. Ulijn, *Adv. Mater.*, 2016, n/a-n/a.

3. I. Nnanna and J. Xia, *Protein-based surfactants: synthesis, physicochemical properties, and applications*, 2001.

4. G. Fichman, T. Guterman, J. Damron, L. Adler-Abramovich, J. Schmidt, E. Kesselman, L. J. W. Shimon, A. Ramamoorthy, Y. Talmon, and E. Gazit, *Sci. Adv.*, 2016, **2**, e1500827–e1500827.

5. L. Chen, G. Pont, K. Morris, G. Lotze, A. Squires, L. C. Serpell, and D. J. Adams, *Chem. Commun.*, 2011, **47**, 12071–12073.

6. L. Chen, T. O. McDonald, and D. J. Adams, *RSC Adv.*, 2013, **3**, 8714–8720.

7. L. Chen, S. Revel, K. Morris, L. C. Serpell, and D. J. Adams, *Langmuir*, 2010, **26**, 13466–13471.

8. H. Cui, M. Webber, and S. I. Stupp, *Pept. Sci.*, 2010, **94**, 1–18.

9. T. Shimada, N. Sakamoto, R. Motokawa, S. Koizumi, and M. Tirrell, *J. Phys. Chem. B*, 2012, **116**, 240–243.

10. I. W. Hamley, *Soft Matter*, 2011, **7**, 4122–4138.

11. T. Aida, E. W. Meijer, and S. I. Stupp, *Science (80-.).*, 2012, **335**, 813–817.

12. K. L. Morris, L. Chen, A. Rodger, D. J. Adams, L. C. Serpell, J. Adams, and L. C. Serpell, *Soft Matter*, 2015, **11**, 1174–1181.

13. H. A. M. Ardoña and J. D. Tovar, *Bioconjug. Chem.*, 2015, **26**, 2290–2302.

14. W. Appel, M. Nieuwenhuizen, and E. Meijer, *Supramolecular Polymer Chemistry*, Wiley-VCH Verlag GmbH & Co. KGaA, Weinheim, Germany, 1st edn., 2011.

15. S. S. Babu, V. K. Praveen, and A. Ajayaghosh, *Chem. Rev.*, 2014, **114**, 1973–2129.

16. I. Ramos Sasselli, P. J. Halling, R. V. Ulijn, and T. Tuttle, *ACS Nano*, 2016, **10**, 2661–2668.

17. A. Z. Cardoso, A. E. Alvarez Alvarez, B. N. Cattoz, P. C. Griffiths, S. M. King, W. J. Frith, and D. J. Adams, *Faraday Discuss.*, 2013, **166**, 101–116.

18. Z. Lin, J. J. Cai, L. E. Scriven, and H. T. Davis, *J. Phys. Chem.*, 1994, **98**, 5984–5993.

19. A. Blanazs, J. Madsen, G. Battaglia, A. J. Ryan, and S. P. Armes, *J. Am. Chem. Soc.*, 2011, **133**, 16581–16587.

20. R. Verber, A. Blanazs, and S. P. Armes, *Soft Matter*, 2012, **8**, 9915.

21. A. Z. Cardoso, L. L. E. Mears, B. N. Cattoz, P. C. Griffiths, R. Schweins, and D. J. Adams, *Soft Matter*, 2016, **12**, 3612–3621.

22. L. Chen, J. Raeburn, S. Sutton, D. G. Spiller, J. Williams, J. S. Sharp, P. C. Griffiths, R. K. Heenan, S. M. King, A. Paul, S. Furzeland, D. Atkins, and D. J. Adams, *Soft Matter*, 2011, **7**, 9721–9727.

23. C. Chassenieux and L. Bouteiller, *Rheology. Supramolecular Chemistry: From Molecules to Nanomaterials.*, John Wiley & Sons, Ltd, Chichester, UK, 2012.

24. B. Nystrom and A.-L. Kjøniksen, *Macromolecules*, 1996, **29**, 5215–5222.

25. T. G. Mezger, *The Rheology Handbook: For Users of Rotational and Oscillatory Rheometers*, Vincentz Network, 2006.

26. B. Ozbas, J. Kretsinger, K. Rajagopal, J. P. Schneider, and D. J. Pochan, *Macromolecules*, 2004, **37**, 7331–7337.

27. M. Singh, S. Kundu, A. Reddy M, V. Sreekanth, R. K. Motiani, S. Sengupta, A. Srivastava, and A. Bajaj, *Nanoscale*, 2014, **6**, 12849–12855.

28. A. M. Smith, R. J. Williams, C. Tang, P. Coppo, R. F. Collins, M. L. Turner, A. Saiani, and R. V Ulijn, *Adv. Mater.*, 2008, **20**, 37–41.

29. K. A. Houton, K. L. Morris, L. Chen, M. Schmidtmann, J. T. A. Jones, L. C. Serpell, G. O. Lloyd, and D. J. Adams, *Langmuir*, 2012, **28**, 9797–806.

30. H.-G. Braun and A. Z. Cardoso, *Colloids Surf. B. Biointerfaces*, 2012, **97**, 43–50.

31. E. R. Draper, K. L. Morris, M. a. Little, J. Raeburn, C. Colquhoun, E. R. Cross, T. O. McDonald, L. C. Serpell, and D. J. Adams, *CrystEngComm*, 2015, **17**, 8047–8057.

32. K. L. Morris, L. Chen, J. Raeburn, O. R. Sellick, P. Cotanda, A. Paul, P. C. Griffiths, S. M. King, R. K. O'Reilly, L. C. Serpell, and D. J. Adams, *Nat. Commun.*, 2013, **4**, 1480.

33. H. A. M. Ardoña, K. Besar, M. Togninalli, H. E. Katz, and J. D. Tovar, *J. Mater. Chem. C*, 2015, **3**, 6505–6514.

34. R. Mammadov, A. B. Tekinay, A. Dana, and M. O. Guler, *Micron*, 2012, **43**, 69–84.

35. X. Mu, K. M. Eckes, M. M. Nguyen, L. J. Suggs, and P. Ren, *Biomacromolecules*, 2012, **13**, 3562–71.

36. S. Fleming, P. W. J. M. Frederix, I. Ramos Sasselli, N. T. Hunt, R. V Ulijn, and T. Tuttle, *Langmuir*, 2013, **29**, 9510–9515.

37. J. T. Pelton and L. R. McLean, *Anal. Biochem.*, 2000, **277**, 167–76.

38. K. M. Eckes, X. Mu, M. a. Ruehle, P. Ren, and L. J. Suggs, *Langmuir*, 2014, **30**, 5287–5296.

39. S. a Sandford, D. M. Hudgins, S. a Sandford, and L. J. Allamandola, *J. Phys. Chem.*, 1994, **98**, 4243–4253.

40. S. Sathaye, A. Mbi, C. Sonmez, Y. Chen, D. L. Blair, D. J. Pochan, J. P. Schneider, and D. J. Pochan, *Wiley Interdiscip. Rev. Nanomed. Nanobiotechnol.*, 2014, **2**, 1–59.

41. W. S. S. Rasband, *U. S. Natl. Institutes Heal. Bethesda, Maryland, USA*.

Chapter 5

5. Structural features of 2NapFF by microscopy and imaging software

5.1. Abstract

Scanning electron microscopy (SEM), laser scanning confocal microscopy (LSCM) and atomic force microscopy (AFM) were used to analyse the 2NapFF solution and Ca-hydrogels with advanced imaging software. SEM measurements allowed characterisation of bundles, threaded fibre-like features and the presence of structures over a large range of sizes indicated a hierarchical structure of the 2NapFF Ca-hydrogels. These measurements also show an increasingly crowded environment with increasing concentrations from 0.06 wt% to 1.0 wt% of 2NapFF. Hence, the mechanical properties of the hydrogels are likely linked to the microstructure instead of solely to the individual primary fibre properties. The Ca-hydrogel nanofibres in between a concentration of 0.01 and 1.0 wt% have the main nanofibre width of 20.5 ± 4.3 nm measured by SEM. There were also detectable fibres with an extended width from tenths of nanometres to few micrometres. LSCM measurements allowed a microstructural snapshot of the Ca-hydrogels. Additionally, LSCM identified that in solution phase no correlation is observable between the microstructure (persistence length of the fibre bundles) and the complex modulus G*, while for the Ca-hydrogel phase, the persistence length of the nanofibre bundles increases with the increase G*. The worm-like structures were found to be highly oriented in the solution phase across concentrations from 0.1 wt% to 1.0 wt%. In the Ca-hydrogel phase, the degree or oriented structures increases from 0.05 wt% to 1.0 wt%. AFM was used for identifying the bundle size, structural parameters and the relevance of the flexibility of the fibre bundles at this size to the hydrogel mechanical properties. With two open-source imaging software, it was possible to identify the size of the nanofibres, quantify the alignment and stiffness of the fibres at a particular length scale of the images and also identify the type of fibre: rod-like (stiff) or worm-like micellar-like (flexible).

5.2. Introduction

Peptide supramolecular materials form bonds and structures that span across multiple length scales, from the atomic interactions to the macroscopic material. The study of complex self-assembled peptide structures is usually a multi-methodological approach.[1]

Naturally, advantages and disadvantages of each characterisation method have to be assessed in order to comprehend the meaning of the obtained results. When choosing the characterisation method, the chemical and physical interactions of the measuring instrument with the sample should be considered. Thus, the characterisation method should be adjusted to the expected properties, sensitivity of the material and the phenomena used for its characterisation. For instance, microscopy techniques can use light (e.g. optical and laser scanning confocal microscopy (LSCM)), electrons (e.g. SEM and transmission electron microscopy (TEM) techniques) or mechanical force (e.g. AFM). The different forms of sample-probe interactions reveal different information about structural features of the sample. The backscattering of the light or electrons results from interactions with the electron shells of the atoms within the material while the mechanical feedbacks reveal the profile and mechanical stability of the structures (Fig. 5.1).

5.2.1. Imaging Techniques

In this project, cross-polarized light microscopy, SEM (Fig. 5.1a), LSCM (Fig. 5.1b) and AFM (Fig. 5.1c) were used to investigate the peptide-based materials.

In recent years, cross-polarized optical microscopy has been used to evaluate birefringence in different samples, for example peptide amphiphiles,[2] aligned dipeptides,[3] and aligned silk-peptide fibres.[4] This technique has the major advantage of allowing preliminary sample inspection without invasive or high-energy methods.

Electron microscopy techniques, such as SEM, have been used previously to characterise peptide fibres.[2,5–9] Modified SEM, with a cryogenic sample holder, cryo-SEM, was also used to characterise peptide-hydrogels.[5,6] With cryo-SEM, the Ulijn group was able to identify that the fibre structure has different nucleation and growth pathways during self-assembly if the gelation method uses a lowering of the pH or an enzymatic initiation.[5] They pointed out that the enzymatically-triggered fibres (with smaller fibre width) were more uniformly produced when compared to the pH-triggered systems (with larger fibre width). They have also pointed out that the enzymatically-triggered fibres at different enzyme concentrations had a similar fibre width, although these samples showed different mechanical properties. [5] Our has also observed a similar homogeneity features by microscopy, samples self-assembled with a with a slow pH--trigger process giving more homogeneous samples when compared to a quick pH-triggered process.[6] Several groups have shown that structural features of peptide fibres can be imaged with cryo-TEM.[10–23]

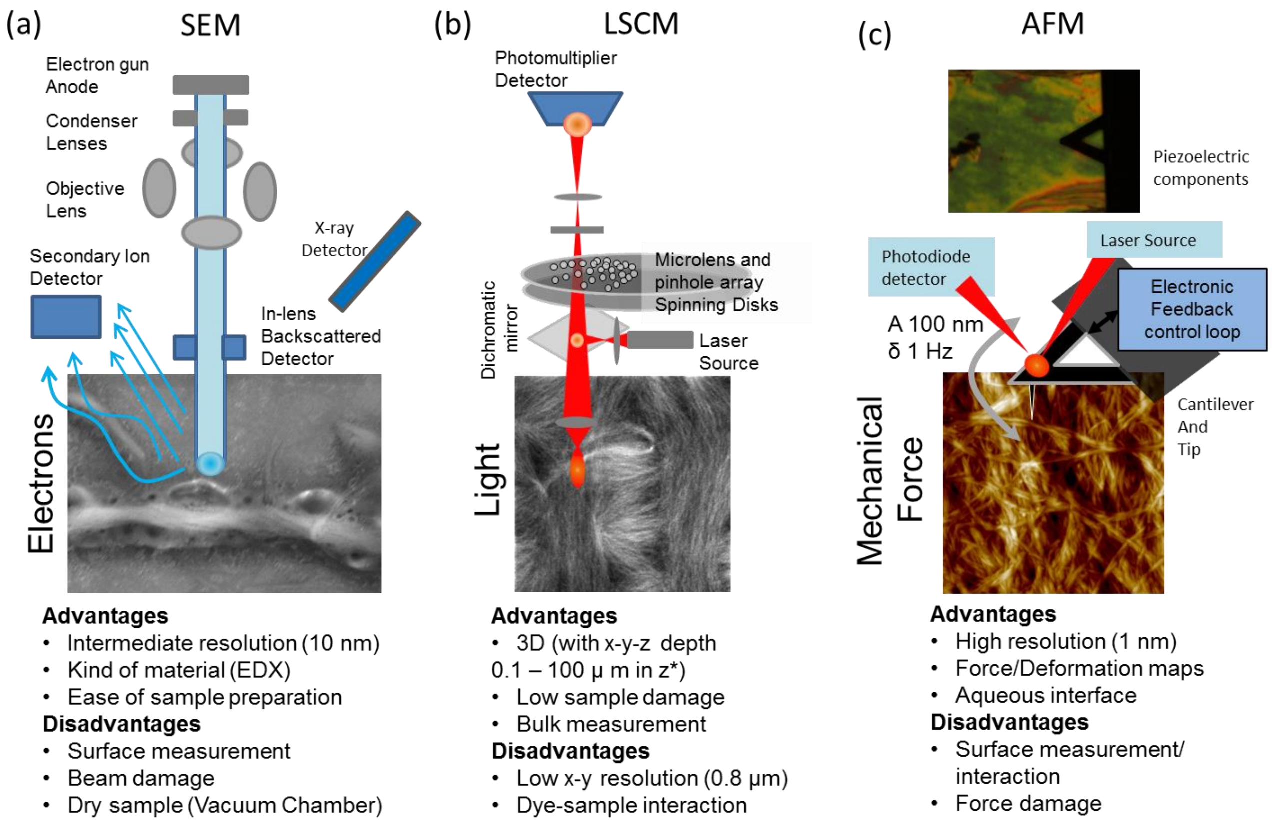

Figure 5.1 – High resolution microscopy characterization techniques suitable for solution and hydrogel peptide-based materials: scanning electron microscopy (SEM, a), laser scanning confocal microscopy (LSCM, b) and atomic force microscopy (AFM, c).

LSCM is a technique of value in observing the 3D features and microstructure of materials with good optical transmittance. LSCM has been used to identify the microstructural alignment of peptide fibres.[3,4] In separate research, a typical dye was shown to adhere to peptide fibres seen by cryo-TEM.[24] This result suggests that dye adhesion to peptide fibres can be used to investigate these materials by LSCM. Surfactant systems have been studied with LSCM. Size measurements of synthetic polymeric nanostructured micelles were conducted by LSCM. However, these measurements are limited to a resolution of 0.5-1 μm.[25] These findings suggest that LSCM is a valuable technique to investigate peptide fibres.

The use of the mechanical force of a nanoscale tip was used to image fibre systems using AFM by various groups[26–34] The peptide fibres were imaged with high detail in both natural and synthetic hydrogel systems by AFM[33,35] The Hartgerink research group have found with AFM that collagen mimetic peptides have hierarchical features.[30] Knowles and Buehler have shown that nanomechanical testing of peptide fibres can be done with AFM.[36] Additionally, the peptide fibre hydration state can also be evaluated by this technique.[31] A detailed study of five amino acid peptide fibres was conducted by AFM.[26] Therefore, this technique has proven extremely useful in peptide characterization.

Scattering techniques allow hydrogel structural information of lower length scales that the microscopy techniques used in this study.[23,37] Dynamic Light Scattering (DLS) and small angle neutron scattering (SANS) have been used to characterise supramolecular gels and peptide-based gels previously.[23,38] One of the big advantage of using scattering techniques such as SANS and DLS is that these techniques look at the sample as a whole while microscopy techniques look at specific locations of a sample to have a nanoscale resolution. DLS is typically used to characterise spherical particles, however recent peptide hydrogel studies by DLS linked auto-correlation function with gel mesh size instead.[37,39] SANS data are used to investigate the size of the primary assembled structure, mesh size, cluster size, molecular orientation within the assembly and the type of fibres.[40]

5.2.2. Length scale

Additionally, each of these techniques is restricted to a length scale over which they can give information. A range of microscopy techniques have been used to characterise peptide hydrogel fibre dimensions in the past years.[20,41] Fig. 5.2 shows that microscopy techniques have the ability to observe the materials from few angstroms to millimetres.

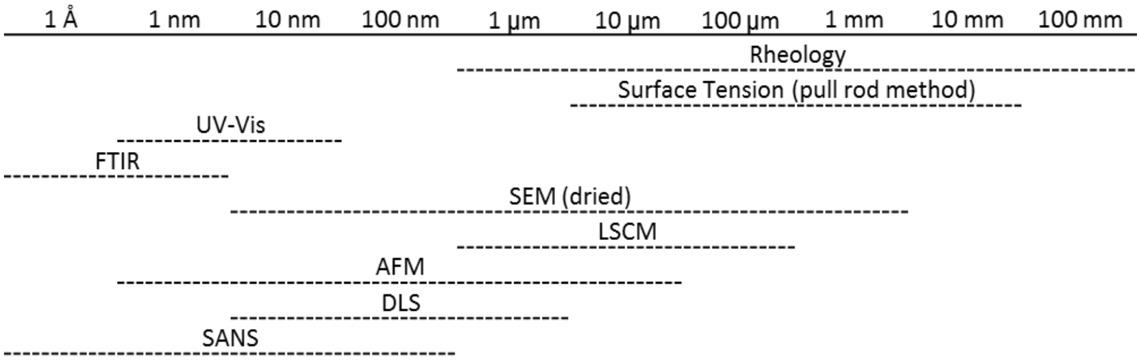

Figure 5.2 – Length scales of the analysis techniques used in the structural analysis of peptide structures.

Recent studies show that the peptide hydrogels have characteristic supramolecular networks that self-assemble without physical or chemical crosslinks.[42] These networks are usually formed by bundled structures, for example, observed in longer peptide amphiphile systems.[43,44] Microscopy allows these structures to be identified. It has also been shown that silk fibre bundles can form by hierarchical self-assembly and alignment of silk nanofibres.[4] Usually, this phenomena is driven by hydrophobic interactions of particular residues such as leucine.[45] Since the bundling features are microstructural characteristics and the microstructure was shown to be the major impact in the mechanical properties, bundling is likely to contribute to the mechanical properties of the solution and hydrogel networks.[46,47]

Apart from the bundling of these primary fibres, peptide materials form complex microstructures with dimensions of the primary worm-like structures, bundling at multiple length scales, number and type of entanglements, homogeneity of the bulk and pore size of the network. For example, the types of cross-links or entanglements were previously discussed in the literature for supramolecular polymers.[42] In their review, Raghavan and Douglas outline three scenarios by which cross-linking can occur in molecular gels.[42] The nanofibres can interact by: (1) a weak attraction between overlapping fibres at cross-link points, (2) forming junction zones between adjacent fibres over small overlapping zones; or (3) fibres could jam into each other at distinct nodes or alternatively, these nodes could be branching points.

Image analysis software has been used in a variety of research fields that require imaging techniques to understand complex nano- and micro-scale phenomena.[48] FiberApp[48] and an ImageJ[49] based package, Fiji,[50] were chosen to analyse the microscopy images because of the polymer physics package, in the case of FibreApp, and the robust open-source nature of these programmes. FiberApp allows characterisation of mechanical properties from images such as different methods for persistence length analysis (e.g. bond correlation function (BCF)), degree of nematic order (obtained from a 2D order parameter), physical discrimination of the type of fibres (e.g. worm-like chain or rod-like obtained from a scaling exponent of the tracked fibres), and angular orientation distribution, among others.

5.2.3. Persistence length, size of the nematic order, order parameter, contour length, bundle diameter, mesh size and type of fibre

The persistence length, λ (or l_p), is a quantifiable measure of the stiffness of a polymer material, therefore valuable to evaluate the mechanical properties of a material. It can be defined as the length (i.e. vector) over which the tangent to the supramolecular polymer chain losses its directional correlation, from the position zero to the max length. The persistence length of peptide bundles is usually correlated with the mechanical properties.[51] In the studies of Kouwer *et al.*, a peptide amphiphile supramolecular system indicates that the plateau modulus (G_0, storage modulus at low shear) is correlated with the persistence length of the bundles, $l_{p,B}$ following Equation 5.1.[51]

$$G_0 = 6\chi \frac{c}{N_B} RT \frac{l_{p,B}^2}{l_C^3} \qquad \text{Equation 5.1}$$

In this equation, χ combines molecular constraints, c is the polymer concentration, N_B is the number of primary fibres in the bundle, R is the gas constant, T is the absolute temperature, $l_{p,B}$ is the persistence length of the bundles and l_C is the average length between the bundle crosslinks, considering the network as a collection of thermal fluctuating bundles.[51] It is possible to identify from Equation 5.1 that the G_0 depends on other microstructural parameters, not only on the persistence length of the bundles.

The size of nematic order is calculated by the measurement of the range of distances at which separate tracked single fibres are oriented in the same direction.

The order parameter depends is a measure of disposition or orientation of the fibres in the image, from 1, fully orientated to close to 0, completely randomly.

Contour length is the end-to-end distance of a fibre measured along the fibre. This was measured for fibres with open ends.

Fibre bundle diameter is a measure of the cross-section of the nanofibres measured, this is taken perpendicular to the fibre axis in a number of fibres for statistical analysis of the width of the fibres. This was measured using Fiji software.

The mesh size is the average gap size between the bundles of fibres. It was established by measuring over 100 distances from over 5 images the length between different bundles.

The observations regarding the type of fibre are based on the average end-to-end distance against the internal contour length plots. Reading these plots, the presence of a plateau for the high contour lengths indicates a trapped state, or rod-like fibre features, while the lack of a plateau indicates a flexible state, or a worm-like chain fibre features.[48] All parameters here discussed except fibre bundle diameter and mesh size were measured using FibreApp.

5.2.4. Fiji and FibreApp imaging software

Fiji imaging software is an intuitive and open-source software package for image analysis in material science and bioscience.[49,50]

The FiberApp program uses an A*-algorithm which works based on pre-selection of the path the fibres present in a microscopy image.[48] The algorithm runs an energy minimisation code in order to minimise an energy value that is obtained for each point at the pixel below of each fibre. The best path is obtained because the increase in intensity of the points at the best fit fibre line (previously selected at an image), would give a higher score. It is possible to invert the image intensity so that a negatively stained image could be analysed as well. Different parameters can be adjusted to gain the best fit possible. For further information on the use of the FiberApp software to track images of fibre-like materials, please consult Usov *et al.*[48]

It is important to note that the ideal images would be those that anyone can follow each fibre by eye. Therefore, the ideal image would have to be diluted successive times because typical hydrogels are formed by an entangled networks of hydrogels. However, in the hydrogel systems studied here, these are strictly dependent on preparation properties which can be altered in the image preparation. The concentration dependence is also critical.[52,53] In Chapter 3 and Chapter 4, as well as previously in similar systems, it was found that the concentration dependence of the hydrogels is fundamental for the understanding of the mechanical properties of low molecular weight peptide-based hydrogels.[54] The microstructure of the hydrogel has also shown to be intrinsically related to the mechanical properties of the hydrogel.[42,55–58] The use of salts and buffers can have a significant impact on the outcome of the self-assembled system.[2,14,33,59–63] The pH of the sample is also of paramount importance for the self-assembly,[6,52,64–66] as it is the mechanism most used in the literature to form hydrogels and has been shown to have an effect even on non-pH triggered methods.[58] Finally, the structure of the gelator molecules is also pH, concentration and salt dependent resulting in different outcomes in mechanical preprties.[64] Several microscopy techniques use high vacuum, such as TEM and SEM. Dehydration of the sample in vacuum can be circumvented with the use of cryogenic methods, if available. These techniques may have significant modification of the fibre structure, most significantly the microstructure. However, using appropriate control samples and carefully adjusted and repeated sample preparation techniques, we can be confident of the significance of the nanostructures imaged with these techniques. As an alternative to these dry and high vacuum techniques, aqueous microscopy techniques can be used to image in the wet state biological materials, techniques such as LSCM[67] and aqueous-AFM[68] or biological-AFM.[69]

In this Chapter, conventional SEM, LSCM and AFM have been used to analyse images by Fiji[50] (ImageJ package[49]) and FiberApp[48] image analysis software. The FiberApp results were used to investigate whether there is any link between the structural analysis outcome of the FiberApp software and the already measured structural properties of the 2NapFF self-assembly systems, in both the solution and Ca-hydrogel phase.[14,70] For example, the appearance of bundles in the image could be identified by the use of orientation distribution plots and the presence of nematic order.

5.3. Results and discussion

A range of microscopy techniques can be used to investigate the surface and bulk of soft materials. In the previous Chapters, findings about the peptide solution and hydrogel structure were supported with the use of SEM, confocal microscopy and optical microscopy. Here, we have quantified the measurements of the 2NapFF solution phase and hydrogel phase with ImageJ[49,50] supported statistical analysis and the FiberApp[48] software for structural and mechanical analysis of the samples through imaging. The solution and hydrogel structure of 2NapFF was further investigated with AFM.

5.3.1. Microscopy software analysis of the 2NapFF solution and Ca-hydrogel material parameters

In this section, the dried 2NapFF solutions and xerogels were investigated with SEM, LSCM and AFM at different concentrations. Structural measurements were conducted with ImageJ and FiberApp software. Here, the main aim is to find features of the hierarchical structure that can extend our understanding of the peptide solutions and hydrogel systems.

5.3.1.1. SEM of the 2NapFF solution and hydrogel phase

SEM images of 2NapFF solution phase

The structures formed by 2NapFF in solution are hard to image in a manner that ensures that no artefacts arise. During the drying process, small fibres and bundles could align themselves, resulting in dramatic structure reorganization. [71] Since the artefacts of SEM sample preparation and limited resolution of LSCM, we are still not able to identify the number of primary fibre-like structures in the solution bundles per unit volume. This number could also be dynamic across the sample and dependent on external stimuli.

SEM images of the 2NapFF Ca-hydrogels

SEM[2,5–9] and cryo-SEM[5,6] imaging was previously used to characterise peptide hydrogels. However, as mentioned above for the solution phase, drying artefacts may well transform the structures present in the bulk of the hydrogel relative to the dried sample. Despite this, the measurable nanofibre bundle size in the bulk of the Ca-hydrogel may be a relevant parameter to characterise the structures formed if we consider these structures are more stable under the SEM electron beam than the solution phase and therefore less transformed from the actual aqueous material.

Here, a silicon wafer was dipped for 30 min in a 2NapFF hydrogel (or Ca-triggered solution) at a particular concentration. Upon removal, the silicon wafer was dried under nitrogen flow for 30 minutes. The uncoated samples were imaged with an SEM at low voltage to avoid beam damage (Materials and Methods, Section 5.5.3.). The 2NapFF SEM images of a concentration between 0.009 wt% and 1.0 wt% are shown in Fig. 5.3, Fig. 5.4 and Fig. 5.5. These samples were prepared individually at those set concentrations. This method for sample preparation was chosen to avoid irreversible structures formed if a dilution method was used to achieve these concentrations.

In some cases, bundles and threaded fibre-like features appeared in the SEM analysis of hydrogels (Fig. 5.3a2), though these could be the result of drying effects. Since the SEM sample preparation procedure is not able to capture fully the bundle properties of the hydrogel, only some examples of bundling are discussed below. Therefore, LSCM and AFM data were used to further investigate the bundling behaviour (Section 5.5.4 and Section 5.5.5, respectively). All samples between 1.0 wt%, the maximum amount investigated here, and 0.01 wt%, including the minimum gelation concentration (mgc) at 0.02 wt%, show the presence of nanofibre structures (Fig. 5.3, Fig. 5.4 and Fig. 5.5).

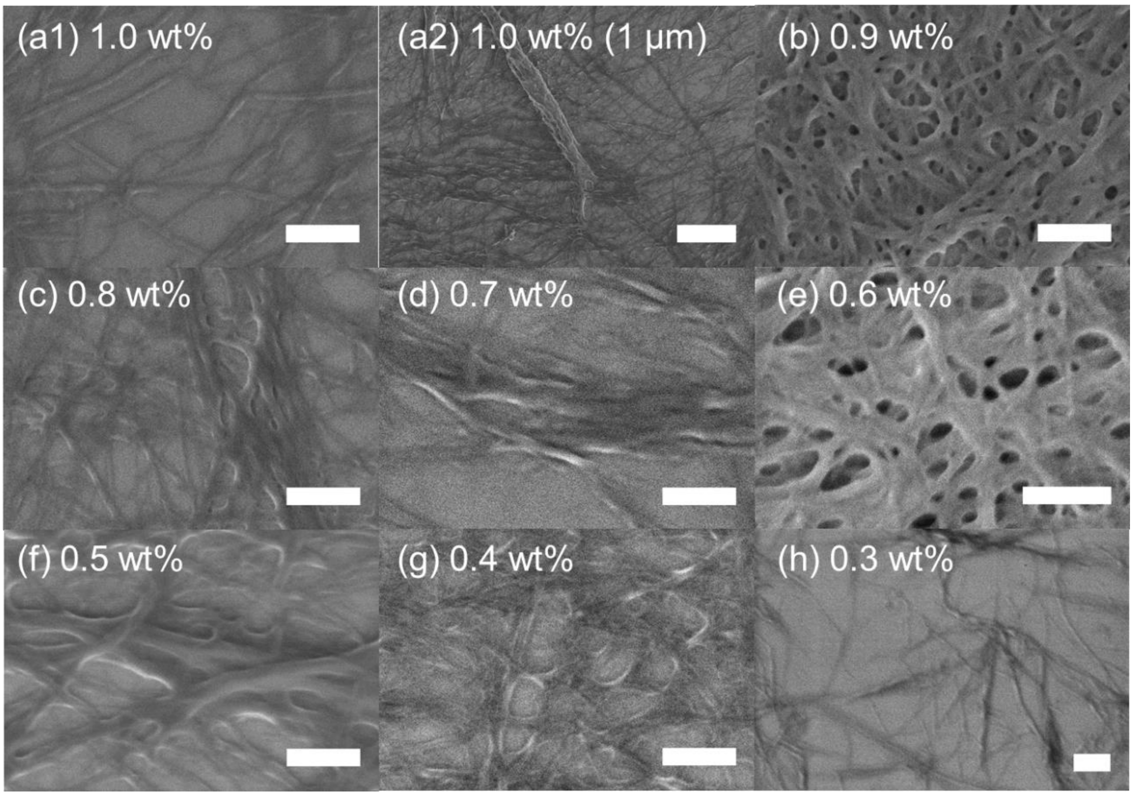

Figure 5.3 – 2NapFF Ca-hydrogels imaged by SEM with no coating at concentrations of 1.0 wt% (a1), 1.0 wt% (a2, 1 μm), 0.9 wt% (b), 0.8 wt% (c), 0.7 wt% (d), 0.6 wt% (e), 0.5 wt% (f), 0.4 wt% (g) and 0.3 wt% (h). Image (a2) shows the typical presence of larger bundles observed with a lower magnification. The scale bars represent 250 nm, except (a2) image has a 1 μm scale bar.

Interestingly, images between 0.07 wt% to 1.0 wt%, above the critical micellar concentration (cmc$_2$), all show entangled fibrillar structures without the presence of the fibre open ends. Fibrillar structures below 0.06 wt% show the ends of the peptide nanofibre structures, to the best of our knowledge not previously shown in the literature for this type of dipeptide-based nanofibre materials. Based on interpretation of the present literature, with no reports of open ends and our investigations, the absence of open ends is a common feature to self-assembled peptide nanofibre in the concentrations investigated, region where they typically form functional materials.

The increase in average fibre width (Fig. 5.3 and Fig. 5.4) and increase in bundle size suggest that the nanostructures are in a crowded environment at concentrations above 2nd cmc, 0.06 wt%. This crowding effect relates to the detected worm-like micelles in this concentration region, prior to hydrogelation. Crowded environments have been described and studied in the literature for larger proteins, typically to understand protein folding and assembly in cellular environments, also crowded environments.[72] It has been reported that then crowding effects have an influence in the fate of protein folding and self-assembly.[73–75] Recent investigations in dipeptide systems also show that crowding effects can modify the secondary structure and mechanical properties of the hydrogels can be changed depending on the amount of polymer additive and order of mixing, i.e. self-assembly process.[76,77] In addition, this crowding observation agrees with the microstructural relation to the mechanical properties, as opposed to the properties being strictly dependent on single fibre characteristics.

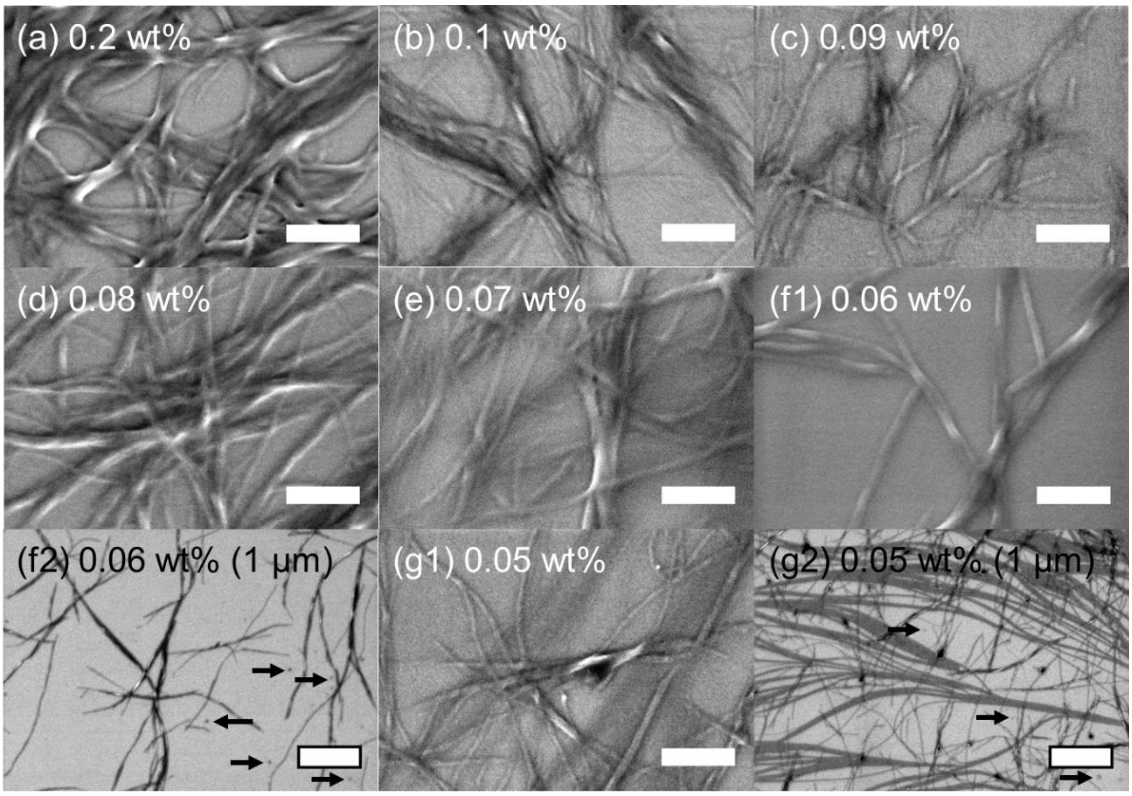

Figure 5.4 – 2NapFF Ca-hydrogels imaged by SEM with no coating at concentrations of 0.2 wt% (a), 0.1 wt% (b), 0.09 wt% (c), 0.08 wt% (d), 0.07 wt% (e), 0.06 wt% (f1), 0.06 wt% (f2, 1 μm), 0.05 wt% (g1) and 0.05 wt% (g2, 1 μm). Image (f2) and (g2) shows the presence of, less often present at these concentrations, spherical aggregates observed with a lower magnification (black arrows). The scale bars represent 250 nm, with exception of (f2) and (g2) images, which have 1 μm scale bars.

The fibre diameter was obtained from over 100 measurements per image in ImageJ and a minimum of three images have been analysed for each data point. In Fig. 5.6, the average nanofibre diameter is plotted as a function of concentration from 0.02 wt% to 1.0 wt%. This result shows a slight increase in the fibre diameter with an increase in concentration from the average results considering the standard deviation. A close consideration of the standard deviation and the nature of the measurement suggest that this increase in the average bundle size for large concentrations from the 1st quartile (Q_1, median of the lower half of the data set) to the median up to the 3rd quartile (M_{75}, medium of the lower 75 % of the data) nanofibres is an effect of the hierarchical nature of the bundles (Fig. 5.6). The bundling is likely the result of lateral assembly of the smaller fibrils that constitute the fibres. In this case, fibrils are defined as the smallest fibre-like constituents of the fibres. The increase in the standard deviation with an increase in concentration also suggests an increase in the number of fibrils that constitute the lateral packing (Fig. 5.6).

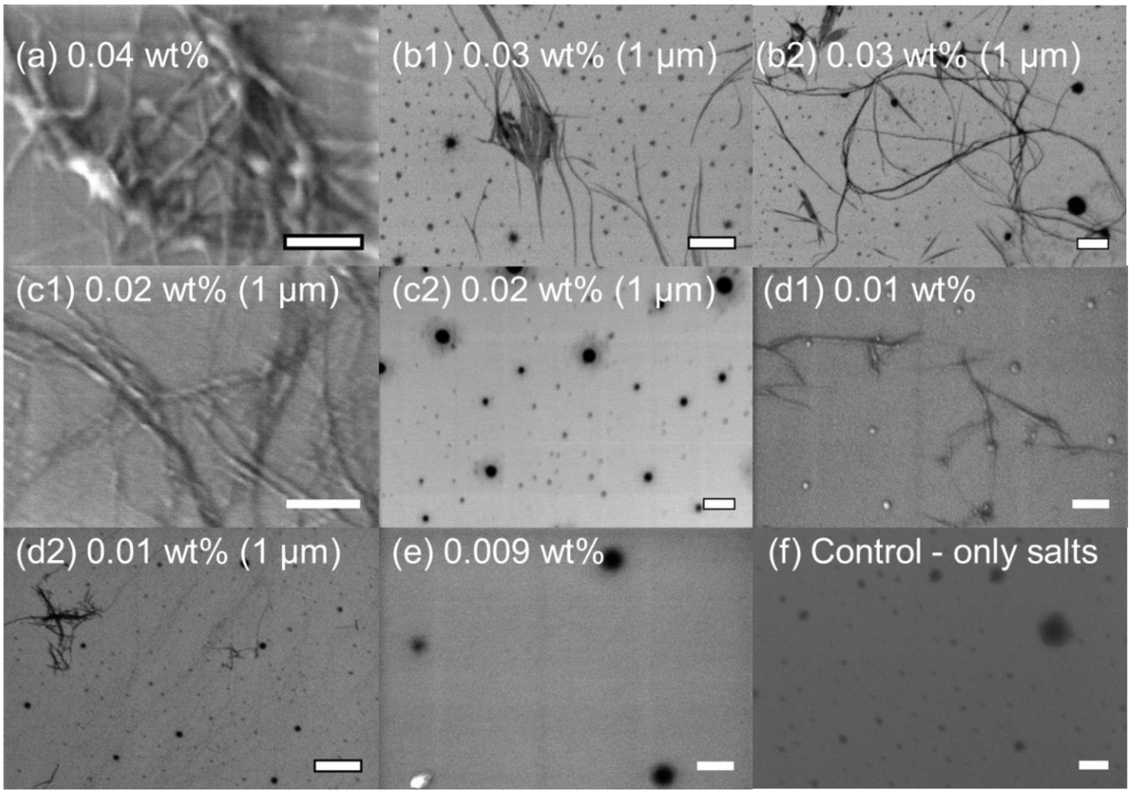

Figure 5.5 – 2NapFF Ca-hydrogels imaged by SEM with no coating at concentrations of 0.04 wt% (a), 0.03 wt% (b1), 0.03 wt% (b2, 1 μm), 0.02 wt% (c1), 0.02 wt% (c2, 1 μm), 0.01 wt% (d1), 0.01 wt% (d2, 1 μm), 0.009 wt% (e) and control sample prepared with the salt conditions used in the 0.03 wt% sample (f). Image (b2), (c2), (d2), (e) and (f) shows spherical aggregates observed with a lower magnification. The scale bars represent 250 nm, except (b1), (b2), (c1), (c2) and (d2) images have 1 μm scale bars.

The number of fibrils in a fibre would be required to estimate the mechanical properties from the images using Kouwer *et al.* mathematical model,[51] denoted with an N_B in Eq 5.1. Another important factor to consider here, apart from the increase in the lateral packing of the fibrils, is the overall number of nanofibres present in the bulk of the hydrogel (N), which is likely to increase with the increase in concentration. These two nanofibre features, the number of laterally packed fibrils that constitute the bundle and the overall number of nanofibres are not resolved by these measurements here, although it is foreseeable that a combination of techniques and simulations may reveal a close estimate in future research. A control sample prepared with the salt conditions used in the 0.03 wt% concentrated sample indicates that the spherical like aggregates shown in the SEM images at lower concentrations could be salt-aggregates (Fig. 5.5f)

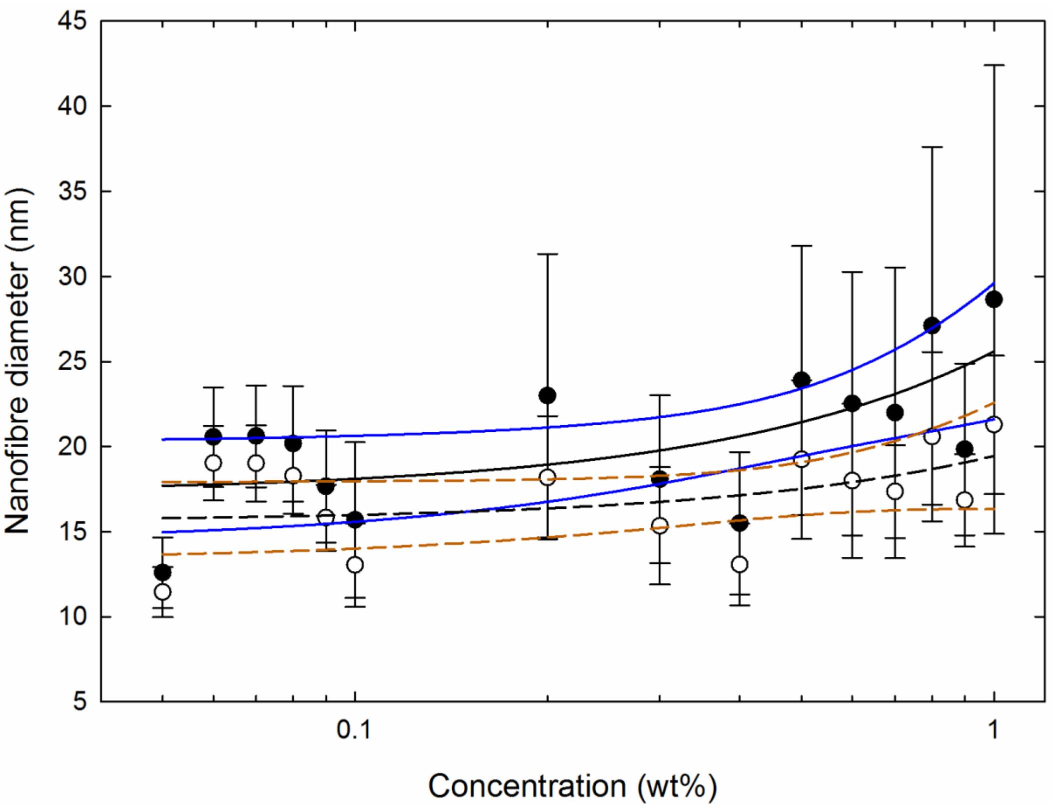

Figure 5.6 – SEM nanofibre diameter measured with ImageJ as function of 2NapFF Ca-hydrogel concentration. The median up to the 3rd quartile, M_{75}, medium of the lower 75 % of the data (black circles) and 1st quartile, Q_1, median of the lower half of the data set (white circles). A linear fit to each of these data sets, M_{75} (black solid line) and Q_1 (black dashed line) fibre diameter averages shows the similarity in the data sets for most concentrations. A statistical analysis of these fits shows 95 % confidence bands plotted for the M_{75} (solid blue) and Q_1 (dashed orange). Each data point was obtained measuring 100 – 250 fibres.

Simultaneous work in our group revealed that the mesh size increases with an increase in concentration for Ca-hydrogels of a similar gelator.[57] A statistical analysis of the SEM imaging data in the form of histograms and cumulative frequency for each of the concentration samples is shown in the Appendix, Section 5.6.1, Fig. 5.29-5.33. In these images, the separated peaks in the histogram analysis and intermediary plateaus in the actual frequency results suggest that there is a hierarchical structure in the 2NapFF Ca-hydrogel phase in the concentration region between 1 wt% to 0.01 wt%. A cumulative plot of these results is shown in Fig. 5.7.

These SEM measurements provisionally suggest an extension of the previously reported mechanism for the salt-triggered hydrogelation, which explained the transition from the solution phase to the Ca-hydrogel as the result of ‘locking-in’ the micellar structures of the solution phase. First, this set of image analyses shows that concentrations above the

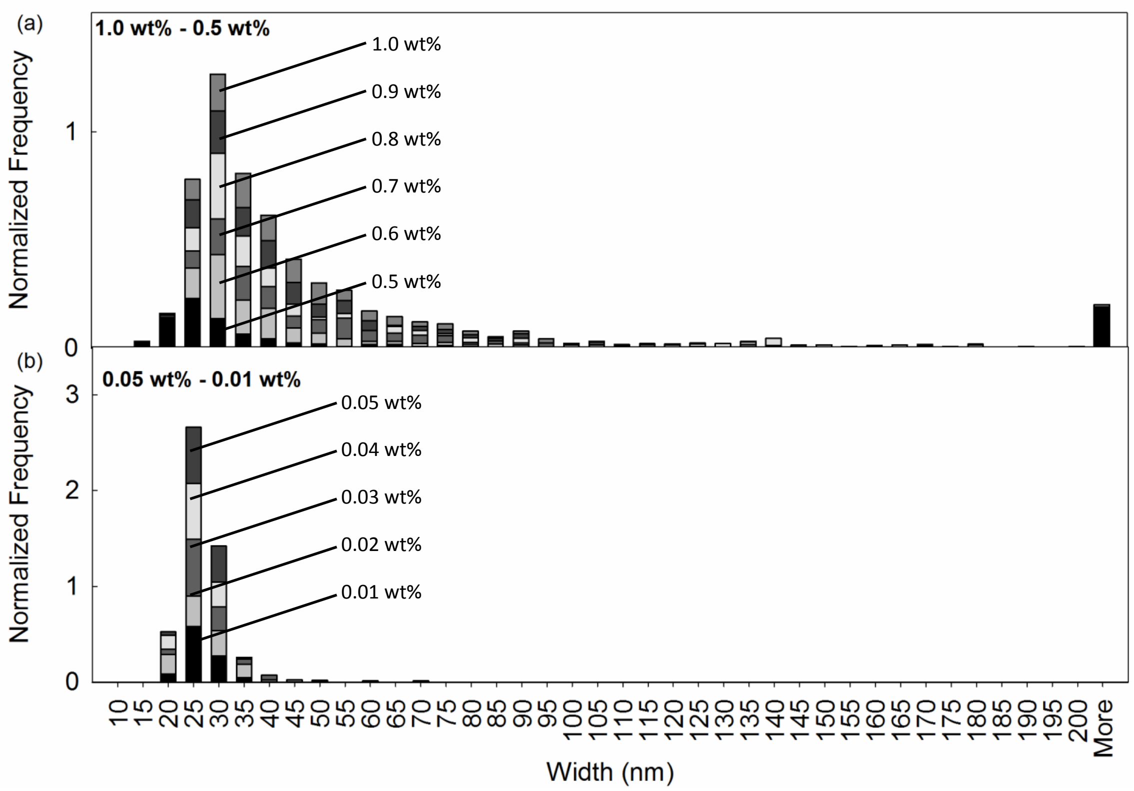

Figure 5.7 – Stacked cumulative SEM fibre width analysis of the data obtained for the concentration region from 1.0 wt% to 0.5 wt% (a) and in the concentration region from 0.05 wt% to 0.01 wt% (b). Each stack shows an aggregated set of data where each different shade of grey scale represents a different concentration. It can be seen that in the high concentration range there is a clear tail, which appears to reflect a typical decay of length scales observed in biological self-assembled systems.[78]

cmc$_2$, 0.06 wt%, have a maximum of lowest identifiable structures at approximately 20 – 35 nm, however these structures always appear to have a tail in the spread of the data for larger widths. Secondly, a cumulative analysis of the histograms in the regions from 1.0 wt% to 0.5 wt% and from 0.05 wt% to 0.01 wt% clearly shows the asymmetric nature of the fibre width distribution (Fig. 5.7), indicating a hierarchical structure of the hydrogel material. Additionally, the step-wise feature in the cumulative part of the data for each concentration also indicates the concentrations at which the material is composed of hierarchical structure (e.g. in the cumulative percentage of Fig. 5.7). Finally, the highest frequency peak in fibre width does not appear to change significantly with the change in concentration across two orders of magnitude in concentration (from 0.01 wt% to 1.0 wt%). Therefore, the number of fibrillar structures is likely to be increasing with an increase in concentration. This result is in agreement with our mechanical strength measurements in Chapter 4 of the hydrogels in this concentration range, which showed an increase in complex modulus, G*, with an increase in concentration in three regions (Chapter 4, Fig. 4.4). Since the minimum gelation concentration (mgc) is 0.02 wt%, it is interesting to note that the hydrogels do not appear to require extended hierarchical features in order to form a self-sustained hydrogel (i.e. a hydrogel that passes the inversion vial test), because from 0.02 wt% to 0.06 wt% the characteristic tail in the data for higher concentrations is not present.

Based on these results, the 2NapFF Ca-hydrogel fibre width is 20.5 ± 4.3 nm, obtained from the medium and standard deviation of M_{75} (defined above) and in the concentration region from 0.01 to 1.0 wt%. At this point, the hypothesis that the mechanical properties may be related to the average fibre width should be discussed. As noted above, SEM measurements are likely overestimations of the structural size with weakly bound, beam-sensitive materials such as self-assembled peptides, because of lateral packing caused by drying artefacts (i.e. minimized by the nitrogen drying methodology). Here, it was shown that 2NapFF Ca-hydrogels have a range of fibre widths, which extend from the tens of nanometres to the micrometre region, existing at concentrations above the corresponding cmc_2 of the solution phase. Therefore, to include the hierarchical nature of the width data sets, a full width average of the complete data set for each concentration was plotted against the complex modulus, G* (Fig. 5.8a). In this Figure, the data for 0.1 and 1.0 wt% were excluded because the number of detected fibre widths above 200 nm was a great percentage of the overall fibres measured for these two particular samples (Section 5.6.1, Fig. 5.29 and Fig. 5.31). This implies that the measurements of structural sizes should be assessed separately for the two distinct length scales, because each fibres of different thickness may impact the mechanical properties differently. If a microscopy technique has a lower (e.g. Confocal Microscopy) or higher (e.g. AFM) resolution, the size of fibre-like features measured is associated with the structure at that particular length scale, particularly within a hierarchical system. Here, in Fig. 5.8a, it is important to note that the x-axis is the average size of all the measurements at each concentration. It is not the actual size measurement of any fibre of that particular sample, as it was previously attempted with the Q_1 and the M_{75}. In this figure, the increase in the average fibre size is followed by an increase in complex modulus, G*. The average size and size distribution is related to the hierarchy of the structure because it includes the complete span of sizes in the structure, from primary assemblies to bundled and entangled structures.

The nanofibres or worm-like structures of the hydrogel networks have characteristic structural features, such as persistence length, L_p (or λ), and contour length, L_c. In other words, the length over which correlations in the direction of the tangent to the nanofibre are lost is the L_p. The L_c in the case of self-assembled supramolecular polymers is its length at maximum physically possible extension. These are both calculated with

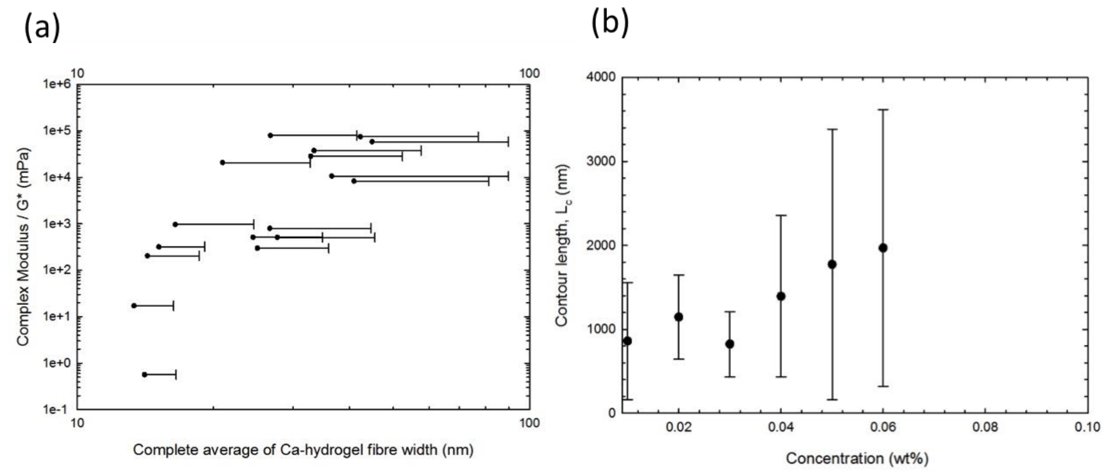

Figure 5.8 – SEM image analysis of 2NapFF Ca-hydrogels: (a) Complex modulus as a function of the corresponding fibre width, measured by the FiberApp software. The complex modulus was obtained at 1 % from strain sweeps measured using a vane-cup geometry. The fibre width was measured by SEM images with ImageJ. Positive error bars are the based on the standard deviation of all measurements obtained for each particular data set. (b) Average contour length, <L_c>, of nanofibres as function of the concentration, measured by the FiberApp software in the visible open end region of the data (0.01 wt% to 0.06 wt%). All axes are in logarithmic scale. The standard deviation and average were calculated for over 3 images at each concentration (the number of fibres found varied from 33 to 171).

FiberApp from images where the nanofibres are semi-manually tracked. These are both independent from the fibres extending above the dimensions of the image captured by SEM, AFM or LSCM. Yet, the images show features of the fibres shown at that length scale, captured by that technique.

As mentioned above, an interesting feature of this SEM data set of 2NapFF gelator is the presence of self-assembled peptide fibres with visible open ends, an uncommon feature seen in supramolecular hydrogel literature.[79,80] Usually these ends are only observed during fibre formation.[81] The nanofibre open ends allowed us to measure the average contour length, <L_c>, using FiberApp software analysis of the fibres with visible open ends from images between 0.06 wt% and 0.01 wt% (Fig. 5.8b). In this plot, the peptide nanofibres in the Ca-hydrogel phase show an increase in the average contour length with increasing concentration in the region that corresponds to the region between the cmc_1 and cmc_2 in the solution phase. The number of fibres found in sets of 3 images varied from 33 fibres at 0.01 wt% to 171 at 0.06 wt%.

In order to confirm the hierarchy of the results and the apparent phase transition at 1.0 wt%, a full range analysis of diameters found for 1.0 wt% 2NapFF Ca-hydrogels through SEM is shown from the nanometre region into the micrometre region (Fig. 5.9a). In this Figure, three regions are visible: a dominant region is visible at 25 ±

5 nm, a broader subsequent region between 200 nm and 400 nm and an several less significant fibre sizes ranging from 400 nm to 1.2 µm.

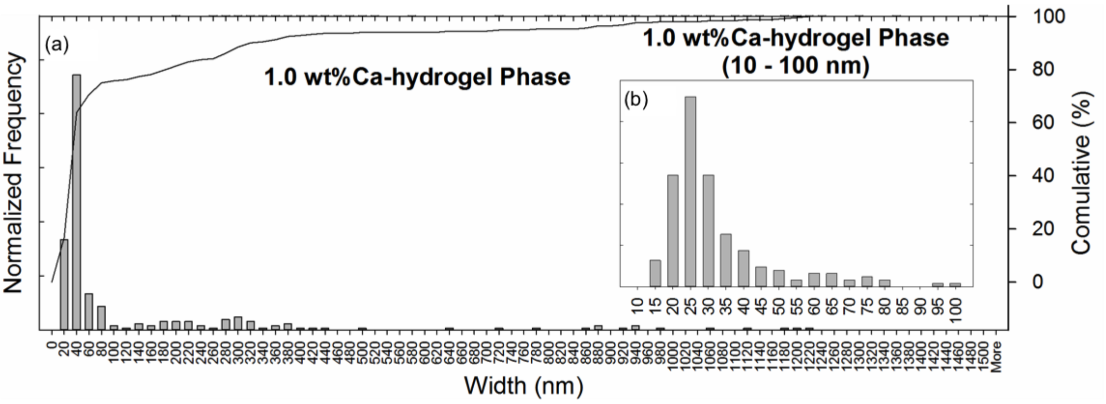

Figure 5.9 – Full SEM image analysis of nanofibre width measurements of the 1.0 wt% 2NapFF Ca-hydrogels (a), 6 images, three of them are shown in Fig. 5.9, n = 435; and (b) focus on the first region of diameters from 1 – 100 nm. Ca-hydrogel samples were diluted 10 times after gelation and immediately dried under nitrogen flow. The data set was normalized.

We were not able to make a comparison between the 2NapFF solution phase and the Ca-hydrogel phase because we were not capable to make a sample preparation with a normal SEM to measure these samples without introducing drying artefacts. However, in an aqueous sample preparation procedure used in wet-AFM (below), the reduced incidence of drying artefacts and the possibility of observing the samples in the aqueous state allowed further insights into the nano- and micro-structure of the solution phase (Section 5.3.1.3). However, there are limitations with the wet-AFM as the interaction is likely made between the AFM cantilever and the fibres only closer to the liquid-air interface, potentially less representative of the overall fibre network in the bulk.

The more stable Ca-hydrogel 2NapFF samples to the electron beam appeared more stable with the sample preparation procedure (Materials and Methods, Section 5.5.3) and in the electron beam of the SEM. This allowed imaging with high resolution of uncoated samples. Features above 400 nm were also present in these samples, however these were found with significantly less frequency. On the low end region of the width measurements, these samples indicated an average calcium fibre width of 29 ± 14 nm (189 measurements), calculated from the average in the width range from 0 to 85 nm (Fig. 5.9b).

A more detailed analysis of the images of Ca-hydrogels at the high concentration of 1.0 wt%, shows that there are hierarchical features such as branching, bundling and threading of the peptide self-assembled structures (Fig. 5.10). These features are typically associated with hierarchical structures and provide further evidence that 2NapFF forms hierarchical structures at high concentrations.

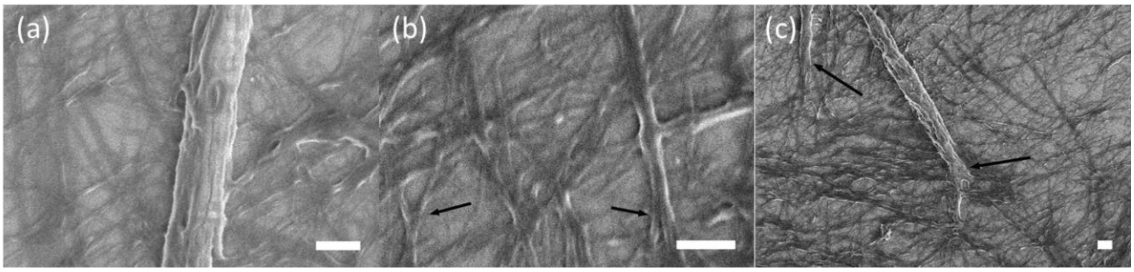

Figure 5.10 – SEM images of crosslinks (in all images), bundling (a), branching (b) and threading (c) in samples of 2NapFF Ca-hydrogels at a concentration of 1.0 wt% with no coating. Arrows indicate the kind of feature being highlighted on that image. All scale bars are 250 nm.

Crosslinks are features that are likely to change with the drying and could exist under applied stress to the network, therefore with dried specimens. It is not possible to decide whether the crosslinks shown here exist in the aqueous environment without applied stress or whether these are indications that this could also be the case in the aqueous phase. Other peptide-based materials studied in the literature show hierarchical structures with branching, bundling and threading features, as discussed in the introduction.

5.3.1.2. LSCM of the 2NapFF solution and hydrogel phase

In Chapter 3 (Fig. 3.13b) and in Chapter 4 (Fig. 4.13), LSCM was used to image the 2NapFF system in the solution phase and the Ca-hydrogel phase, respectively. These investigations were conducted in the 2NapFF concentration range from 0.05 wt% to 1.0 wt%. Here, these images were analysed with ImageJ and FiberApp.

LSCM images of the 2NapFF solution phase

Figure 5.10a shows 3D cross-sections of a 1 wt% 2NapFF peptide solution at pH 10.5 and the statistical analysis of the fibre bundles and persistence length at this length scale in the concentration range between 0.1 wt% and 1.0 wt%. It is important to note, based on the discussion above for SEM measurements that the analysis conducted here relates to the bundle features at this length scale in aqueous environment.

Peptide-based hydrogels usually form networks of fibres or tape structures.[17,56,82,83] Fig. 5.11a shows the 3D network span of the large bundles formed by a solution of 2NapFF at 1.0 wt% and high pH. ImageJ was used to measure the bundle diameter and network mesh size. In the case of the sample at 1.0 wt%, this showed a particular ribbon-like micellar assembly with a short and long width of 5.5 ± 1.2 µm and 14.7 ± 3.4 µm (n =

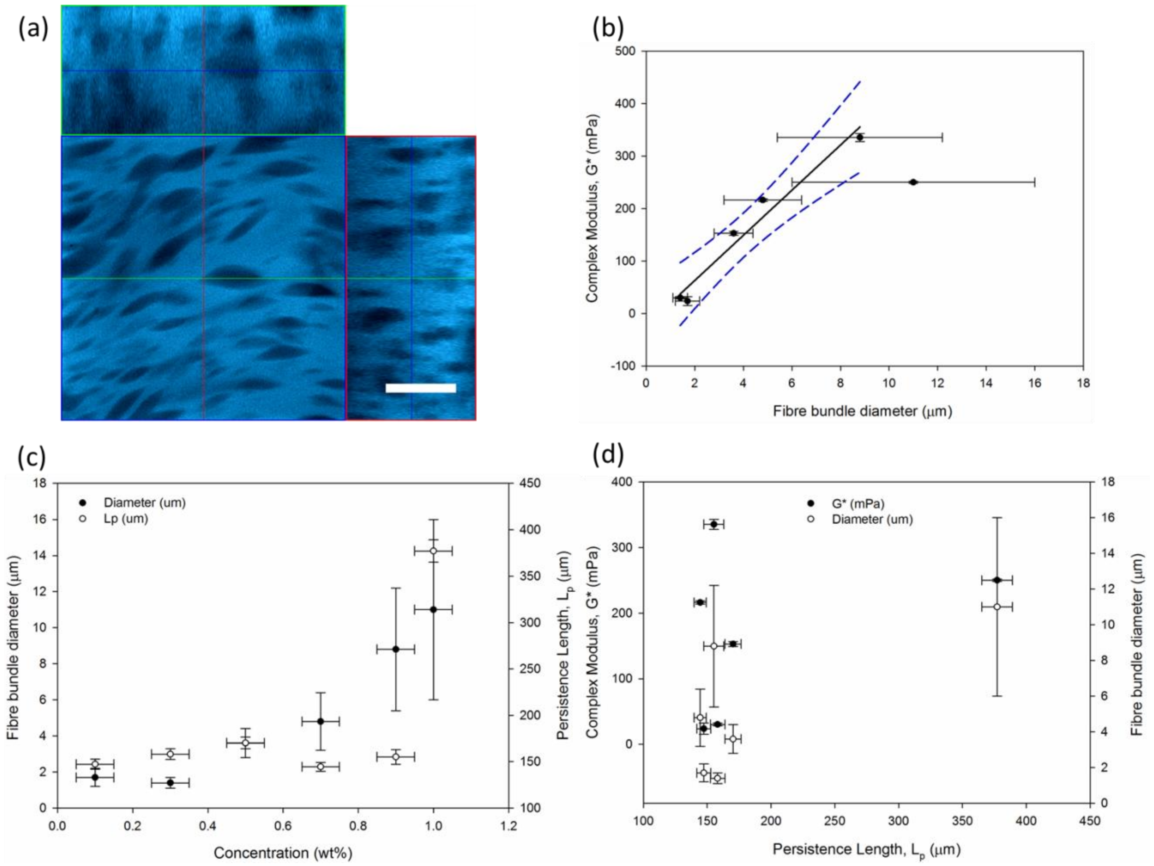

Figure 5.11 – Laser Scanning Confocal Microscopy (LSCM) image: morphological and statistical analysis of the 2NapFF solution phase by ImageJ and FiberApp software. (a) Example of a LSCM image of 1.0 wt% 2NapFF solutions with Nile blue staining with vertical cross-sections of the sample, here obtained in x- and y-axis of the image through the central part of the image as the green and purple line indicate. The scale bar is 5 µm. (b) Complex modulus, G*, obtained by rheological analysis of strain sweeps in the viscoelastic region conducted with vane-cup geometry, as a function of fibre bundle diameter. Line at best fit to the concentration region between 0.1 to 0.9 wt% (black line) and the corresponding 95 % confidence bands to this fit ($R^2 = 0.96$). (c) Fibre bundle diameter and persistence length, L_p, as a function of 2NapFF concentration. (d) G* and fibre bundle diameter as a function of persistence length, L_p.

50), respectively. The mesh size of the 1.0 wt% concentration was easier to calculate than the samples at lower concentration because the 3D distinction between background and ribbon-like structures was clearer for this sample. Here, a mesh size, $\xi = 10 \pm 5$ µm was obtained for 1.0 wt% 2NapFF micellar solution by LSCM. This result is larger than the result previously estimated by our group with 0.5 wt% 2NapFF, of $\xi = 40 - 100$ nm, probed indirectly with the use of dextran's diffusivity to probe the mesh size by ^{1}H-NMR spectroscopy.[57] However, these new results are in agreement with the previous estimation that for higher concentrations more lateral association occurs and consequently, the mesh size increases significantly.

The size of the fibre bundles of at the LSCM length scale is linearly related to the complex modulus, G*, in the concentration region from 0.1 to 1.0 wt% (Fig. 5.11b). The best fit was obtained by a linear equation ($y = y_0 + ax$) with $y_0 = -2.3$ and $a = 4.3$ ($R^2 = 0.96$). A fit to the complete data set, including the 1.0 wt%, resulted in a fit with a lower R^2 (= 0.76). Since the visual analysis of the image suggested a bundling and more compact packing micellar phase, and additionally the full fit had a lower confidence statistic, this concentration was not included in the fit calculation. Since 1.0 wt% 2NapFF is possibly the start of a new micellar phase, in the following discussion only the results between 0.1 and 0.9 wt% are analysed at first. In Fig. 5.11c, the persistence length of the fibre bundles at micrometre length scale does not change with an apparent increase in bundle diameter and an increase with concentration. This result suggests that the mechanical properties of individual fibres (e.g. single fibre bending rigidity) may not be the major factor in the macroscopic behaviour of the hydrogels (e.g. hydrogel shear deformation response). As with the concentration-independent persistence length, also the G* and bundle diameter are independent of the persistence length in this concentration region (Fig. 5.11d). The persistence length of the bundles is approximately 155 ± 10 µm ($R^2 = 0.97$).

As pointed out in Chapter 3, Section 3.3.1., 1.0 wt% 2NapFF solutions already appear to form structures with a distinct appearance and behaviour. These structures are similar to other systems investigated by light and small angle neutron scattering (SANS) and by statistical studies, which described the structures as ribbon-like worm micelles.[84–86] The ribbon-like worm structures, identified here by LSCM, have a higher persistence length (377 ± 12 µm, $R^2 = 0.98$) and have a larger width in comparison to their lower concentration counterparts.

Additionally, the LSCM images were analysed with an orientation distribution function of FibreApp. The propensity to form larger bundles is determined by the orientation distribution parameter, S_{2D}. Therefore, an S_{2D} close to 1 indicates the fibres are predominantly aligned, while if the S_{2D} is close to 0, the fibres are randomly oriented and not aligned. This result shows that for the worm-like structures present in each LSCM image, all the samples appear aligned, because the S_{2D} is above 0.5 for all samples (Fig. 5.12). Samples with higher molecular crowding (i.e. higher concentration, above 0.3 wt%) appear more aligned than samples at lower crowding (i.e. lower concentration, at 0.3 and 0.1 wt%).

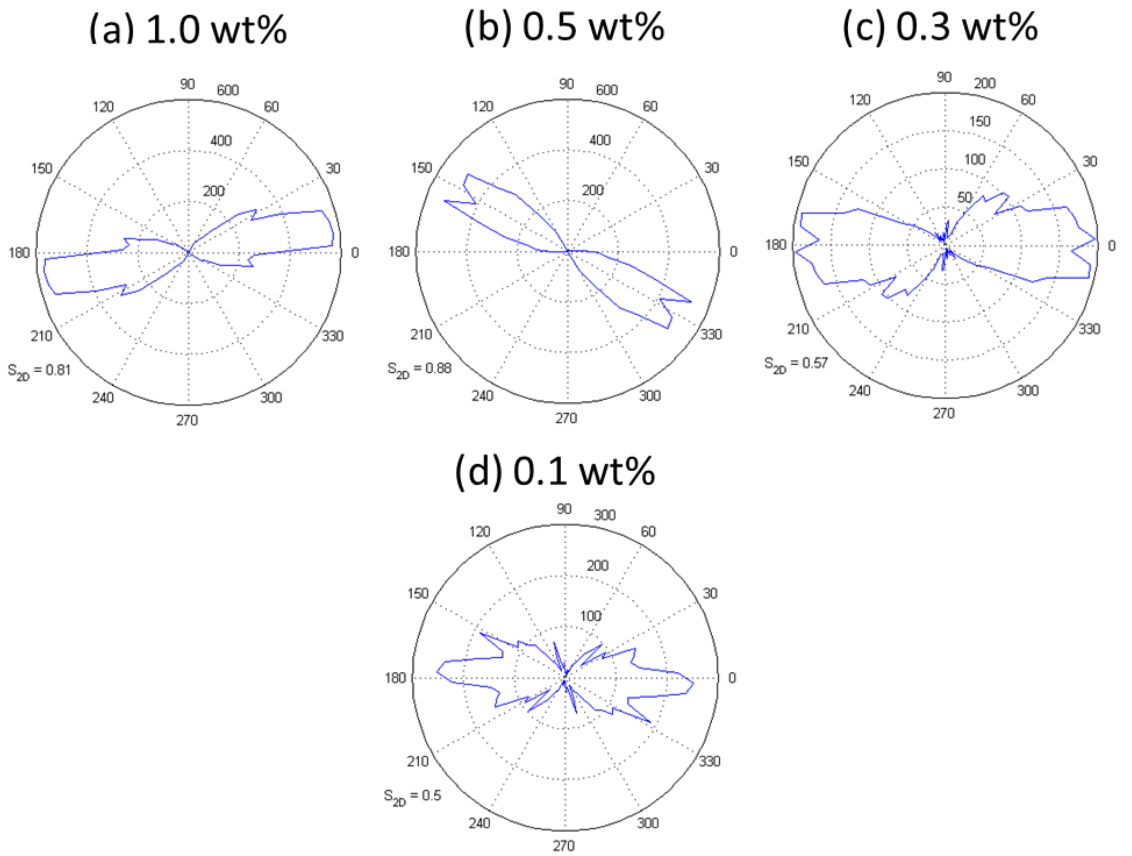

Figure 5.12 – Orientation distribution plots and the orientation distribution parameter, S_{2D} for the LSCM images of 2NapFF solution phase from 1.0 wt5 to 0.1 wt%. At 0.05 wt%, no worm-like structures were identified. The circular axes represent the direction of the orientation in degrees. The latitude axis represents the distance of the fibres measured.

LSCM images of the 2NapFF Ca-hydrogels

In this section, we have attempted to further analyse with ImageJ and FiberApp statistical analysis the structure of the hydrogel network of 2NapFF Ca-hydrogels. The LSCM experimental conditions to image Ca-hydrogels required a significantly larger pinhole and a larger number of scans, which resulted in lower resolution, even at 100x oil magnification objectives (Materials and Methods, Section 5.5.4) because of the shift in the emission spectra of the coated peptide nanofibres in the presence of the calcium ions observed in the LSCM itself by changing the detector filter and in side experiments in a fluorescence spectrometer.

All 2NapFF Ca-hydrogel LSCM images within the concentration region from 0.05 to 1.0 wt% show entangled fibre- or worm-like structures with increasing lateral alignment of the structures (Chapter 4, Fig. 4.13). This represents the hierarchical features of the Ca-hydrogel phase, equivalent to the solution phase. All ImageJ measurements of these images have diameters below the expected resolution of the images (0.6 – 0.8 μm), thus we have not considered these measurements reliable. However, FiberApp image analysis software provided additional structural information about the hydrogels at the micrometre length scale on the LSCM images. Persistence length of the bundles, $L_{p,B}$, 2D order parameter, S_{2D}, and scaling exponent analysis provided quantitative and qualitative information.

The calculated $L_{p,B}$ for 2NapFF Ca-hydrogels from 0.05 wt% to 1.0 wt% is shown in Table 5.1.

Table 5.1 – FiberApp analysis of LSCM images of 2NapFF Ca-hydrogel in the concentration region from 0.05 wt% to 1.0 wt%. $L_{p,B}$, S_{2D} and a.u. stands for persistence length of the bundles, orientation parameter and arbitrary unit. The type of fibre suggested by the data analyses was obtained using the methods of Usov *et al.*,[48] using the scaling exponent function.

Concentration (wt%)	**$L_{p,B}$ (μm)**	**R^2**	**S_{2D} (a.u.)**	**Type of Fibres**
1	314 ± 3.2	0.99	0.89	Rods - trapped
0.5	86.7 ± 1.4	0.98	0.79	Rods - trapped
0.3	55.5 ± 1.7	0.96	0.43	Rods - trapped
0.1	14.1 ± 1.0	0.95	0.094	Rods to WLC
0.05	13.2 ± 0.4	0.99	0.083	WLC - flexible

In Table 5.1, the measurements of $L_{p,B}$ were obtained with confidence of fit above 95% (R^2) for each case. This result shows that with increasing concentration in this concentration region, the persistence length of the bundles increases (Fig. 5.13a). To the best of our knowledge, this is the first time that a quantifiable feature of the microstructure of a supramolecular peptide material is shown to be directly correlated with the mechanical properties, G* (Fig. 5.11b).

This result supports the hypothesis that the mechanical properties of the supramolecular hydrogels are determined significantly by their microstructure, because LSCM focuses on microstructural aqueous features of the hydrogels. It is interesting to note that there is a change in correlation between the $L_{p,B}$ (persistence length of the bundles) measured at the microstructural level between the solution phase and the Ca-hydrogel phase. In the solution phase, there is a lack of correlation of the microstructural $L_{p,B}$ (Fig. 5.11d), however, after triggering hydrogelation, the worm-like structures are visibly transformed at their microstructural level since the measurement of $L_{p,B}$ of the Ca-hydrogels is correlated with G* (Fig. 5.13b).

In the Ca-hydrogel LSCM images analysed, the orientation parameter showed a rapid increase in between 0.3 wt% and 0.5 wt%, and changes from 0.083 at 0.05 wt% to 0.89 at 1.0 wt% (Table 5.3). The raw measurements of the orientation distribution are shown in Fig. 5.14. This result suggests that the fibres constituting the system have a

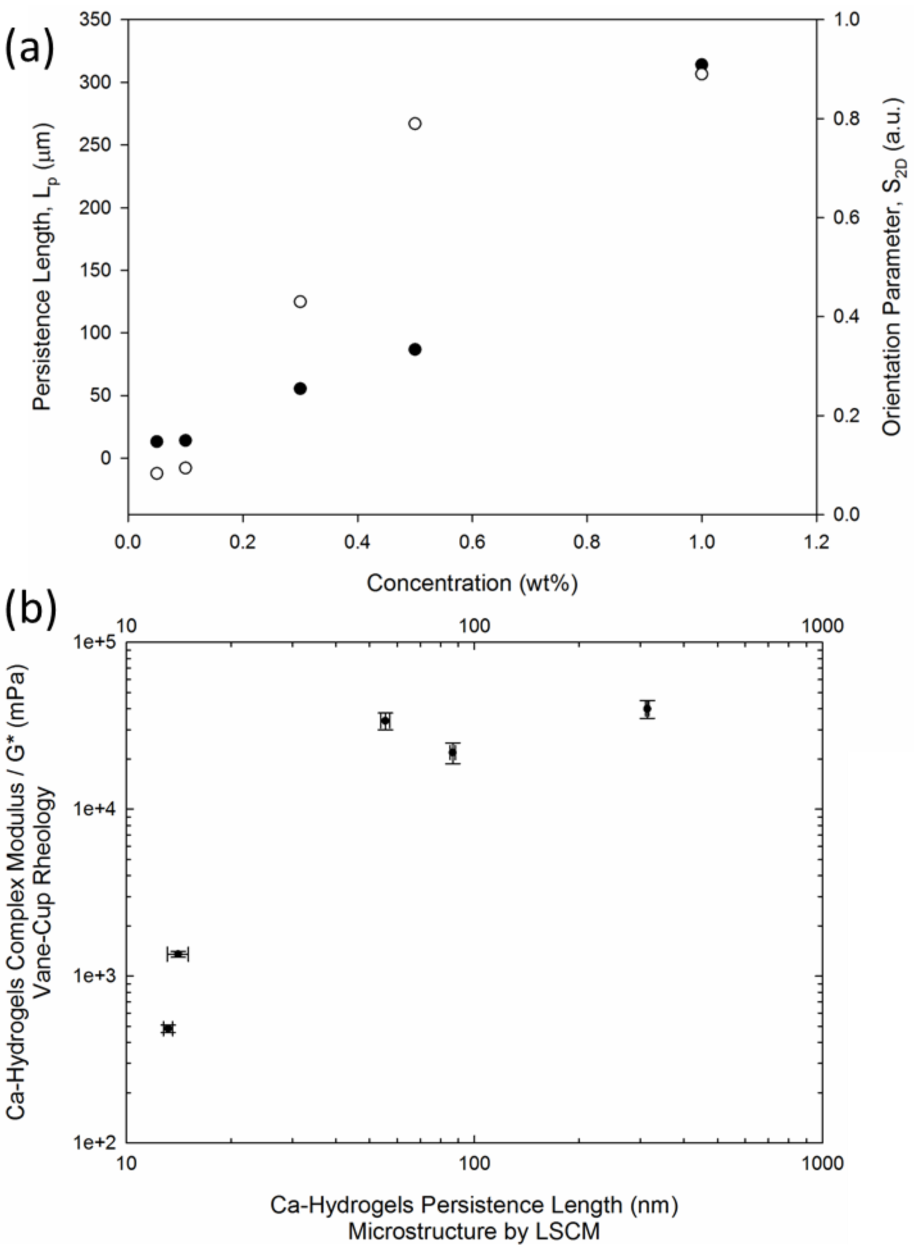

Figure 5.13 – FiberApp analysis of LSCM images of 2NapFF Ca-hydrogel in the concentration region from 0.05 wt% to 1.0 wt%. a.u. stands for arbitrary unit. Persistence length, Lp (black) and the orientation parameter, S_{2D} (white) are plotted as function of 2NapFF concentration (a). Complex Modulus, G*, was measured by rheology using a vane geometry, as a function of $L_{p,,B}$ (b). In plot (b) both axis are in Log-scale. G* error bars are the standard deviation of 3 rheology measurements and $L_{p,B}$ error bars are obtained from standard deviations of over 50 tracked fibres by FibreApp for each set of images at a fixed concentration.

significantly different microstructure with different concentrations, from randomly oriented fibres to aligned bundles at microscale. This result further supports our findings in Chapter 4 because it suggests that the starting micellar phase at each concentration influences the final Ca-hydrogel microstructure at that particular concentration.

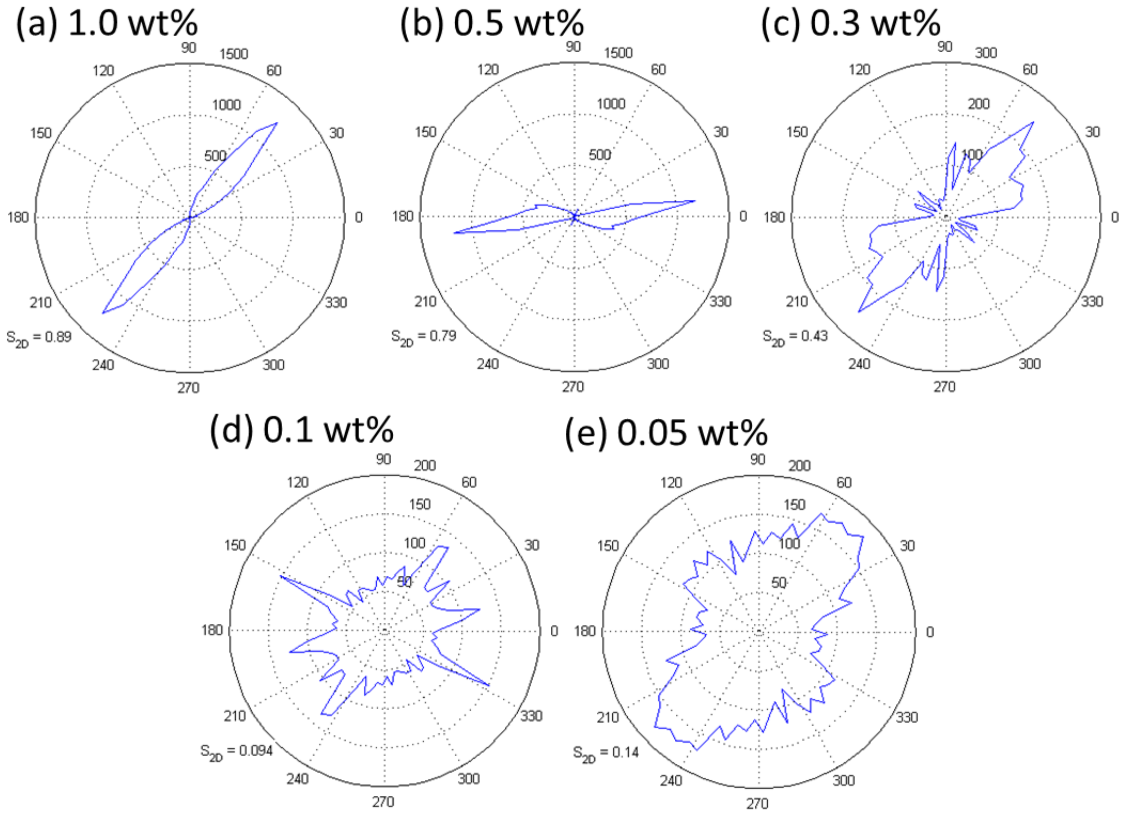

Figure 5.14 – Orientation distribution plots and the orientation distribution parameter, S_{2D} for the LSCM images of 2NapFF Ca-hydrogels from 1.0 wt% to 0.05 wt%. The circular axes represent the direction of the orientation in degrees. The latitude axis represents the distance of the fibres measured.

Furthermore, the scaling exponent analysis also revealed that a transition is present for the type of perceived fibre-like features in the Ca-hydrogel phase. At 0.05 wt%, the fibres fit a WLC model (flexible structures), while at concentrations above 0.1 wt%, they fit a rod-like structure model (stiffer structures). This transition in the microstructure can be seen by the scaling exponent plots in Fig. 5.15 for 0.1 wt% and, in particular for 0.05 wt%. At 0.1 wt% and 0.05 wt%. The fibres tracked appear to plateau for higher contour lengths when compared to the steep decrease in average end-to-end distance, L_{EE}, for 0.3 wt%, 0.5 wt% and 1.0 wt%. This method of analysis is reviewed for other fibre-like systems by Usov *et al*.[48]

It is important to note that the structural features measured here are characteristic features of the material at this length scale, the microscale. It is likely that the measurements conducted at lower length scales with AFM, by scattering methods with SANS (from a few angstroms to tenths of nanometres) or DLS (a few nanometres to thousands of nanometres) will reveal characteristic structural features of lower length scales. So, we used AFM to investigate the mechanical and structural properties from the use of imaging software in these images.

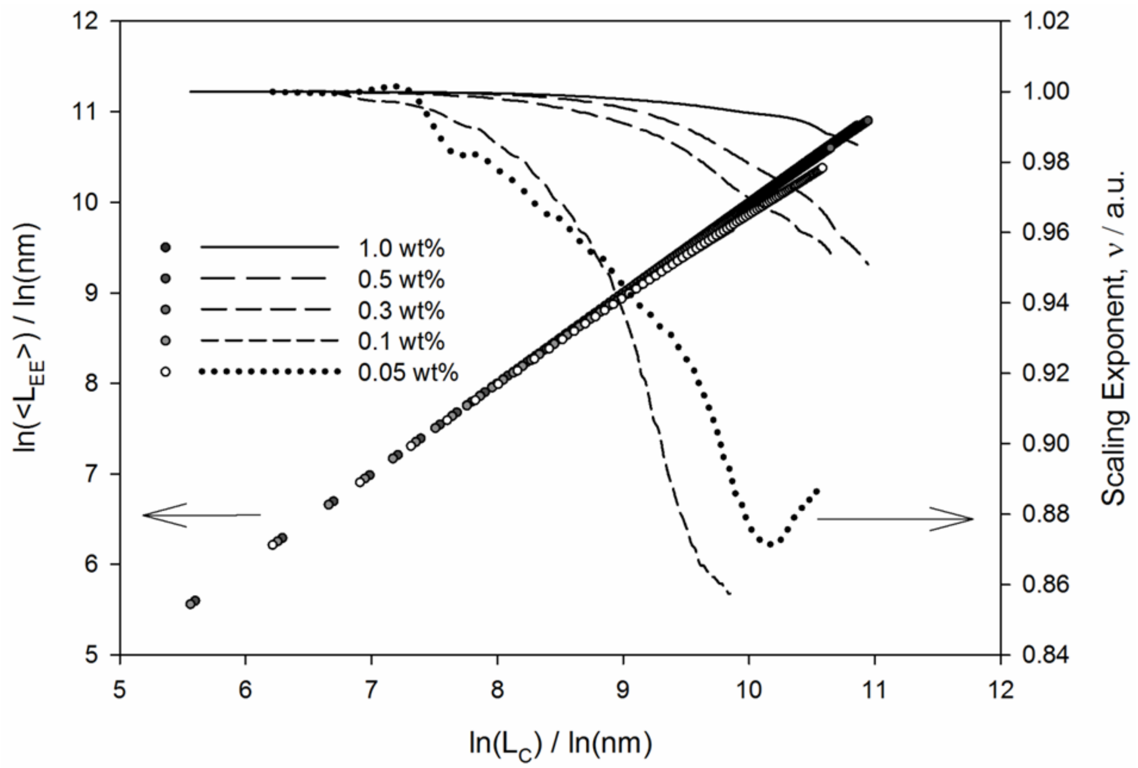

Figure 5.15 – Average end-to-end distance (L_{EE}) and scaling exponent as a function of the internal contour length (L_C) plots for hydrogels of 2NapFFat 1.0 wt%, 0.5 wt5, 0.3 wt%, 0.1 wt% and 0.05 wt%.

5.3.1.3. AFM of the 2NapFF solution and hydrogel phase

Samples of 2NapFF solutions and hydrogels were prepared on a silicon wafer as described in the Materials and Methods, Section 5.5.1 These peptide-based systems were investigated at the liquid-air interface, with the intention to minimize the artefacts identified with other sample preparation protocols while still maintaining the hydrogel aqueous environment. The samples were still visibly wet and in the aqueous state during and after the AFM imaging operation. However, it is likely that some evaporation processes occur at the liquid-air interface because the sample preparation requires small sample volumes. Also, from operational experience, the force applied in the sample by the cantilever appeared to capture a wide z-axis range of tenths of nanometres if there were fewer fibres at the interface or they were less entangled. Thus, the result in the imaged sample concentration may well be above the actual concentration of the solution prepared. However, nanofibre flexibility appears to be retained, considering the cantilever speed is 0.5-1.25 Hz. In order to minimize the evaporation effects, the room humidity was kept at 50 % throughout the experiments. Nevertheless, AFM images show smaller structural features inaccessible by the other microscopy techniques used here, since it is capable of higher resolution than SEM and LSCM microscopy techniques. Here, images of the height profile and peak force error (PFE) are used to characterise each of the samples. The PFE signal comes from perturbations in the x-y axis of the cantilever tip. PFE images are shown here in parallel to the height images because they are more sensitive to lateral perturbations of the cantilever tip than height profile images.

AFM images of the 2NapFF solution phase

The 2NapFF solution phase at pH 10.5 was imaged by AFM at concentrations of 0.05 wt% (Fig. 5.16), 0.1 wt% (Fig. 5.176), 0.5 wt% (Fig. 5.18) and 1.0 wt% (Fig. 5.19). In Fig. 5.16, the 0.05 wt% images of the 2NapFF solution phase suggest that the crowding effects of the sample in the aqueous state may misrepresented by this microscopy technique and sample preparation procedure. Here, the cantilever tip is likely to interact with different layers of worm-like structures because it oscillates in the perpendicular direction in relation to the silicon surface (z-axis). This multi-layer interaction is expected when the sample is significantly thick in the z-axis (the chosen oscillation amplitude permits high z-axis resolution). The choice of sample preparation procedure was done based on an extended method development and previous experience from the Luning Liu group of the Bioscience department of the University of Liverpool.

At all concentrations, AFM images of 2NapFF solution phase show worm-like structures. These appear mostly aligned in bundles as observed previously with LSCM images and with difficulty by SEM. The histograms of the fibre width are shown in Fig. 5.20. These results and the FibreApp imaging analysis results are shown in Table 5.2. These results are plotted in combination with the analysis of Ca-hydrogel AFM corresponding images, below. Both of these sets of images reveal structural characteristics of the two phases of 2NapFF, before and after gelation.

These AFM results indicate an average worm width of 18 ± 7 nm for the 2NapFF solution phase. These are accurately called small bundles if we use the worm-like micellar structure to sub-10 nm measurements from TEM and SANS. The persistence length is the micrometre length region. Furthermore, the S_{2D} (0.44 ± 0.15) indicates that the structures are likely to be forming aligned domains, which were measured to be of approximately 569 ± 217 nm junctions at this length scale. All scaling exponent analysis (Table 5.2, type of fibre) fitted best to a WLC model to describe the structures present in the solution phase.

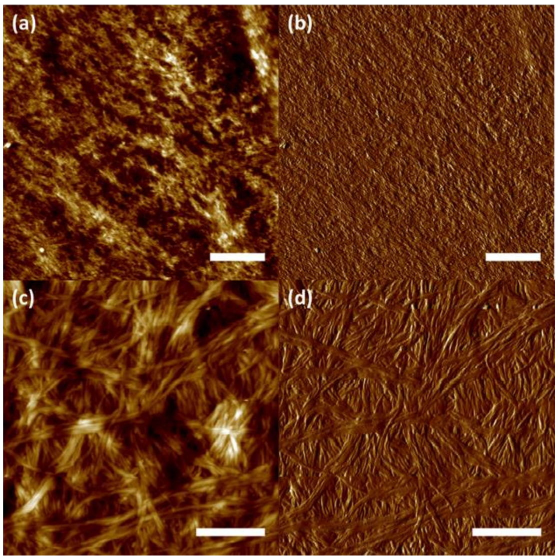

Figure 5.16 – AFM images of the 2NapFF solution phase at pH 10.5 at 0.05 wt% at low (a,b, scale bar: 5 µm) and high (c,d, scale bar: 500 nm) resolution in the height (a,c) and peak force error (b,d) channels.

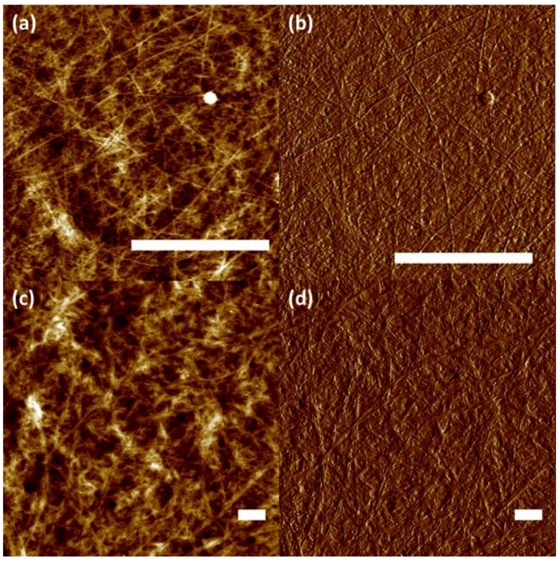

Figure 5.17 – AFM images of the 2NapFF solution phase at pH 10.5 at 0.1 wt% at low (a,b, scale bar: 5 µm) and high (c,d, scale bar: 500 nm) resolution in the height (a,c) and peak force error (b,d) channels.

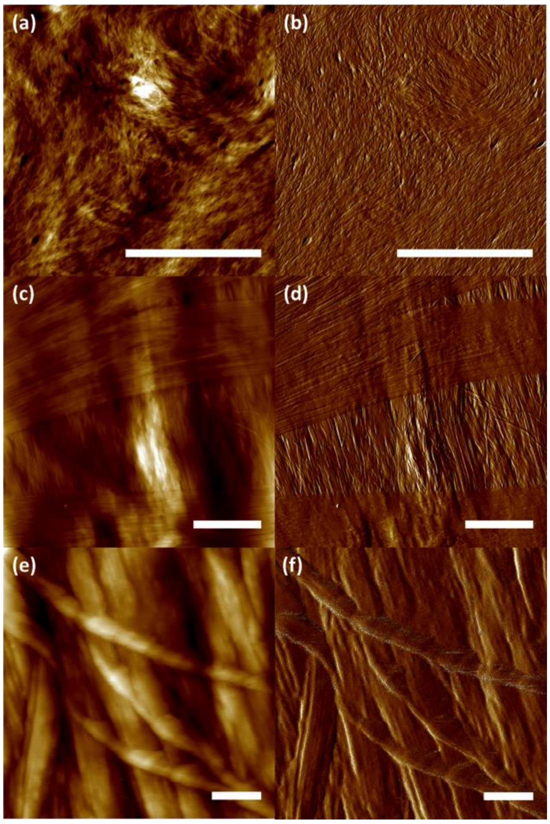

Figure 5.18 – AFM images of the 2NapFF solution phase at pH 10.5 at 0.5 wt% at low (a,b, scale bar: 5 µm), intermediate (c,d, scale bar: 500 nm) and high (e,f, scale bar: 100 nm) resolution in the height (a,c) and peak force error (b,d) channels.

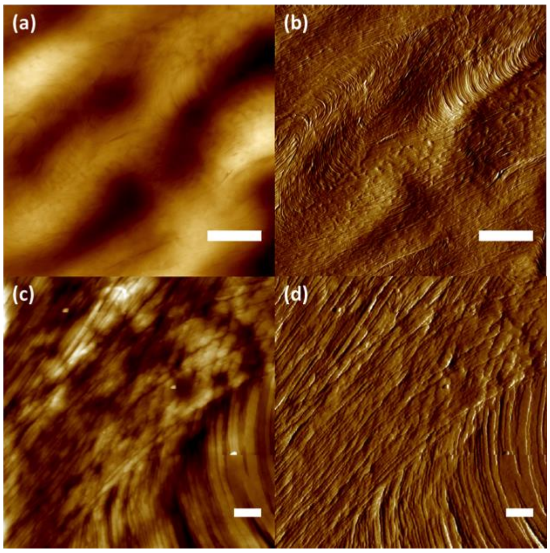

Figure 5.19 – AFM images of the 2NapFF solution phase at pH 10.5 at 1.0 wt% at low (a,b, scale bar: 5 µm) and high (c,d, scale bar: 500 nm) resolution in the height (a,c) and peak force error (b,d) channels.

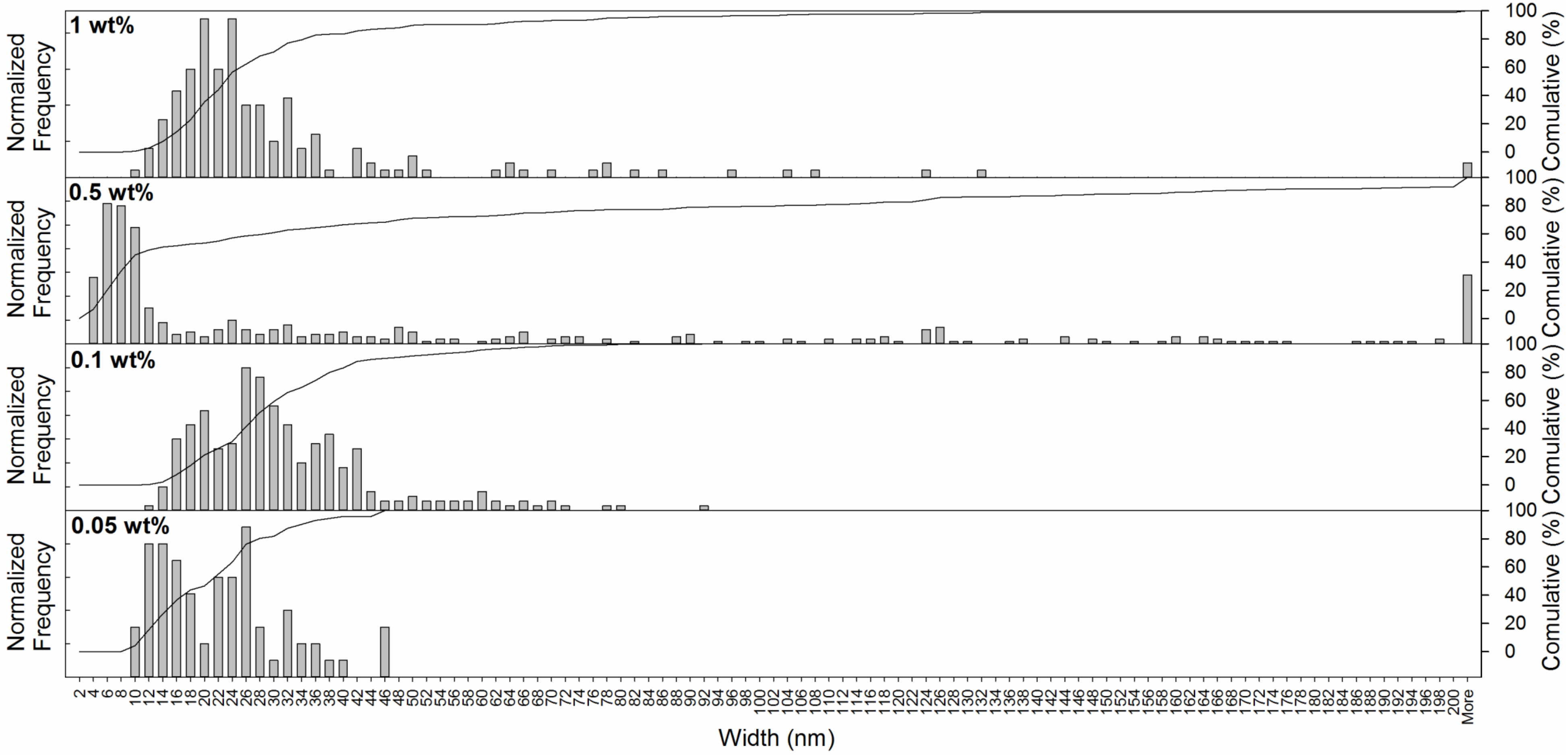

Figure 5.20 – Full set of histograms and cumulative analysis of AFM images of 2NapFF solutions in concentration range from 1.0 to 0.05 wt% and the width region from 2 to 200 nm. All data sets were normalized. Each histogram was made based on over 100 measurements.

Table 5.2 – AFM image analysis results to the 2NapFF solution phase at concentrations from 0.05 wt% to 1.0 wt%. The two highest peaks in fibre width of the histograms in Fig. 5.20 are shown in the column L_W. FibreApp was used to obtain the persistence length, L_P, and the confidence of the fit R^2, orientation parameter, S_{2D}, the nematic order (obtained with the 2D order parameter function) and the type of fibre, obtained by the scaling exponent function. WLC stands for worm-like chain model.

c (wt%)	L_W (max's) / nm	L_P (µm)	R^2	S_{2D} (a.u.)	Nematic order (nm)	type of Fibre
1	20, 24	4.21 ± 0.08	0.99	0.31	468	WLC
0.5	6, 24	4.35 ± 0.21	0.98	0.41	894*	WLC
0.1	20, 26	9.30 ± 0.38	0.98	0.37	432	WLC
0.05	12, 14	7.81 ± 0.15	0.99	0.66	483	WLC
Overall	**18 ± 7**	**6.4 ± 2.5**		**0.44 ± 0.15**	**569 ± 217**	

AFM images of the 2NapFF Ca-hydrogel phase

Samples of 2NapFF solutions at pH 10.5 were salt-triggered with $Ca(NO_3)_2$ to form a hydrogel film at the top of a silicon wafer. AFM images of the Ca-hydrogel phase were obtained at 0.05 wt% (Fig. 5.21), 0.1 wt% (Fig. 5.22), 0.5 wt% (Fig. 5.23) and 1.0 wt% (Fig. 5.24).

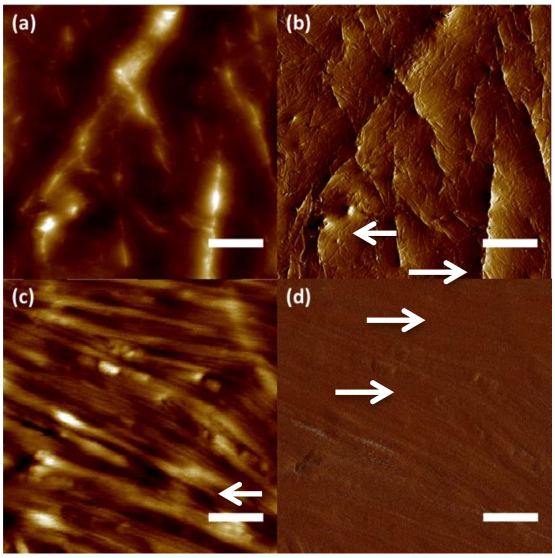

Figure 5.21 – AFM images of the 2NapFF Ca-hydrogel phase at pH 10.5 at 0.05 wt% at low (a,b, scale bar of 5 µm) and high (c,d, scale bar of 500 nm) resolution in the height (a,c) and peak force error (b,d) channels. Arrows point to open ends.

Here, in Fig. 5.21, it can be seen that 2NapFF 0.05 wt% Ca-hydrogel nanofibre structures exist in larger amounts per unit area than expected in a 99.95 wt% water sample. Therefore, it is likely that the cantilever tip similarly compresses these nanofibres during the measurement against the silicon surface. Also, the 0.05 wt% samples prepared in the small sample volumes required by the technique (i.e. 50 – 100 µL) retained the water for less time than samples with higher concentrations of 2NapFF.

However, nanofibres with open ends are still visible in Fig. 5.20b (arrows), as previously observed by SEM at the same concentration. Higher edges in Fig. 5.20b appear to indicate that water evaporation rearranged the fibres in this aligned manner upon slight drying.

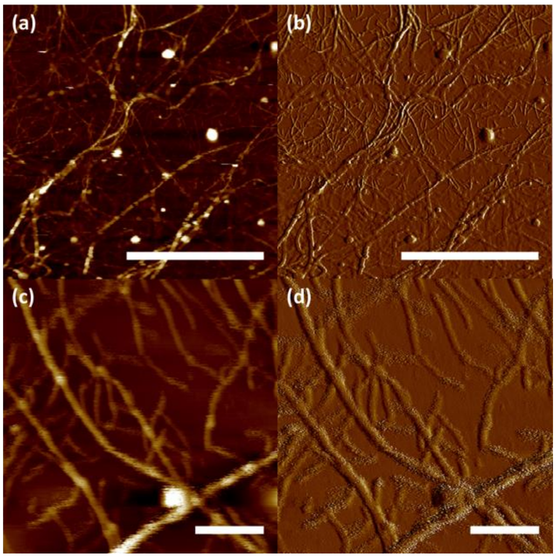

Figure 5.22– AFM images of the 2NapFF Ca-hydrogel phase at pH 10.5 at 0.1 wt% at low (a,b, scale bar of 5 μm) and high (c,d, scale bar of 500 nm) resolution in the height (a,c) and peak force error (b,d) channels.

Fig. 5.22 of 0.1 wt% 2NapFF shows a distinct microstructure to the 0.05 wt% 2NapFF sample (Fig. 5.21). As mentioned above, these higher concentration samples were more self-sustained when the cantilever scanned the liquid-air interface. Interestingly, some spherical structures appear to be present in between the hydrogel network at 0.1 wt% (Fig. 5.22). In Fig. 5.22c and Fig 22d an attraction point is visible near a white spherical aggregate. Fig. 5.22a and Fig. 5.22b show several junction zones between nanofibres. Furthermore, 0.5 wt% and 1.0 wt% 2NapFF images of Ca-hydrogel networks in Fig. 5.23 and Fig. 5.24, respectively, show a variety of cross-linking features of all types discussed by Raghavan and Douglas and discussed in page 155.[42] The possibility of forming a variety of cross-linking types is likely to be the dominant factor for hydrogel formation at one of the lowest minimum gelation concentrations (mgc of 0.02 wt%) of these hydrogels among supramolecular gelators for comparable concentrations.[17] The

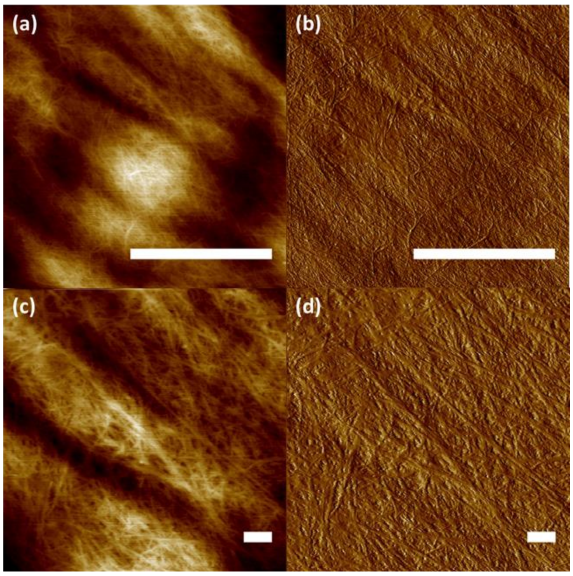

Figure 5.23 – AFM images of the 2NapFF Ca-hydrogel phase at pH 10.5 at 0.5 wt% at low (a,b, scale bar of 5 μm) and high (c,d, scale bar of 500 nm) resolution in the height (a,c) and peak force error (b,d) channels.

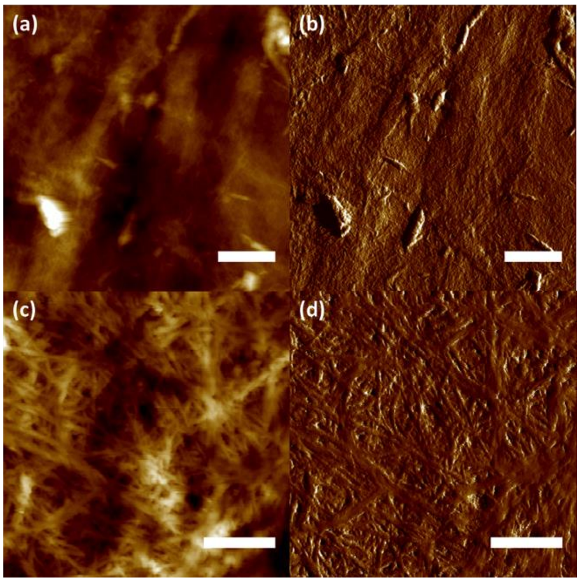

Figure 5.24 – AFM images of the 2NapFF Ca-hydrogel phase at pH 10.5 at 1.0 wt% at low (a,b, scale bar of 5 μm) and high (c,d, scale bar of 500 nm) resolution in the height (a,c) and peak force error (b,d) channels.

low mgc can be linked with superior mechanical properties at minimal concentrations as shown in Chapter 4.

It can be observed with these images of 2NapFF molecular gels that an increase in concentration promotes an increase in the number of cross-links, therefore forming a denser hydrogel network (Fig. 5.21, Fig. 5.22, Fig. 5.23 and Fig. 5.24). This trend was also seen for MAX8 peptide gelator.[19]

Analogously to the solution phase analysis, ImageJ was used to measure the width of fibres and bundles present in the Ca-hydrogel samples from 0.05 wt% to 1.0 wt%, histograms of the fibre width spread are shown in Fig. 5.25. A summary of these worm width measurements and FibreApp measurements of L_P, 2D orientation parameter (S_{2D}), size of the nematic order (i.e. obtained from the 2D orientation parameter) and type of fibre is shown in Table 5.3.

Table 5.3 – AFM image analysis results to the 2NapFF Ca-hydrogel phase at concentrations from 0.05 wt% to 1.0 wt%. The two highest peaks fibre width of the histograms in Fig. 5.25 are shown in the column L_w. FibreApp was used to obtain the persistence length, L_P, and the confidence of the fit R^2, orientation parameter, S_{2D}, the nematic order (obtained with the 2D order parameter function) and the type of fibre, obtained by the scaling exponent function.

c (wt%)	L_W (max's) / nm	L_P (µm)	R^2	S_{2D} (a.u.)	Nematic order (nm)	type of Fibre
1	24, 28	4.25 ± 0.33	0.95	0.13	569	rod
0.5	26, 30	3.34 ± 0.10	0.99	0.2	660	rod
0.1	28, 32	4.47 ± 0.05	0.99	0.22	427	rod
0.05	32, 38	3.01 ± 0.09	0.99	0.17	495	rod
Overall	**30 ± 4**	**3.77 ± 0.7**		**0.18 ± 0.04**	**538 ± 100**	

Interestingly, the AFM images revealed a similar degree of the nematic order between the 2NapFF solution phase and hydrogel phase of 569 ± 217 nm and 538 ± 100 nm, respectively. This result suggests that the nanoscale bundles do not change significantly; an apparent reduction in the standard deviation and size may indicate that these become slightly more packed and homogeneous upon hydrogel formation. In Fig. 5.26, the ImageJ and FibreApp results are plotted for both the solution phase and hydrogel phase of 2NapFF in the concentration range from 0.05 wt% to 1.0 wt%. Fig. 5.26a shows that the Ca-hydrogels worm-like fibres have a slightly higher width than the corresponding worm-like structures at high pH in the solution phase. This result suggests that the Ca^{2+} ions allow further bundling of the solution phase individual fibres. The dispersion of the width results is also greater in the solution phase for higher concentrations, 0.5 wt% and 1.0 wt% (Fig. 5.20), when compared to the Ca-hydrogel phase at corresponding

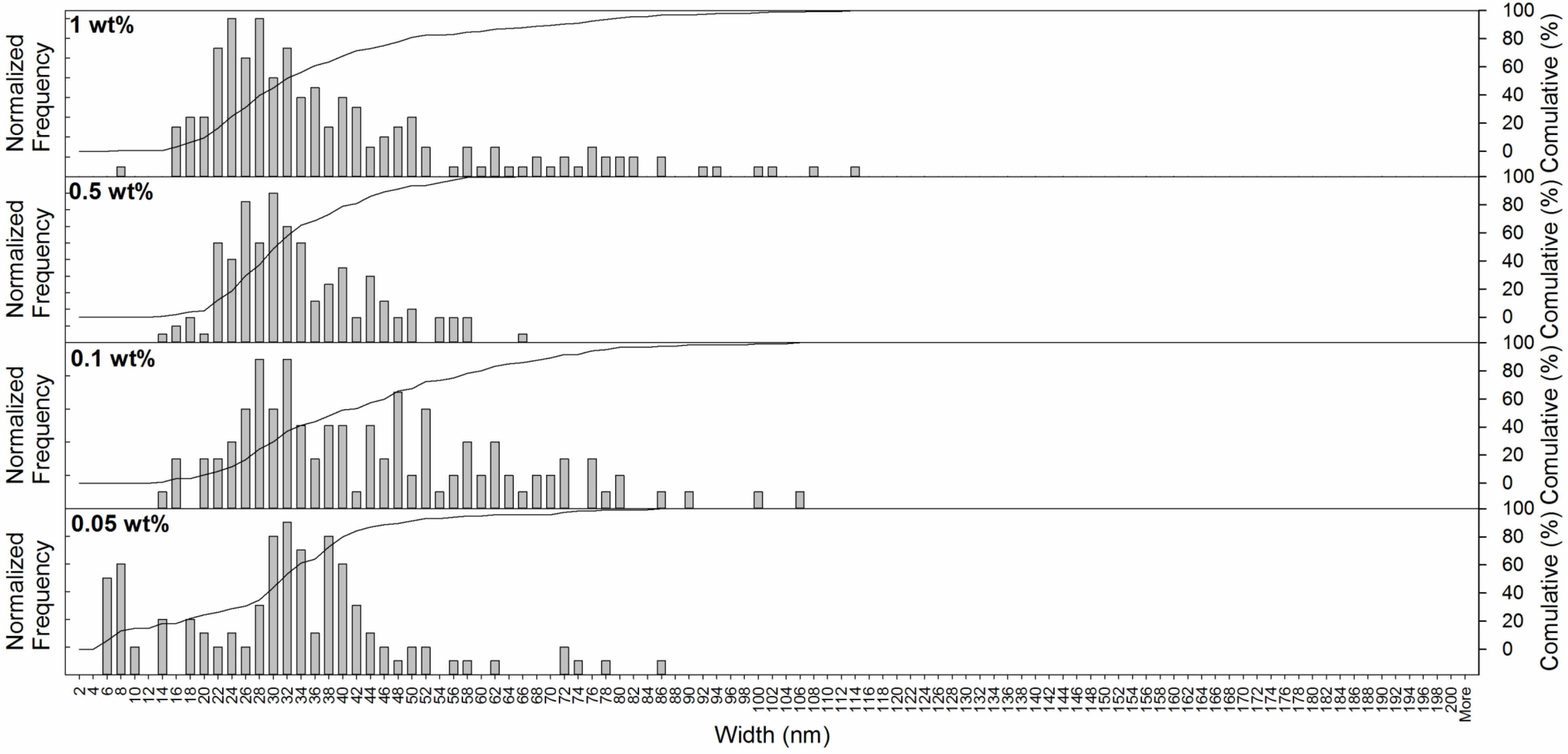

Figure 5.25 – Full set of histograms and cumulative analysis of AFM images of 2NapFF Ca-hydrogels in concentration range from 1.0 to 0.05 wt% and the width region from 2 to 200 nm. All data sets were normalized. Each histogram was made based on over 100 measurements.

concentrations (Fig. 5.25). In Fig. 5.26b, a similar L_P at higher concentrations (0.5 wt% and 1.0 wt%) between the solution phase and the Ca-hydrogel phase was obtained by AFM measurements. Interestingly, at lower concentrations (0.05 wt% and 0.1 wt%), the persistence length is different between the solution and Ca-hydrogel phase. However, all of these L_P results are within a narrow region between 3 to 10 μm for both 2NapFF solutions and hydrogels. The difference in L_P at lower concentrations could be explained by less crowding effects when compared to the higher concentrations.

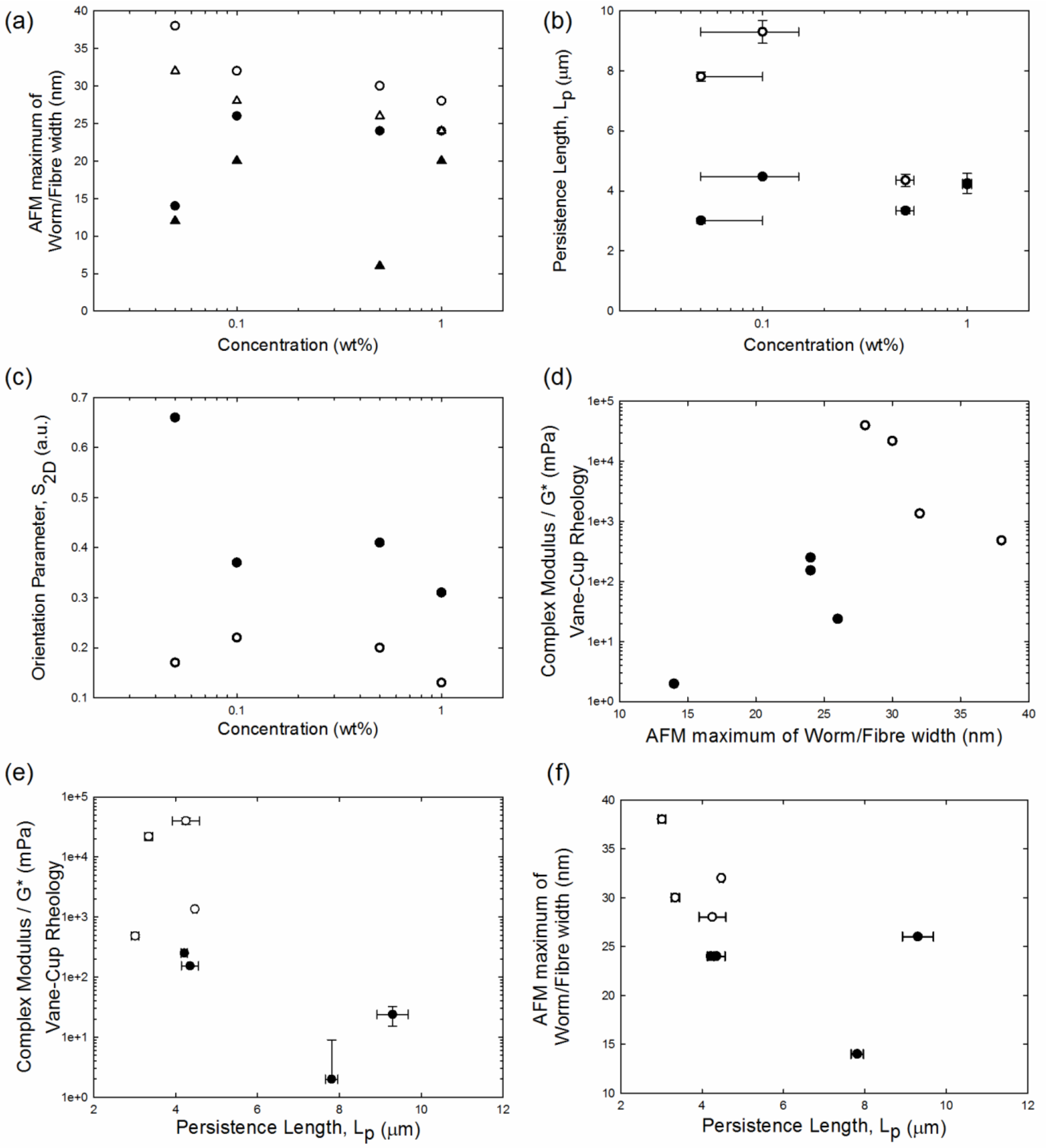

Figure 5.26 – AFM image analysis results obtained by ImageJ and FiberApp analysis software for the solution phase (white) and Ca-hydrogel phase (black) of 2NapFF: (a) 1st peak (circles) and 2nd peak (triangles) of worm/fibre width as a function of concentration; (b) Persistence Length, L_P as a function of concentration; (c) Orientation parameter, S_{2D}, as a function of concentration; (d) Complex modulus, G*, as a function of 1st peak of worm/fibre width; (e) G* as a function of L_P; and (f) 1st peak of worm/fibre width as a function of L_P.

The AFM order parameter measurements (S_{2D}) indicate that at the nanoscale the Ca-hydrogel phase forms more randomly oriented worm/fibre-like structures than the solution phase across the concentration range studied here (Fig. 5.26c). The fibre width measured by AFM for both the solution phase and the hydrogel phase is uncorrelated at the concentrations studied here (Fig. 5.26d). Unexpectedly, a slightly lower persistence length of the Ca-hydrogel nanostructures correlates to higher moduli, while slightly higher persistence length in the solution phase is linked with lower mechanical properties (Fig. 5.26e). This result suggests that at this scale the structural features are not related to macroscopic features. The slightly higher persistence length of the solution phase bundles may be linked with the slightly larger formation of nematic bundles (Table 5.2 and Table 5.3). Finally, L_P is not correlated with the peak width of the worm-like structures of the solution phase nor the hydrogel phase.

5.4. Conclusions

Microscopy techniques are useful techniques for characterisation of peptide-based materials. Optical microscopy provided information regarding the birefringence in the 2NapFF solution phase. SEM imaging of peptide Ca-hydrogels revealed an overall type of nanostructure and approximate sized structures in the Ca-hydrogels, including bundles and some single fibrillar bundle features in the case of 2NapFF. Imaging under hydration informs more accurately of the solution and hydrogel structure.

With LSCM, the microstructure can be accurately represented and with the use of FibreApp image analysis software, peptide-based hydrogel systems can be studied with regards to the link between their microstructure and their mechanical properties. The 2NapFF shows by LSCM that the microstructure is linearly correlated with the mechanical properties measured by oscillatory rheology. The solution phase is imaged by this technique with standard operation, while the Ca-hydrogel phase requires more delicate adjustment of the acquisition parameters (e.g. short observation times and a larger number of scans), possibly because the calcium ions may interact with the Nile blue or change its absorption/emission properties. With the experimental setup tested, no single fibres features were possible to image. LSCM samples were reproducible and allowed a 3D perspective of the hydrated hydrogels with bundle size resolution.

From the imaging techniques used in this Chapter, the AFM imaging was the most valuable for analysis of the solution and hydrated hydrogel structural features such as nanofibre flexibility and size, examining its liquid-air interface. AFM can overcome the SEM and LSCM limits in resolution and the requirement of working under vacuum (with SEM, dehydrated samples) or use of additives (with LSCM, which were shown to change the hydrogelation kinetics[87]). The major disadvantage of AFM imaging is the fact that the imaging can only be conducted at the sample interface and cantilever vertical resolution in a 3D aqueous environment introduces an apparent higher concentration if no dilution methods are used. The major advantage in using AFM techniques to investigate hydrated samples of 2NapFF are to comprehend the bundling and type of cross-links of the worm/fibres, understanding of the features such as persistence length, orientational distribution of the fibres/bundles, sizes of the nematic order and type of fibre based on the physical bending behaviour of these structures. The analysis of these parameters is made by FibreApp and ImageJ software.

These microscopy techniques and analysis software gave evidence that 2NapFF forms hierarchical structures in the solution phase and in the hydrogel phase by the ImageJ derived histogram analysis of the SEM and AFM images. The diameter of the primary fibres was only accessible by SANS,[88] with different levels of bundling features are shown by size measurements for both solutions and hydrogels by SEM and LSCM. The persistence length, L_P of the fibre structures is different at different hierarchical levels. At the microscale, measured by LSCM, the L_P of the fibre bundles appears to be linearly correlated with the mechanical properties of the hydrogels measured by oscillatory rheology. At the nanoscale, measured by SEM and AFM, the persistence length is approximately constant across length scales and in the order of a few micrometres for both the solution phase and the hydrogel phase. The 2NapFF hydrogel phase has more randomly oriented worms/fibres than the solution phase, which was shown to form aligned domains at both the nanoscale and microscale. These findings resulted from the FibreApp analysis of the orientation distribution and a 2D order parameter analysis. This result agrees with our previous findings with NMR spectroscopy.[3] It was only possible to probe the mesh size of the hydrogels with LSCM in the order of tenths of micrometres for the 1.0 wt% solution phase. The AFM images of 2NapFF Ca-hydrogel samples show periodicity along the fibre axis. However, the accurate quantification of the pitch size requires further analysis and exploration with different sample preparations in order to investigate less crowded environments.

The major changes from the solution phase to the Ca-hydrogel phase reside in the microstructural changes, while nanoscale features of the worm-like structures do not change as significantly for concentrations above the 2nd cmc, except a small increase in the size of the bundles with hydrogelation. AFM image analysis at nanoscale suggests that fibres in the solution phase are best fitted to a worm-like chain model, while Ca-hydrogel samples are best fitted to a rod-like model.

5.5. Materials and methods

5.5.1. Solution and hydrogel sample preparation

The amount of 2-napthalene-diphenylalanine (2NapFF) used in this project was mostly synthesised by Dave Adams and partially synthesised by myself using previously described methods.[89] A solution of 2NapFF was prepared by dissolution of a weighted amount of the gelator in a basic solution with approximately 1.2 eq. of NaOH from a stock basic solution at 1M. This is termed in this Chapter as the solution phase.

Ca-Hydrogels were prepared by adding the suitable amount from a stock solution of 200 mg/mL of calcium nitrate to make a final peptide to calcium molar ration of 1:2.

5.5.2. Sample preparation and standard operation procedure (SOP) for optical microscopy

Optical microscopy was carried out using a Nikon Eclipse Microscope and image analysis was done with ImageJ.[49] Samples were prepared as described above. They were poured onto a microscope slide and examined in the bright field and in between cross-polarized lenses.

5.5.3. Sample preparation and SOP for SEM

SEM images were obtained using a Hitachi S-4800 FE-SEM at 0.5 to 1 keV. 5x5 mm diced silicon wafers were used to probe the gels. The gels were prepared as described above in volumes of 2 mL. In solution/gel sample preparation, either a Si-wafer was dipped for 30 minutes in the solution/gel sample or gels were transferred carefully to the top of the Si-wafer as shown in Fig. 5.27. In either case, the samples were subsequently allowed to dry for a further 30 minutes under nitrogen flow (approximately 0.5 atm above atmospheric pressure). In the method development phase, an alternative drying method was tested, in which samples were allowed to dry overnight at room temperature.

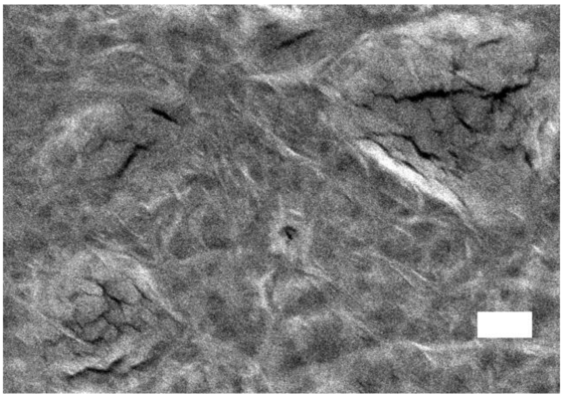

Figure 5.27 – Example of beam damage on a dense film of 0.5 wt% 2NapFF geled with the GdL method and dried under nitrogen flow. The dark areas show cracks in the film caused by prolonged exposure at high kV (above 3 keV). Scale bar is 1 μm.

No coatings were applied to the gels. To avoid charging, a low voltage SEM was used (0.5 to 1 keV) at a 1.5 to 3 mm working distance with the deceleration mode (i.e. deceleration V = 2 keV, from 3 to 1 keV). The low kV was used to avoid sample beam damage (Fig. 5.27)

When mentioned, samples were sputter coated with Au with a K500X manual sputter coater from Quorum Technologies Ltd. Interferometric techniques show that the coating thickness can be calculated for Au/Pd coating with the equation 5.2.

$$d\ (\text{Å}) = 7.5\ I\ t \qquad \text{Equation 5.2}$$

This equation is obtained for V = 2.5 kV and a target to specimen distance = 50 mm, with (t) the time in minutes, (I) the current in mA and (d) the thickness in Å. All coated samples were coated with just approximately 5-10 nm gold.

5.5.4. Solution and hydrogel sample preparation and SOP for LSCM

Confocal microscopy images were taken using a Zeiss LSM 510 Meta confocal microscope. A Zeiss Plan-Apochromat 100x/1.40 Oil M27 objective was used for all images selected. Fluorescence from Nile blue was excited using a 633 nm Helium–Neon laser (with power adjusted between 10 to 25%, unless specified) and emission detected with a band pass filter between 650 and 710 nm. Liquid samples of the solution phase or hydrogel phase were prepared in situ, using the same methodology as described above except solutions (Chapter 3) and hydrogels (Chapter 4) were prepared with an aliquot of Nile Blue staining was added to the initial ddH_2O used to dissolve the peptide from a stock solution of 20 mg/mL to make a final 0.05 mg/mL in the dissolved peptide gelator starting solution. Solutions were poured in MatTek dishes (20 mm diameter glass coverslip) made of uncoated borosilicate glass, while hydrogels were prepared in the MaTeK dishes directly to avoid disruption of the hydrogels.

Two background control samples of 0.05 mg/mL Nile blue in pH 10.5 water solutions are shown in Fig. 5.28. Fig. 5.28a was obtained in the bulk of the solution and Fig. 5.28b was obtained at the glass-solution interface of the glass dishes.

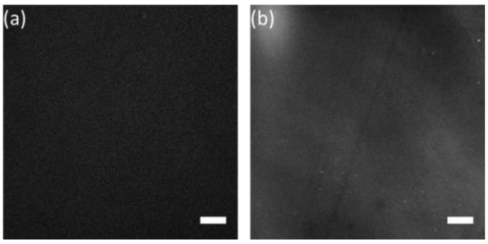

Figure 5.28 – Control Samples of 0.05 mg/mL Nile Blue at pH 10.50 dd H_2O, images at in the bulk (a) and at the glass-liquid interface (b). Scale bars are 20 μm.

No Nile blue emits in the region of the band-pass filter used between 638 nm and 758 nm, this is likely because the basic conditions of the molecular environment change the excitation/emission conditions of Nile blue as shown in the literature.[90,91] Fig. 5.28b was obtained with 60% laser power selected and a 700 gain, both significantly higher than the typically 10 – 25 % power level and no gain used to obtain the peptide solution and hydrogel images. Once the Nile blue is present, the interaction of the dye with the peptide structures appears to be sufficient to make a stable complex that allows Nile Blue to absorb and emit in the desired region, even at pH 10.5.

Another problematic case with regards to sample resolution is the adjustment of gain and offset of the LSCM. These two parameters were kept constant for each batch of images being analysed for size measurements.

For each image, the following parameters were selected to successfully image peptide hydrogels: selection of objective, adjustment of laser power, gain, offset, scan speed, average or sum of a set number of scans. The aim was to obtain an image where the fibres could be traced while reducing the impact of the beam on thermal fluctuations, heating, change in concentration or degradation of the sample.

LSCM images were randomly analysed with regards to the fibre-tracking step in order to avoid preconceived ideas or trends in the raw measurements obtained from the images.

5.5.5. Solution and hydrogel sample preparation and SOP for AFM

Solution and hydrogel samples of 2NapFF were prepared as described above. AFM samples were prepared by drop casting the solution under a solvent atmosphere on freshly clean diced Silicon Surface (5x5 mm) from Agar Scientific.

Atomic force Microscopy (AFM) images were recorded under ambient conditions (22 C and 45 ± 5 % humidity) using a Bruker Multimode 8 operating in the tapping-mode regime using ScanAsyst-Air-HR tips (PPP-NCH, 300-330 kHz, 42 N/m). The typical conditions used were scan rates 0.5-1.25 Hz, scan angle 90° and with feedback signals optimized. Images shown are subjected to a first-order plane-fitting procedure to compensate for sample tilt.

Images were first processed by Nanoscope Analysis software package (Bruker) by following the following procedure: (1) Open Image; (2) Line by line compensation tool; (3) flatten image if the surface is visible; and exporting the image. At this stage, height and fibre pitch features were measured if appropriate. Finally, the processed image was analysed by ImageJ and FiberApp as detailed below (Section 5.5.6 and Section 5.5.7, respectively).

With solution and hydrogel samples, the sample preparation may be adjusted to reveal single fibre features or microstructural features. In the case of this project, a preference for the microstructural features and imaging the samples in an aqueous environment made a challenging sample preparation process. On one hand, a too heterogeneous sample height (above 1 μm roughness, defined here as maximum height of the sample) would render imaging impossible due to contact with the cantilever when scanning the surface. On the other hand, a thin sample would also evaporate quicker and be prone to flattening of the 3D structures by the forces applied in the cantilever measurement and a slight increase in temperature in the point of contact because of the temporary white light and the permanent laser in the imaging region. Therefore, samples were prepared, in situ, in the case of the Ca-hydrogels (i.e. gels triggered in the silicon wafer) and imaged within the following 5 minutes afterwards. In both cases, the solution phase and the hydrogel phase, it is expected that when the sample is significantly thick (in the z-axis), above the oscillation amplitude used here (100 – 150 nm), the imaging operation may flatten the 3D structure of the micellar and hydrogel systems. The choice of sample preparation method was based on previous findings which indicate that the microstructure and cross-links are key features that characterise the hydrogels.[58,92] Therefore, the methods used here did not require dilution of the sample, bound to change the microstructure, and used sample volumes above 50 – 100 μL, in order to preserve the aqueous state of the sample for enough time to provide an image of the hydrated state of the self-assembled hydrogels.

5.5.6. ImageJ software analysis

The image size was calibrated and a scale bar was added with ImageJ. Fibre width measurement or mesh size measurements were conducted. These measurements were exported to Excel and SigmaPlot for a statistical analysis.

5.5.7. FiberApp software analysis

The images with scale bar processed by ImageJ were marked with the fibre tracking feature of the FiberApp software. The parameters for A* path finding algorithm and fibre bending flexibility of the fit were adjusted to obtain the best visually identifiable fit, based on guidelines suggested by Usov *et al.*[48,93] Furthermore, the images were analysed for persistence length, orientation parameter, 2D order parameter, scaling exponent. In each of these measurements, the resolution of the measurements and size/range of the area to be fitted has inputted in the software.

5.5.8. Rheology measurements

Hydrogels mentioned in this Chapter were prepared as mentioned above in plastic cups and analysed by vane geometry in an Anton Paar MCR 301 rheometer. Strain-sweep measurements (0.5 Hz frequency) were followed by frequency-sweep measurements in the viscoelastic region (0.5% stain) of 2NapFF.

5.6. Appendix

5.6.1. Histogram analysis by ImageJ of the SEM images of Ca-hydrogels

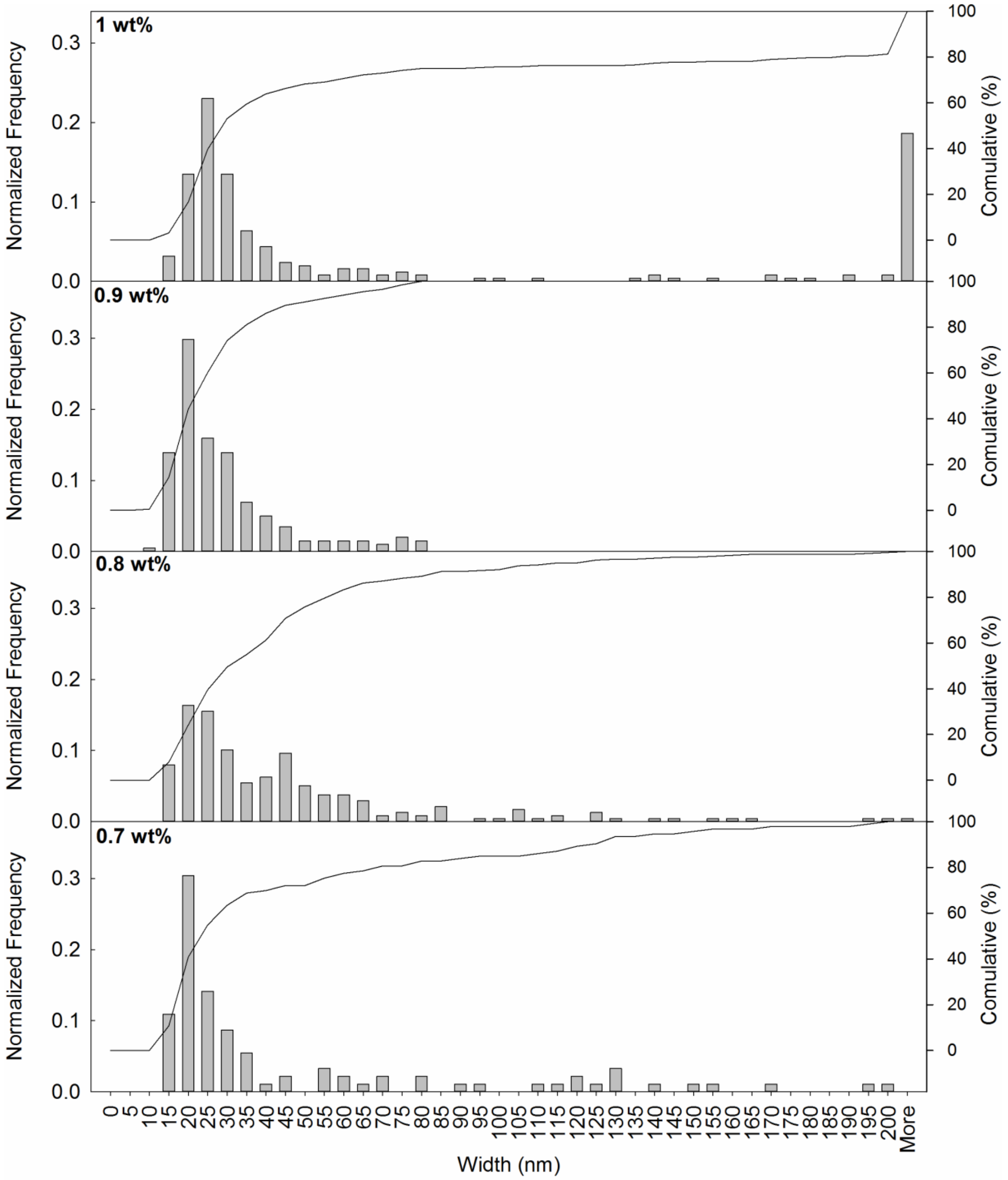

Figure 5.29 – Full set of histograms and cumulative analysis of Ca-hydrogels from 2NapFF data in concentration range from 1.0 to 0.7 wt% and the width region from 10 to 200 nm. All data sets were normalized. Each histogram was made base on over 100 measurements.

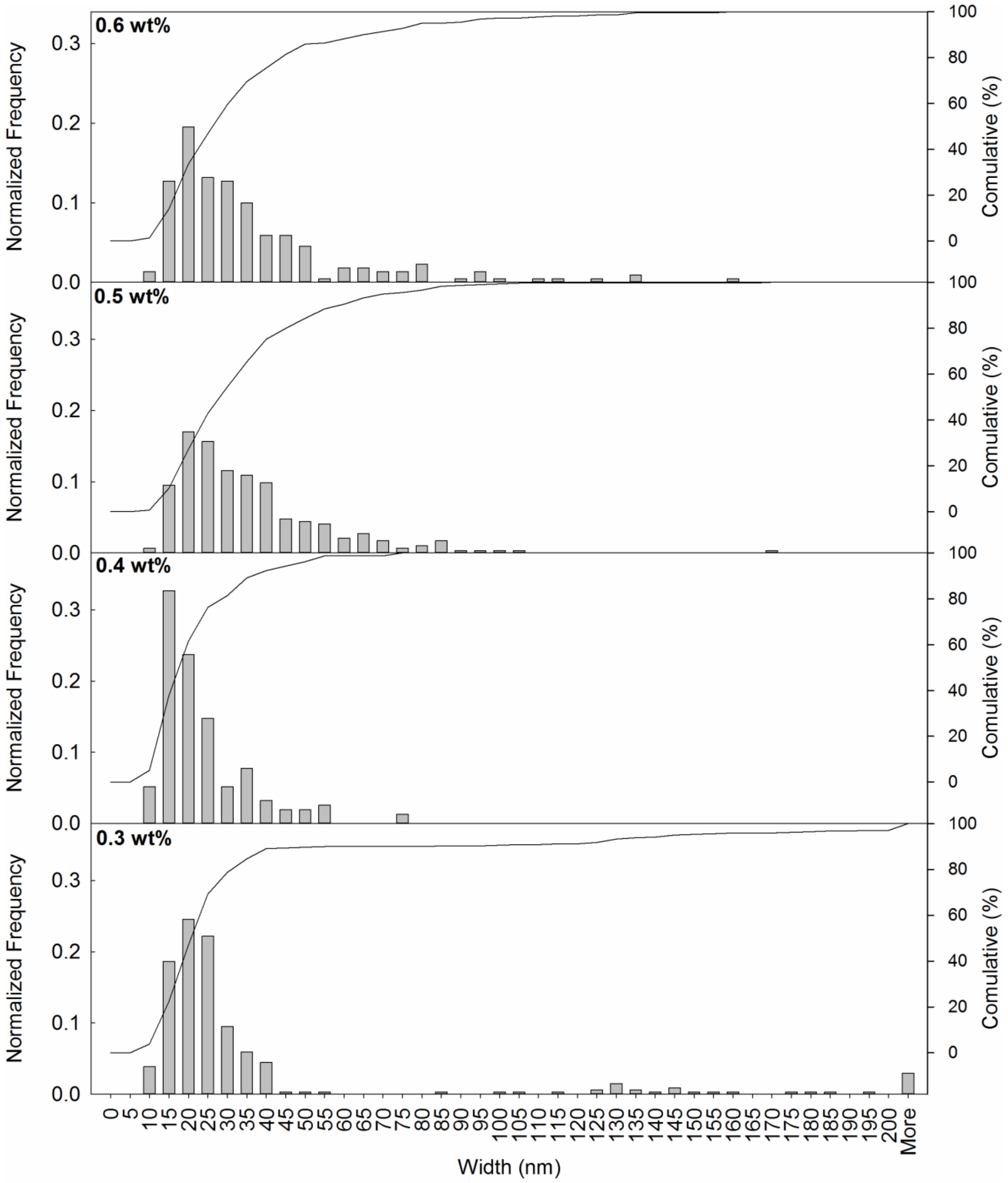

Figure 5.30 – Full set of histograms and cumulative analysis of Ca-hydrogels from 2NapFF data in concentration range from 0.6 to 0.3 wt% and the width region from 10 to 200 nm. All data sets were normalized. Each histogram was made base on over 100 measurements.

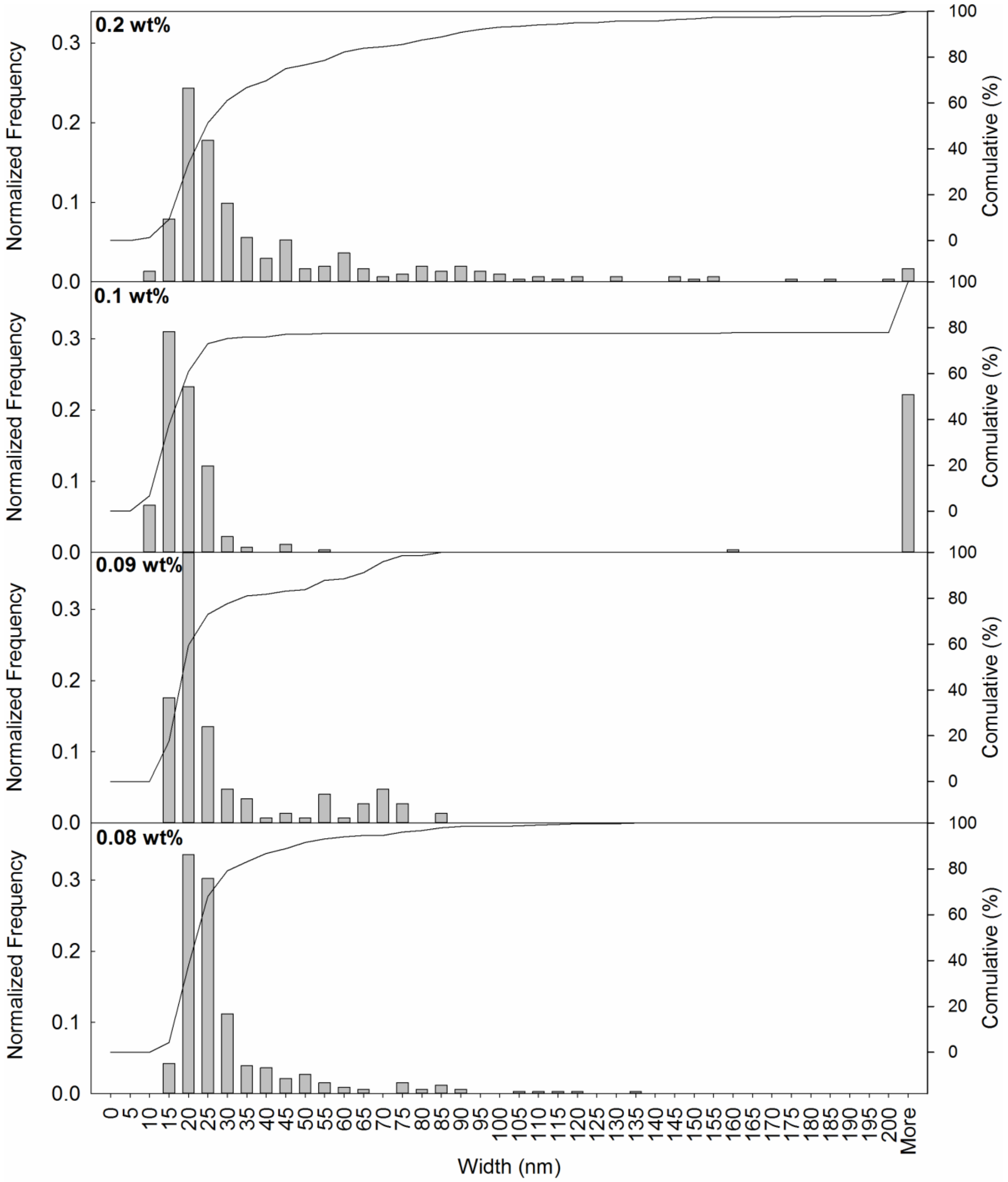

Figure 5.31 – Full set of histograms and cumulative analysis of Ca-hydrogels from 2NapFF data in concentration range from 0.2 to 0.08 wt% and the width region from 10 to 200 nm. All data sets were normalized. Each histogram was made base on over 100 measurements.

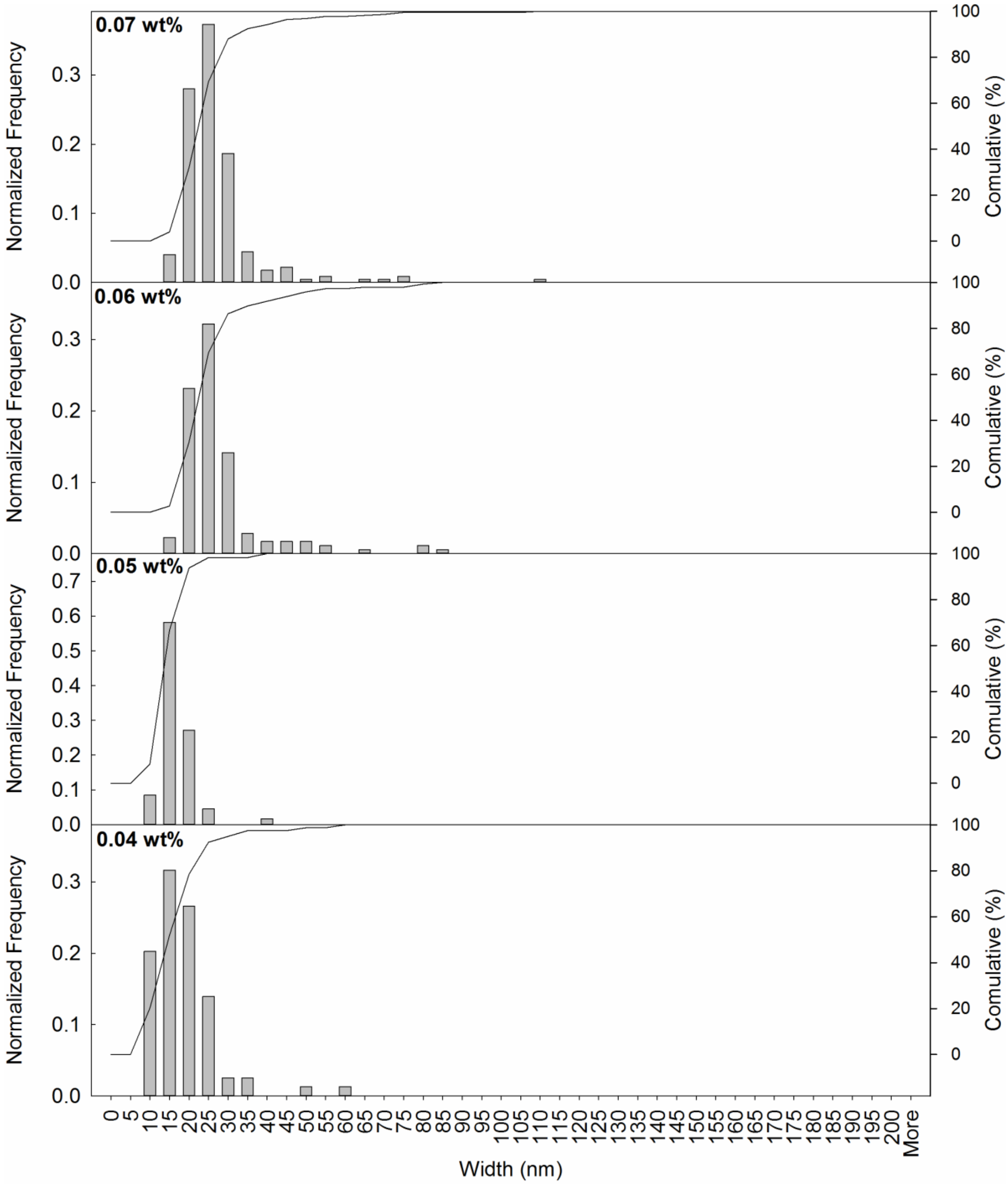

Figure 5.32 – Full set of histograms and cumulative analysis of Ca-hydrogels from 2NapFF data in concentration range from 0.07 to 0.04 wt% and the width region from 10 to 200 nm. All data sets were normalized. Each histogram was made base on over 100 measurements.

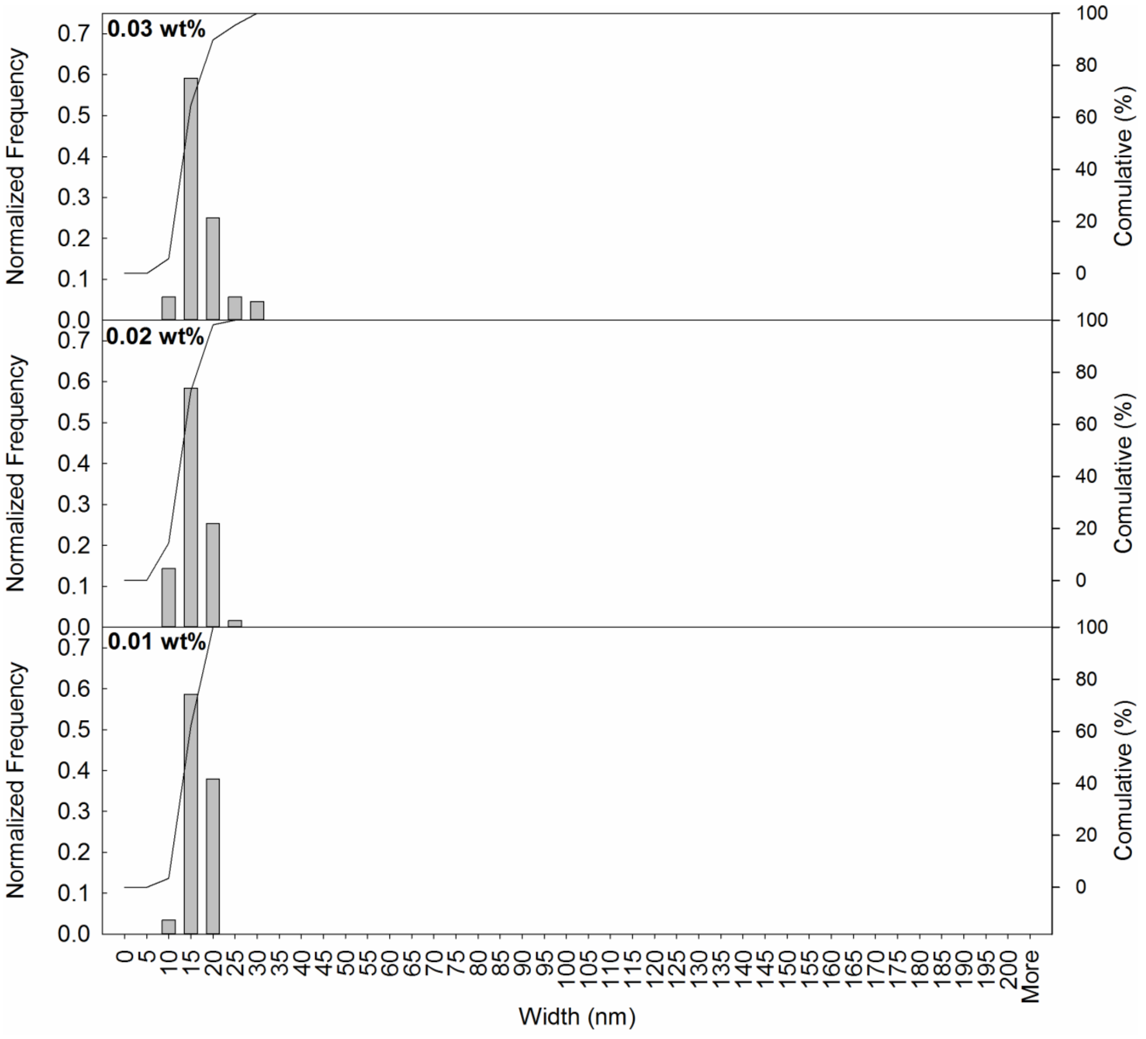

Figure 5.33 – Full set of histograms and cumulative analysis of Ca-hydrogels from 2NapFF data in concentration range from 0.03 to 0.01 wt% and the width region from 10 to 200 nm. All data sets were normalized. Each histogram was made base on over 100 measurements.

5.7. References

1. M. Bartolini, M. Naldi, J. Fiori, F. Valle, F. Biscarini, D. V. Nicolau, and V. Andrisano, *Anal. Biochem.*, 2011, 414, 215–225.
2. S. Zhang, M. A. Greenfield, A. Mata, L. C. Palmer, R. Bitton, J. R. Mantei, C. Aparicio, M. O. de la Cruz, and S. I. Stupp, *Nat. Mater.*, 2010, 9, 594–601.
3. M. Wallace, A. Z. Cardoso, W. J. Frith, J. A. Iggo, and D. J. Adams, *Chem. Eur. J.*, 2014, 20, 16484–16487.
4. Q. Lu, S. Bai, Z. Ding, H. Guo, Z. Shao, H. Zhu, and D. L. Kaplan, *Adv. Mater. Interfaces*, 2016, 3, 1500687.
5. K. Thornton, A. M. Smith, C. L. R. Merry, and R. V Ulijn, *Biochem. Soc. Trans.*, 2009, 37, 660–4.
6. D. J. Adams, M. F. Butler, W. J. Frith, and M. Kirkland, *Soft Matter*, 2009, 5, 1856–1862.
7. E. F. Banwell, E. S. Abelardo, D. J. Adams, M. A. Birchall, A. Corrigan, A. M. Donald, M. Kirkland, L. C. Serpell, M. F. Butler, and D. N. Woolfson, *Nat. Mater.*, 2009, 8, 596–600.
8. S. Mondal, L. Adler-Abramovich, A. Lampel, Y. Bram, S. Lipstman, and E. Gazit, *Nat. Commun.*, 2015, 6, 8615–5.
9. F. Tantakitti, J. Boekhoven, X. Wang, R. V. Kazantsev, T. Yu, J. Li, E. Zhuang, R. Zandi, J. H. Ortony, C. J. Newcomb, L. C. Palmer, G. S. Shekhawat, M. O. de la Cruz, G. C. Schatz, and S. I. Stupp, *Nat. Mater.*, 2016, 15, 469–476.
10. B. Adhikari and A. Banerjee, *Soft Matter*, 2011, 7, 9259–9266.

11. E. L. Bakota, O. Sensoy, B. Ozgur, M. Sayar, and J. D. Hartgerink, *Biomacromolecules*, 2013, 14, 1370–8.

12. V. Breedveld, A. P. Nowak, J. Sato, T. J. Deming, and D. J. Pine, *Macromolecules*, 2004, 37, 3943–3953.

13. V. Castelletto, G. Cheng, B. W. Greenland, I. W. Hamley, and P. J. F. Harris, *Langmuir*, 2011, 27, 2980–2988.

14. L. Chen, T. O. McDonald, and D. J. Adams, *RSC Adv.*, 2013, 3, 8714–8720.

15. G. Cheng, V. Castelletto, C. M. Moulton, G. E. Newby, and I. W. Hamley, *Microscopy*, 2010, 10, 4990–4998.

16. R. C. Claussen, B. M. Rabatic, and S. I. Stupp, *J. Am. Chem. Soc.*, 2003, 125, 12680–1.

17. X. Du, J. Zhou, J. Shi, and B. Xu, *Chem. Rev.*, 2015, 115, 13165–13307.

18. R. Huang, W. Qi, R. Su, J. Zhao, and Z. He, *Soft Matter*, 2011, 22, 245609–7.

19. R. A. Hule, R. P. Nagarkar, A. Altunbas, H. R. Ramay, M. C. Branco, J. P. Schneider, and D. J. Pochan, *Faraday Discuss.*, 2008, 139, 251–264.

20. R. Mammadov, A. B. Tekinay, A. Dana, and M. O. Guler, *Micron*, 2012, 43, 69–84.

21. R. Li, C. C. Horgan, B. Long, A. L. Rodriguez, L. Mather, C. J. Barrow, D. R. Nisbet, and R. J. Williams, *RSC Adv.*, 2015, 5, 301–307.

22. K. L. Morris, A. Rodger, M. R. Hicks, M. Debulpaep, J. Schymkowitz, F. Rousseau, and L. C. Serpell, *Biochem. J.*, 2013, 450, 275–83.

23. G. Yu, X. Yan, C. Han, and F. Huang, *Chem. Soc. Rev.*, 2013, 42, 6697–722.

24. H. v. Berlepsch, E. Brandenburg, B. Koksch, and C. Böttcher, *Langmuir*, 2010, 26, 11452–11460.

25. F. Fergg, F. J. Keil, and H. Quader, *Colloid Polym. Sci.*, 2001, 279, 61–67.

26. R. Flamia, P. A. Zhdan, M. Martino, J. E. Castle, and A. M. Tamburro, *Biomacromolecules*, 2004, 5, 1511–8.

27. S. Grigoriou, E. K. Johnson, L. Chen, D. J. Adams, T. D. James, and P. J. Cameron, *Soft Matter*, 2012, 8, 6788–6791.

28. W. Helen, P. de Leonardis, R. V. Ulijn, J. E. Gough, N. Tirelli, and P. de Leonardis, *Soft Matter*, 2011, 7, 1732–1740.

29. A. Maslovskis, J. Guilbaud, I. Grillo, N. Hodson, A. F. Miller, and A. Saiani, *Langmuir*, 2014, 30, 10471–10480.

30. L. E. R. O'Leary, J. a. Fallas, E. L. Bakota, M. K. Kang, and J. D. Hartgerink, *Nat. Chem.*, 2011, 3, 821–828.

31. K. Pagel and B. Koksch, *Curr. Opin. Chem. Biol.*, 2008, 12, 730–739.

32. A. Parbhu, H. Lin, J. Thimm, and R. Lal, *Peptides*, 2002, 23, 1265–70.

33. S. Roy, N. Javid, P. W. J. M. Frederix, D. A. Lamprou, A. J. Urquhart, N. T. Hunt, P. J. Halling, and R. V Ulijn, *Chemistry*, 2012, 18, 11723–31.

34. H. Xu, A. K. Das, M. Horie, M. S. M. S. Shaik, A. M. Smith, Y. Luo, X. Lu, R. F. Collins, S. Y. Liem, A. Song, P. L. A. Popelier, M. L. Turner, P. Xiao, I. a Kinloch, and R. V Ulijn, *Nanoscale*, 2010, 2, 960–966.

35. A. S. Mostaert, R. Crockett, G. Kearn, I. Cherny, E. Gazit, L. C. Serpell, S. P. Jarvis, and A. S. Mostaert, *Arch. Histol. Cytol.*, 2009, 72, 199–207.

36. M. M. J. M. J. Buehler and Y. C. Y. C. Yung, *Nat. Mater.*, 2009, 8, 175–188.

37. C. Rochas and E. Geissler, *Macromolecules*, 2014, 47, 8012–8017.

38. B. Ozbas, K. Rajagopal, L. Haines-Butterick, J. P. Schneider, D. J. Pochan, and J. Darrin, *J. Phys. Chem. B*, 2007, 111, 13901–8.

39. W. Wang and S. A. Sande, *Polym. J.*, 2015, 47, 302–310.

40. T. Yucel, C. C. M. Micklitsch, J. P. Schneider, and D. J. Pochan, *Macromolecules*, 2008, 41, 5763–5772.

41. V. J. Nebot and D. K. Smith, *Techniques for the Characterisation of Molecular Gels* in Functional Molecular Gels, Ed. B. Escuder, J.F. Miravet, RSC Publishing, 2014.

42. S. R. Raghavan and J. F. Douglas, *Soft Matter*, 2012, 8, 8539.

43. M. Guvendiren, H. D. Lu, and J. A. Burdick, *Soft Matter*, 2012, 8, 260.

44. S. Tsonchev, K. L. Niece, G. C. Schatz, M. A. Ratner, and S. I. Stupp, *J. Phys. Chem. B*, 2008, 112, 441–447.

45. S. Banta, *WO Pat. WO/2008/011,204*, 2008.

46. S. Fleming and R. V Ulijn, *Chem. Soc. Rev.*, 2014, 43, 8150–77.

47. I. W. Hamley, *Soft Matter*, 2011, 7, 4122–4138.

48. I. Usov and R. Mezzenga, *Macromolecules*, 2015, 48, 1269–1280.

49. W. S. S. Rasband, *U. S. Natl. Institutes Heal. Bethesda, Maryland, USA*.

50. J. Schindelin, I. Arganda-Carreras, E. Frise, V. Kaynig, M. Longair, T. Pietzsch, S. Preibisch, C. Rueden, S. Saalfeld, B. Schmid, J.-Y. Tinevez, D. J. White, V. Hartenstein, K. Eliceiri, P. Tomancak, and A. Cardona, *Nat. Methods*, 2012, 9, 676–82.

51. P. H. J. Kouwer, M. Koepf, V. A. Le Sage, M. Jaspers, A. M. van Buul, Z. H. Eksteen-Akeroyd, T. Woltinge, E. Schwartz, H. J. Kitto, R. Hoogenboom, S. J. Picken, R. J. M. Nolte, E. Mendes, and A. E. Rowan, *Nature*, 2013, 493, 651–655.

52. D. J. Adams, L. M. Mullen, M. Berta, L. Chen, and W. J. Frith, *Soft Matter*, 2010, 6, 1971.

53. M. Berta, W. J. Frith, M. Kirkland, R. Holman, and P. Schuetz, *Annu. Trans. Nord. Rheol. Soc.*, 2013, 21, 273–280.

54. F. C. MacKintosh, J. Käs, and P. A. Janmey, *Phys. Rev. Lett.*, 1995, 75, 4425–4428.

55. I. T. Norton and W. J. Frith, *Food Hydrocoll.*, 2001, 15, 543–553.

56. L. Chen, J. Raeburn, S. Sutton, D. G. Spiller, J. Williams, J. S. Sharp, P. C. Griffiths, R. K. Heenan, S. M. King, A. Paul, S. Furzeland, D. Atkins, and D. J. Adams, *Soft Matter*, 2011, 7, 9721–9727.

57. M. Wallace, D. J. Adams, and J. A. Iggo, *Soft Matter*, 2013, 9, 5483–5491.

58. J. Raeburn, C. Mendoza-Cuenca, B. N. Cattoz, M. A. Little, A. E. Terry, A. Zamith Cardoso, P. C. Griffiths, and D. J. Adams, *Soft Matter*, 2015, 11, 927–935.

59. R. L. Baldwin, *Biophys. J.*, 1996, 71, 2056–63.

60. A. Ghosh, M. Haverick, K. Stump, X. Yang, M. F. Tweedle, and J. E. Goldberger, *J. Am. Chem. Soc.*, 2012, 134, 3647–3650.

61. B. Ozbas, J. Kretsinger, K. Rajagopal, J. P. Schneider, and D. J. Pochan, *Macromolecules*, 2004, 37, 7331–7337.

62. S. Roy, R. V Ulijn, N. Javid, J. Sefcik, and P. J. Halling, *Langmuir*, 2012, 28, 16664–16670.

63. Y. Zhang and P. S. Cremer, *Curr. Opin. Chem. Biol.*, 2006, 10, 658–63.

64. L. Chen, S. Revel, K. Morris, L. C. Serpell, and D. J. Adams, *Langmuir*, 2010, 26, 13466–13471.

65. A. Z. Cardoso, A. E. Alvarez Alvarez, B. N. Cattoz, P. C. Griffiths, S. M. King, W. J. Frith, and D. J. Adams, *Faraday Discuss.*, 2013, 166, 101–116.

66. J. Raeburn, G. Pont, L. Chen, and Y. Cesbron, *Soft Matter*, 2012, 8, 1168–1174.

67. M. Bates, B. Huang, G. T. Dempsey, and X. Zhuang, *Science*, 2007, 317, 1749–1753.

68. D. J. Marchand, E. Hsiao, and S. H. Kim, *Langmuir*, 2013, 29, 6762–6769.

69. I. Casuso, F. Rico, and S. Scheuring, *J. Mol. Recognit.*, 2011, 24, 406–413.

70. K. A. Houton, K. L. Morris, L. Chen, M. Schmidtmann, J. T. A. Jones, L. C. Serpell, G. O. Lloyd, and D. J. Adams, *Langmuir*, 2012, 28, 9797–806.

71. C. Whitehouse, J. Fang, A. Aggeli, M. Bell, R. Brydson, C. W. G. Fishwick, J. R. Henderson, C. M. Knobler, R. W. Owens, N. H. Thomson, D. A. Smith, and N. Boden, *Angew. Chem. Int. Ed.*, 2005, 44, 1965–1968.

72. D. A. White, A. K. Buell, T. P. J. Knowles, M. E. Welland, and C. M. Dobson, *J. Am. Chem. Soc.*, 2010, 132, 5170–5175.

73. D. Homouz, M. Perham, A. Samiotakis, M. S. Cheung, and P. Wittung-Stafshede, *Proc. Natl. Acad. Sci. U. S. A.*, 2008, 105, 11754–9.

74. N. Javid, S. Roy, M. Zelzer, Z. Yang, J. Sefcik, and R. V. Ulijn, *Biomacromolecules*, 2013, 14, 4368–4376.

75. J. Rosen, Y. C. Y. Kim, and J. Mittal, *J. Phys. Chem. B*, 2011, 115, 2683–2689.

76. M. M. Hassan, A. D. Martin, and P. Thordarson, *J. Mater. Chem. B*, 2015, 3, 9269–9276.

77. G. Pont, L. Chen, D. G. Spiller, and D. J. D. Adams, *Soft Matter*, 2012, 8, 7797–7802.

78. Y. Chen, H. X. Gan, and Y. W. Tong, *Macromolecules*, 2015, 48, 2647–2653.

79. L. Deng, Y. Zhao, H. Xu, and Y. Wang, *Appl. Phys. Lett.*, 2015, 107, 43701.

80. A. D. Martin, A. B. Robinson, and P. Thordarson, *J. Mater. Chem. B*, 2015, 3, 2277–2280.

81. T. P. J. Knowles and M. M. J. Buehler, *Nat. Nanotechnol.*, 2011, 6, 469–479.

82. A. Aggeli, M. Bell, N. Boden, J. N. Keen, P. F. Knowles, T. C. B. McLeish, M. Pitkeathly, and S. E. Radford, *Nature*, 1997, 386, 259–262.

83. J. D. Hartgerink, E. Beniash, and S. I. Stupp, *Proc. Natl. Acad. Sci. U. S. A.*, 2002, 99, 5133–5138.

84. A. Pinazo, L. Pérez, M. R. Infante, and R. Pons, *Phys. Chem. Chem. Phys.*, 2004, 6, 1475–1481.

85. M. Bergström and J. S. Pedersen, *Langmuir*, 1999, 15, 2250–2253.

86. J. Xia, D. Liu, and C. L. Zhong, *Phys. Chem. Chem. Phys.*, 2007, 9, 5267–5273.

87. J. Raeburn, L. Chen, S. Awhida, R. Deller, M. Vatish, I. Matthew, and D. J. Adams, *Soft Matter*, 2015, 11, 3706-13.

88. A. Z. Cardoso, L. L. E. Mears, B. N. Cattoz, P. C. Griffiths, R. Schweins, and D. J. Adams, *Soft Matter*, 2016, 12, 3612–3621.

89. L. Chen, S. Revel, K. Morris, C. S. L, D. J. Adams, L. C. Serpell, *Langmuir*, 2010, 26, 13466–13471.

90. M. M. Davis and H. B. Helzer, *Anal. Chem.*, 1966, 38, 451–461.

91. J. Jose, Y. Ueno, and K. Burgess, *Chem. Eur. J.*, 2009, 15, 418–423.

92. J. Raeburn, A. Zamith Cardoso, and D. J. Adams, *Chem. Soc. Rev.*, 2013, 42, 5143–56.

93. I. Usov, J. Adamcik, and R. Mezzenga, *ACS Nano*, 2013, 7, 10465–10474.

6. Conclusion and future work

Supramolecular peptide hydrogels can form adaptable materials over four orders of magnitude in mechanical properties. Understanding the self-assembly kinetic pathway, gelator-solvent phase diagram and the links between structure and gelator properties over multiple length scales gives some degree of prediction of the mechanical properties of peptide hydrogels.

The kinetic pathway of the hydrogelation can be controlled by the pK_a of carbonic acid with the use of gaseous CO_2 (Chapter 2). When the apparent pK_a of the gelator is close to the pK_a of carbonic acid and the solution is not a worm-like micellar phase at high pH, a hydrogel membrane is formed as opposed to a bulk gel. The CO_2 triggered hydrogels can also form bulk hydrogels for gelators with a pK_a above the pK_a of carbonic acid. The hydrogel membranes have different mechanical properties to bulk hydrogels and can be controlled by a variety of methods. Although the kinetic pathway is not the sole determinant of the final rheological properties, the different self-assembly pathways form nanostructures with different diameters and degrees of stiffness. Further studies on the impact of hydrogel history could extend the knowledge of the gelation process. Use of the CO_2 method to trigger gelation may enable novel applications in the biomedical setting where CO_2 is already used in low quantities.[43,86]

The phase diagram of 2NapFF was obtained at pH 10.5 and 25 °C (Chapter 3). The temperature dependent phase diagram was also possible to obtain for the region of worm-like micellar structures between 15 to 45 °C. The 2NapFF gelator can form hierarchical structures in the solution phase. As with other related surfactants, phase transitions in the peptide gelator solution phase depend on concentration and temperature.

In dipeptide systems at concentrations between 0.001 and 1 wt% the following can be formed: a free-flowing molecular phase, a spherical aggregate micellar phase, a worm-like micellar phase or a packed worm-like micellar phase. Conductance and rheological measurements are most informative to characterise the solution phase of peptide supramolecular hydrogels.

A correlation between the solution phase properties and the hydrogel properties was found for 2NapFF with the Ca-switch methods across a concentration range from

0.001 to 1.0 wt% (Chapter 4). It was found that the 2NapFF solution phase already has the characteristic β-sheet aggregates present in the corresponding Ca-hydrogel phase, for concentrations above 0.3 wt %. However, for lower concentrations, sphere-to-worm transitions occur between the cmc_1 and cmc_2 as well as possible molecular packing transformations. Further research with the same gelator using other methods to form a hydrogel should reveal the domain of applicability of the links observed here between solution and hydrogel phase.

A combination of microscopy techniques can be adjusted to non-covalently bound peptide supramolecular hydrogels to reveal optical and structural properties at different length scales. In Chapter 5, atomic force microscopy (AFM), scanning electron microscopy (SEM) and laser scanning confocal microscopy (LSCM) were used to further investigate the structural features of the solutions and hydrogels. Hydration and the location of the interaction used for the measuring technique (e.g. liquid-air interface or bulk) should be taken into account when measuring peptide assemblies by surface tension, microscopy and rheology. With LSCM, the microstructure can be accurately represented and, with the use of FibreApp image analysis software, peptide-based hydrogel systems can be studied with regards to the link between their microstructure and their mechanical properties. Our LSCM results with 2NapFF show that the microstructure is linearly correlated with the mechanical properties measured by oscillatory rheology. Microscopy techniques gave evidence that 2NapFF forms hierarchical structures in the solution phase and in the hydrogel phase by the ImageJ derived histogram analysis of the SEM and AFM images. The diameter of the primary fibres was only accessible by SANS,[265] with different levels of bundling features shown by very polydisperse size measurements for both solutions and hydrogels by SEM and LSCM. The persistence length, L_P of the fibre structures is different at different hierarchical levels. At the microscale, measured by LSCM, the L_P of the fibre bundles appears to be linearly correlated with the mechanical properties of the hydrogels measured by oscillatory rheology. At the nanoscale, measured by SEM and AFM, the persistence length is approximately constant across length scales and in the order of a few micrometres for both the solution phase and the hydrogel phase. The 2NapFF hydrogel phase has more randomly oriented worms/fibres than the solution phase, which was shown to form aligned domains at both the nanoscale and microscale. FibreApp analysis of low molecular weight peptide hydrogels reveals the orientation distribution and a 2D order parameter analysis. This result agrees with our previous findings with NMR spectroscopy.[3] The AFM images of 2NapFF Ca-hydrogel samples show periodicity along the fibre axis. However, the accurate quantification of the pitch size requires further analysis and exploration with different sample preparations in order to investigate less crowded environments.

In summary, this Thesis confirms that distinctions in self-assembly process allow for a broad range in the kinetic mechanism of hydrogelation, the final material properties and the structure of supramolecular peptide-based hydrogels.[3] A new CO_2 pH-switch method to form hydrogels with peptide-based LMWG self-assembly was developed and explained. The solution phase of an interesting gelator was fully characterised and the phenomena of the transition to peptide hydrogels was described. Links between the solution phase and the peculiar peptide hydrogels were found, which allow some predictability of the outcome of a gelation trigger based on the solution phase properties. Finally, new analysis open source software was used for the first time with peptide-based hydrogel microscopy images at different length scales and this results revealed the importance of each of the length scales to the final mechanical properties and dynamics of the hydrogel network.

In the development of this work, one should consider to establish the procedure for better understanding of the type of cross-links between the hydrogel fibres and identification of chemical groups at the surface of the peptide fibres. Finally, it is likely that understanding the multi-component packing forces would give increased control to make tuned functional-materials beyond structuring.